Enhanced energy storage performance of BaTiO$_3$ and BiFeO$_3$ - based dielectric ceramics and their thin films for capacitor applications

A Thesis Submitted to

Indian Institute of Technology Guwahati

for the Degree of

Doctor of Philosophy

By

Shashi Priya Balmuchu

Under the supervision of

Prof. Pamu Dobbidi

Department of Physics
Indian Institute of Technology Guwahati
Guwahati-781039, Assam, India
April, 2024


भारतीय प्रौद्योगिकी संस्थान गुवाहाटी
Indian Institute of Technology Guwahati

INDIAN INSTITUTE OF TECHNOLOGY GUWAHATI
Department of Physics
Guwahati – 781039

STATEMENT

The present thesis entitled, "**Enhanced energy storage performance of $BaTiO_3$ and $BiFeO_3$ - based dielectric ceramics and their thin films for capacitor applications,**" has been carried out by me under the supervision of Prof. Pamu Dobbidi, Department of Physics, Indian Institute of Technology Guwahati. This work has not been submitted elsewhere for the award of any degree.

April, 2024

Shashi Priya Balmuchu
Department of Physics,
Indian Institute of Technology Guwahati,
Guwahati – 781 039

भारतीय प्रौद्योगिकी संस्थान गुवाहाटी
Indian Institute of Technology Guwahati

INDIAN INSTITUTE OF TECHNOLOGY GUWAHATI

Department of Physics

Guwahati – 781039

CERTIFICATE

It is certified that the work described in this thesis, entitled "**Enhanced energy storage performance of $BaTiO_3$ and $BiFeO_3$ - based dielectric ceramics and their thin films for capacitor applications**", done by Ms. Shashi Priya Balmuchu, a Ph.D. student of the Department of Physics, Indian Institute of Technology Guwahati, for the award of the degree of *Doctor of Philosophy* has been carried out under my supervision. This work has not been submitted elsewhere for the award of any degree.

Pamu Dobbidi

Professor,

Department of Physics,

Indian Institute of Technology Guwahati
Guwahati – 781 039.

April, 2024

.


Indian Institute of Technology Guwahati

Dedicated to Singhbonga

and my family

ACKNOWLEDGMENTS

Great achievement is usually born of great sacrifice and is never the result of selfishness."**—** Napoleon Hill.

It is well said by the American author that to achieve something great, one must be willing to give up something of value, whether it is time, energy, resources, or other things. I thought getting a Ph.D. wasn't really my thing quite a few times, but fortunately, things worked out, and I received countless acts of kindness, support, and encouragement from people around me, which kept me going all the way through. Five and half years of consistent hard work, belief, and devotion made this Ph.D. journey accomplished.

Firstly, I am deeply indebted to my thesis supervisor, Prof. D. Pamu, for his guidance, advice, and fruitful criticism. His knowledge, skills, and expertise give me strength, motivation, and direction to think, express, and do my research work freely. I appreciate his willingness to hear the research problem patiently and provide a solution for it. I would also like to acknowledge the freedom and independence provided to us to utilize the lab and instrumental facilities.

I want to extend my sincere thanks to my doctoral committee members, Prof. S. Ravi (Chairman), Prof. Dilip Pal, and Prof. Nageswar Rao Peela, for their academic guidance throughout my research journey. I would like to appreciate their valuable suggestions and advice, which helped me to improve my research work.

I am incredibly grateful to Prof. A Perumal, head of the Department of Physics, and former head of the department, Prof. Subhradeep Ghosh, for their academic support and guidance. I want to thank them for availing of departmental facilities. I am also grateful to all the faculty members of the Physics department. I would also like to thank Dr. Sidananda Sarma and Mr. Aditya Kalita Sir for their technical assistance. My special thanks to all scientific officers and staff members in our department, central instruments facility, and center for nanotechnology.

I sincerely acknowledge the financial support from the Indian Institute of Technology Guwahati and the Ministry of Human Resource and Development for completing my research and thesis work. Also, I would like to express my heartfelt thanks to Science and Engineering Research Board (SERB)/Department of Science and Technology (DST), New Delhi; the Board of Research in Nuclear Sciences (BRNS), Mumbai; Defense Research and Development Organization (DRDO), New Delhi; and Board of Research in Fusion Science & Technology (BRFST), Gandhinagar, Gujarat through research projects for various experimental facilities. The XRD facility provided by DST, New Delhi, through the FIST program [SR/FST/PSII-020/2009] is also acknowledged.

I am also grateful to my seniors Dr. Mahesh Peddigari, Dr. Pallabi Gogoi, Dr. Srinivas Pattipaka, Dr. Susmita Rabha, Dr. Apurba Das, Dr. Prajna Paramita Mohapatra, and Sunil Gone for sharing their knowledge and their guidance for the instrumental operations. I want to thank my research team members Radhika, Dr. Anil, Subingya, Jaharlal, Karanjit, Somnath, Naphisa, Ganesh, Dipankar, Jogi Veera, Suchandra, Rekha, Dr. Ravi, Rajib, Dhanraj and all other lab members for their analytical and technical support. I want to thank them for their kind cooperation and for making a healthy environment. I would also like to acknowledge my Ph.D. seniors: Dr. Indu Kalpa Dihing, Dr. Ranjan Kalita, Dr. Karuna Sindhu Mallik, Dr. Nagendra Kumar, Dr. Sasmita Behera, and Dr. Pragya Gupta from the Department of Physics for their elderly suggestions and support. I want to thank my friends at IIT Guwahati, especially (2018) all batchmates, Ankita Di, Susmita Di, Dhanesh, Madonna, Sounak da, Anupama, Himali, Jagdish, Didwmsha, and Jinnat for creating a friendly and homely atmosphere. I would also like to thank Dhansingh, Neha, Ajit, Hilter, Abhinav, Nirmala, Sandeep, Sarita, Purnima, and Manisha for their encouraging words and mental support.

Finally, I would like to express my deepest gratitude to my family, especially my parents (Laxman Kr. Balmuchu and Yashmati Balmuchu), my grandparents (Lt. Mangu Balmuchu and Lt. Nanhi Balmuchu), brothers (Manjeet, Vikram, and Shubham), sisters (Neetu and Rajlaxmi), Aunties (Basanti Balmuchu and Sumitra Kalundia), my nieces (Kavya, Divya, Navya, and Shreya) and all family members and relatives for their evergreen blessings and moral support.

I want to acknowledge Almighty Singhbonga for giving me the strength and positive energy to accomplish my goal and desire. I am grateful to everyone I encountered on my voyage for helping to make my Ph.D. journey memorable for me.

Shashi Priya Balmuchu

IIT Guwahati, Guwahati

Assam, India, 781039

Abstract

The rising global demand for energy consumption for meeting the commercial and economic growth concerns for sustainable energy resources, generation, harvesting, and storage. The energy storage devices include electrochemical capacitors, batteries, fuel cells, and dielectric capacitors. Among these storage devices, dielectric ceramics offer inherently high power density and ultrafast charging/discharging time ranging from micro-nano to second time. This thesis mainly focuses on lead-free dielectric ceramics and thin films for energy storage applications. A detailed investigation of two systems, (1-x)$BaTiO_3$-$x$$BiFeO_3$ (BTBF) and (1-x)$BaTiO_3$-$x$$Bi[Zn_{2/3}(Nb_{0.85}Ta_{0.85})_{1/3}]O_3$ (BT-BZNT) from $BaTiO_3$-$BiMeO_3$ (where *Me* is trivalent or average trivalent metal ions) solid solution family in the bulk form is carried out. The ferroelectric studies for both compositions are analyzed to evaluate energy storage performance. The BTBF3 composition displayed a W_{rec} and η (%) of ~ 40 mJ/cm^3 and 60.92%, respectively, at 25 kV/cm applied field, which is sufficiently lower as compared to other $BaTiO_3$-$BiMeO_3$ systems. A significant improvement in energy storage performance is observed in BT-BZNT ceramics. A remarkably high W_{rec} of 2.06 J/cm^3 with an η (%) of 78% is achieved for BT-BZNT3 ceramics at an applied field of 180 kV/cm. The ultrahigh-energy efficiency of up to 96% is observed for higher concentrations in BT-BZNT ceramics. Herein, BT-BZNT3 and BT-BZNT4 ceramics exhibited a comparable energy storage performance at a lower applied field of 180 kV/cm, demonstrating the excellence of BT-BZNT ceramics over other $BaTiO_3$-$BiMeO_3$ family.

Similarly, the BLFO thin films at different oxygen partial pressures (OPPs) (15, 20, 25, and 30 SCCM) are deposited on n-type silicon and quartz substrates using pulsed laser deposition technique. Among the deposited films, 20 SCCM deposited films exhibited an enhanced energy storage density of 2.09 J/cm^3, having an energy efficiency of 78.42% at the applied field of 488 kV/cm. The lower leakage current density of ~1.08×10^{-7} is estimated for 20 SCCM film, attributing to dense microstructure and favorable oxygen ambiance. It is known that the physical properties of ferroelectric thin films are very sensitive to the presence of interfaces. These interfaces will inevitably influence the electrical properties and parameters of ferroelectric devices. Thus, the BLFO/BTO bi-layer thin films with varying top layer thicknesses and BZNT/BTO multi-layer heterostructures with alternate stacking of BTO and BZNT layers are deposited on n-type and Pt Si substrates. The heterostructure with

BLFO/BTO3 displays an improved W_{rec} of 11.65 J/cm^3 with η of 85% at 746 kV/cm. The interfacial layer between BLFO and BTO enhances the energy density and efficiency ascribed to the enhancement of E_{BDS} induced via the interfacial barrier effect on the conducting filaments. Similarly, a remarkable enhancement in recoverable energy density (W_{rec}) of 52.19 J/cm^3 with energy efficiency (η) of 92.21% at 2.58 MV/cm is achieved for the higher number of stacking layered films among the BZNT/BTO multi-layer films. The enhancement in energy storage performance may be attributed to the intervening ferroelectric BTO and BZNT layers in the multilayered BZNT/BTO3 films. In both cases, a low value of leakage current density in the order of ~10^{-6} A/cm^2 and ~10^{-7} A/cm^2 is also observed for BLFO/BTO3 and tetra-layer BZNT/BTO films at an applied field of ± 500 kV/cm respectively. The improved response of bi-layer (BLFO/BTO) and multi-layer (BZNT/BTO) films assures their appropriateness for energy storage device applications.

Publications

Refereed Journal

1. **Balmuchu, S.P.**, Mangalampalli, S.K. and Dobbidi, P., 2022. Dielectric spectroscopy and ferroelectric studies of multiferroic bismuth ferrite modified barium titanate ceramics for energy storage capacitor applications. **Materials Science and Engineering: B**, 282, p.115791.
2. **Balmuchu, S.P.** and Dobbidi, P., 2022. The effect of La doping on multiferroic $BiFeO_3$ ceramic through structural, dielectric, magnetic, ferroelectric, and optical studies. **Physica B: Condensed Matter**, 638, p.413937.
3. **Balmuchu, S.P.**, Sahu, S. and Dobbidi, P., 2023. Enhanced magnetic properties and leakage current mechanism in bismuth lanthanum ferrite thin films coupled with impedance and magnetic studies. **Vacuum**, p.112356.
4. **Balmuchu, S.P.**, Radhika, E. and Dobbidi, P., 2023. The impact of oxygen partial pressure in modifying energy storage property of lanthanum doped multiferroic bismuth ferrite thin films deposited via pulsed laser deposition. **Journal of Energy Storage**, 71, p.108179.
5. **Balmuchu, S.P.**, Sahu, S. and Dobbidi, P., 2024. The effect of interfacial charge-induced multiferroic properties of $Bi_{0.993}La_{0.007}FeO_3/BaTiO_3$ bilayer thin films: Performance modulation and energy storage applications. **Surfaces and Interfaces**, 44, p.103653.
6. **Balmuchu, S.P.** and Dobbidi, P., 2024. Reduced leakage current and enhanced energy storage performance of BZNT/BTO multilayer structures: Implications in electronic devices. **Applied Surface Science**, 652, p.159358.
7. **Balmuchu, S.P.**, Malapati, V., Chilaka, R.R. and Dobbidi, P., 2024. Effective strategy for achieving superior energy storage performance in lead-free $BaTiO_3$–$Bi(Zn_{2/3}(Nb_{0.85}Ta_{0.15})_{1/3})O_3$ ferroelectric ceramics. **Ceramics International**.

Publications outside thesis

1. Khatun, H., Pamu, D., **Balmuchu, S.P.**, Singh, N.S. and Sarma, U., 2023. Power enhancement of piezoelectric energy harvester using ZnOnf-PDMS composite with PVDF filler. ***Sensors and Actuators A: Physical***, *364*, p.114812.
2. **Balmuchu, S.P.**, Pathak, R. and Dobbidi, P., 2023. Composition-driven (barium titanate-based ceramics) pseudo-binary system for energy storage applications through ferroelectric studies. ***Applied Physics A***, *129*(11), p.767.

3. Radhika, E., **Balmuchu, S.P.**, Sridhar, V. and Dobbidi, P., 2023. Effect of ZnO on structural and dielectric properties of AlN ceramics. **Journal of Materials Science: Materials in Electronics**, 34(26), p.1799.
4. Rabha, S., Das, A., Gonne, S., Mohapatra, P.P., **Balmuchu, S.P.**, Radhika, E. and Dobiddi, P., 2022. Dielectric and leakage characteristics of MTO/STO bilayer films deposited by RF magnetron sputtering technique for optical and electronic applications. **Materials Science and Engineering: B**, 282, p.115790.

5. **Balmuchu, S.P.**, Bora, S. and Dobbidi, P., 2022. The influence of Mg^{2+} on bismuth sodium–potassium titanate ceramics on the structural, dielectric, and ferroelectric properties. Journal of Materials Science: Materials in Electronics, 33(34), pp.25704-25716.
6. **Balmuchu, S.P.** and Dobbidi, P., 2021. Temperature-dependent broadband dielectric and ferroelectric properties of $Ba_{(1-x)}Sr_xTiO_3$ ceramics for energy storage capacitor applications. **Journal of Materials Science: Materials in Electronics**, 32, pp.9623-9639.

Conferences and workshops attended

1. Presented poster at the "International Conference On Advanced Materials And Mechanical Characterization (ICAMMC-2021)" (VIRTUAL MODE, 2- 4 December 2021), organized by the Department of Physics and Nanotechnology and Department of Mechanical Engineering, SRM Institute Of Science And Technology in association with the Indian Institute Of Science (IISc), Indian Institute of Technology (IIT) Delhi, IIT Madras, IIT Hyderabad, IIT Indore, Indian Institute Of Metals Chennai Chapter, ASM International Chennai Chapter, Indian Ceramic Society, Indian Physics Association, and American Ceramic Society India Chapter.
2. Presented a paper and participated at the 65th DAE Solid State Physics Symposium Organised by: Bhabha Atomic Research Center, Mumbai Sponsored by: Board of Research in Nuclear Sciences (BRNS) Department of Atomic Energy, Government of India held at Bhabha Atomic Research Centre, Mumbai, during 15 - 19 December 2021
3. Effect of oxygen gas pressure in lanthanum doped multi-ferroic bismuth ferrite thin films deposited via Pulsed laser deposition technique, Shashi Priya Balmuchu given oral presentation in the 2022 The 6th International Conference on Materials Sciences and Nanomaterials (ICMSN 2022) (virtual mode) London, United Kingdom July 12-14, 2022.
4. Dielectric and ferroelectric properties of $BaTiO_3$-$Bi(Zn_{2/3}(Nb_{0.85}Ta_{0.15})_{1/3})O_3$ composites

for energy storage applications, Shashi Priya Balmuchu presented an oral and poster in the 66th DAE Solid State Physics Symposium held at Birla Institute of Technology Mesra, Ranchi, Jharkhand, India on December 18-22, 2022.

5. Presented poster at the "International Conference on Magnetic Materials and Applications (ICMAGMA-2023) 04 - 06 Dec. 2023 held at Ramoji Film City, Hyderabad, organized by the Magnetics Society of India (MSI) in association with Defence Metallurgical Research Laboratory (DMRL) and Mishra Dhatu Nigam Limited (MIDHANI).

Table of Contents

2 Materials synthesis

List of Figures

List of Tables

List of symbols and abbreviations

Units of measurements

M	Meter
cm	Centimeter
µm	Micrometer
nm	Nanometer
Å	Angstrom
°C	Centigrade (degree)
K	Kelvin
Hz	Hertz
kHz	Kilo Hertz
MHz	Mega Hertz
GHz	Giga Hertz
h	Hour
F	Farad
pC	Pico Coulomb
µC	Micro Coulomb
N	Netwon
V	Volt
eV	Electron volt
Pa	Pascal
GPa	Giga Pascal
g	gram
W	Watt
esu	Electrostatic unit
A	Ampere

Electrical Measurements

ε_r	Relative permittivity
$\tan\delta$	Loss tangent
A	Area of electrodes
ε_r	relative permittivity
ε_0	Permittivity of vacuum
ε'	Real part of permittivity
ε''	Imaginary part of permittivity
σ_{ac}	AC-conductivity
χ_e	Electric susceptibility
J	Leakage current density
E	Electric field
C	Capacitance
d	Thickness
σ	Stress
η	Strain
P	Polarization
P_{max}	maximum polarization
P_r	remnant polarization
E_c	Coercive field
E_{BDS}	Electric breakdown strength
P-E	Polarization electric field
p	Dipole moment
V	Unit cell volume
Z	Impedance
Z'	Resistance
Z''	Reactance
f_0	Resonant frequency
f_a	Anti-resonance frequency

Q	Quality factor
τ	Relaxation time
DC	Direct current
AC	Alternating current
γ	Degree of diffuseness
E_A	Activation energy
ω	Angular frequency
k_B	Boltzmann constant
T_C	Curie temperature
ρ_{ac}	AC-resistivity
ξ	Decay length
$N(E_F)$	Density of states
R_H	Hopping length
W_H	Hopping energy

Optical Measurements

α	Absorption coefficient
n	Refractive index
λ	wavelength
E_g	Optical bandgap
h	Planck’s constant
z_0	Rayleigh length
λ	Wavelength
c	Velocity of light
$h\nu$	Photon energy

Other parameters

θ	Angle
D	Crystallite size

FWHM	Full width at half maximum
a, b, c	Lattice parameters
χ^2	Chi-square
R_{Bragg}	Bragg factor
Rf	Profile factor
F	Orientation factor
ρ	Density
wt.	Weight
rms	Root mean square
CSSR	Conventional solid-state reaction
PLD	Pulsed laser deposition
RT	Room temperature
RF	Radio frequency
FE	Ferroelectric
AFE	Antiferroelectric
RFE	Relaxor ferroicelectric
PNR	Polar nanoregions
OMP	Oxygen mixing percentage
OPP	Oxygen partial pressure
SCCM	Standard Cubic Centimeter per Minute
VRH	Variable range hopping
CCD	Charge-coupled device
SCLC	Space charge limited conduction
SE	Spectroscopic ellipsometry
SEA	Spectroscopy ellipsometry analyzer

SPDR	Split post dielectric resonator
MIM	Metal-insulator-metal
XRD	X-Ray diffraction
AFM	Atomic force microscopy
XPS	X-ray Photoelectron spectroscopy
SEM	Scanning electron microscopy
FESEM	Field emission scanning electron microscopy
FETEM	Field emission transmission electron microscope
HRTEM	High-resolution transmission electron microscope
SAED	Selected area electron diffraction
EDS	Energy dispersive X-ray spectrometer
BTO	Barium Titanate ($BaTiO_3$)
BFO	Bismuth Ferrite ($BiFeO_3$)
BLFO	Bismuth Lanthanum Ferrite ($Bi_{0.993}La_{0.007}FeO_3$)
BZNT	Bismuth Zinc Niobium tantalite $Bi[Zn_{2/3}(Nb_{0.85}Ta_{0.15})_{1/3}]O$

Introduction

Chapter 1

1.1 Introduction

With the growing global population and ongoing economic growth, there is a greater demand for energy in various electronic and automotive sectors, necessitating the development of different energy generation and storage technologies. The global energy demand has been raised more than twice in the last 40 years, per the International Energy Agency's (IEA) report [1]. From 1973 to 2016, the total energy consumption of the world increased from 54,207 terawatt-hours (TWh) to 111,125 TWh [2]. According to the report [3], the global market for stationary and transportation energy storage is expected to grow at 2.5-4 TWh per year by 2030, or roughly 3-5 times the current 800-gigawatt-hours (GWh) market. Consequently, electrical energy storage devices play a significant effect in the development of sustainable renewable technologies, such as energy conversion and storage. Energy storage equipment in the electrical system collects extra energy during periods of high production, stores it as a reservoir, and then releases it as needed. Due to industrial and commercial purposes, energy consumption has significantly increased over the past few decades. As a result, there is a greater reliance on electrical energy to power electronics and machinery today.

1.2 Current interest in the field of energy storage

Large numbers of publications for energy applications are generated for investigating the research topic of energy storage. A survey on the Scopus database shows the growing interest in energy storage in the last decade, as portrayed in **Figure 1. 1**. The report summarizes the literature survey for energy storage technologies with a timeline. **Figure 1. 1(a)** and **(b)** display the rise of publications associated with interest within different countries and a number of publications related to lead-free dielectric storage systems. With time, interest in the energy storage application is gaining attention, and constant effort by researchers has been made in the forward direction. This also suggests the recent progress and increasing demand for energy storage technologies in the near future.

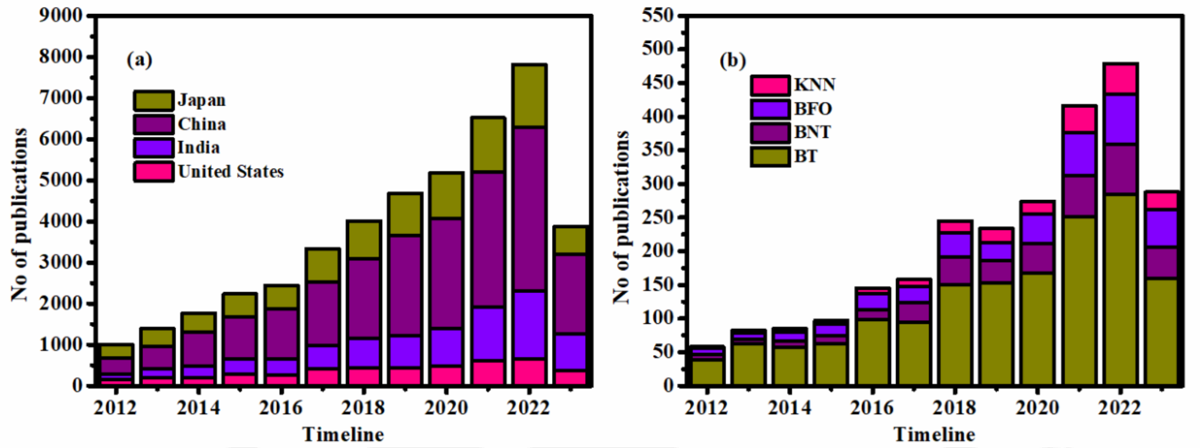

Figure 1. 1: Number of annual publications for energy storage capacitors based on Scopus database: (a) country-wise, (b) different dielectric ceramics.

The mainstream electrical energy storage systems (EESSs) are batteries, fuel cells, dielectric capacitors, electro-capacitors, etc. [4][5]. **Figure 1. 2(a)** is a graph comparing the various energy storage devices. The power density and energy density of storage systems vary significantly due to the charge-discharge process and differences in energy storage mechanisms. The energy density vs. power density of EESSs is generally depicted by the Ragone plot, named after David Vincent Ragone. The Ragone plot in the graph shows the different energy storage systems and their energy storage and power density comparisons. The chart indicates that batteries and fuel cells offer a higher energy density than electrochemical and dielectric capacitors but have low power density due to the slow mobility of charge carriers [6]. As a result, they have limited utility in high-power electronics. Electrochemical capacitors exhibit high power density and moderate energy density, but their charging and discharging processes are quite slow. Further, electrochemical capacitors can only be used at low operating voltages and are costlier compared to dielectric capacitors. The electrostatic capacitors offer inherent high power densities, ultrafast charging-discharging rates (a few milliseconds to nanoseconds), low cost, and a long lifetime suitable for high voltage applications. The dielectric capacitors overcome the limitations of electrochemical capacitors and batteries, which exhibit ultrafast charge-discharge capability and make them favorable for pulsed power equipment.

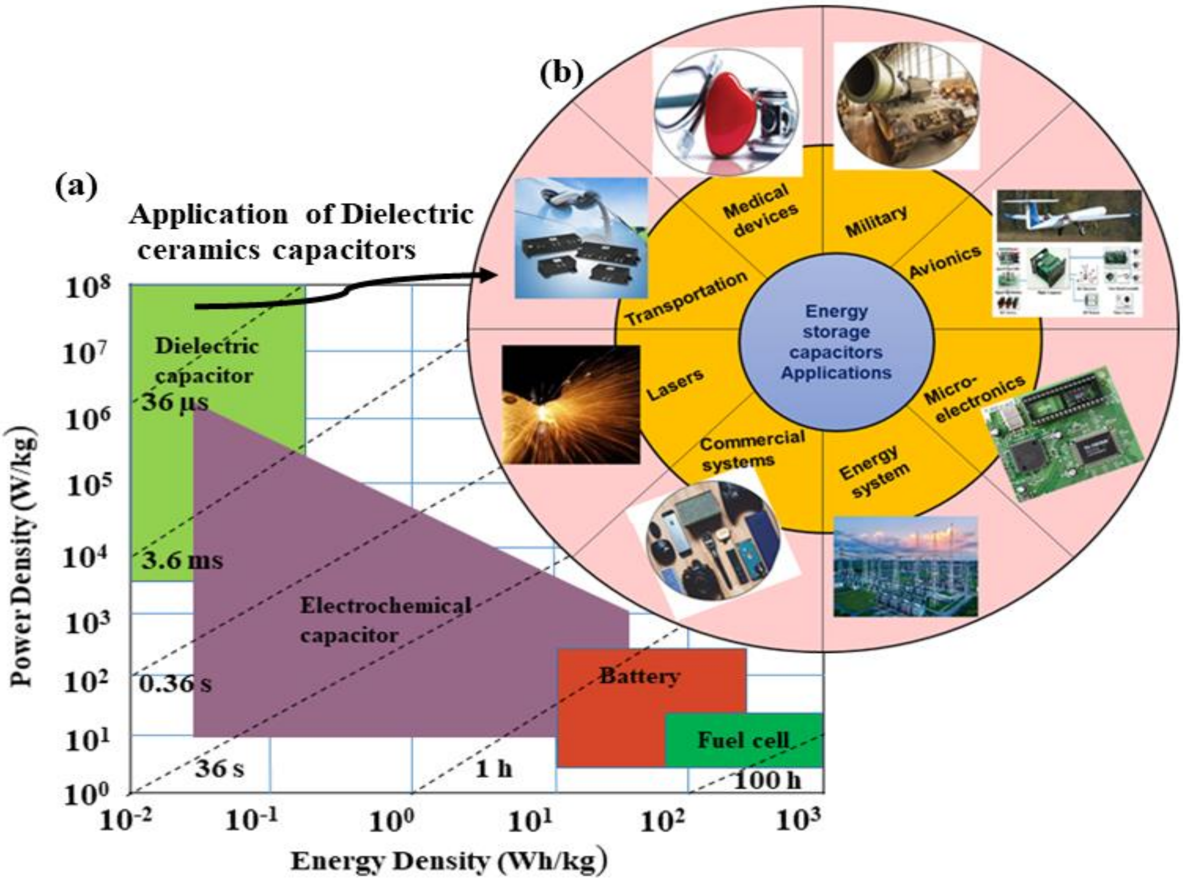

Figure 1. 2: (a) Comparison between different energy storage systems, (b) Pulsed power device applications of dielectric ceramics.

Dielectric capacitors' reduced device volume (volumetric efficiency) can be improved by increasing their discharge energy density, and these are useful in many portable electronic devices [1]. In addition, the range of applications for dielectric capacitors can be substantially expanded if their energy density is comparable to that of fuel cells and batteries.

1.3 Dielectric capacitors: Their usage in pulsed power applications

Dielectric capacitors are used in a wide variety of pulsed power applications, some of which are shown in **Figure 1. 2(b)**. They can be useful in spacecraft, medical equipment (surgical lasers, pacemakers, X-ray units), hybrid electric vehicles, scientific research (high-power accelerators, nuclear effects simulations), commercial systems (metal forming, food sterilization, camera flash), high-intensity magnetic field experiments, and military systems (radars, electrochemical guns, ballistic missiles, active armor, high-power microwave devices) [4][7][8]. Dielectric capacitors are crucial components in hybrid electric vehicles (HEVs). In electric hybrid vehicles, the energy storage capacitors can be helpful during low battery backup, as dielectric capacitors take a few milliseconds to charge and discharge. For instance, the electrification of the transportation sector was aided by the popularity of the Toyota Prius hybrid electric vehicle, leading to the introduction of products like the all-electric Nissan Leaf and the plug-in GM Volt [9].

1.3.1 Why dielectric ceramic capacitors are of interest?

Though the batteries provide high energy density and reliability and are used for stable and long-term energy supplies, they face a serious disposal issue. The batteries' use and self-life are limited, and a vast number of raw materials, metals, and non-metal used to produce batteries generate environmental pollution (greenhouse gas, hazardous waste, and toxic emissions) during different stages of processing. This processing includes mining, manufacturing, transportation, collection, storage, treatment, disposal, and recycling [10]. Conversely, using liquid electrolytes involving chemical reactions in electrochemical capacitors also adds to the environmental risk. At the same time, the fuel cell is too expensive to manufacture due to the high cost of catalysts. The hydrogen gas in the fuel cell is highly inflammable, burns in air at concentrations ranging from 4 to 75%, and hence requires safety measures. The usage of these storage systems will have severe environmental and social impacts. In detail, with the help of the illustration in **Figure 1. 3**, attempted to demonstrate the different energy storage systems with their merit and demerits. Accordingly, in terms of sustainability, the research has been focused on quantifying externalities and reducing risk by replacing these energy storage systems with dielectric capacitors.

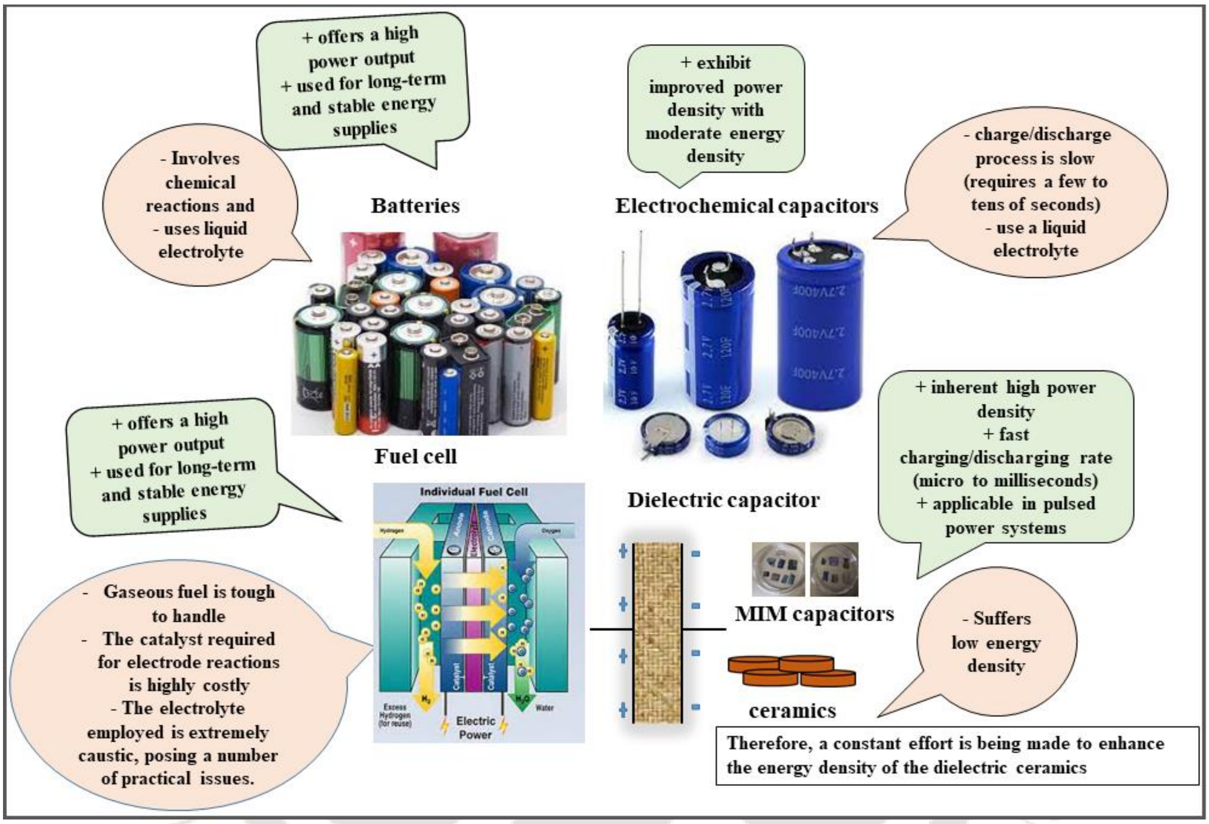

Figure 1. 3: Various types of energy storage systems with their advantages and disadvantages [1][6].

1.3.2 Essential background of dielectric capacitor

A common example of a capacitance device is a dielectric capacitor or plane-parallel capacitor, which consists of two electrode panels separated with dielectric materials. Dielectric capacitors can store energy in the form of an electrostatic field, with an applied electric field, through polarization, which is caused by the separation of electric charges of the dielectric materials. **Figure 1. 4(a)** depicts a plane parallel capacitor composed of two electrode panels separated from one another with a dielectric material sandwich between them. **Figure 1. 4(b)** shows some of the dielectric capacitor's advantages. Along with pulsed power applications, dielectric capacitor offers numerous advantages of high-power density, better temperature stability, ultrafast charge, and discharge rate (~µs to ns), good fatigue endurance, high safety, and reliability.

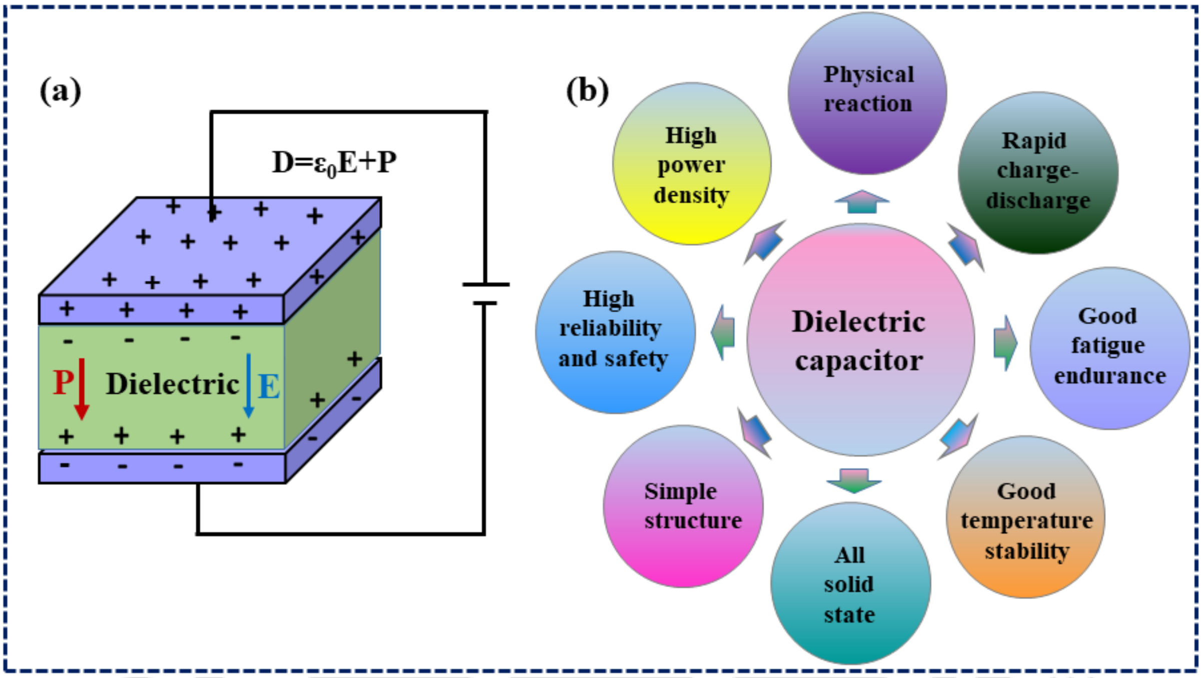

Figure 1. 4: Dielectric capacitors [11] and advantages of dielectric capacitors [12].

1.4 Polarization mechanism in dielectric materials

A dielectric is made up of either polar or nonpolar molecules.

1.4.1 Polar molecules

Polar molecules are ones in which positive and negative charge centers do not coincide with each other and they have a permanent electric dipole. Since the molecules are randomly orientated the net dipole moment will be zero without an electric field. However, in the presence of an electric field molecule will have a finite dipole moment. Some well-known examples of polar molecules are H_2O, N_2O, NH_3, and HCl. **Figure 1. 5(a)** and **(b)** depict polar molecules in the presence and absence of an electric field.

1.4.2 Nonpolar molecules

Non-polar molecules are those whose positive charge coincides with a negative charge in the absence of an electric field as illustrated in **Figure 1. 5(c)** so, they have zero dipole moment. Examples of non-polar molecules include N_2, O_2, H_2, methane, etc. With an electric field, positive charges tend to align in the electric field direction and negative charges in the opposite direction of the electric field as displayed in **Figure 1. 5(d).** As a result electric field within the dielectric material is reduced. The molecule is then said to be induced polarized. In terms of applied electric field, the induced polarization can be written as follows

$$\vec{P} = \varepsilon_0 \alpha \vec{E} \qquad (1.1)$$

here, α denotes the polarizability of the material.

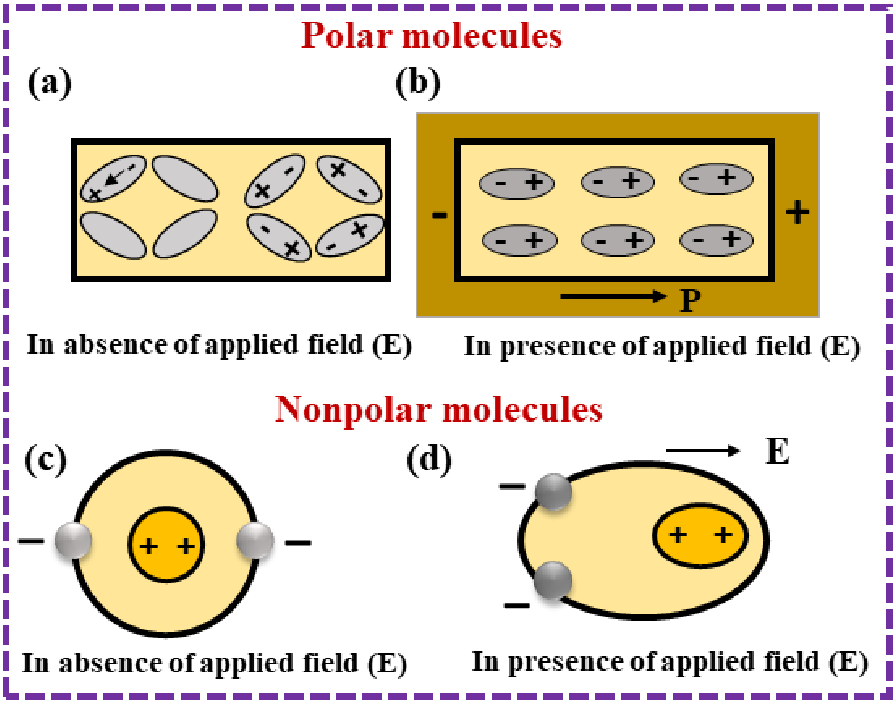

Figure 1. 5: (a) Polar molecules in the absence of an electric field (b) Polar molecules in the presence of an electric field (c) Non-polar molecules in the absence of an electric field where the center of positive charge coincides with a negative charge, (d) Charge separation in presence of an electric field.

1.4.3 Dielectric Polarization

Dielectric materials have no free electrons to participate in conduction so, when they are placed in the electric field, partially no current flows in them, unlike the conductors. Instead, the charge carriers slightly displace away from their equilibrium position, resulting in a net dipole moment ($\vec{\mu}$) and the atom is said to be polarized. This phenomenon is referred to as polarization of the material, expressed in terms of net dipole moment ($\vec{\mu}$) per unit volume as, $\vec{P} = \sum(\vec{\mu}/V)$. The positive charges will get displaced in the applied field direction and the negative charge will move away opposite to the direction of the field. Based on resonance and relaxation regimes, there are four different types of polarization mechanisms involved in the dielectric material. This polarization mechanism includes electronic ($\vec{P}_e$), ionic ($\vec{P}_i$), dipolar ($\vec{P}_{dp}$) and space charge ($\vec{P}_{sc}$) polarization. Electronic and ionic polarization is displacement polarization whereas, dipolar and space charge polarization comes under orientation polarization. Each polarization process relates to cut-off frequency. Above the cut-off frequency, the corresponding polarization mechanism becomes inactive and does not contribute to the polarization response. All the polarization mechanism in the dielectric material is depicted in **Figure 1. 6** and discussed below:

1.4.3.1 Electronic polarization:

As depicted in **Figure 1. 6(a)**, a dipole moment is formed with an electric field in the molecules because the electron cloud outside the nucleus moves relative to the nucleus, which creates the displacement in positive and negative charges. This phenomenon is known as electronic polarization and is observed in a frequency range of 10^{12} to 10^{15} Hz (UV region). For this polarization to occur, at least one atom is required.

1.4.3.2 Ionic polarization:

Figure 1. 6(b), shows the displacement of positive and negative ions under an applied electric field. The displacement of charges from its equilibrium positions induces a net dipole moment. This mechanism is known as ionic polarization in which at least two atoms are required. Ionic polarization will respond to infrared frequencies and occurs at frequencies between ~10^9 to 10^{12} Hz.

1.4.3.3 Dipolar or orientation polarization:

High thermal energy causes large fluctuations, leading to random molecular dipole orientation. In the presence of an external applied electric field, dipoles tend to align in the applied field direction. This alignment of permanent dipoles in the applied electric field direction is called orientation polarization and is shown in **Figure 1. 6(c).**

1.4.3.4 Space charge or interface polarization:

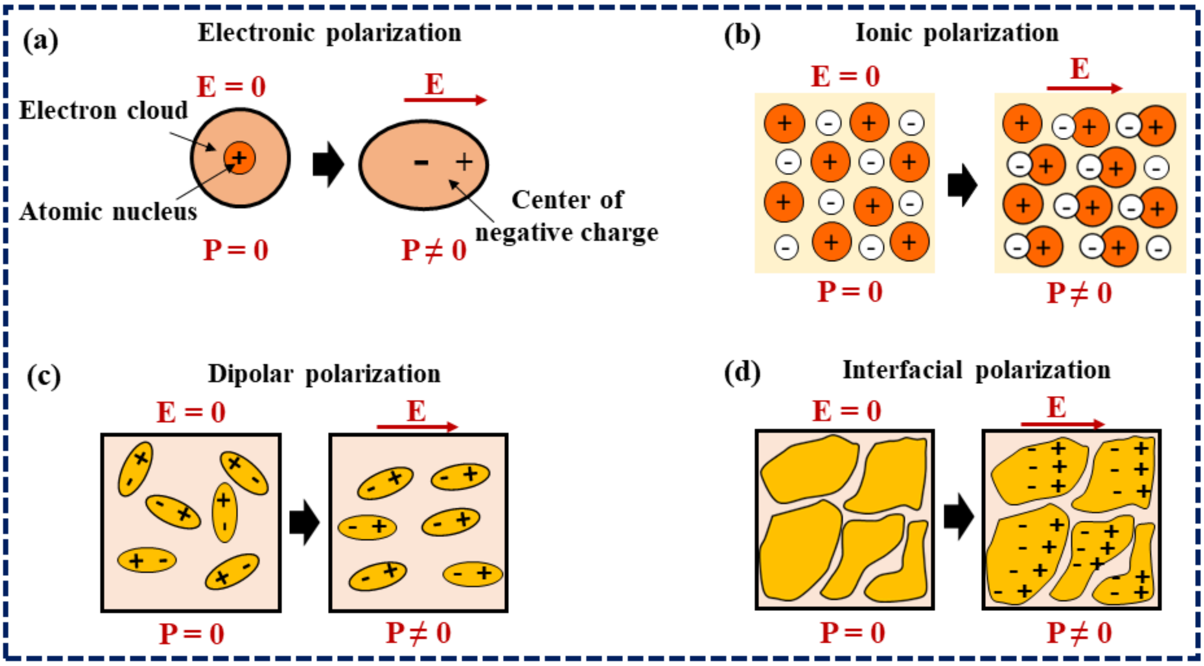

Figure 1. 6: Different types of polarization mechanisms present in dielectrics [13].

This type of polarization occurs when the charge carriers move through dielectrics and are restricted from moving due to the barriers, it can be grain boundaries (the electrons "pile up") or any other interface (like electrode-material interface). Due to this, the charges accumulate at the interface between two materials or regions inside a material with an applied electric field as depicted in **Figure 1. 6(d)**. At low frequencies, dipolar polarization will respond which occurs below 10^9 Hz in the frequency range of 10^6 to 10^9 Hz while, space charge polarization is below 10^3 Hz. The net contribution from all types of polarization can be expressed as:

$$\vec{P}_{total} = \vec{P}_e + \vec{P}_i + \vec{P}_{dp} + \vec{P}_{sc} \tag{1.2}$$

In linear dielectric systems, in terms of electric field, polarization can be expressed as below:

$$\vec{P} = \chi_e \varepsilon_0 \vec{E} = (\varepsilon_r - 1)\varepsilon_0 \vec{E} \tag{1.3}$$

here, χ_e, ε_r and ε_0 denotes the electric susceptibility, dielectric constant (or relative permittivity), and vacuum permittivity of the dielectric material respectively. Also, the dielectric constant can be expressed as,

$$\varepsilon_r = \frac{\varepsilon}{\varepsilon_0} \tag{1.4}$$

A material's dielectric permittivity is a measure of its ability to store electric charge, whereas its dielectric loss quantifies the loss of electrical energy. The ratio of imaginary (ε") and real (ε') permittivity gives the dielectric loss (Loss tangent, tanδ) as written below:

$$tan\delta = \frac{\varepsilon''}{\varepsilon'} \tag{1.5}$$

The sum of the intrinsic and extrinsic losses gives the total dielectric loss. The interaction of alternating electric field with the phonon system is attributed to the intrinsic dielectric losses and it occurs in perfect crystals. The crystal symmetry, temperature, and alternating current field frequency influenced the intrinsic dielectric losses. Extrinsic losses are caused by crystal lattice imperfections such as vacancies, microstructural defects, impurities, porosity, order disorder, micro-cracks, grain boundaries, dislocations, random crystallite orientation, dopant atoms, and so on. Since extrinsic losses are generated by lattice defects, and hence good material preparation can reduce them. Therefore, low dielectric losses and, a high dielectric constant are desired properties for applications in the electrical and electronic industries.

1.5 Some crucial criteria to determine energy storage performance

1.5.1 Dielectric permittivity

The energy storage capability of dielectric capacitors is dependent on the capacitance (C) and electric polarization of the material. **Figure 1. 7(a-b)** depicts the schematic representation of a dielectric capacitor. The capacitance of the materials can be expressed in the term of voltage (V) and the incremental change in the charge (Q) as follow:

$$C = \frac{dQ}{dV} = \frac{\varepsilon_0 \varepsilon_r A}{d} \tag{1.6}$$

here, ε_r, ε_0, d, and A are the relative dielectric permittivity, dielectric permittivity in free space thickness of the dielectric material, and area of the electrode respectively.

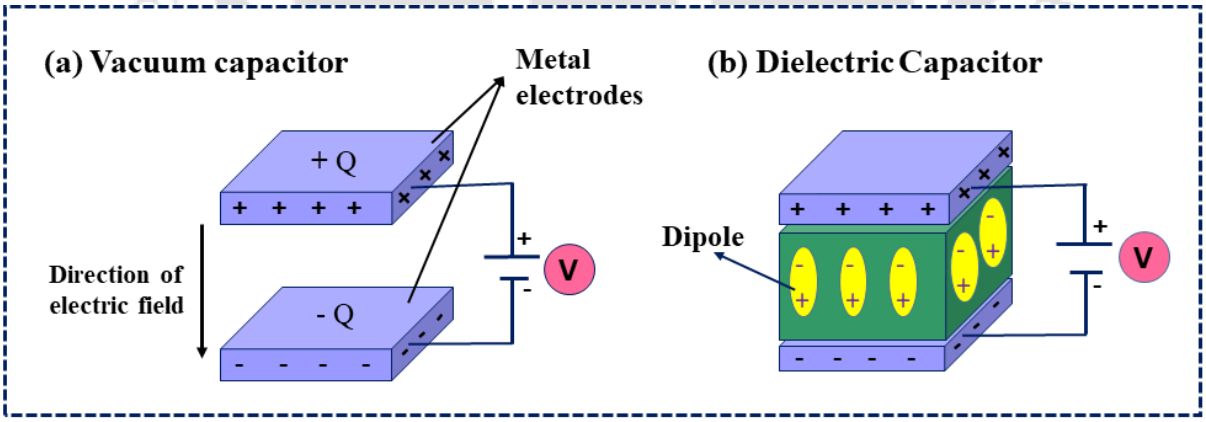

Figure 1. 7: Schematic illustration of energy stored in (a) vacuum capacitor, and (b) dielectric capacitor.

1.5.2 Stored energy density (W)

When an external electric field is applied to the dielectric material or during the charging process, a non-zero charge on two plate capacitors is induced, due to which electric dipole tends to align themselves in the field direction. The dielectric polarization throughout the charging process is illustrated in **Figure 1. 7(b)**. When the outside voltage becomes equal to the voltage difference produced by charge accumulation then the charging process of the capacitor ceases and the capacitor will fully charge. As a result, the electrostatic energy stored during the charging process stored in the dielectric layer can be expressed as:

$$W = \frac{J}{V_{vol.}} = \frac{\int_0^{Q_{max}} V dq}{Ad} = \int_0^{D_{max}} E dD \qquad (1.7)$$

where, J, E, V_{vol}, $Q_{max,}$ and D are stored energy, applied electric field (E=V/d), volume ($V_{vol.}$ = A×d), the maximum value charge acquired at the maximum electric field, and the electrical displacement respectively. The electric displacement can be expressed as $D = \varepsilon_0\varepsilon_r E = P+\varepsilon_0 E$. Hence, the stored energy density can be rewritten as:

$$W = \int_0^{P_{max}} E dP \qquad (1.8)$$

where P and P_{max} represent the spontaneous polarization and maximum polarization under the maximum electric field. Since the applied electric field has no effect on the electric displacement or permittivity in linear dielectrics (LDs), then W can be defined as:

$$W = \frac{1}{2}\varepsilon_0\varepsilon_r E^2 \qquad (1.9)$$

From, **Eq. (1.9)** it is clear that applied electric field and permittivity affect energy storage density, depending on whether the dielectric is linear or nonlinear [11].

1.5.3 Recoverable energy density (W_{rec})

In nonlinear dielectrics including ferroelectrics (FEs), relaxor ferroelectrics (RFEs), and antiferroelectrics (AFEs) materials energy dissipation is unavoidable and is quantified as joule heat loss, the deformation for determining W_{rec} is expressed as:

$$W_{rec} = \int_{P_r}^{P_{max}} EdP \qquad (1.10)$$

where P_r is the remnant polarization. The nonlinear dielectric experiences considerable energy losses during the charging and discharging processes. Using the Sawyer Tower circuit depicted in **Figure 1. 8(a)**, the P-E loops are used to calculate the recovered energy density for such materials.

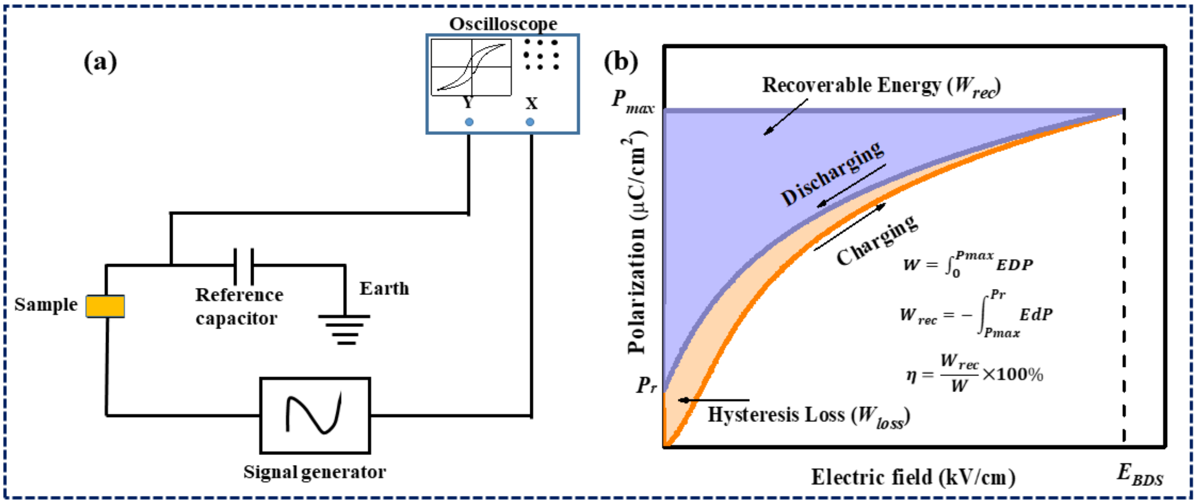

Figure 1. 8: (a) Schematic diagram of the Sawyer-Tower circuit for the P-E loop measurement; (b) graphical illustration of the assessment of energy storage parameters [14].

1.5.4 Energy efficiency (η)

Similarly, η of the P-E loop can be calculated using the relation:

$$\eta = \frac{W_{rec}}{W} = \frac{W_{rec}}{W_{rec}+W_{loss}} \qquad (1.11)$$

where W_{loss} is the energy dissipated and is represented by hysteresis loss. **Figure 1. 8(b)** illustrates the charging/discharging process and W_{rec}, W_{loss} shown in purple and orange colors respectively with their energy efficiency (η). **Figure 1. 8(b)** illustrates the typical monopolar ferroelectric hysteresis loop. Using this P-E loop, the stored energy of the material can be calculated using **Eq. (1.8)** and the area between the discharge curve and polarization axis in the ferroelectric curve gives the recoverable energy density which can be determined using **Eq. (1.10)**. The energy efficiency is evaluated using **Eq. (1.11)**. The total-colored portion (purple + orange) in the ferroelectric hysteresis curve indicates the total stored energy in the capacitor. The orange portion shows the W_{loss} and the purple portion represents the W_{rec} in the dielectric material.

1.5.5 Electric breakdown strength (E_{BDS})

E_{BDS} is another important parameter, which influences the energy storage performance. The W_{rec} and η of the material are highly dependent on the E_{BDS}. The electrical resistance of the dielectric material significantly drops at a high applied electric field, and it becomes zero at the certain maximum electric field which is known as the breakdown strength (E_{BDS}). The E_{BDS} of the dielectric capacitors depends on the dielectric permittivity and energy bandgap of the material. At the same time, the microstructural parameters, such as material density, phase crystallinity, sample thickness, grain size, grain homogeneity, and defect chemistry, also significantly influence the breakdown strength. The external parameters such as surrounding temperature, pressure, operating frequency, and electric field application time also affect the E_{BDS} of the material. Several other mechanisms involve dielectric failure such as intrinsic electric breakdown, partial discharge, thermal runaway, and electrostatic compressive forces. For achieving a higher sustainability of capacitance under a larger E_{BDS}, high-quality dielectric materials with dense microstructure are essential.

Other crucial energy storage parameter includes discharge time, thermal stability, and fatigue endurance. Rapid charging/discharging is a distinctive characteristic of dielectric capacitors. This quick discharge generates a large current, which results in a high power in the capacitor. The discharging rate is measured in terms of discharge time, represented by $\tau_{0.9}$. Dielectric capacitors must have a high electric fatigue endurance to maintain their physical integrity over time and perform reliably during charging and discharging. Ferroelectric loops at a particular electric field are typically measured during repetitive cycling to determine the fatigue life of dielectric capacitors. For energy storage capacitors, good thermal stability is an essential requirement for the dielectric material in addition to high fatigue endurance.

1.6 Dielectric materials for energy storage capacitors

1.6.1 Different classifications of dielectric materials

Dielectric ceramics are classified into different types based on ferroelectric domain structure. **Figure 1. 9(a-e)** illustrates the schematics of permittivity and polarization as a function of applied fields for different dielectric materials. In general, the dielectric materials are broadly categorized into linear and nonlinear dielectrics. Due to the absence of permanent dipoles, a linear dielectric (LD) material almost shows constant permittivity and linear polarization response. Non-linear dielectric materials including para-electric (PE), ferroelectric (FE), and anti-ferroelectric (AFE) possess permanent dipoles due to the presence of non-centre symmetry. However, PE systems have no ferroelectric domains but have permanent dipoles that show slight non-linear response in P-E and ε_r - E characteristics with an electric field and once the electric field is removed, the materials come back to their nonpolar state. Ferroelectric material, without the presence of an electric field, has a net electric dipole moment and shows spontaneous polarization. They exhibit superior polarization values, but their low breakdown strength, high dielectric loss, large remnant polarization, and hysteresis loss cause them to store less energy. As ferroelectric systems have large hysteresis loops displaying huge energy loss, practically undesirable for real applications. As the name suggests, in anti-ferroelectric materials, the polarization aligns oppositely in an adjacent crystalline lattice, hence showing zero polarization without an electric field. With the application of an electric field, AFE materials show double hysteresis loops because of reversible phase transitions AFE↔FE phase transitions. AFE materials are best suited for energy storage applications because of the high discharge energy density. The majority of AFE materials are lead-based, which limits their use for practical applications. Relaxor ferroelectric (RFE) materials are a type of ferroelectric material with polar nano regions (PNRs) that, on the other hand, have better energy storage performance. The PNRs are responsible for the dielectric relaxation and decrease in long-range ferroelectric ordering and are also responsible for the slimmer P-E loops of relaxor materials. These characteristics are essential for high-energy storage performance in dielectric ceramics.

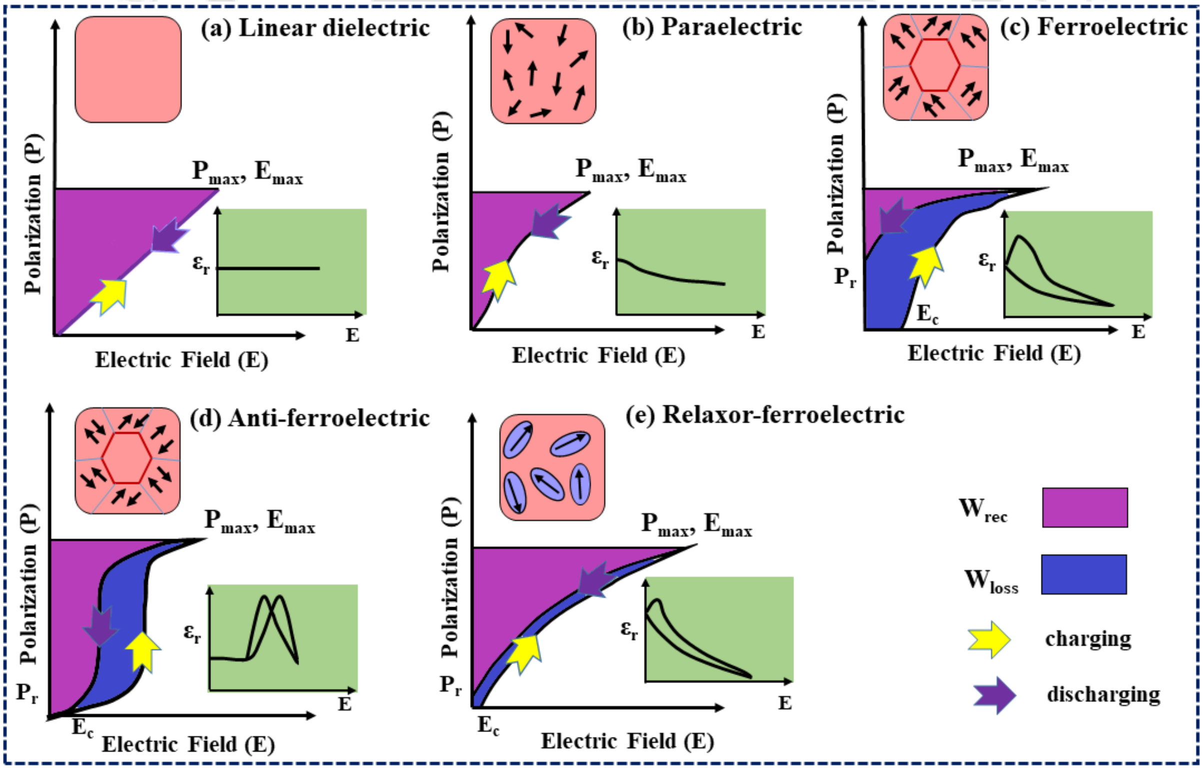

Figure 1. 9: Categorization of dielectric materials with ε_r-E curves, domain wall structure, and their corresponding P-E hysteresis loop (attributed to [15]).

1.6.2 Types of dielectric materials

Attaining enhanced energy storage performance in one material is a difficult task. As such, much research on dielectric materials with high energy potential has been centered on polymers, composites, glass ceramics, and ceramics [15]. Polymer dielectrics display a high breakdown field (> 7 MV/cm); however, poor thermal stability (< 100°C) and low dielectric permittivity (< 10) make their application limited [7]. Several polymer-based composites containing dielectric ceramic fillers in varying shapes and concentrations have been developed recently to increase their permittivity. Composite materials can boost energy storage performance but struggle with problems like ceramic filler aggregation and polymer/ceramic interface incompatibility. Compared to polymer dielectrics, glass-based oxide dielectrics have a higher breakdown field (> 10 MV/cm) and higher permittivity. However, energy storage performance is hindered by the interface effect between the crystalline and amorphous phases. Simultaneously, the synthesis of high-quality pore-free glass ceramics is complex. In the case of dielectric ceramics, the dielectric constant is 10−2000 with a breakdown strength of 0.1−1 MV/cm. **Figure 1. 10(a-b)** represents the statistical data on the percentages of publications in 2012-2022 based on the "ISI Web of Science database" for various dielectric materials. As depicted in **Figure 1. 10(a)**, dielectric ceramics received a considerable amount of interest among all other dielectric materials. The development of these dielectrics has advanced significantly in recent years, but each dielectric material appears to have its limitations. For instance, despite having a large breakdown field, polymer dielectrics limit their suitability due to their significantly low dielectric permittivity and poor thermal stability, making dielectric capacitors a long-term objective for energy storage applications. Nowadays, ceramic-based dielectrics are mainly focused on taking several variables into account, such as fundamentality, environmental adaptability, energy storage potential, and so forth.

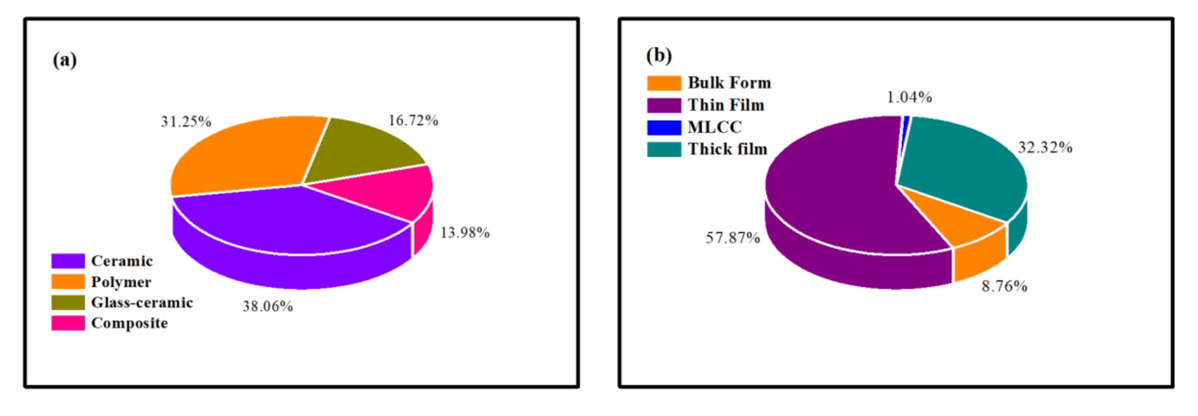

Figure 1. 10: Number of publications on energy storage (a) with different types of materials, and (b) different forms of dielectric ceramic: bulk ceramic, thin film, multi-layer ceramic capacitors (MLCCs), and thick film in the period of 2012-2022.

Depending on their thickness, dielectric ceramics can be classified into four groups: bulk ceramics (>100 µm), multi-layer ceramic capacitors (MLCCs), thin films (<1 µm), and thick films (1-100 µm). MLCCs and thin films have a high E_{BDS} due to the lesser quantity of pores, impurities, and defects, which results in a high W_{rec} [15]. The higher value of E_{BDS} in thick films as compared to thin films can be fabricated into multilayer structures, which can acquire more electrical energy. Additionally, thick films are more suitable for device integration than bulk ceramics due to their small volume and high E_{BDS}. Bulk ceramics, on the other hand, can store more electrical energy due to their simple manufacture, better mechanical qualities, low cost, and vast volume. It is worth noting that if the bulk form of dielectric materials has good energy storage capabilities, their thick film and thin film exhibit better energy storage performance. Furthermore, the properties of bulk materials give preliminary investigation for fabricating high-performance thick and thin films. Therefore, bulk materials are gaining increasing research attention due to their simple fabrication procedure and low cost compared to thin and thick films. According to the statistical data, it is stated that bulk ceramics are of fundamental relevance for research expansion in addition to thin and thick films.

1.7 Ferroelectric ceramics for energy storage applications

1.7.1 Bismuth Sodium Titanate ($Bi_{0.5}Na_{0.5}TiO_3$), BNT

BNT ($Bi_{0.5}Na_{0.5}TiO_3$) belongs to the perovskite family with an ABO_3 structure and was found by Smolenskii et al. in 1961. BNT system exhibits rhombohedral phase structure with space group *R3c* at room temperature up to 200 °C. With elevated temperature, it undergoes a series of phase transitions. As the temperature rises to 320 °C, it transforms from rhombohedral to tetragonal phase (*P4bm*); across the region, it coexists in rhombohedral and tetragonal phases. At ~ 520 °C, BNT transforms from a tetragonal to a cubic phase with a *Pm3m* space group [12]. **Figure 1. 11** shows the crystal symmetry of pure BNT ceramics exhibiting a rhombohedral phase with a lattice parameter, a = b = c = 3.885 Å with phase angles $\alpha = \beta = \gamma = 89.830$ [16]. Pure BNT ceramics are not a good choice for electric energy storage because of their high conductivity, significant dielectric loss, and strong ferroelectricity ($E_c = 73$ kV cm^{-1}, $P_r = 38$ μC cm^{-2}) [15].

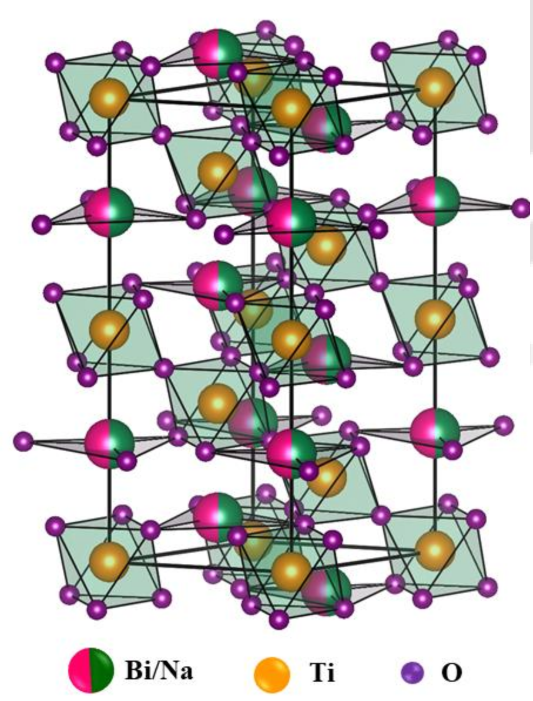

Figure 1. 11: Crystal structure of $Bi_{0.5}Na_{0.5}TiO_3$.

BNT-based systems for energy storage applications gained interest at the beginning of 2014 after the work reported by Lue et al. [17][18] on a binary solid solution with KN ($KNbO_3$). Similarly, several additives such as $CaZrO_3$, $SrZrO_3$, and MgO were substituted in the BNT to enhance their energy storage capabilities by introducing the relaxor phenomenon in the system [19][20][21].

1.7.2 Potassium Sodium Niobate, $K_{0.5}Na_{0.5}NbO_3$ (KNN)

KNN ($K_{0.5}Na_{0.5}NbO_3$) has received significant attention over the last 20 years due to its exceptional piezoelectric performance and environmental friendliness. KNN is a solid solution of sodium niobate and potassium niobite, which is the combination of ferroelectric and anti-ferroelectric systems, possessing an MPB analogous to that of the PZT system if the Na/K is in a 50/50 ratio [22]. KNN near MPB is reported to exhibit good piezoelectric (d_{33} ~ 148 pC/N) and dielectric response [23]. It displays an orthorhombic phase structure at RT and high T_C at ~ 420 °C. Mainly, the research interest focuses on their electro-optic, piezoelectric, and electro-caloric effects. The low E_{BDS} and high P_r result in a low W_{rec}, making undoped KNN ceramic unsuitable for electrical energy storage.

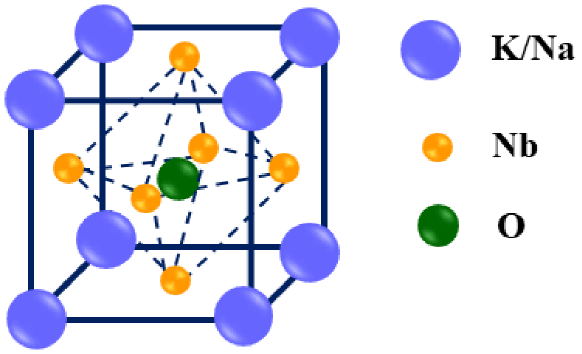

Figure 1. 12: Crystal structure of $K_{0.5}Na_{0.5}NbO_3$.

The crystal symmetry with an orthorhombic phase of pristine KNN is depicted in **Figure 1. 12**. The primary challenge associated with KNN ceramics is poor densification because of the volatile components such as K_2O and Na_2O, which quickly evaporate during high-temperature sintering [24]. Therefore, optimization of the sintering temperature of KNN is complicated with the solid-state reaction method.

1.7.3 Bismuth Ferrite, $BiFeO_3$ (BFO)

BFO is a multiferroic system that possesses anti-ferromagnetic Néel temperature ($T_N \sim$ 370 °C) and high Curie temperature ($T_C \sim$ 830 °C) [25][26]. **Figure 1. 13** illustrates that BFO exhibits the rhombohedral distorted perovskite structure with a space group of *R3c* with a = 3.965Å and an octahedral FeO_6 tilting angle of 11°. Researchers are interested in the BFO due to the coexistence of magnetic and ferroelectric responses at room temperature, which makes it applicable in their wide range of applications, such as data storage, spintronics, and electromagnetic devices [26][27].

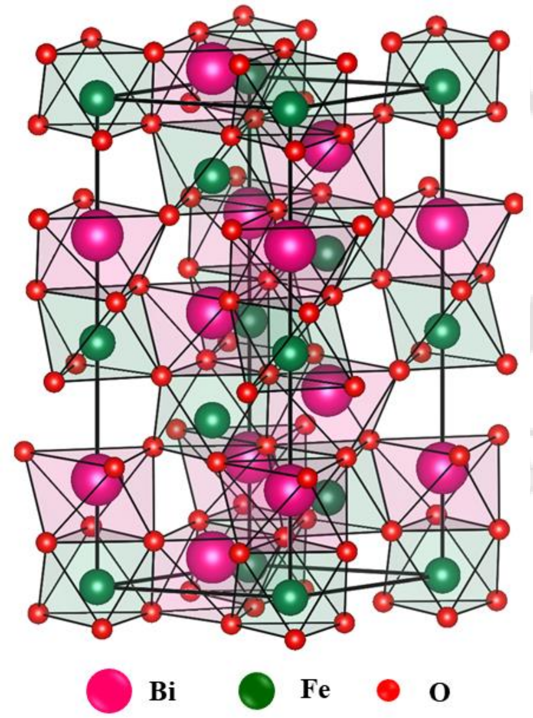

Figure 1. 13: Crystal structure of $BiFeO_3$.

The applicability of BFO for energy storage mainly originated from the stereochemically active 6s lone pairs, which are attributed to high polarization (100 $\mu C\ cm^{-2}$).

Furthermore, the high Curie temperature of BFO finds usage in high-temperature applications. Due to its considerable leakage current, pure-phase BFO with appreciable enhanced ferroelectric properties is very difficult to obtain. A major challenge in BFO is to control the formation of secondary phases such as $BiFe_4O_9$, $Bi_{25}FeO_{39}$, and $Bi_{25}FeO_{40}$ [28] during synthesis, leading to low resistivity and poor ferroelectricity that restricts their usage in various applications [25].

1.7.4 Barium titanate, $BaTiO_3$ (BTO)

BTO is a well-known ferroelectric material with various uses, including nonlinear optic devices and dielectric capacitors. In 1946, BTO was discovered to be the first polycrystalline ceramic material to exhibit ferroelectricity. BTO has a tetragonal phase at room temperature, with a lattice constant of a=3.99095 Å and c= 4.0352Å [15]. At elevated temperatures (~ 125 °C), BTO exhibits cubic symmetry and is in a paraelectric state. As the temperature declines below 125 °C, the paraelectric cubic state of BTO changes to the ferroelectric tetragonal phase. When the temperature is further decreased, the tetragonal phase transforms to an orthorhombic state at ~ 8 °C. Finally, at -71°C, BTO again changes its phase from orthorhombic to rhombohedral phase [29]. **Figure 1. 14** displays the dielectric constant versus temperature for pristine BTO. The structures and characteristics of BTO have been extensively studied for more than 50 years after the discovery of ferroelectricity and piezoelectricity in this system [30]. BTO-based ceramics have received immense attention for electric energy storage because of their high ε_r, low dielectric loss, and medium E_{BDS}. Still, the wide square-shaped hysteresis loops in BTO render it inappropriate for energy storage applications with small E_{BDS}, low W_{rec}, and low η. Therefore, the energy storage performance of BTO can boosted by compositional modification, fabricating ceramics/polymer composites, and so on.

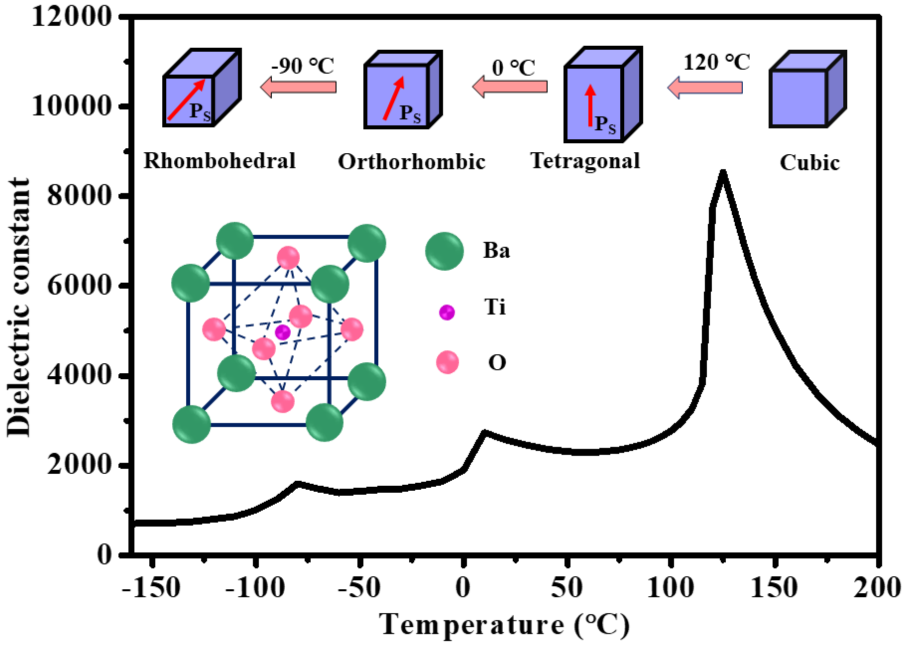

Figure 1. 14: Temperature variation of the dielectric constant of a $BaTiO_3$ single crystal.

The lead-free perovskite materials include BTO, BNT, KNN, $AgNO_3$ (AN), and $NaNbO_3$ (NN) systems. Among them, BT and NN-based materials show low recoverable energy density (W_{rec}), KNN-based materials suffer poor thermal stability, and AN-based materials face high raw material cost and undergoes complex processing. Processing and synthesis of BNT materials is a challenge as Bi is highly volatile due to the high-temperature sintering process, and it is difficult to maintain chemical stoichiometry. KNN and BNT systems suffer a lack of chemical stability and densification at high-temperature heat treatment due to the evaporation of chemicals like sodium, potassium, and bismuth. Whereas BTO-based systems are chemically stable and acquire high dielectric permittivity and low dielectric loss. These additional properties are advantageous for energy storage capacitor applications.

1.8 A brief overview of relaxor dielectric ceramics

More than half a century ago, the relaxor ferroelectrics (RFEs) system, a new class of dielectric materials, was discovered by Smolenskii and group in 1961 [31]. The relaxor behavior is first observed in an ABO_3 perovskite structured ferroelectric system in lead magnesium niobate ($Pb(Mg_{1/2}Nb_{2/3})O_3$) PMN and later in lead scandium tantalate ($Pb(Sc_{1/2}Ta_{1/2})O_3$) (PST). In these systems, relaxor behavior arises due to the partial or full substitution of Mg^{2+}, Sc^{3+}, Nb^{5+}, and Ta^{5+} ions in the B-site, creating a nonstoichiometric disordered solid-solution. Similarly, relaxor behavior is also observed in $Pb_{1-x}La_x(Zr_{1-y}Ti_y)_{1-x/4}O_3$ (PLZT), $Ba(Ti_{1-x}Zr_x)O_3$, and $Ba(Ti_{1-x}Sn_x)O_3$ materials. Later, the altered PZT materials were categorized as a special class of FE materials, known as RFEs, after L.E. Cross popularized the term in 1987. He proposed that a material can be classified as RFE if it satisfies three key criteria: (i) a diffused phase transition from the ferroelectric to the paraelectric phase or broad temperature-dependent dielectric permittivity; (ii) the presence of dielectric relaxation or the frequency-dependent dielectric maximum temperature (T_m); and (iii) there is no macroscopic symmetry break in the vicinity of T_m.

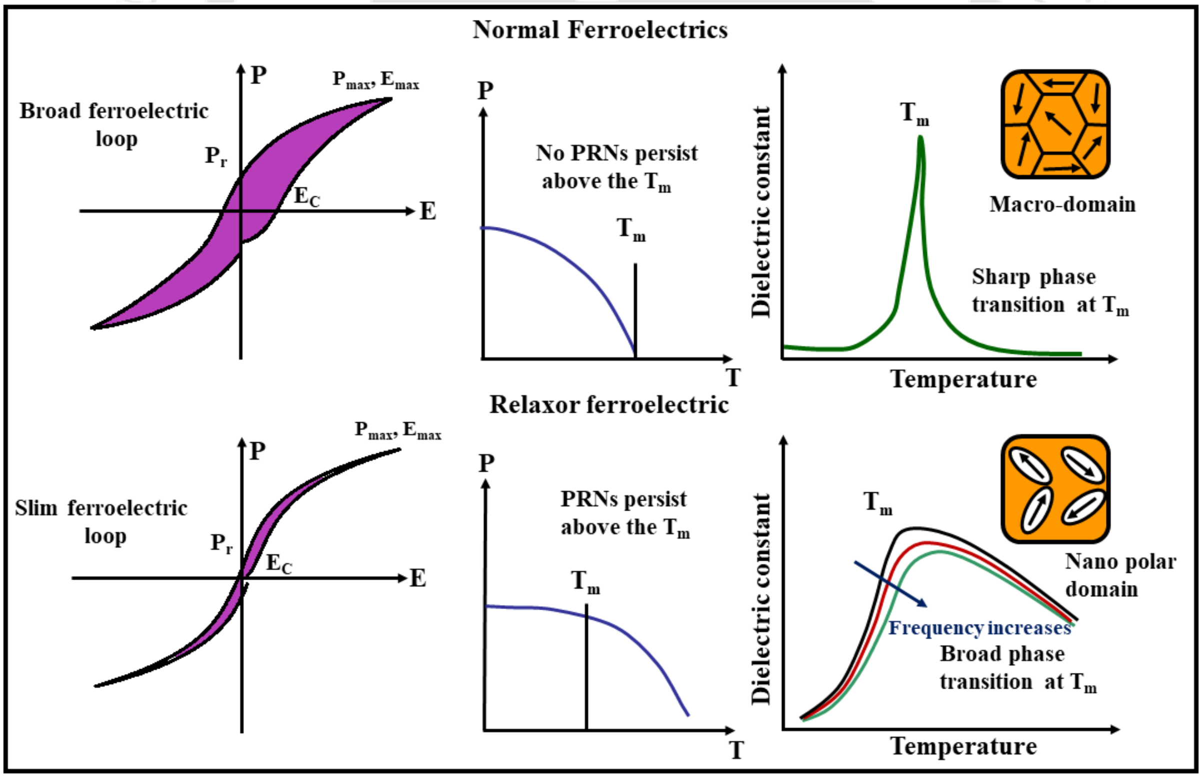

Figure 1. 15: Comparison between normal ferroelectric (FE) and relaxor ferroelectric materials (RFE) [31].

Figure 1. 15 illustrates the distinguishing features of RFEs from FE material. The origin of relaxor behavior in such systems is thought to be owing to their compositionally induced disordered nature, which happens as a result of symmetry breakdown at the nanoscale level. This is owing to the creation of polar nanoregions (PNRs), which can significantly impact material characteristics. Typically, these PNRs arise above the temperature-dependent maximum permittivity (T_m) zone known as the 'Burns' temperature (T_D), in which the T_m shifts towards higher temperature as frequency increases. Due to the distinguishable features of REFs from FE materials and their potential advantage in energy storage applications, the REF systems have been rigorously explored in the last 30 years. Different BTO-based lead-free REF systems studied for energy storage capacitor applications are discussed as follows:

1.9 BTO-based relaxor ferroelectric ceramics

Lead-free RFEs usually accomplished in $BaTiO_3$ (BTO) based series, exhibit equivalent excellence response to its anti-ferroelectric materials. The total P_{max} of the BTO-based ceramics can efficiently be adjusted by combining these BTO-based solid solutions with others, such as polar Bi^{3+}-based $BiMeO_3$ (where *Me* denotes trivalent or average trivalent cation) [32]. The most extensively investigated composite system of BTO-based ceramics is $BaTiO_3$-$Bi(Me)O_3$. **Table 1. 1** summarizes the current interest in $BaTiO_3$-$BiMeO_3$-based solid-solution for energy storage applications.

Table 1. 1: A literature survey of energy storage performance of BTO-based solid solutions.

Compositions	***W_{rec} (J/cm^3)***	***η (%)***	***E_{BDS} (kV/cm)***	***Ref.***
(0.7-x)BFO-0.3BTO-$xBaZn_{1/3}Nb_{2/3}O_3$+0.1 wt%MnO_2	1.61	74.89	180	[33]
$0.20BiFeO_3$-(0.05)$BaTiO_3$-$0.25BiScO_3$–$0.50SrTiO_3$ ceramics	3.4	85.6	230	[32]

$(0.67\text{–}x)BFO\text{–}0.33BTO\text{–}xBa(Mg_{1/3}Nb_{2/3})O_3$	1.56	75	125	[34]
BTO-0.125BMN	1.89	83	240	[35]
$0.7[0.88BTO\text{-}0.12Bi(Zn_{2/3}Nb_{1/3})O_3]\text{-}0.3BNT$	3.82	94.4	265	[36]
$0.95BTO\text{-}0.05Bi(Ni_{2/3}Ta_{1/3})O_3$	0.55	87.15	117	[37]
$0.93BTO - 0.07YNbO_4$	0.61	86.8	170	[38]
$0.85BTO\text{–}0.15Bi(Mg_{1/2}Zr_{1/2})O_3$	1.25	95.4	185	[39]
$0.92BTO\text{–}0.08Bi(Mg_{1/2}Ce_{1/2})O_3$	1.26	68.5	250	[40]
$0.9BTO\text{–}0.1Bi(Mg_{2/3}Nb_{1/3})O_3$	1.13	90	144	[41]
$0.86BTO\text{–}0.14Bi(Zn_{1/2}Ti_{1/2})O_3$	0.81	94	120	[42]
0.88BST-0.12BZN	1.62	99.8	225	[43]
$0.85BTO\text{-}0.15Bi(Mg_{0.5}Sn_{0.5})O_3$	3.05	95	220	[44]
0.9BTO-0.1BMH	3.38	87	240	[45]
$(1\text{-}x)BTO\text{-}xBi(Mg_{0.5}Zr_{0.5})O_3$	2.9	86.8	220	[46]
0.6BTO-0.4BMT	4.49	93	290	[47]
0.85BTO-0.15BZS	2.41	91.6	280	[48]
$0.88(Ba_{0.8}Sr_{0.2})TiO_3\text{-}0.12Bi(Zn_{2/3}Nb_{1/3})O_3$	1.62	99.8	225	[49]
$0.85BTO\text{-}0.15Bi(Mg_{0.5}Zr_{0.5})O_3 + MnCO_3$	1.61	94.3	230	[50]
$0.88BTO\text{-}0.12Bi(Li_{1/3}Hf_{2/3})O_3$	1.65	95.6	230	[51]
$0.94BTO\text{-}0.06Bi_{2/3}(Mg_{1/3}Nb_{2/3})O_3$	4.55	92	520	[52]
$0.88BTO\text{–}0.12Bi(Mg_{1/2}Ti_{1/2})O_3$	1.81	88	224	[53]
$0.7\ BTO\text{–}0.3\ BiScO_3$	2.3	-	225	[54]

$0.7SrTiO_3$-$0.3(0.65BaTiO_3$-$0.35Bi_{0.5}Na_{0.5}TiO_3)$	1.40	90	196	[55]
0.92BTO- $0.08K_{0.73}Bi_{0.09})NbO_3$	2.51	86.9	327	[56]
0.9BTO-$0.1Bi(Li_{0.5}Ta_{0.5})O_3$	2.2	89	280	[57]
0.9BTO-$0.1(Bi_{0.9}Na_{0.1})(In_{0.8}Zr_{0.2})O_3$	1.33	88	180	[58]
0.9BTO-$0.1Bi(Mg_{2/3}Nb_{1/3})O_3$	1.13	95.8	113.5	[41]
0.6BTO-$0.4Bi(Mg_{1/2}Ti_{1/2})O_3$	4.49	93	340	[59]

Several $BaTiO_3$-Bi(*Me*)O_3, (here *Me* denotes trivalent or average trivalent cation) systems have recently been studied, including BT-$BiScO_3$, BT-$BiYbO_3$, BT-$Bi(Zn_{1/2}Ti_{1/2})O_3$, BT-$Bi(Mg_{1/2}Ti_{1/2})O_3$, BT-$Bi(Mg_{1/2}Nb_{1/2})O_3$, etc, with relaxor behavior displaying better energy storage performance [60][42]. Combining Bi(Me)O_3 and $BaTiO_3$ can assist in the creation of PNR by breaking the long-range ferroelectric order. Because of the comparable electronic structures of Pb^{2+} and Bi^{3+}, the hybridization between Bi 6p and O 2p is anticipated to raise the maximum polarization. Furthermore, these $BaTiO_3$-Bi(Me)O_3 systems' energy storage performance is unaffected by external temperature changes with broad temperature-stable dielectric properties.

Various binary or ternary solid solution systems based on $BaTiO_3$-$BiMeO_3$ including $BaTiO_3$-$BiFeO_3$ (BTO-BFO) have been throughly explored [61][62][63][64][65][66][67][68][69][32]. Undoped BFO-BTO-based ceramic with higher BFO contents have high P_{max}; however, its ΔP is low due to the fact that it is unsuitable for energy storage applications [70]. In recent years, researchers have focused on enhancing the energy storage performance of the BFO-BTO system. The composition with 0.75BFO-0.25$(Ba_{0.99}La_{0.01})TiO_3$ ceramics is reported to exhibit a large W_{rec} of 0.61 J/cm^3 by Calisir et al.[71]. Similarly, $Ba(Mg_{1/3}Nb_{2/3})O_3$ substituted BFO-BTO bulk ceramics exhibited double hysteresis loops with improved energy storage performance W_{rec} of 1.56 J/cm^3 with η of 75% and also showed wide temperature stability in temperature range of 25-190 °C [34]. Likewise, enhanced energy storage performance is observed for the Nd-doped BFO-BTO system with W_{rec} 1.81 J/cm^3 [72]. Meanwhile, the previous studies report that the bulk ceramics with $BaTiO_3$-$Bi(Zn_{2/3}Nb_{1/3})O_3$ composition displayed a large W_{rec} of 0.79 J/cm^3 and η of 93.5% at an applied field of 131 kV/cm [73]. Further, the Ta substituted bulk composition with $0.87BaTiO_3$-$0.13Bi[Zn_{2/3}(Nb_{0.85}Ta_{0.15})_{1/3}]O_3$ exhibited greatly improved energy storage performance with W_{rec} of 1.44 J/cm^3 and η of 92.5% at 218 kV/cm [74]. Here, Ta is mainly substituted for Nb in $BaTiO_3$-$Bi(Zn_{2/3}Nb_{1/3})O_3$ composition, expecting to decrease the energy loss and leakage current density at the higher applied electric field.

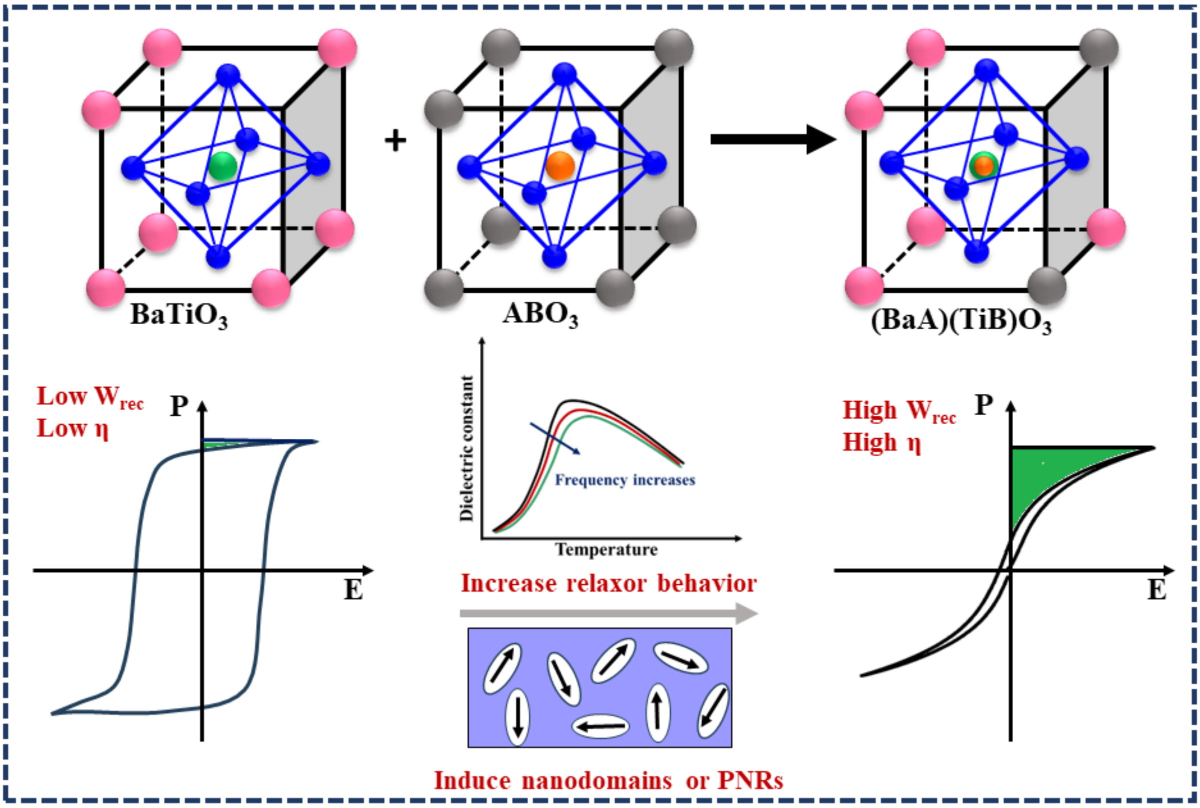

Figure 1. 16: Procedure for tailoring BTO-based relaxor ferroelectrics [15].

Additionally, adding Bi-based compounds can accelerate the densification process and lower the sintering temperature, which leads to a low dielectric loss, large activation energy, and dense microstructure in BTO-Bi(Me)O_3 ceramics, which favor high E_{BDS}. Ogihara et al. first examined the energy storage capabilities of the BTO-Bi(Me)O_3 family in 2009 on 0.7BTO-0.3$BiScO_3$ (BTO-BS) ceramics [54]. Using 0.2 mm thick BTO-BS ceramics, enhanced energy storage (W_{rec}) of 2.3 J/cm^3 is obtained at 225 kV/cm. Meanwhile, 15 µm thick single dielectric layer capacitors can produce a significant W_{rec} of 6.1 J/cm^3 in the same composition together with exceptional thermal stability. Improved energy storage capabilities of BTO-BS ceramics triggered the curiosity of the BTO-Bi(*Me*)O_3 family toward the electrical energy storage system. **Figure 1. 16** demonstrates the tailoring strategy to improve the relaxation behavior by inducing nano-domains or PNRs and optimizing the microstructure via A and B-sites co-doping.

1.10 Thin films for energy storage devices

Developing a material into thin films provides an extension to improve the functionality of the system. A material is termed a thin film when its thickness layer ranges from fractions of a nanometer (monolayer) to several micrometers, as shown in **Figure 1. 17**. Meanwhile, with the rapid evolution of miniaturization, integration, and lightweight, film capacitors for energy storage have gained increasing attention. In contrast to their bulk equivalent, thin films possess pore-free and dense microstructure with low lattice imperfections and defects, which can withstand the larger applied electric field. Several factors, such as the method of material deposition, fabrication, choice of substrate, variations in crystal phase, disorder, and defect within poly-/nano-crystalline and amorphous materials, can all affect the different properties of thin films. Also, due to these factors, thin film exhibits a much more comprehensive range of structure, electrical, chemical, mechanical, and optical properties than their bulk counterparts. As the material's dielectric strength is inversely proportional to the thickness of the material, the dielectric strength becomes dimension-independent, which reaches the intrinsic one when the thickness decreases to a critical value. Due to this reason, the dielectric films show a larger breakdown strength than that of bulk ceramics.

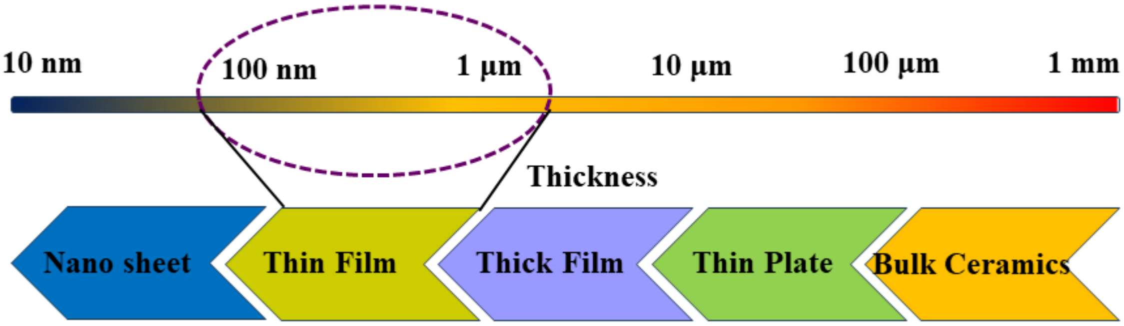

Figure 1. 17: Comparison of dielectric materials based on thickness, highlighting the thickness range of thin film.

Thin films naturally develop interfaces with the substrate, layers below or above, or the environment. Additional modifications may be seen at these interfaces and interfacial regions due to chemical composition, bonding configurations, confinement, environmental exposure, physical mixing, and prevailing morphology. Consequently, dielectric ceramic films have become the best material to exhibit gigantic energy densities (>100 J/cm^3) and highly high storage efficiencies (>80%) under the influence of massively applied electric fields (>3 MV/cm) [75]. Several studies have been conducted on dielectric films to be applicable for energy storage device applications. Various processing technologies, such as sol-gel, tape casting, screen printing, magnetron sputtering, chemical solution deposition, pulsed laser deposition, atomic layer deposition, etc., have been employed. The different parameters affecting the films' energy storage performance are deposition technique, substrate, stress between the film composition, substrate clamping, film thickness, grain size, etc. With the expansion of microelectronics technology demand for data storage, transducers, and microelectromechanical systems (MEMS), the ferroelectric thin film has become a crucial component. Ferroelectric thin films and Si complementary metal oxide semiconductors

(CMOSs) were successfully integrated in 1993, marking the beginning of the industrialization of ferroelectric memory. Since then, ferroelectric materials and device development have advanced from single crystal to thin film and separate to integrated devices [76]. In the years after that, ferroelectric thin film materials such as BFO, PZT, and BTO have been extensively explored in various domains, such as memory devices, detectors, piezoelectric MEMSs, and so on [76].

Zhang et al. reported on $Bi_{0.97}Nd_{0.03}FeO_3$ thin films with enhanced energy storage density of 10.43 J/cm^3 by lowering leakage current density through co-doping Ti and Zn [77]. It was anticipated that the Ti^{4+} and Zn^{2+} atoms substituting for Fe^{3+} would diminish the oxygen vacancies, attributed to the smaller leakage current than pristine BFO. Xu et al. anticipated that Dy, Sm, La, and Gd substituted BFO thin films would attain huge energy density [78]. A representative of the BFO family, $Bi_{1-x}Nd_xFeO_3$ is evaluated to acquire high energy efficiencies of 80-88% with giant energy densities of 100-150 J/cm^3 at an applied field of 2-3 MV/cm. There have been attempts to look into ways to enhance energy storage performance via strong interlayer couplings in layered heterostructures [79][80][81][82]. Zhang et al. put forward an effective way to enhance the energy storage performance and the E_{BDS} by constructing F-I-F (ferroelectric-insulator-ferroelectric) opposite double-heterojunction configuration of $PZT/Al_2O_3/PZT$ multilayer thin films [83]. It was thought that the insulator layer between the ferroelectric heterojunctions would induce the built-in electric field (E_{in}) by different fermi levels and also counteracts the external electric field (E_{ex}), resulting in the depletion of the carrier concentration in the AO layer that improves the E_{BDS} and insulating strength of the AO layer. Similarly, tri-layered $BiFeO_3/Bi_{3.25}La_{0.75}Ti_3O_{12}/BiFeO_3$ films exhibited large W_{rec} of 65.5 J/cm^3 at 2.75 MV/cm. The enhanced energy storage capabilities are ascribed to the large polarization of the BFO layer with the reduction in leakage current density and large E_{BDS} due to the interfacial effect hindering the formation of electric trees [84]. Likewise, the BCT/BZT and BTO/BST multi-structured films are claimed to have super energy storage characteristics in multilayer films made using similar and dissimilar combinations of dielectric material and solid-solution ceramics films [85][86]. **Table 1. 2** summarizes the review of the monolayer, bilayer, and multi-layer films with enhanced energy storage characteristics.

Table 1. 2: Energy storage performance of thin films

materials	***Substrate***	***Fabrication method***	W_{rec} ***(J/cm^3)***	***η (%)***	E_{BDS} ***(MV/cm)***	***Ref.***
BFO	ITO	PLD	0.19	43	-	[87]
Ti and Zn co-doped $Bi_{0.97}Nd_{0.03}FeO_3$	ITO	metal-organic decomposition	10.43	87	0.35	[77]
$0.88BTO–0.12Bi(Mg_{0.5}Ti_{0.5})O_3/PbZrO_3$	$Pt(1111)/Ti/SiO_2/Si$	Sol-gel	33	70	1.050	[79]
BFO/BTO bilayer films	SRO buffer (100) STO	Rf magnetron sputtering	51.2	73	2.600	[80]
BTO- BST thick films	Mylar substrates	Tape casting	1.16	-	0.218	[81]
BFO/BTO bi-Layers	$LaNiO_3$ Buffer $Pt/Ti/SiO_2/(100)Si$	rf magnetron sputtering	71	61	-	[82]
$PbZrO_3/PbZr_{0.52}Ti_{0.48}O_3$	$Pt(111)/Ti/SiO_2/Si$	Sol-gel	28.2	50	2.410	[88]
PZT/AO/PZT	$Pt(111)/Ti/SiO_2/Si$	Sol-gel	63.7	81.3	5.71	[83]
BCT/BZT multilayer	(001) Nb: STO	Magnetron sputtering	52.4	72.3	4.5	[85]
BTO/BST superlattices	(100) MgO single crystal	PLD	46	75	5	[86]
$BFO/Bi_{3.25}La_{0.75}Ti_3O_{12}/BFO$	$Pt(111)/Ti/SiO_2/Si$	CSD	65.5	74.2	2.75	[56]

1.11 Literature gap and motivation of thesis work

- ✓ It is observed that most of the research on energy storage applications is focused on solid-solution of the $BaTiO_3$-$BiMeO_3$ family. For materials to exhibit improved properties, synthesis methods, microstructure, and relatively high sample density are the dominant factors. For this, the selection of materials, as well as doping concentration, should be optimized. It is also noticed from the previous investigation that the MPB regime in this solid solution displays better properties. Many studies focus on $(1-x)BaTiO_3-xBiFeO_3$ (where x =0.7-1). It is believed that $(1-x)BaTiO_3-xBiFeO_3$ system with composition range from (x=0.0-0.3) with pseudo-cubic nature will display high strain response in nano-domain. Hence, it exhibits a better ferroelectric response, enhancing energy storage properties. It is also evident from the literature that no composition is explored in the broadband frequency region (1MHz to 1GHz); the present study is conducted to investigate the thermal stability of the composition in broadband frequency regimes.

  Other bulk systems with $(1-x)BaTiO_3-x[Bi-(Zn_{2/3}(Nb_{0.85}Ta_{0.05})_{1/3})O_3]$ composition in x range from 0.05 to 0.025 is explored from $BaTiO_3$-$Bi(Me)O_3$ family exhibiting relaxor ferroelectric nature. This composition $(1-x)BaTiO_3-x[Bi(Zn_{2/3}(Nb_{0.85}Ta_{0.05})_{1/3})O_3]$ with MLCCs is explored, showing enhanced energy storage performance. However, this composition is not studied for bulk ceramics.

- ✓ Literature suggests that rare-earth doped BFO films displayed improved energy storage performance if the leakage current density is reduced. Very few studies are concentrated on the BFO for energy storage performance, and most of the films are deposited on single crystal substrates. The present work is the fabrication of monolayer $Bi_{0.993}La_{0.007}FeO_3$ (BLFO) thin films on economical friendly conducting ($Pt/Ti/SiO_2/Si$) substrates compared to single crystal substrates, which are costly to be used for practical applications.

- ✓ Many studies are carried out on BFO/BTO bilayer and multilayer films for different purposes, such as the magnetoelectric coupling effect, photovoltaic effect, and energy storage capacitor applications. The physical phenomena occurring at the multiferroic heterostructure interfaces motivated to investigation of the multiferroic properties of BLFO/BTO thin films. Herein, the multiferroic response with energy storage performance is investigated. So far, BLFO/BTO bilayer films have not been reported. However, very few reports are available for top layer thickness variation of bilayer thin films.

Certain efforts have been made to investigate the possibilities of enhancing the energy storage performance in ferroelectrics via strong interlayer couplings in layered heterostructures. Previous reports on multilayer and superlattices with alternating stacking of two dielectric materials displayed enormous recoverable energy densities. The enhanced discharge energy density in the multilayer films is attributed to charge transfer controlled by space charge and interlayer charge coupling. Till now, no studies are available on different numbers of stacking layers in BZNT/BTO composition. Taking advantage of the interface phenomenon, multilayer thin films with alternate stacking of two different dielectric materials are grown into BZNT/BTO multilayer films. Here, the effect of the number of stacking layers on energy storage performance is investigated.

1.12 Objective of the thesis work:

In this present work, bulk ceramics and thin films are synthesized for energy storage capacitor applications. The objective of the current thesis work includes:

- ✓ To synthesize BTO-BFO solid-solution ceramics using the conventional solid-state reaction method (CSSR) and to investigate its multiferroic behavior and energy storage performance.

- ✓ Development of BTO-$BiZn_{2/3}(Nb_{0.85}Ta_{0.15})_{1/3}O_3$ homogeneous solid-solution for tuning energy storage performance.
- ✓ Optimization of phase pure bismuth ferrite by chemical modification with rare earth element (La) and the development of BLFO thin films for energy storage capacitor applications.
- ✓ Fabrication of BLFO/BTO bilayer hetero-structures and exploring the induced interfacial effect in enhancing the energy storage of the thin films.
- ✓ Development of multilayer BZNT/BTO heterostructures to observe the dominance of alternate interfacial effect in enhancing the breakdown strength, reducing the leakage current density, and optimizing breakdown strength and electric parameters to improve energy storage response in alternating stacked multilayer thin films.

1.13 Outline of the thesis work

In this present work, the structural, microstructural, dielectric, and ferroelectric studies of lead-free barium titanate-based dielectric ceramic solid solutions and their thin films for energy storage capacitor applications have been reported. The first working chapter deals with the fundamental inorganic materials (BTO) and their chemical modification with other ABO_3 structures ($BiMeO_3$, *Me* is trivalent or averagely trivalent) for tuning the structural, morphology, and electric properties. Substitution of $Bi(Me)O_3$ into the $BaTiO_3$ matrix is expected to help break the long-range ferroelectric order to establish PNRs. An optimum amount of $Bi(Me)O_3$ composition addition is optimized to tune the microstructure, dielectric, and ferroelectric properties to acquire enhanced energy storage performance in $BaTiO_3$-$Bi(Me)O_3$ solid solutions. The second section of the work describes the optimization of pure phase BFO with chemical substitution of rare earth and excess Bi addition. Further, the bulk ceramics powder of BLFO is used to develop an in-house PLD target to be utilized for BLFO thin film fabrications. The effect of oxygen partial pressure on structural, microstructural, dielectric, and ferroelectric properties of BLFO thin films is investigated. The final section describes the bilayer (BLFO/BTO) thin films developed to study the induced interfacial effect on dielectric, ferroelectric, and magnetic properties. It also involves the development of multilayer heterostructures of alternate stacking of BTO and BZNT layers to obtain multilayer thin films. The thesis is organized into six chapters covering the introduction and preparation procedure of ceramics and thin films, followed by three working chapters and summarizing with conclusions and future scopes. Each section of the thesis is briefly discussed below:

Chapter I discusses the introduction and current interest in the field of energy storage applications. The requirement of energy storage systems and application of the dielectric materials in pulsed power devices. Different types of dielectric materials and their usage in energy storage applications, relaxor ferroelectric systems, barium titanate-based dielectric ceramics, and the strategies to improve and enhance their ferroelectric properties for practical applications. A strong emphasis has been given to BTO-based solid-solution, monolayer, bilayer, and multilayer thin films for their applicability in energy storage applications. Further, the improved energy storage performance of monolayer, bilayer, and multilayer thin films is discussed. The research gap and objectives of the thesis work are further emphasized.

Chapter II gives detailed information about the experimental techniques and the synthesis route followed for the preparation of bulk ceramics and the deposition of thin films. The bulk ceramic synthesis is carried out using the conventional synthesis method, i.e., solid-state reaction method. A high-energy ball mill is used to obtain the fine powders with highly densified ceramics. The milling parameters, calcination, and sintering temperature are optimized for the desired phase structure with relatively high density. The heat treatment to the samples is given using the laboratory furnace Nabertherm, and the density of the prepared samples is measured using Archimedes’ principle. The phase structure is confirmed via XRD and Raman spectroscopy. The sample′s morphology is checked using FESEM analysis. The elemental compositions and distribution are verified using the EDX in FESEM and XPS. The dielectric response of the ceramics is checked using an LCR meter and impedance analyzer. The ferroelectric measurements are carried out via a ferroelectric tester. The optical response is observed with the help of UV-visible spectroscopy. The pulsed laser deposition technique is used for the deposition of monolayer, bilayer, and multilayer films. The target mainly used for the deposition of the thin films is manually prepared in the laboratory using the solid-state reaction technique. The target used is pressed into 20 mm in diameter and 10mm in thickness. The surface topology of the deposited films is observed using AFM analysis, and IV characteristics are done to check the device response of the films.

Chapter III: In this section, the combination of Bi(Me)O_3 with $BaTiO_3$ ceramic is studied systematically and presented in two sections.

Section I discusses the solid-solution of $(1-x)BaTiO_3$-$xBiFeO_3$ (x=0.0-0.3) ceramic termed as BTBF composition synthesized using solid-state reaction method. The energy storage performance is mainly evaluated from the ferroelectric hysteresis curves obtained for BTBF samples. The W_{rec} and η(%) of 40 mJ/cm^3 and 60.92%, respectively, are found for BTBF1 composition, which exhibited improved energy storage performance compared to other solid solutions. However, the energy density and efficiency value obtained in this study are lower for high-energy-density applications.

Hence, in section II, another composition with the $BaTiO_3$-Bi(Me)O_3 family is explored. Lead-free ($(1-x)BaTiO_3$-$xBi[Zn_{2/3}(Nb_{0.85}Ta_{0.15})_{1/3}]O_3$) composition with x ranging from 0.05 to 0.25 is fabricated using the same synthesis route. The electrical parameter influencing the energy storage performance is investigated. The correlation between oxygen vacancies/defects, activation energy, and breakdown strength is studied. A remarkably high W_{rec} of 2.06 J/cm^3 with an η of 78% is achieved for BTO-BZNT3 ceramics at an applied field of 180 kV/cm. The ultrahigh-energy efficiency of up to 96% is observed for higher concentrations in BTO-BZNT ceramics. In the present investigation, BT-BZNT3 and BT-BZNT4 ceramics displayed a comparable energy storage performance at a low applied field of 180 kV/cm, demonstrating the excellence of BT-BZNT ceramics over other $BaTiO_3$-$BiMeO_3$ family. The enhanced energy storage performance is attributed to the lower oxygen vacancies/defects in the higher BZNT substituted ceramics confirmed through XPS analysis. Therefore, the BTO-BZNT ceramics can have potential applications in advanced pulsed power capacitors.

Chapter IV describes the optimization to achieve pure phase bismuth ferrite (BFO) with doping with lanthanum. The optimized $B_{0.993}L_{0.007}FeO_3$ composition is used further to fabricate the thin films on n-type silicon and quartz substrates using the PLD technique. The deposition of thin films is optimized at different oxygen partial pressures (OPPs) under 15, 20, 25, and 30 SCCM. The effect of OMPs is then studied to observe the multiferroic behavior. Among the deposited BLFO films, the film deposited at 20 SCCM displayed better crystallinity, dense microstructure, and low surface roughness. The HRTEM image and SAED pattern obtained using TEM analysis verified the crystal structure of BLFO films, which crystallizes into rhombohedral crystal symmetry. The films deposited at 20 SCCM displayed the high dielectric constant of $\varepsilon_r \sim 447$ with minimum loss tangent of $\tan\delta \sim 0.202$ and improved W_{rec} of 2.09 J/cm^3 with η of 78.42%, respectively. The dense microstructure and favorable oxygen ambiance contributed to the lower leakage current density of $\sim 1.08\times10^{-7}$ A/cm^2 at ± 500 kV/cm, further improving energy storage performance.

Chapter V presents the fabrication of bi-layer and multilayer heterostructure films.

The First section presents the development of bi-layer thin film deposited using the PLD technique. Single layers, BTO, and BLFO thin films are initially optimized for fabricating bilayer thin films of BLFO/BTO thin films with variation in the top layer. The film with higher

(BLFO) top layer thickness exhibited good crystallization, uniform smaller grain size, and dense microstructure among the deposited heterostructures. The BLFO/BTO3 film displays a high W_{rec} of 11.65 J/cm^3 with η of 85%. The improved overall response- low remnant polarization, large maximum polarization, high breakdown strength, and low leakage current of the heterostructures is attributed to low oxygen vacancies/defects in the BLFO/BTO3 films.

The second part of this chapter describes the multilayer heterostructures with alternate BZNT and BTO layers, in which bilayer (BZNT/BTO), BZNT/BTO1, tri-layer (/BTOBZNT/BTO), BZNT/BTO2 and tetra-layer (/BZNTBTO/BZNT/BTO), BZNT/BTO3 structure is designed by PLD technique. In this study, energy storage performance is evaluated with a number of stacking layers. Tetra-layer films with an increasing number of layers exhibited better crystallinity, better microstructure, and lower defects owing to multiple interfaces. With several stacking layers, the ferroelectric hysteresis loops of the heterostructures displayed a linear response, owing to the space charge located in interfacial layers. The enhanced energy storage performance may be attributed to the intervening ferroelectric BTO and BZNT layers in the multilayered BZNT/BTO3 films. An improved W_{rec} of 52.19 J/cm^3 with η of 92.21% is achieved for the higher number of stacking layered films. The small leakage current value ($\sim 10^{-7}$ A/cm^2 at ±500 kV/cm) in the deposited tetra-layered BZNT/BTO multilayer structure assures its appropriateness for the device applications. Hence, the abundant interfaces are introduced by periodically stacking the different layers of BTO and BZNT, resulting in improved energy storage performance.

Chapter VI concludes with a brief summary of the thesis work and its key output and highlights the future scope in the field of energy storage capacitor application. This chapter also unveils the experimental limitations with requisite improvement to carry the research in the forward direction.

Chapter 2

Experimental methods and characterizations

2 Materials synthesis

This chapter discusses the preparation method of bulk ceramics as well as the deposition of thin films. It describes the experimental procedure followed for the preparation of BTO-based solid solution and thin films. This chapter also discusses the different characterization techniques implemented to analyze the material characteristics. The bulk ceramic preparation is carried out using a solid-state reaction method and thin films are developed by pulsed laser deposition technique. This chapter also includes brief descriptions of the working principles of different characterization techniques used.

2.1 Synthesis of BTO and BTO-based ceramic powders

There are different processing methods used to synthesize the bulk ceramics powders. The method includes sol-gel, hydrothermal, wet chemical routes, co-precipitation, combustion, conventional solid-state reaction methods (CSSR), and so on. The synthesis method highly influences the purity, grain size, morphology, and crystallinity of the prepared powders. Even if the same starting reagents are used, the ceramics displays quite different properties when prepared by different preparation route. In the present thesis work, the CSSR method is followed for the synthesis of BTO and BTO-based solid-solution.

2.1.1 Conventional solid-state reaction method (CSSR)

The CSSR method is the most widely used, simplest, and high-temperature synthesis technique in solid-state chemistry. It involves subjecting the different solid reagents to direct, high-temperature reactions. This approach employs simple oxides, carbonates, nitrates, fluorides, and oxalates as reagents. Therefore, this technique is a thermodynamically stable, inexpensive, and user-friendly method. The starting reagents are initially weighed as per the stoichiometric ratio obtained by the reaction **Eq. (2.1-2.4)** and uniformly mixed by a high-energy ball mill. The powder can be either dry milled or wet milled according to the requirement. In the case of the present work, the powder is wet ball milled in the distilled water medium. After ball milling, the powders are dried and calcined at an optimized temperature to obtain the desired phase. Later, the obtained pure phase powders are compacted into cylindrical discs to achieve densification and sintered at optimized sintering temperature. The complete recipe for sample preparation using the CSSR technique is shown in **Figure 2. 1**.

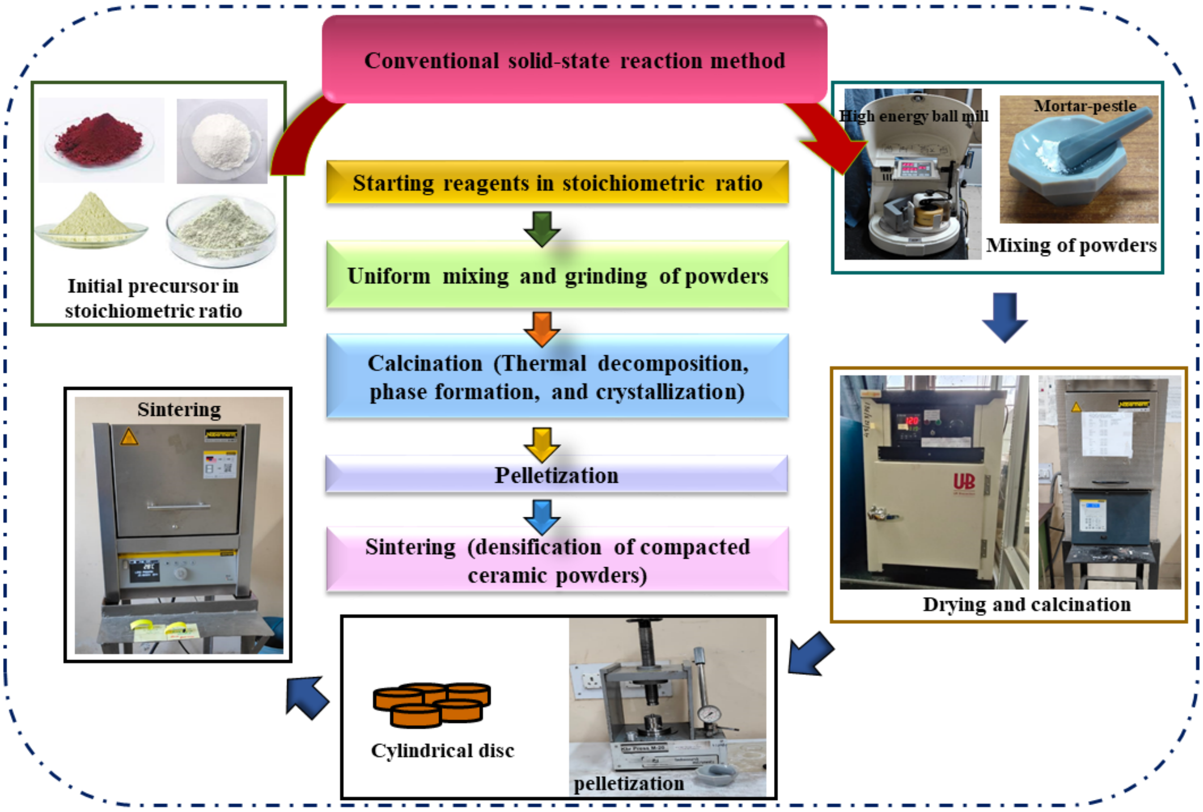

Figure 2. 1: Flow of synthesis procedure by conventional solid-state reaction method.

2.1.2 Starting reagents in stoichiometric proportion

Analytical grade reagents with purity >99.99% are important to achieve the desired phase. The raw materials including $BaCO_3$, TiO_2, Bi_2O_3, Fe_2O_3, ZnO, Nb_2O_5, and Ta_2O_5 are procured from ACROS Organic, Sigma Aldrich, Alfa-Aesar, and JiangXiHaiTe Advance Material. The initial starting reagents in the stoichiometric ratio are weighed (AG135, M/s METTLER TOLEDO, AG135, with accuracy ± 0.01 gm) for preparing $BaTiO_3$, $BiFeO_3$, $Bi_{0.993}La_{0.007}FeO_3$, and $Bi[Zn_{2/3}(Nb_{0.85}Ta_{0.15})_{1/3}]O_3$ compositions, respectively as per the following reaction method:

$$BaCO_3 + TiO_2 \rightarrow BaTiO_3 + CO_2 \tag{2.1}$$

$$Bi_2O_3 + Fe_2O_3 \rightarrow 2BiFeO_3 \tag{2.2}$$

$$0.993Bi_2O_3 + 0.007La_2O_3 + Fe_2O_3 \rightarrow 2Bi_{0.993}La_{0.007}FeO_3 \tag{2.3}$$

$$Bi_2O_3 + ZnO + Nb_2O_3 + Ta_2O_5 \rightarrow BiZn_{2/3}(Nb_{0.85}Ta_{0.15})_{1/3}O_3 \tag{2.4}$$

2.1.3 Sample preparation

For uniformly mixing the starting materials, a mortar pestle and a ball mill (Pelverisette 6, M/s Fritsch GmbH, Germany) are used. The raw powders in the stoichiometric ratio are poured into a zirconium jar with zirconium balls of diameter 5mm. The powder-to-ball ratio is kept at 1:10, and distilled water is used as a grinding medium. The mixture is grounded for 5 h at a rotation speed of 150 rpm (rotation per minute). The slurry obtained is dried in the hot air oven (M/s Optics Technology) and calcined at optimized calcination temperature. As-prepared BTO powder is calcined for 6 h at 1000 °C, and BFO, BLFO, and BZNT powders are calcined for 30 minutes at 800 °C. Usually, calcination is the common thermal process used in ceramic preparation. It is used to decompose the carbonates, sulfates, and hydrates to obtain the desired phase. It is also used to remove the volatile substance or impurities from the sample. The temperature of calcination is above the decomposition temperature of one of the reactants and below their melting temperature. In this heat treatment process, the calcination temperature, dwelling time, heating rate, heating atmosphere, etc, are major factors that influence the phase formation of the sample. The calcination temperature is usually determined by thermogravimetric and differential scanning calorimetry analysis (TGA-DSC). The phase formation is then identified using the XRD pattern of the calcined samples. After achieving the desired phase, the calcined powders are again ball-milled at 300 rpm for 10 h to bring down the initial particle size and to improve the density of the samples. The surface-to-volume ratio increases with the particle size reduction, which enhances the chemical reactivity of the particles. Further, the maximum density of the specimens with lower defects and better compaction can be achieved at significantly lower sintering temperatures.

2.1.4 Compaction of the cylindrical discs

Since the microstructural and structural properties highly influence the physical properties of the sample, a highly densified ceramics disc with uniform grain size and minimum defect is desired. The ceramic powders obtained after re-grinding are, however, non-elastic and are difficult to shape into discs of the desired dimension. Therefore, binding agents (or pressing lubricants) such as clays and polymers are added to the dry powders that provide adequate mechanical strength and elasticity to withstand the subsequent pressing processes, which include handling and high-temperature sintering. For pressing dry powder ceramics, polyethylene glycol (PEG) and polyvinyl alcohol (PVA) are regarded as the most effective binders. Herein, in the synthesized fine powders, the PVA (5 wt% PVA solution) is added, mixed uniformly, and pressed using a KBr hydraulic press (M-20, M/s Technosearch Instruments, India) into cylindrical discs of 1-5 mm in thickness and 10 mm in diameter. The pressure of 30-40 kg/cm^2 is applied uniaxial to prepare the cylindrical green discs. The pressure applied on the top surface of the die can be expressed as follows,

$$P_x = P_a \, exp^{\frac{-4\mu KL}{D}} \tag{2.5}$$

where P_a and P_x denote the pressure applied and pressure gradient respectively. The μ, and K, represent the friction coefficient, and a constant, respectively. The variables L and D are the dimensions referring to the length and diameter of the die, respectively. The cylindrical discs are prepared and then sintered at the optimized sintering temperature. During this process, the organic binder PVA evaporates at 400-600 ℃, unaffecting the electrical properties of the ceramics.

2.1.5 Sintering

Sintering is a post-calcination process, performed for compacting the material, heated in a controlled atmosphere below the melting point of the desired phase. It is usually carried out to enhance the crystal quality by achieving the maximum possible density, enhancing grain growth (reducing the total area of grain boundary), and minimizing defects. High relative density and minimum porosity are important to achieve enhanced dielectric and ferroelectric properties. Therefore, the optimal sintering temperature is the one at which the ceramics exhibit their highest relative density.

The two most common sintering methods are the solid-state sintering (SSS) method and liquid-phase sintering (LPS). Densification occurs in the SSS process due to the agglomeration of solid particles, while in the LPS process, a liquid phase is present throughout the sintering process. LPS offers the advantages of being easy to control the microstructure, and inexpensive to process, however, a potential downside of the LPS process is that it may alter the mechanical properties of the ceramics. Accordingly, an SSS process is implemented for carrying out the thesis work. For sintering the as-prepared green discs, a high-temperature conventional furnace (LHT 04/18, M/s Nabertherm GmbH, Germany; with a temperature range from 25˚C-1800˚C) is used. SSS is mainly driven by an excess of surface-free energy. It is a complicated process that depends on the material and furnace parameters. Mainly, highly dense material is accomplished via the three interconnected stages, namely the initial stage, the intermediate stage, and the final stage as shown in **Figure 2. 2**. In the first phase (initial stage), the rearrangement of the particles with the formation of neck growth takes place, and end of this stage, the relative density of compactness increases to almost 60-65%. During the intermediate stage, the neck growth between the particles evolves rapidly through grain boundary diffusion, lattice diffusion, and surface diffusion with the reduction in pores and enhancement in grain growth taking place. At the end of this stage, with shrinkage of volume, the relative density enhances from 65%- 90%. In the final stage, the densification is comparatively slower than in the initial and intermediate stages. This stage involves the removal of isolated pores within the grain boundaries and grains via the processes of grain boundary diffusion and lattice diffusion respectively. The final stage of sintering begins at approximately 90 to 95 percent of theoretical density.

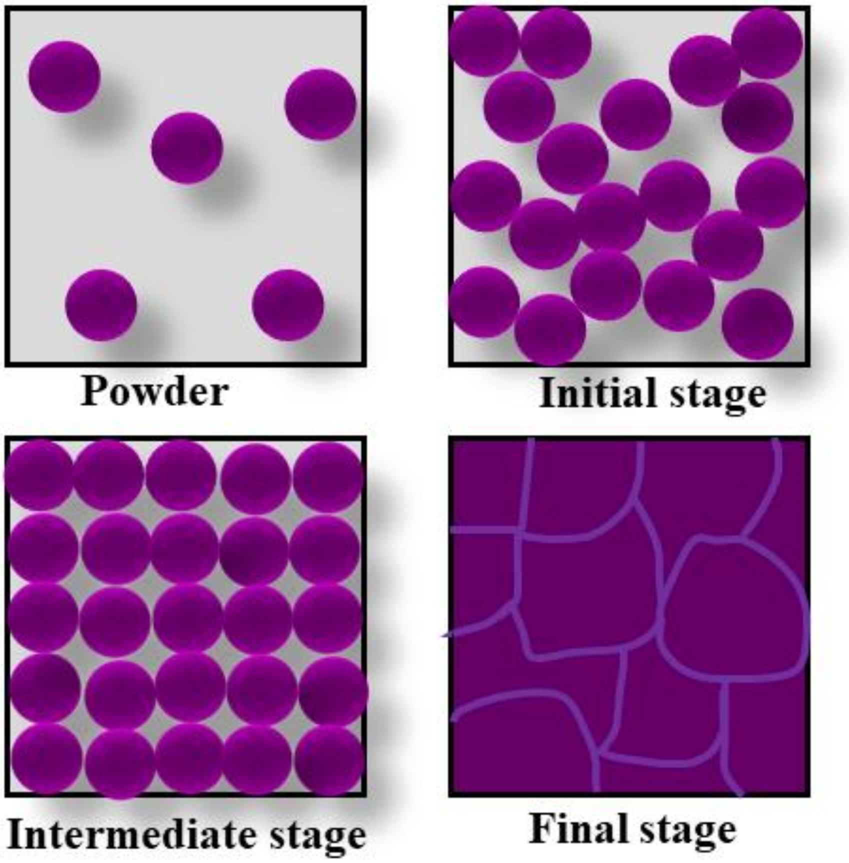

Figure 2. 2: Depicting various stages of the sintering process, starting from powder to initial stage, going through intermediate to final stage.

2.2 Thin film deposition

2.2.1 Preparation of BTO, BLFO, and BZNT targets

The BTO ceramic target for film deposition is synthesized using the CSSR method. Analytical grade reagents, including $BaCO_3$ (M/s ACROS Organic, USA, ≥99%) and TiO_2 (M/s Sigma-Aldrich, USA, 99.99%), are weighed as per the stoichiometric proportion stated in **Eq. 2.1**. These powders are mixed and wet milled in distilled water (as a grinding medium) in a zirconium jar using a high-energy ball mill (Fritsch GmbH, Pulverisette 6, Germany) with a powder-to-ball ratio of 1:10. The mixture is grounded for 5h at 150 rpm speed. The powder obtained after drying the slurry is calcined at 1000 °C for 6 h. This powder is again ball milled for 10 hours at 300 rpm to reduce the particle size and achieve densification. The organic binder PVA is mixed with the dried powders before pressing it into a target of 20 mm diameter and 4mm thickness using KBr Press (M/sTechno Search Instruments, M-20, India). Finally, the target prepared is sintered at the optimized temperature of 1250 °C for 2h.

Following the same procedure, the BLFO and BZNT targets are developed. For preparing these targets, raw materials include La_2O_3, Bi_2O_3, ZnO, Nb_2O_5, and Ta_2O_5 (M/s Sigma-Aldrich, USA), and Fe_2O_3 (M/s JiangXiHaiTe Advance Material, China) are used. The calcination of the BLFO and BZNT powders is done at 800 °C for 2 h, and the targets are sintered at 800 °C for 30 minutes, respectively.

2.2.2 Pulsed laser deposition (PLD)

Various techniques are used for film deposition, including spin coating, sputtering, thermal evaporation, tape casting, pulse laser deposition (PLD), molecular beam epitaxy (MBE), and more. Mainly, film deposition techniques are divided into two types: chemical vapor deposition and physical vapor deposition methods. PLD comes under the physical vapor deposition method and is the most versatile deposition technique used for the deposition of complex oxides compared to other deposition methods. PLD can produce adhering thin films of a variety of materials, including semiconductors, metals, and insulators. This technique provides chemical homogeneity, high crystallinity, and control on stoichiometry and thickness of the film. The illustration of the PLD is shown in **Figure 2. 3**. In the thesis work, PLD is mainly used for the fabrication of BLFO, BLFO/BTO bilayer, and BZNT/BTO multilayer films.

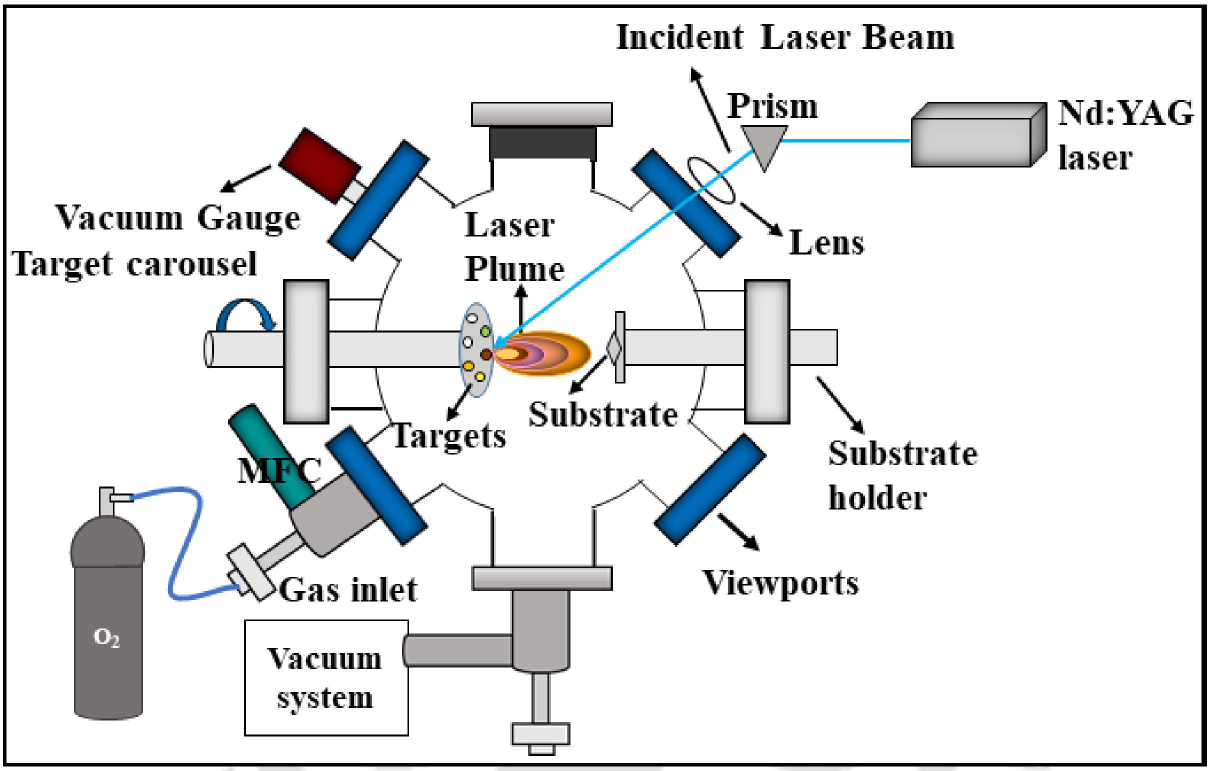

Figure 2. 3: Schematic illustration of the PLD setup.

The PLD is a physical vapor deposition technique that uses a pulsed laser beam to ablate target material. As a result, the target material vaporizes as a plume, which subsequently condenses and is deposited on a substrate that is placed opposite to the target in a reduced atmospheric pressure. **Figure 2. 4** depicts the schematic diagram of the laboratory PLD setup. The PLD reaction chamber is a spherical vessel of a 16-inch chamber made up of stainless steel furnished with a target holder, multiple viewports, substrate holder, pressure gauges, gas inlet port, and vacuum systems. The MFC (Mass flow controller) is connected to the deposition chamber to regulate the flow of working gas supplied through the gas line from the gas cylinder.

The Pirani gauge (for the high-pressure regime, 10^3-10^{-3} mbar) and the compact penning gauge (for the low-pressure regime, 10^{-2} to 10^{-7} mbar) are equipped to monitor the pressure inside the chamber. The PLD targets and substrate are mounted onto the target carrousel and substrate holder stage via 150 CF ports opposite each other. The substrate holder is supplied with a resistive heater to maintain the given temperature during the deposition. Before each deposition, the reaction chamber is evacuated to a 10^{-6} mbar low pressure.

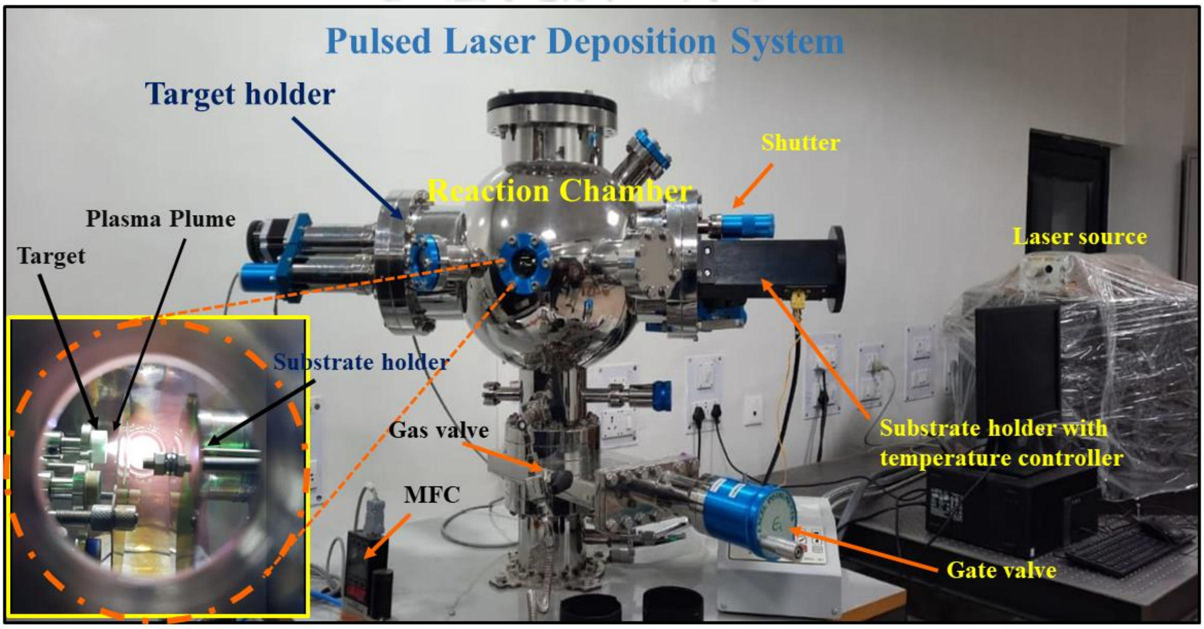

Figure 2. 4: Pulsed laser deposition setup and zoomed view during thin film deposition.

2.2.3 Film growth

As depicted in **Figure 2. 5**, a thin film undergoes several distinct growth stages, each of which influences the microstructure and physical properties of the resulting film. The growth mode of the films is determined by the correlation between (i) the surface energy of the film (γ_f), (ii) the surface energy of the substrate (γ_s), and (iii) the energy of the film-substrate interface (γ_i)[2]. The interaction of all these energies, along with some possible strain, influences the nucleation and film growth. The synthesis of thin films can be categorized into three basic growth modes: the Frank-Van der Merwe model, the Volmer-Weber model, and the Stranski-

Krastanov model. Based on the Volmer-Weber model, the island growth phenomenon arises when the atoms within a deposit have stronger bonds with one another than with the substrate. This island growth mode is observed when the substrate and film are heterogeneous. For instance, the polycrystalline thin films with a rough surface are typically formed with the continual growth of the islands. The other kind of film growth described by Frank and Vander Merwe's model (layer growth) is obtained when the atoms in the deposit are more strongly bound to the substrate than to each other. In this layer growth, a monolayer is initially formed, followed by the formation of a second layer. Hence, layer-by-layer growth is two-dimensional, suggesting that complete film formation before the growth of subsequent layers. This growth mode is typically observed when the substrate and film are completely homogeneous, such as the epitaxial growth of oxide and semiconductor materials. The mixed growth (Stransky and Krastanov) S-K model combines the layer-by-layer growth and island growth characteristics. In the S-K mode, the thin films grow two-dimensionally in layer-by-layer mode before growing three-dimensionally in island mode. It takes place when the generated stress has an effect after the growth has occurred in only two dimensions.

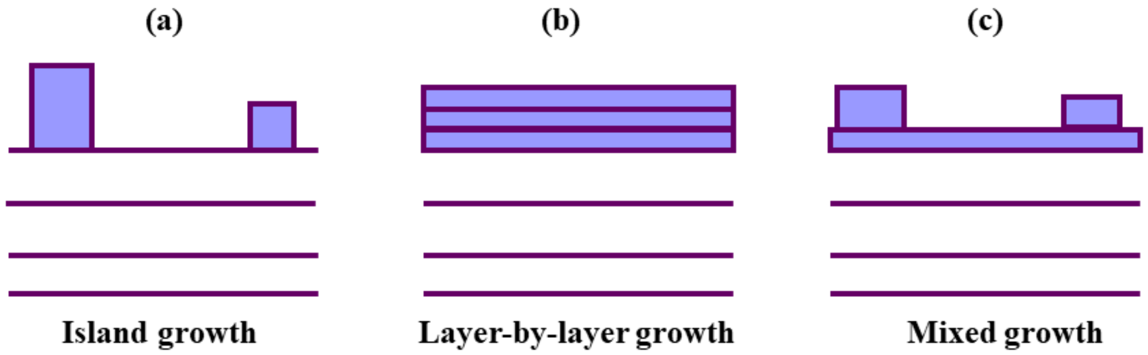

Figure 2. 5: Different film growth modes during deposition (a) Frank-Van der Merwe model, (b) Volmer-Weber model and (c) Stranski-Krastanov model.

2.2.4 Deposition parameters

There are various deposition parameters to be taken care of during the deposition of the thin films. These parameters include substrate temperature, background gas, the kinetic energy of the deposition flux, deposition rate, and vacuum quality, which significantly affect the quality of thin films. In the case of oxide films, background gas or ambiance during film deposition is essential to obtain the stoichiometric film. The deposition rate with a background as the pressure can tune the structural and microstructural properties. In the present thesis work, all films are deposited at fixed laser influence of 80 mJ from Nd: YAG laser source (M/s InnoLas Laser GmbH, SpitLight compact 400, Germany) employing high power 3rd harmonic (λ= 355 nm) wavelength, pulse width ~10 ns and pulse repetition rate of 10 Hz, and, maintaining the target to substrate distance of 5 cm. Also, the deposition rate plays a significant role in determining the quality of thin films. A high deposition rate degrades the film quality because of the decreased chance for relaxation of film, while a low deposition rate results in unreasonable long runs of deposition.

2.3 Characterization techniques

2.3.1 X-ray diffractometer (XRD)

XRD is a simple and powerful non-destructive structural analytic technique that is fundamentally used for the identification of phase and determination of crystal structure of polycrystalline materials. Using XRD diffraction patterns, information regarding the crystal structure of crystalline materials, like crystalline size, defects, and texture, can be extracted. The X-rays have a wavelength of the same order (λ= 1.5406 Å) as that of the lattice spacing of the crystalline phase to produce diffraction patterns. For a given crystal system having a particular d-spacing, when incident by X-ray with wavelength λ, the various orders (*n*) of reflection take place at the specific angle θ that follow the Bragg condition [89]:

$$n\lambda = 2d \operatorname{Sin}\theta \tag{2.6}$$

Bragg's law is valid only when the path difference between two scattered waves is equal to an integral multiple of the incident λ.

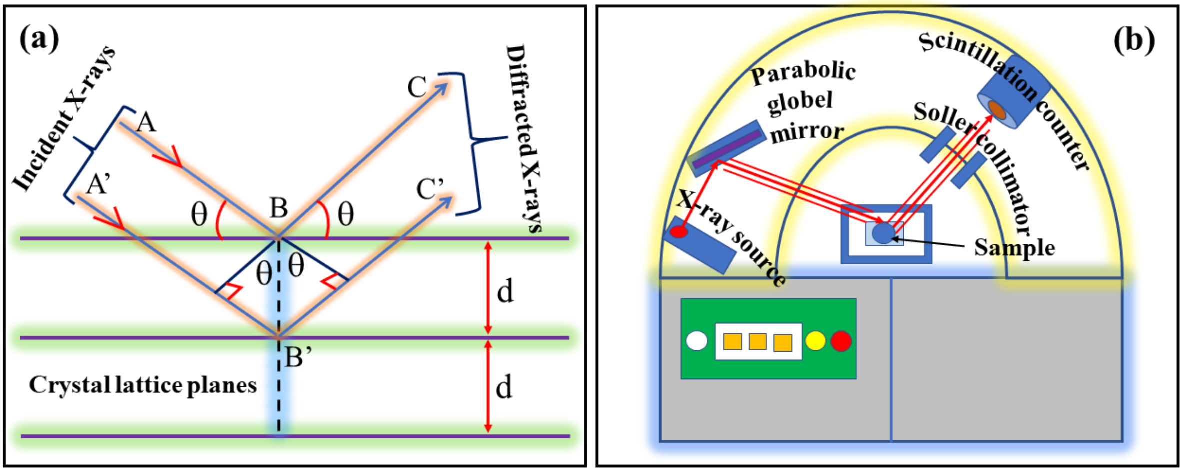

Figure 2. 6: (a) illustration of Bragg's law for X-ray diffraction and (b) XRD.

Figure 2. 6 displays a Braggs law reflection and XRD. From **Figure 2. 6(a)**, it can be inferred that when the path difference between ABC and A'B'C' paths differs by an integer number of λ, then the diffracted X-rays show constructive interference. In this thesis, BTO-based ceramics and thin films are characterized by an XRD (TTRAX-III 18 kW, M/s Rigaku, Japan) with CuK α (λ = 1.5406 Å) radiation. **Figure 2. 6(b)** schematic illustrates the diagram of the XRD instrument. The XRD pattern of BTO-based ceramics and their thin film is performed between the 2θ range of 20-80° with the scanning step size of 0.02° and scanning rate of 3°/minute. Before the measurement, to account for the instrumental broadening, the 2θ calibration is performed using the standard Si sample, which is approximately equal to 0.15°. Furthermore, all XRD patterns of BTO-based ceramics and thin films are Rietveld refined using the Fullprof software.

Firstly, the Rietveld refinement method was described by the Dutch physicist Hugo Rietveld. Using this method on the XRD pattern, exact structural information such as bond length, bond angle, lattice parameter, space group, and atomic positions of the compound are explored. The fitting of the experimental patterns with the theoretical Rietveld refinement is based on the least square method using a pseudo-Voight function and polynomial function to refine the peak shape and the background. The Rietveld method not only needs information about the crystal structure but also some structural parameters (lattice constant, Wyckoff position, and phase fraction) of the material. During the refining phase, different parameters, such as half-width parameters (U, V, W), Wyckoff positions, scale factor, lattice parameters, zero correction, and background, are refined while occupancy is kept constant. The quality of the refinement is then confirmed by the reliability factors, such as χ^2, R_p (profile factor), R_{wp} (weighed profile factor), and R_{exp} (expected weight factor). To achieve the best fit (χ^2 value close to unity), the values of other reliability factors should be minimal.

2.3.2 Density measurement

The bulk density is evaluated by Archimedes' method. According to the Archimedes principle, a body (disc) fully or partially immersed in a fluid experiences an upthrust equal to the weight of the fluid displaced. Before performing density measurements, the sintered discs are dried in the oven at 100 °C for 30 minutes. The reading of the measurement of the discs in different situations is noted. Initially, the dried disc is measured and its weight is taken as W_d. Later, the sample is suspended in the distilled water (with density ρ_w) to obtain the wet weight of the sample as W_w. Finally, the sample is taken out of the water and its weight is noted as W_{dw}. Then, the bulk density (apparent density) is calculated using the formula:

$$\rho_a = \left(\frac{W_d}{W_w - W_{dw}}\right) \times \rho_w \tag{2.7}$$

Furthermore, the relative density of the pellets is obtained from the theoretical density (ρ_{th}) and apparent density (ρ_a) calculated as follows

$$Relative\ density = \frac{\rho_a}{\rho_{th}} \times 100\% \tag{2.8}$$

2.3.3 Raman spectroscopy

Raman spectroscopy is originated from the Raman effect. In 1928, Sir Chandrasekhara Venkata Raman discovered the Raman scattering phenomenon [90]. It is a popular technique to analyze the sample molecule vibration. It measures the intensity and wavelength of light that is inelastically scattered light from the molecules. Raman spectroscopy does not require any sample preparation because it is very sensitive to the chemical composition, crystal structure, and bonding. These characteristics make it a very interesting instrument for revealing material in any physical form, such as solids, liquids, and gases.

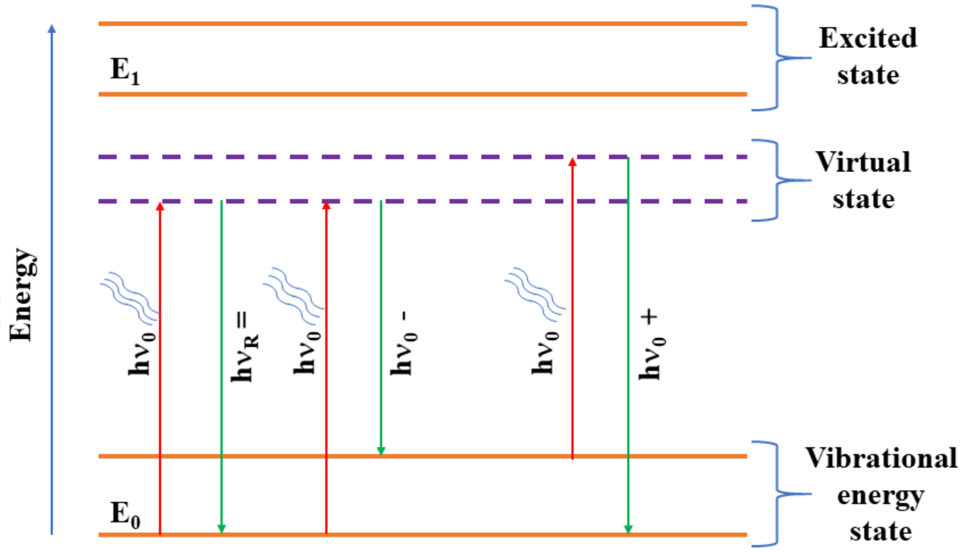

Figure 2. 7: Representation of the different energy levels in Raman and Rayleigh scattering.

A small amount of light may be scattered elastically or inelastically when a monochromatic light falls on the sample. Because of the energy difference between the incident and scattered light, the Raman effect is observed. Based on the lower, higher, and equal energy of scattered light compared to the incident light energy, it is classified into three categories: Stokes, anti-Stokes, and Rayleigh scattering, respectively, as shown in **Figure 2. 7**. Raman spectroscopy is used to measure the Stokes lines, as their intensity is higher than the anti-Stokes line and the anti-Stokes lines are measured with fluorescing samples. The magnitude of the

Raman shifts is mostly unaffected by the wavelength of incident light. Water is usually used as an ideal solvent for liquid samples because the Raman scattering is low, so it does not affect the sample too much. In the case of a solid sample, the sample can be directly placed on a glass substrate, and the measurement can be performed. In the present thesis work, the Raman spectroscopic analyzer (LabRam HR800, M/s Horiba Jobin Yvon, Japan) is used with an Ar-ion laser source of 514 nm excitation wavelength. This instrument is equipped with a specific heating/cooling (THMS600, Linkam) sample stage. Each spectrum is captured using a Peltier-cooled charge-coupled device detector and backscattered geometry equipped with a 50 × objective lens) and the proper edge filter. An Ar^+ ion excitation laser source with $\lambda = 514$ nm and an 1800 mm^{-1} grating is used for the low-temperature micro-Raman measurement. The grating is fixed throughout the temperature scan to ensure high position accuracy. The Raman spectroscopy system has a spectral resolution of 1 cm^{-1}.

2.3.4 Field emission scanning electron microscopy (FESEM)

The microstructure and chemical composition of the BTO-based ceramics and thin films are analyzed via FE-SEM (Sigma, M/s Zeiss, Germany). The elemental composition is analyzed using the energy-dispersive X-ray spectrometer (EDS) equipped with the same instrument. Before the sample analysis, to expose the source, the sample is coated with a thin layer of gold (~ 10 nm). As the samples used in the investigation are non-conducting, the coating prevents the sample from reducing thermal damage, charging, and enhancing the signal of secondary electrons for topographic imaging of the specimens. **Figure 2. 8** Illustrated the schematic diagram of the FE-SEM instrumentation and interaction of electron beam during sample analysis.

In the SEM analysis, the electron emitted in an electron gun by a tungsten filament thermionically or field emission is accelerated with high kinetic energy and is focused on the sample surface (anode) using electromagnetic lenses. In the case of FESEM, the electron is emitted from the field. Due to the different signals based on the interaction between the electron and samples, the energy of the electron beam is dissipated. Among these, backscattered (BE) and secondary electrons (SE) are used for microstructure analysis and photons for elemental analysis. Backscattered electrons revealed compositional variations, whereas secondary electrons can describe typical topographic images. The chemical characterization of the sample is carried out using the EDS technique, which yields peaks corresponding to the energy levels in which X-rays are received. A unique peak of the spectrum is observed for each atom, and the peak intensity describes the concentration of the elements present in the synthesized sample.

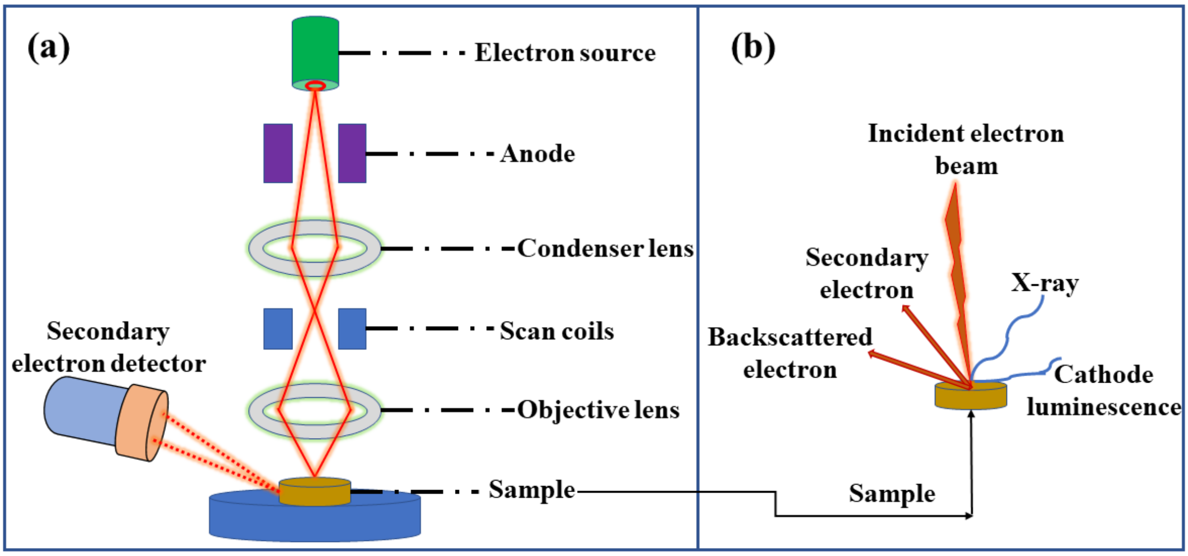

Figure 2. 8: (a) The block diagram of FESEM, (b) Interaction of the surface of the sample with a beam of electrons and creation of signals such as backscattered electrons, transmitted electrons, secondary electrons, X-rays, and cathodoluminescences.

2.3.5 Field emission transmission electron microscopy (FETEM)

FETEM is an electron microscope with higher resolution than standard microscopes. FETEM employs a high-intensity electron beam to identify the crystal structure, size, shape, lattice imperfection, defect, and compositional element present in the nanoparticles or nanocrystals. The basic principle of this technique involves the electron beam incident to a thin sample in which some part of the beam is transmitted from the specimen. This transmitted beam is divided into three components: i) direct transmitted beam, ii) inelastic, and iii) elastic electron beam. The contrast of an image in TEM is associated with the ratio of the directly transmitted electrons to that of the elastic scattering electrons. **Figure 2. 9** shows the schematic outline of the FETEM instrument. Mainly, its components are divided into four sections, including an electromagnetic lens, the sample holder (it consists of the mechanical arm to hold and control the specimen's position), and the electron gun (which is made of an anode, cathode, and a tungsten filament usually emits the electron) and the image recording system. The FETEM works similarly to a slide projector in which the projector emits a light beam that passes through the slide. Only a portion of the light beam can pass through the patterns painted on the slide. As a result, when the beam is transmitted and hits the screen, the patterns on the slide are replicated, resulting in an enlarged image of the slide.

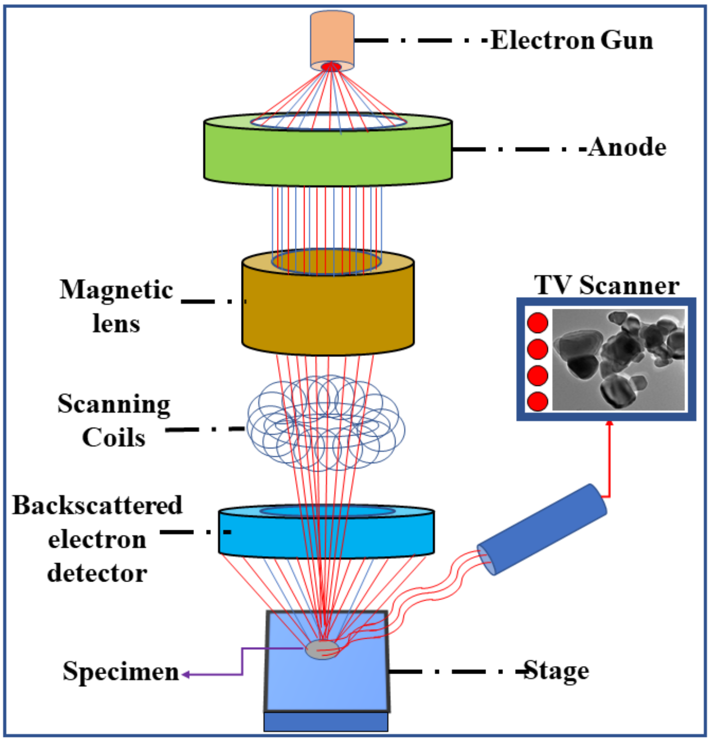

Figure 2. 9: Schematic view of field emission transmission electron microscope illustration.

In this thesis, the FETEM analysis of the BLFO monolayer thin films is examined using the FETEM instrument (2100F, M/s JEOL, Japan) operated at 200 kV to capture the crystallographic structure and morphology. Further, the films are analyzed by high-resolution transmission electron microscopy images (HRTEM), bright-field TEM images, and the selected area diffraction (SAED) patterns. The instrument has an accelerating voltage range of 60 to 200 kV in 50 V steps, a resolution of 1.9 Å to 1.4 Å, and a tilt of ± 25°. The typical specimens have a magnification range of 50 X to 1,500,000 X, making them an incredibly sophisticated tool for the characterization of nanomaterials. A CCD (charge-coupled device) high-resolution camera with a resolution of 2.672 × 2.672 K is also integrated, producing an image of the sample in exceptionally high resolution.

2.3.6 X-ray Photoelectron spectroscopy (XPS)

XPS is a technique for obtaining qualitative and quantitative information on the elemental composition of surfaces. This method gives information regarding the elemental identification electronic state and chemical valence state of the element present on the surface of the specimens. When the sample is exposed to an X-ray beam, photoelectrons are ejected. It is the photoelectric phenomenon in which the inner core photoelectrons are ejected through a transfer energy process from the photons, which gives information about the electronic state of elements that exist within the sample. **Figure 2. 10** illustrates the photoemission process in XPS and the ejection of core-level electrons. XPS gives us information regarding the binding energy of electron orbitals and peak position in the spectrum, which allows us to identify the atomic position of the sample. Mg K_α and Al K_α are the commonly used sources. The composition of the sample can be determined quantitatively by measuring the relative areas of the photoelectron peaks.

In XPS, the photoemission process is elastic, which means that photons completely transfer their energy to electrons. **Eq. 2.9** describes the relationship between the measured kinetic energy, the binding energy, and the energy of the photons when the electrons leave the sample without interacting with anything else and reach the spectrometer.

$$BE = h\nu - KE - \phi_s \qquad (2.9)$$

where BE denotes binding energy, hν represents the energy of the photons produced by the X-ray source, KE symbolizes the kinetic energy of the photoelectrons detected by the spectrometer, and ϕ_s is the work function of the particular material. It can be noted that only the core levels with a BE less than the energy of the photons are accessible by XPS.

In the present work, the ionic state of the sample is confirmed using the XPS instrument (PHI5000*Versa*Probe III, M/s ULVAC-PHI, Inc.). During the measurements, the samples are irradiated with an X-ray beam of Al Kα radiation (hν=1486.6 eV) at an electron emission angle of 45°, and spectra of the sample's core level are collected over an area of 100 μm. During the spectral acquisition, the base pressure is maintained at 10^{-7} mbar. Using the same instrument and a He (I) source of energy (hν = 21.22 eV), ultraviolet photoelectron spectroscopy (UPS) is used to analyze the work function (ϕ_{SA}) of the sample [91][92].

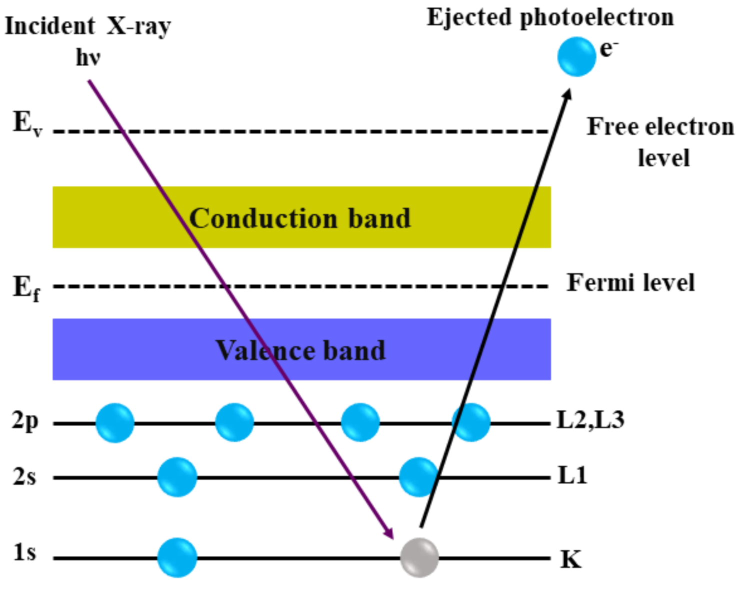

Figure 2. 10: Schematic representation of the XPS process.

2.3.7 Physical property measurement system (PPMS)

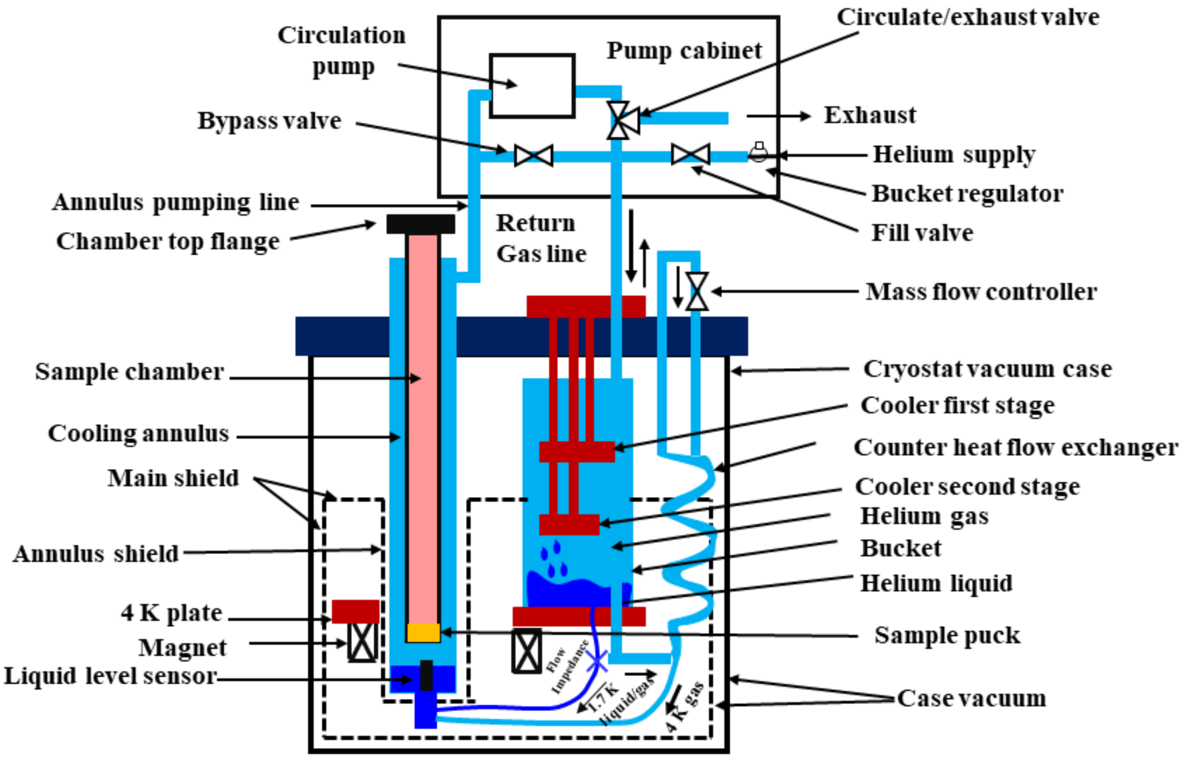

Figure 2. 11: Schematic diagram of PPMS.

PPMS is used to analyze the magnetic and electric transport properties of the sample in a well-controlled magnetic field and temperature environment. The types of samples measured using this instrument include powder, bulk, and thin film form. In the present work, the magnetic properties of bulk ceramics as well as thin films are measured using the PPMS facility (DynacCool, M/s Quantum Design, USA) furnished with VSM. The device employs a two-stage pulse tube cooler to cool both the superconducting magnet and the temperature control system. As a result, the configuration can provide continuous low-temperature control precise field and temperature sweep modes. The magnetic moment and temperature precision are quoted as ± 0.5% and ± 15 %, respectively. The PPMS is made up of a superconducting magnet and a hybrid digital/analog magnet controller that precisely controls the magnetic field. The cryostat is the most critical component of the PPMS system, as it is responsible for keeping all of the system's vital components at the required temperature. **Figure 2. 11** illustrates a block diagram of the cryostat control system and all of its components. The pulse tube cry cooler is divided into two stages; the first operates at 45 K, while the second operates at about 4.2 K. The circulation pump, main and low-temperature flow, bucket and liquid helium, 4 K plate, annulus radiation shield, cooling annulus, and main radiation shield are the primary components cooled by these two stages.

Furthermore, for performing the electrical measurements, we have fabricated a capacitor by coating the sintered cylindrical disc on both smooth surfaces with highly conductive silver ink (M/s Sigma-Aldrich, resistivity ~ 1.59 μΩ/cm, ≥ 99%). The films deposited on the conducting substrate n-type Si and Pt Si substrates are taken for electrode pattern using the shadow mask. An Al coating as a top and bottom electrode is designed on the surface of thin films using a thermal evaporator. Then, the electrical characteristics, such as dielectric, impedance, ferroelectric, and I-V characteristics, are measured in a metal-insulator-metal (MIM) configuration.

2.3.8 Dielectric measurements and impedance spectroscopy

In this present thesis work, the dielectric response of the sintered samples and the thin films is performed using an LCR meter (M/s Wayne Kerr Electronics Pvt. Ltd., 4300) in the frequency range from 100 Hz to 1MHz. The temperature-dependent measurement from RT to 500 °C is conducted with the LCR meter attached to the PID controller (Proportional-Integral-Derivative) (3216, Eurotherm). The RF impedance material analyzer (M/s Agilent Technologies, E4991A) is used for measurements in the high-frequency range from 1MHz - 1GHz in the wide temperature range from -160˚C to 400 ˚C. Liquid nitrogen is used as a cooling or heating medium for temperature-dependent measurements with a temperature control system (M/s Novocontrol, BDS 2300). The schematic representation of a typical RF impedance/material analyzer is shown in **Figure 2. 12**.

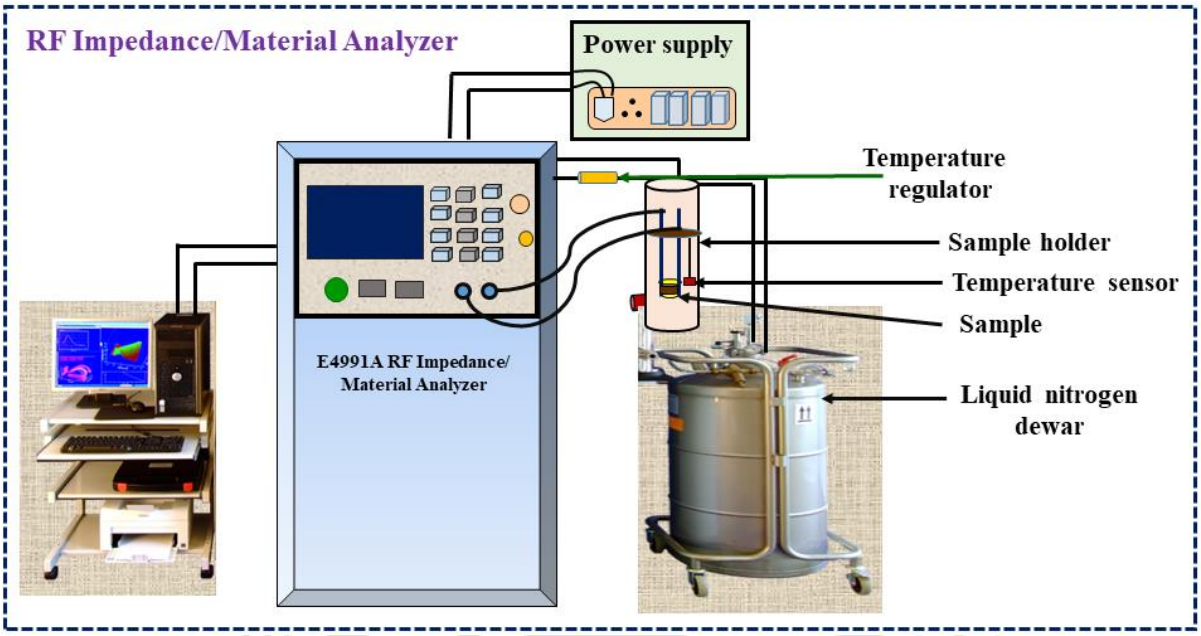

Figure 2. 12: RF Impedance/Material Analyzer set-up.

The investigation of the dielectric behavior of the synthesized material is important to understand the phase transition, relaxation phenomenon, and polarization mechanism in the material. The dielectric response is related to the electrical energy storage and dissipation in the material. The relative permittivity (ε_r) and loss tangent (tanδ) with frequency and temperature are studied for bulk and thin film samples. Furthermore, the electrical properties of the sample are investigated by Impedance spectroscopy measurement. This technique usually measures the resistance of a material, both the real part (*x*-axis) and the imaginary part (y-axis). The obtained data for the material is displayed in a complex-plane plot called the Nyquist or Cole-Cole diagram. As alternating voltage signal V= V_o cosωt is applied between the electrodes of the sample as depicted in **Figure 2. 13**, there will be a phase shift (φ) between applied voltage (V) and resultant response current (I) as given below:

$$V(t) = V_0 \exp(jwt) \tag{2.10}$$

$$I(t) = I_0 \exp(jwt + \varphi) \tag{2.11}$$

where E_0, I_0, ω, φ represent the amplitude of potential, the amplitude of current, angular frequency, and phase, respectively.

and

$$\exp(j\varphi) = cos\varphi + jsin\varphi \tag{2.12}$$

then, the impedance in complex form is given by

$$Z^* = \frac{E}{I} = Z_0 \frac{\exp(jwt)}{\exp(jwt+\varphi)} \tag{2.13}$$

Thus, impedance is the ratio of an oscillating voltage to an oscillating current having a magnitude Z_0 and a phase angle ∅. In the Cartesian complex plane, the impedance is divided into real and imaginary parts:

$$Z^* = Z' + jZ'' \tag{2.14}$$

here, Z' and Z'' are the resistive and reactive components of the impedance.

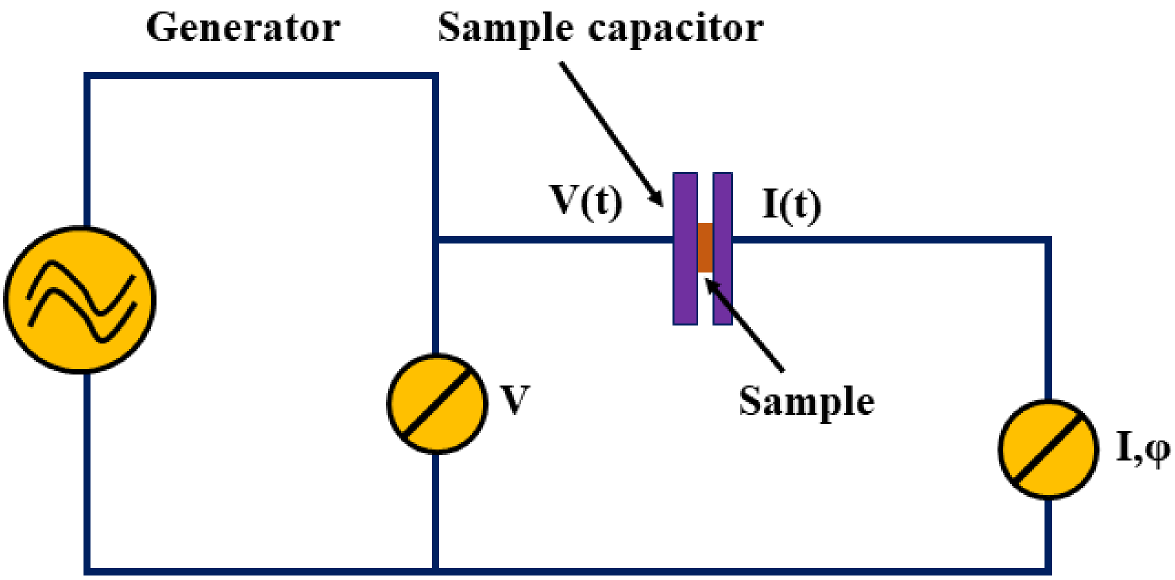

Figure 2. 13: Schematic representation of phase-sensitive voltage and current analyzer.

2.3.9 Ferroelectric measurements

For ferroelectric materials, the studies are focussed on domains and their response to external factors such as temperature, stress, electric field, and others. The P-E loop is the most effective and simple method for understanding ferroelectric materials. This is a simple and effective method to understand ferroelectric ceramics.

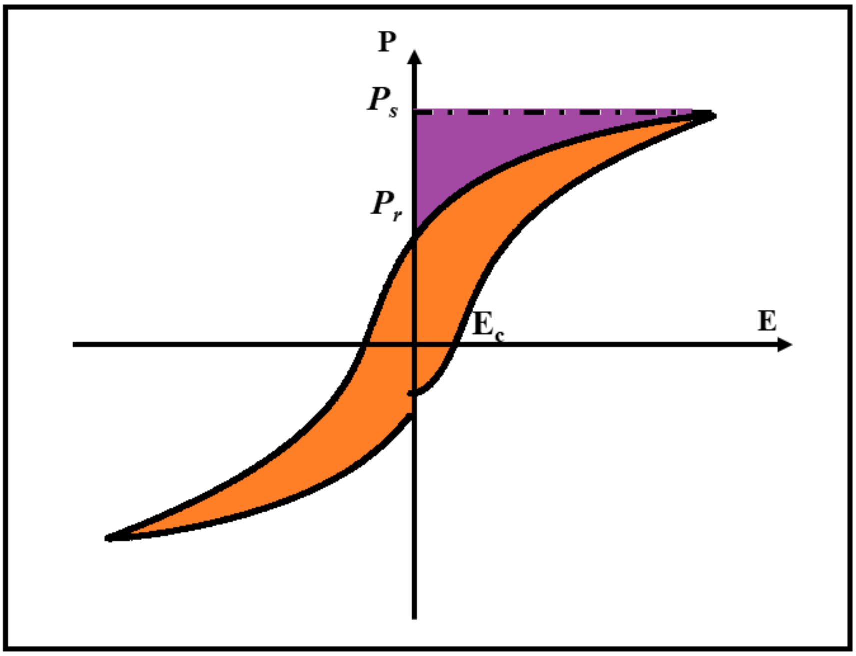

Figure 2. 14: Typical ferroelectric hysteresis loop.

Generally, all ferroelectric ceramics have their distinct P-E loop, just like a signature. However, in the case of a polycrystalline material, the grains are split into many domains to attain energy minima, i.e., the direction of the domains is randomly distributed to attain net zero macroscopic polarization. With the application of an electric field, these domains are brought into a polar state through an induced macroscopic polarization. Subsequently, the induced polarization increases gradually with the increase of electric field strength and reaches a maximum value called saturation polarization (P_s). At the removal of the electric field, some of the domains will back-switch, while others won't, and thereby, a net non-zero polarization develops, leading to the remnant polarization (P_r) even at zero electric fields. To attain zero polarization, an electric field must be applied in the opposite direction, and this field at zero polarization is called the coercive field (E_c) or coercivity. Again, a similar rearrangement of the polarization occurs when the electric field is increased in the opposite direction, resulting in the so-called P-E or hysteresis loop. For ferroelectric ceramics, the spontaneous polarization P_s can be calculated by intersecting the polarization axis with the extrapolated linear segment, as shown in **Figure 2. 14**.

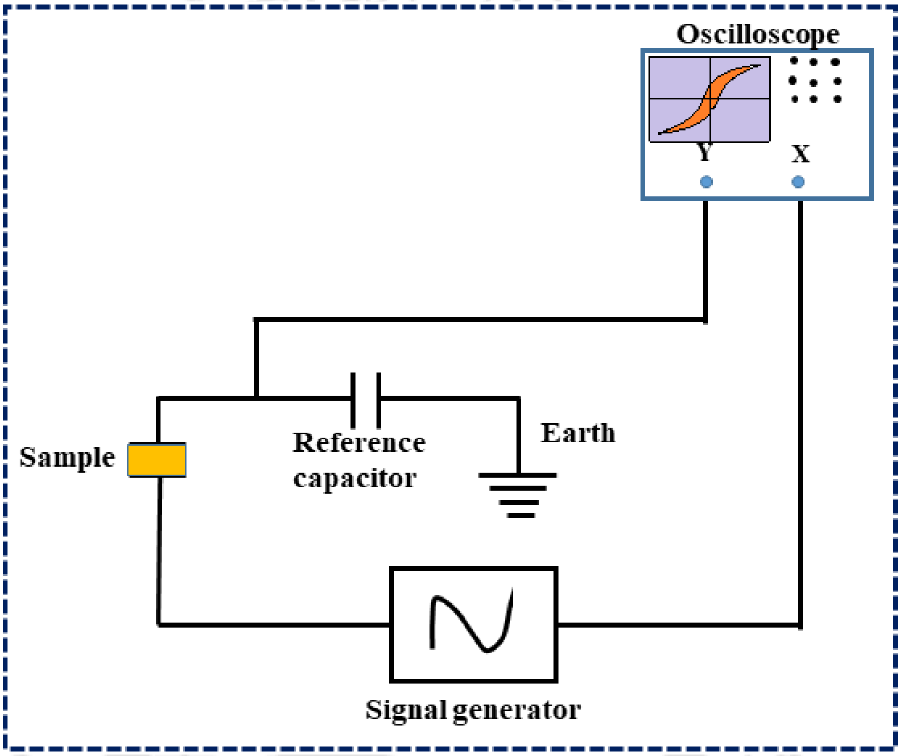

Figure 2. 15: Representation of Sawyer-Tower circuit for P-E loop measurements.

Valasek described the first P-E loop in Rochelle salt. However, progress in ferroelectric research was slow at the time. This could be because of the difficulties in determining the P-E loop, which was solved in 1930. The first electronic circuit to measure the ferroelectric characteristics was invented by Sawyer and Tower of Rochelle Salt in 1930. **Figure 2. 15** depicts the schematic connection of the Sawyer-Tower circuit. An AC input voltage (V_{in}) is applied to the ferroelectric capacitor, and the applied input voltage can be read on the horizontal axis (*x*-probe) of an oscilloscope. Then, the applied electric field (E) is calculated using the input voltage (V_{in}) and the thickness (d) of the sample:

$$E = \frac{V_{in}}{d} \tag{2.15}$$

The voltage across the reference capacitor (C_r) induces polarization in the sample and can be measured on the vertical axis (*y*-probe) of an oscilloscope. Thus, the P-E loop is constructed in the oscilloscope based on the electrical polarization calculated using the formulas:

$$Q = \frac{V_0}{C_r} \tag{2.16}$$

$$P = \frac{Q}{A} \tag{2.17}$$

where Q, P, and A represent the charge, polarization, and sample surface area, respectively. The ferroelectric hysteresis in the thesis work is obtained using a ferroelectric tester (Precision LCII, Radiant Technologies. Inc, USA) for the electrode-designed samples.

2.3.10 Leakage current characteristics

One of the key characterizations of device applications is the examination of leakage currents. The majority of applications rely on applying an external voltage to thin-film or bulk ceramic capacitors, which causes leakage current to occur. Defects that cause property degradation may be the source of the leakage current. Understanding the conduction mechanism in the samples can help you find solutions for lowering the leakage current. Therefore, to determine which conduction processes are in charge of the leakage current, it is crucial to examine the charging mechanism in samples. In this dissertation, the leakage current was measured using a Keithley parameter analyzer (M/s Tektronix, 4200A-SCS, USA).

2.3.11 Atomic Force Microscopy (AFM)

A simplified diagram of an atomic force microscope (AFM) is shown in **Figure 2. 16**. The AFM is a highly effective imaging method for capturing topographical images on nanoscale samples, including their size, shape, and roughness. By scanning the sample with the AFM, a three-dimensional surface profile can be obtained. An AFM instrument includes a flexible (silicon or silicon nitride) cantilever with a sharp tip, signal processing unit, controller, and scanner. The Atomic interactions between the sample surface and the tip determine the surface topography as the tip scans the surface. According to Hooke's law, the cantilever bends as a result of the Van der Waals forces exerted by the atoms between the sample surface and the tip.

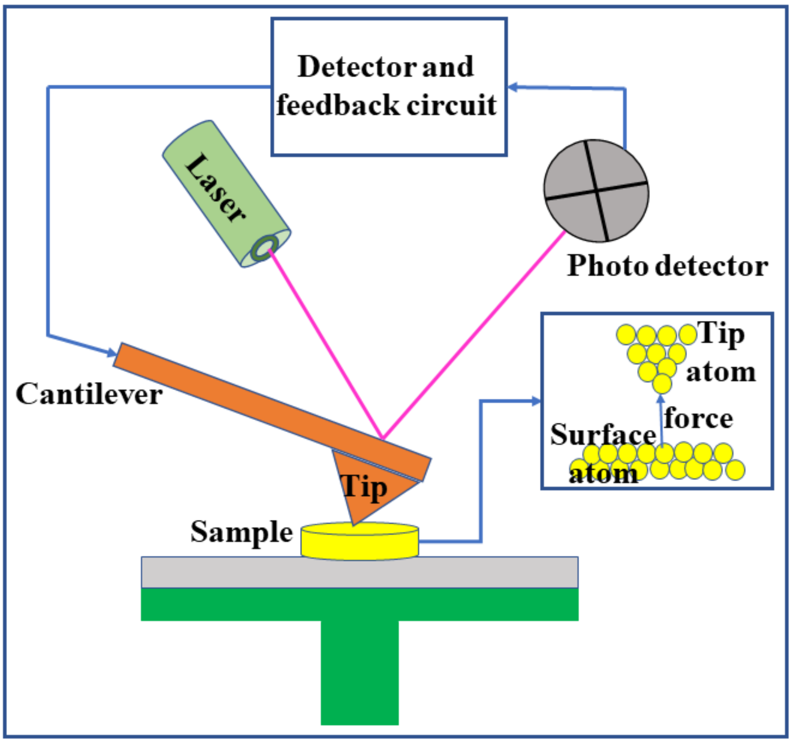

Figure 2. 16: Block diagram of the atomic force microscopy.

Figure 2. 16 shows a laser being reflected off the cantilever's top surface and into a photodetector to measure this deflection. The detected signals are then sent to the signal processing unit, which produces the topography image as well as amplitude and phase. In this

thesis work, the atomic force microscope (M/s Brucker; Innova SPM) is used to obtain AFM topological images of the thin films.

2.3.12 Optical characterization

The optical characteristics of the samples are examined utilizing a UV-VIS-NIR spectrophotometer (UV 3101PC, M/s Shimadzu) in this thesis work. The basic parameters such as optical bandgap energy (E_{gap}), linear refractive index (n), optical packing density (P_0), and film thickness (d) can be examined via transmission spectra. When light strikes the film, some is reflected, while some light is transmitted through the interfaces of film-substrate, air-film, and substrate-air. As the beams came from a single coherent source, both the transmitted and reflected light display the interference pattern. **Figure 2. 17(a)** shows the optical transmission through a film with thickness d and refractive index n deposited on a quartz substrate with thickness d_s and the refractive index n_s. **Figure 2. 17(b)** displays the transmittance spectrum of a film deposited onto a substrate examined in the 200 -850 nm wavelength range.

The E_{gap} of the sample is extracted from the absorbance spectra recorded in the UV-visible range. The direct band gap energy is estimated following the Taucs equation and can be expressed as [93][94]:

$$\alpha h\nu = A(h\nu - E_{gap})^m \tag{2.18}$$

where hν and α are the photon energy and absorption coefficient respectively. A denotes constant and is a transition parameter dependent on the value of m. The value of m corresponds to 1/2 and 2 for allowed direct and indirect transitions, while 3/2 and 3 for forbidden direct and indirect transitions [94][95].

The Swanepoel’s envelope method is employed to derive the refractive index (n) of the films based on the following expressions [96][97]:

$$n = [N + N^2 - n_s^2{}^{0.5}]^{0.5} \qquad (2.19)$$

$$N = 2n_s\left(\frac{T_M - T_m}{T_M.T_m}\right) + \frac{n_s^2+1}{2} \qquad (2.20)$$

where T_M denotes the transmittance maximum and T_m represents the transmittance minimum at a particular λ. The refractive index of the transparent substrate, n_s equal to 1.51 (for amorphous SiO_2 substrate). Hence, the thickness of the films (d) can be estimated using the relation below [98][99]:

$$d = \frac{M\lambda_1\lambda_2}{2[n(\lambda_1)\lambda_2 - n(\lambda_2)\lambda_1]} \qquad (2.21)$$

where M is the number of oscillations between two extrema (M=1 between two consecutive extremas consecutive maxima or minima). Similarly, the optical packing density (P_0) of the films is determined using the following expression [100][101]:

$$P_0 = \left(\frac{n_f^2-1}{n_f^2+2}\right)\left(\frac{n_b^2+2}{n_b^2-1}\right) \qquad (2.22)$$

where, n_f and n_b are the refractive indices of the thin films and the bulk composition, respectively.

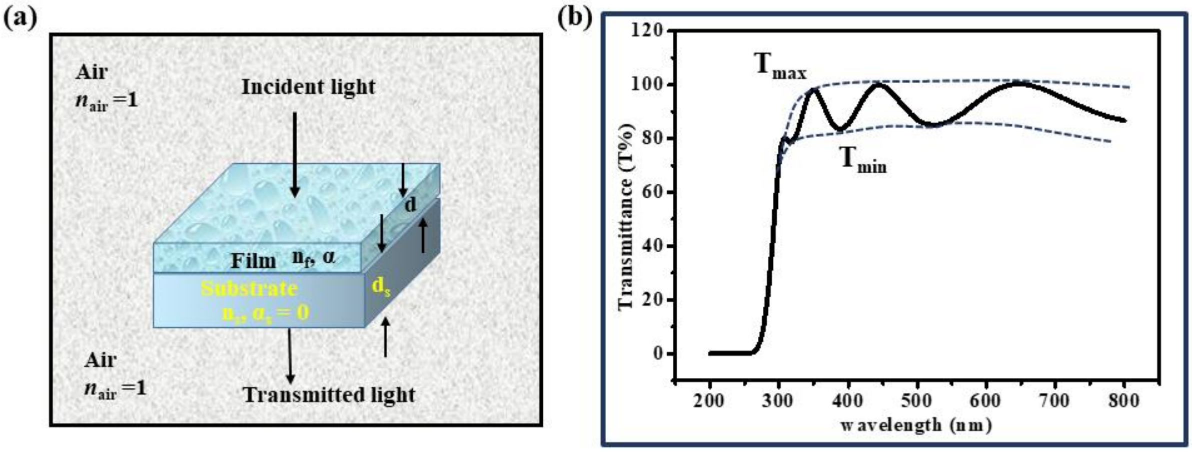

Figure 2. 17: (a) Illustration of light transmittance through different interface mediums of the thin film, (b) transmission spectra of a thin film.

Chapter 3

Evaluation of energy storage performance in $BaTiO_3$-$BiFeO_3$ and $BaTiO_3$-$Bi[Zn_{2/3}(Nb_{0.85}Ta_{0.15})_{1/3}]O_3$ solid solutions

This chapter describes the fabrication, characterization, and evaluation of the energy storage performance of $BaTiO_3$ (BTO) based dielectric ceramics. The study includes the substitution of $BiFeO_3$ (BFO) and $Bi[Zn_{2/3}(Nb_{0.85}Ta_{0.15})_{1/3}]O_3$ (BZNT) in the BTO matrix to form a solid solution.

3 $BaTiO_3$-$BiFeO_3$ and $BaTiO_3$-$Bi[Zn_{2/3}(Nb_{0.85}Ta_{0.15})_{1/3}]O_3$ ceramics

3.1 Introduction

The ferroelectric systems with ABO_3 perovskite structure have proven extremely useful in various electronic applications such as capacitors, thermistors, and electrocaloric and storage information devices [102]. Among the lead-free perovskite systems, BTO is one of the most explored ferroelectric ceramics with good chemical stability, high dielectric permittivity, and temperature-stable dielectric characteristics [103]. It usually possesses a large dielectric constant because of long-range ordered spontaneous polarization [104]. However, immense energy loss makes them unsuitable for field energy storage applications due to non-polarization response and extensive P_r induced by slow-moving macro-domain reversal [105]. Therefore, chemical modification and tailoring are needed to adjust its comprehensive performance. BTO-based systems were widely studied with different compositions to fine-tune their properties

[106]. Pure BTO at RT is ferroelectric and changes its phase to a paraelectric state around 120°C. The properties deteriorate as the material enters the paraelectric state (>120°C), which restricts its further application in elevated temperatures. The addition of $BiMeO_3$ (*Me* symbolizes trivalent and average trivalent metal ions) compounds with $BaTiO_3$ improves the temperature-dependent dielectric behavior due to the weakly coupled polarization in the polar nano regions (PNRs) that develops from the substitution of Bi^{3+} and Me^{3+} in place of Ba^{2+} and Ti^{4+} [107]. Combining $Bi(Me)O_3$ and $BaTiO_3$ can assist in the creation of PNR by breaking the long-range ferroelectric order. Because of the comparable electronic structures of Pb^{2+} and Bi^{3+}, the hybridization between Bi 6p and O 2p is anticipated to raise the maximum polarization. Previous studies suggested that a solid solution of $BaTiO_3$-$Bi(Me)O_3$ formed by another perovskite (ABO_3) structure with Bi^{3+} at the A-site and multiple cations at the B-site can be used to tune BTO ceramics [108]. The ferroelectric and relaxor ferroelectric properties of Bi_2O_3-doped $BaTiO_3$ ceramics resulted in an extensive study of $BaTiO_3$-$BiMeO_3$ compositions. The most studied lead free composition are $BaTiO_3$-$BiYO_3$ [109]; $BaTiO_3$-$BiScO_3$ [110]; $BaTiO_3$-$Bi(Mg_{1/2}Zr_{1/2})O_3$ [111][112]; $BaTiO_3$-$Bi(Mg_{2/3}Nb_{1/3})O_3$ [113][114]; $BaTiO_3$-$Bi(Mg_{1/2}Ti_{1/2})O_3$ [115]; $BaTiO_3$-$BiFeO_3$ [116] and $BaTiO_3$-$Bi(Zn_{1/2}Zr_{1/2})O_3$ [60][103] systems with relaxor behavior displaying better energy storage performance.

Various binary or ternary solid solution systems based on $BaTiO_3$-$BiMeO_3$ including $BaTiO_3$-$BiFeO_3$ have been throughly explored [32][61][62][63][64][65][66][67][68][69]. Undoped BFO-BTO-based ceramic with higher BFO contents have high P_{max}; however, its ΔP is low due to the fact that it is unsuitable for energy storage applications [70]. In recent years, researchers have focused on enhancing the energy storage performance of the BFO-BTO system. The composition with 0.75BFO - 0.25$(Ba_{0.99}La_{0.01})TiO_3$ ceramics is reported to exhibit a large W_{rec} of 0.61 J/cm^3 by Calisir et al. [71]. Similarly, $Ba(Mg_{1/3}Nb_{2/3})O_3$ substituted BFO-BTO bulk ceramics exhibited double hysteresis loops with improved energy storage performance W_{rec} of 1.56 J/cm^3 with η of 75% and also showed wide temperature stability in the temperature range of 25-190 °C [34]. Likewise, enhanced energy storage performance is observed for the Nd-doped BFO-BTO system with W_{rec} 1.81 J/cm^3 [72]. Meanwhile, the previous studies reported that the bulk ceramics with $BaTiO_3$-$Bi(Zn_{2/3}Nb_{1/3})O_3$ composition displayed a large W_{rec} of 0.79 J/cm^3 and η of 93.5% at an applied field of 131 kV/cm [73]. Further, the Ta substituted bulk composition with $0.87BaTiO_3$-$0.13Bi[Zn_{2/3}(Nb_{0.85}Ta_{0.15})_{1/3}]O_3$ exhibited greatly improved energy storage performance with W_{rec} of 1.44 J/cm^3 and η of 92.5% at 218 kV/cm [74]. Here, Ta is mainly substituted for Nb in $BaTiO_3$-$Bi(Zn_{2/3}Nb_{1/3})O_3$ composition, expecting to decrease the energy loss and leakage current density at the higher applied electric field. Additionally, adding Bi-based compounds can accelerate the densification process and lower the sintering temperature, which leads to a low dielectric loss, large activation energy, and dense microstructure in BTO-$Bi(Me)O_3$ ceramics, which favor high E_{BDS}. In this chapter two series of $BaTiO_3$-$Bi(Me)O_3$ family; $(1\text{-}x)BaTiO_3$-$xBiFeO_3$ (BTBF) in x range from 0.0 to 0.3 and $(1\text{-}x)BaTiO_3$-$xBi[Zn_{2/3}(Nb_{0.85}Ta_{0.15})_{1/3}]O_3$ (BT-BZNT) in x range from 0.05 to 0.25 is synthesized using solid-state reaction route. These compositions are further investigated for energy storage performance from the ferroelectric response.

3.2 Sample preparation of BTBF and BT-BZNT ceramics

The lead-free $(1\text{-}x)BaTiO_3$-$xBiFeO_3$ (x = 0.00, 0.1, 0.2, and 0.3 abbreviated as BTO, BTBF1, BTBF2, and BTBF3, respectively) and $(1\text{-}x)BaTiO_3$-$xBi[Zn_{2/3}(Nb_{0.85}Ta0.15)_{1/3}]O_3$ (x=0.05, 0.10, 0.15, 0.20 and 0.25) solid-solutions are prepared by the solid-state reaction route. Analytical grade reagents including $BaCO_3$ (M/s ACROS Organic), TiO_2, Bi_2O_3, ZnO, Nb_2O_5, and Ta_2O_5 (M/s Sigma Aldrich), and Fe_2O_3 (M/s JiangXiHaiTe Advance Material) with a purity of 99.99% are used as a starting material. The complete recipe for sample preparation is discussed in **Chapter 2.** The BTBF and BT-BZNT samples are sintered at 1050°C and 1250°C, respectively for 2 hr to achieve a maximum relative density range of 93-97%.

3.3 Results and discussion: BTBF solid-solution

The XRD pattern of the ceramics has been recorded to check the phase purity and the crystal structure, as shown in **Figure 3. 1(a)**. The prepared compositions revealed the pure perovskite structure with no other phases, suggesting that $BiFeO_3$ (BFO) has thoroughly diffused into the host lattice ($BaTiO_3$) to form a new homogeneous solid solution [20][21]. The diffraction peaks for pure BTO are indexed with JCPDS card 01-074-9807. The corresponding peaks of the BFO added system are matched with the values of reflection reported for PDF#34-0411 [117] and indexed with JCPDS card no. 00-066-0524.

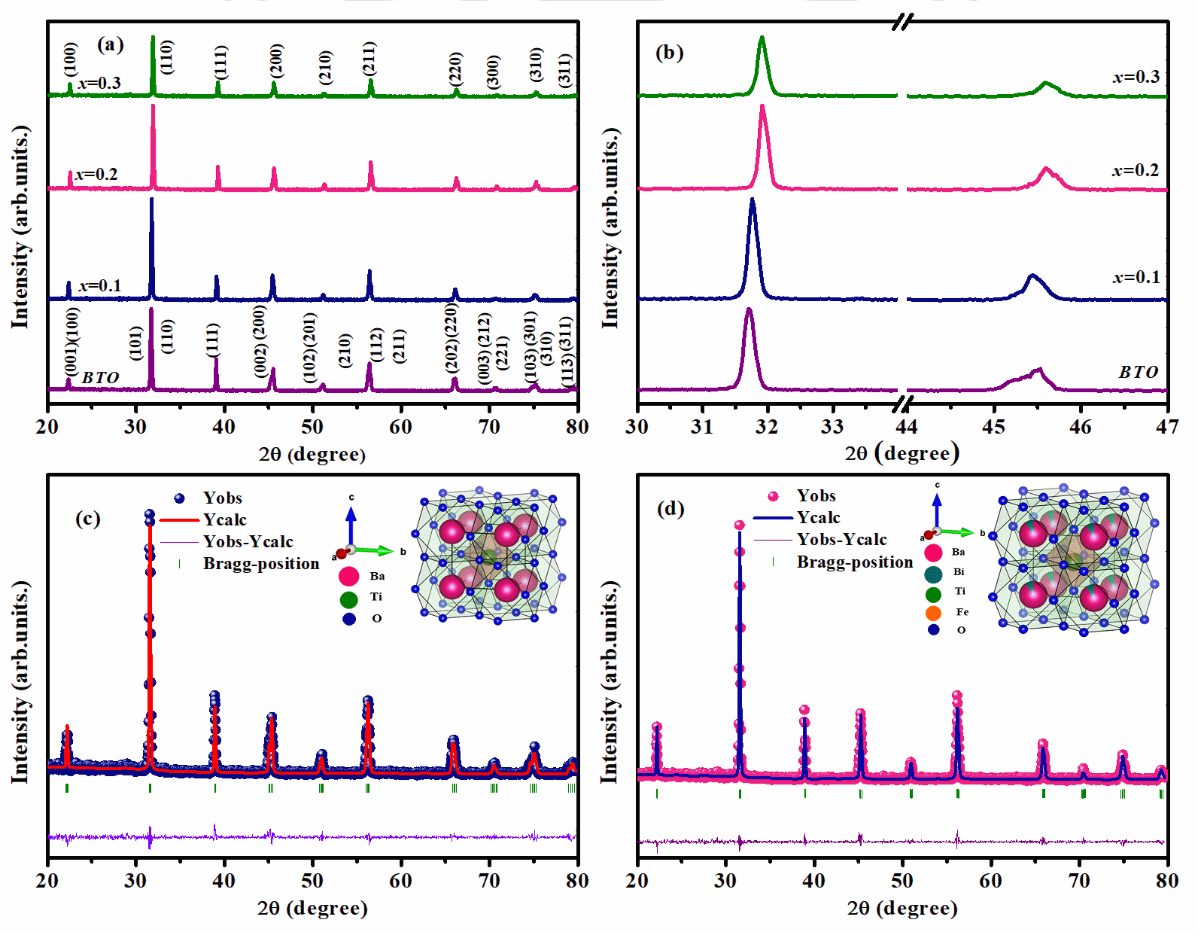

Figure 3. 1: (a) Room-temperature XRD patterns of (1-x) BTO-xBFO ceramics, (b) magnified view of shifting of 2θ ~32° and 2θ ~ 45.5° reflection towards the higher angle, Rietveld Refined XRD patterns for (c) pure BTO (d) BBFT1 and inset images represent the respective VESTA generated images of BTO and BTBF1 ceramics.

The disappearance of the (200) peak splitting around $2\theta \sim 45.5°$, shown in the magnified view in **Figure 3. 1(b)** indicates the phase change. The pure BTO exhibits a tetragonal phase at room temperature. With the addition of rhombohedral BFO, the prepared ceramics changed their phase from tetragonal symmetry (*P4mm* space group) to pseudo-cubic phase (*pm-3m* space group). **Figure 3. 1(b)** also shows the magnified view of shifting of reflection around 2θ ~32° and $2\theta \sim 45.5°$ towards a higher angle with increasing BFO content due to the dissimilarity in ionic radii of *A* and *B* site cations resulting in the lattice distortion of a unit cell. In the *A* site, the Ba^{2+} (1.61Å) ion has larger ionic radii compared to Bi^{3+} (1.03Å) [109]. However, at the *B* site, Ti^{4+} and Fe^{3+} have similar ionic radii of 0.605 Å and 0.60 Å, respectively [118]. The shifting of diffraction peaks (θ) towards the higher angle is observed due to the lattice distortion (shrinkage) because of the decrease in lattice parameter by the introduction of a smaller ion in place of a bigger ion. Hence, the formation of BTO-based solid solution with BFO lead to decrease of the lattice constant [63].

Table 3. 1: Structural parameters for the prepared ceramics obtained by Rietveld refinement of the XRD patterns.

Composition	**c/a**	χ^2	**Volume(Å^3)**
BTO	1.0060	2.85	64.3862
***x*=0.1**	1.0032	2.57	64.3769
***x*=0.2**	1.0028	2.88	64.3242
***x*=0.3**	1.0023	2.68	64.3083

To verify the crystal structure and to calculate the lattice parameter (unit cell volume), the Rietveld refinement of the XRD pattern of the ceramics is carried out via Fullprof software. **Figure 3. 1(c-d)** shows the Rietveld fitting result of the XRD pattern of the BTO and BTBF1 ceramics. The pseudo-Voigt function is used to fit the diffraction peak profiles. The pure BTO and BFO added specimens are refined by tetragonal symmetry. The refinement result suggests the confirmation of phase-shifting from tetragonal to mixed phase (i.e., pseudo-cubic symmetry) with decreased lattice parameters. The crystal structure of BTO and BTBF1 ceramics generated after refinement is shown in the inset of **Figure 3. 1(c)** and **(d)**, respectively. The dark green and orange portion observed for BTBF1 ceramic represents the substitution of Bi and Fe ions in place of Ba and Ti, respectively. The obtained refinement parameter of the prepared ceramics is given in **Table 3. 1**.

Raman Spectra for all specimens (200-800 cm^{-1}) measured at RT are presented in **Figure 3. 2**. All-optical modes are Raman inactive for pure BTO with cubic symmetry. In contrast, eight Raman active modes can be seen with tetragonal symmetry. The Ti^{4+} ions are placed sufficiently far away from O^{2-} ions in the case of tetragonal BTO lattice, whereas, under cubic symmetry, the triply generated modes split into A_1, B_1, and E modes. Hence, the theoretical optical mode for tetragonal BTO can be represented as $\Gamma = 3A_1 + B_1 + E$. Due to electrostatic interaction among the ions, the A_1 and E modes further split into transverse (TO) and longitudinal (LO) optical modes. Raman spectra of the pure tetragonal BTO sample exhibit four dominant peaks at 255, 307, 517, and 716 cm^{-1} assigned to $A_1(2TO)$, $\{B_1 + E(TO) + E(2LO)\}$, $\{A_1(3TO) + E(4TO)\}$ and $\{A_1(3LO) + E(4LO)\}$ modes, respectively [23][24]. Among these four peaks, two peaks at 255 and 517 cm^{-1} can also be seen for Raman inactive cubic phase BTO due to the shift of position of Ti^{4+}. At the same time, the other two intense peaks at 307 and 716 cm^{-1} are characteristic tetragonal peaks of pure BTO [62]. These peaks generally arise due to the asymmetry within the TiO_6 octahedral of BTO and phonon propagation along the c-axis [119]. Raman spectra obtained for the BFO-added compositions show weaker and broader peaks with no remarkable shift. The intensity of signature tetragonal peaks at 307 and 716 cm^{-1} diminishes sharply for BFO mixed compositions and finally becomes broader and flat for x = 0.3 composition. The reduced peak intensity with increasing BFO concentration indicates the mixed tetragonal and cubic symmetry phase. Hence, Raman spectra are evident for the phase change of the prepared specimens from tetragonal symmetry to pseudo-cubic symmetry.

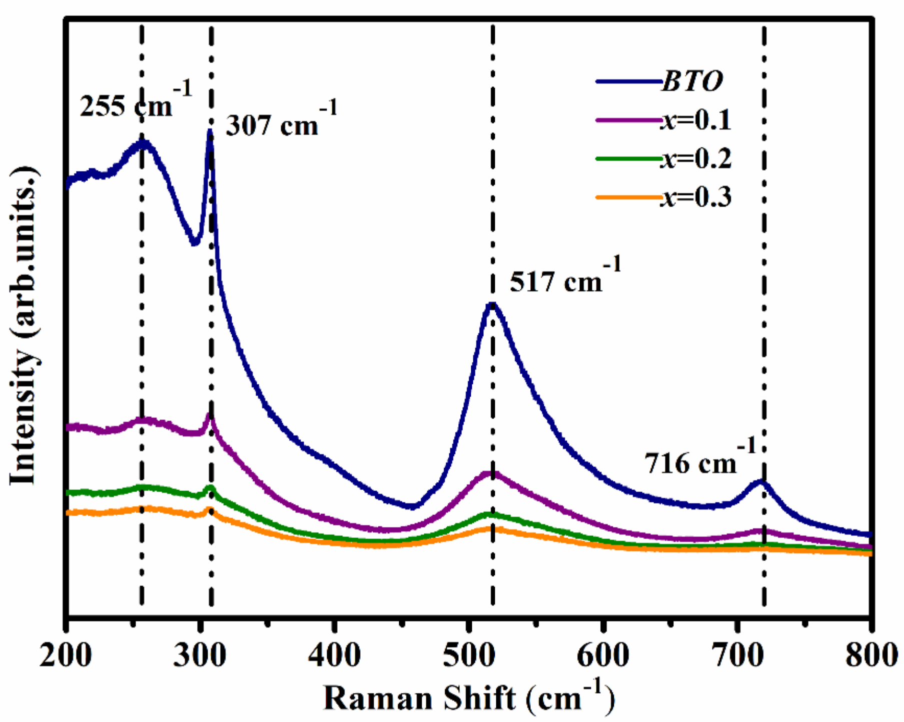

Figure 3. 2: Room temperature Raman spectra of (1-x)$BaTiO_3$-$x$$BiFeO_3$ for x = 0.00, 0.1, 0.2, and 0.3.

The field emission scanning electron microscopy (FESEM) technique provides information on surface morphologies such as grain growth, the shape of grains and grain boundaries, voids, defects, porosity, etc. **Figure 3. 3(a-c)** shows the surface micrographs of BTBF1, BTBF2, and BTBF3 ceramics sintered at 1050°C for 30 minutes. All the micrographs are recorded at the same magnification of 30 KX using an in-lens detector. The grain size has been averaged using Image-J software, and its distribution via histogram is represented in the inset of **Figure 3. 3**. The decrease in grain size of the composition is observed with the addition of BFO content. With the addition of BFO, the crystal lattice's volume decreases, which can be seen as grain growth suppression in BFO-added ceramics. An increase in the concentration of BFO inhibits grain growth and reduces the size of grains. The composition with $x = 0.1$ (BTBF1) showed a homogeneous, well-packed, and densified microstructure with an average grain size of 0.664 μm. The non-uniform and porous microstructure is observed for composition $x = 0.2$ and 0.3 (BTBF2 and BTBF3) specimens with an average grain size of 0.661 μm and 0.536 μm, respectively. The large grains with smaller grains at the boundary indicate inhomogeneous grain growth [116]. The relative density of the samples has deteriorated with the increasing content of BFO (from 96% for BTBF1 to 93% for BTBF3), which may be the reason for non-uniform grain size with porous microstructures. The surface morphology and grain average size of specimens are tabulated in **Table 3. 2**.

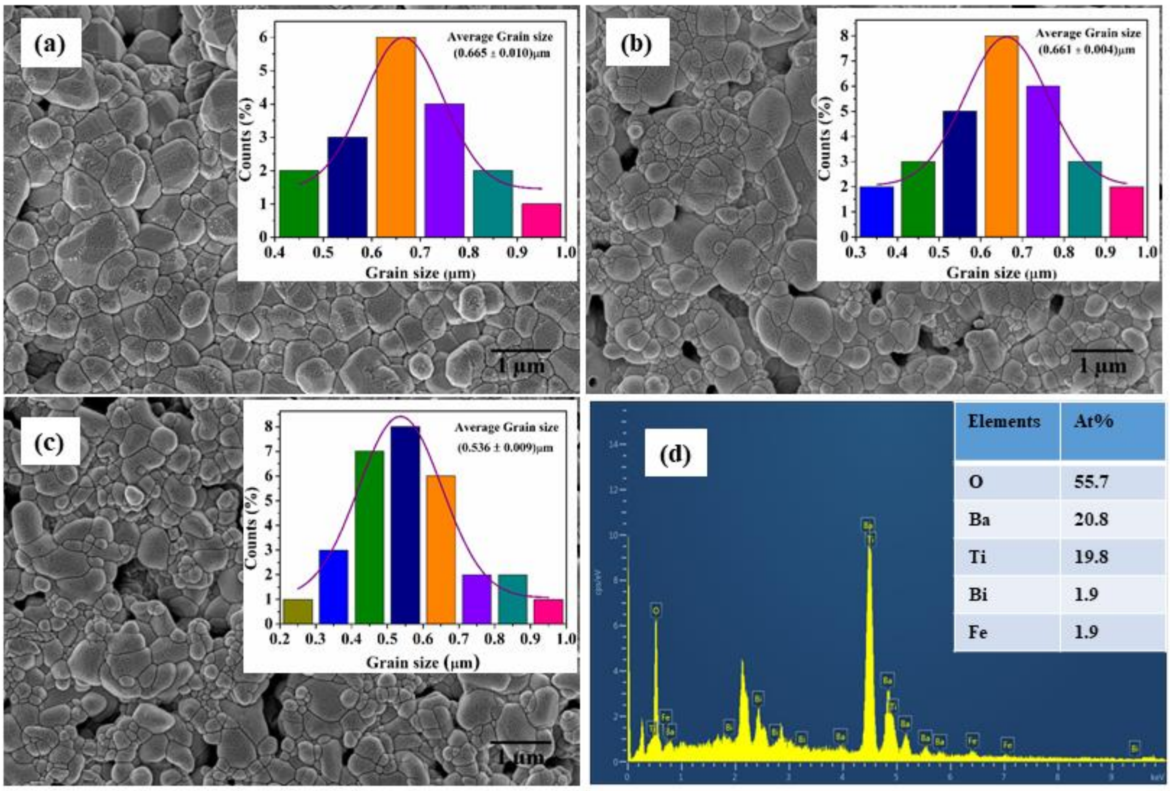

Elements	At%
O	55.7
Ba	20.8
Ti	19.8
Bi	1.9
Fe	1.9

Figure 3. 3: FESEM image of (a) BTBF1, (b) BTBF2, (c) BTBF3, and (d) EDX spectrum of spectra of BTBF1. The inset shows the grain size distributions of respective ceramics.

Energy dispersive X-ray analysis (EDAX) is a technique to identify the elemental composition. EDAX spectra show the different elements existing in the sample via spectra of corresponding peaks. **Figure 3. 3(d)** depicts the EDAX spectra of BTBF1 ceramic recorded for quantitative analysis of all the elements present in the specimen. The spectra reveal the presence of all the elements according to the stoichiometric ratio of the elements present in the empirical formula of BTBF1 composition. Hence, the phase purity of the ceramic is verified. The inset of **Figure 3. 3(d)** shows the obtained atomic % value of all the elements present in BTBF1 ceramic.

Table 3. 2: Average grain size of BTBF1, BTBF2 and BTBF3 ceramics.

Composition	**Average grain size (µm)**	**Surface morphology**
BTBF1	0.664 ± 0.010	Uniform grain size
BTBF2	0.661±0.004	Non-uniform grain size with a porous microstructure
BTBF3	0.536± 0.008	Non-uniform grain size with a porous microstructure

Figure 3. 4 shows the temperature (-140°C-300°C) dependence of the (ε_r) of the BTBF ceramics for a frequency range of 1MHz to 1GHz. Pure BTO sequentially undergoes a phase transition from ferroelectric phase to paraelectric phase, i.e., from rhombohedral to orthorhombic ($T_{R\text{-}O}$), orthorhombic to tetragonal ($T_{O\text{-}T}$) and tetragonal to cubic (T_C) phase at ~ -90°C, ~5°C and ~120°C, respectively [106]. For BTBF1 ceramics, two dielectric peaks around 60°C and 150°C are observed. These peaks are believed to be the phase transition peaks for $T_{O\text{-}T}$ and T_C phase transitions. For the specimens with higher BFO concentrations, the peaks at a lower temperature almost disappeared. Only the Tc is observed to be shifted from 150°C to 180°C with increasing BFO content. The loss tangent also showed a similar trend as the

dielectric constant. It almost shows the hump around the transition temperature. A gradual increase in the value of loss tangent with increasing temperature is observed and is ascribed to the thermally activated charge carriers. The loss tangent is directly related to conductivity. Therefore, the conductivity begins to dominate with a temperature rise, resulting in a surge in tan δ [118]. The BTBF1 ceramic showed an improved (ε_r) with low dielectric loss.

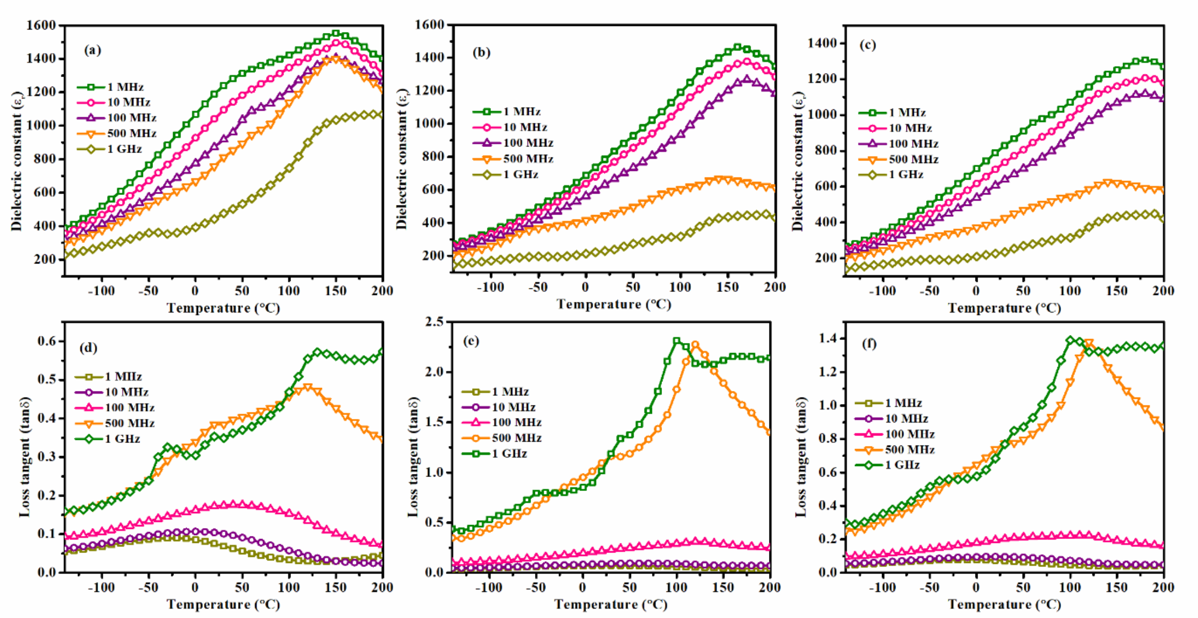

Figure 3. 4: Temperature-dependent dielectric constant at the selected frequency for (a) BTBF1, (b) BTBF2, and (c) BTBF3 ceramics and (d), (e) and (f) represents the corresponding loss tangent.

Complex impedance is an effective technique to study the electrical characteristics of the specimens. This approach helps establish the correlation between the materials' electric/conduction mechanism and microstructures [120]. Detailed studies can be made on dielectric relaxation mechanisms associated with the effect of bulk (grains), grain boundaries, and electrode contribution to conductivity [121][122]. The frequency-dependent electrical properties in terms of complex impedance (Z^*) and complex modulus (M^*) can be represented by the following related parameters:

$$\text{Complex impedance, } Z^*(\omega) = Z' - JZ'' = R_s - \frac{j}{\omega C_s} \tag{3.1}$$

where, Z'=|Z|cosθ and Z''= |Z|sinθ [123].

$$\text{Complex modulus, } M^* = \frac{1}{\varepsilon^*} = M' + jM'' \tag{3.2}$$

$$\text{Complex permittivity, } \varepsilon^* = \frac{1}{M^*} = \varepsilon' - j\varepsilon'' \tag{3.3}$$

$$\text{Complex Admittance, } Y^* = Y' + jY'' = \frac{1}{R_p} + j\omega C_p \tag{3.4}$$

$$\text{Loss tangent, } \quad tan\delta = \frac{\varepsilon''}{\varepsilon'} = \frac{M''}{M'} = \frac{-Z'}{Z''} = \frac{Y''}{Y'} \tag{3.5}$$

where $j = \sqrt{-1}$, the imaginary factor and $\omega = 2\pi f$ [27,28].

At different varying temperatures, the real part of impedance (Z') with frequency ranging from 1 MHz to 1 GHz is shown in **Figure 3. 5(a-c)** for all the compositions. All the composition shows the decreasing Z' values with increasing frequency and temperature, indicating the rise in conductivity. The magnitude of Z' is seen to be large at low frequencies, which reduces with a rise in frequency, and then it merges for all temperatures. Due to the surge in defect concentration and charge accumulation at the grain boundaries, the high value of Z' is observed at the low-frequency region. With the rise in frequency, the drop in Z' value may be due to the release of space charge polarization, which lowers the material's barrier properties [124]. At the low-frequency region, the declining Z' is noticed with the temperature rise, indicating the material's negative temperature coefficient of resistance (NTCR) phenomenon [120][124]. **Figure 3. 5(d-e)** depicts the frequency dependence of the imaginary part of the impedance (Z'') or loss spectrum of the respective compositions. The decrease in the trend of the Z'' value can be seen with a rise in temperature as well as frequency. The change in Z'' as a function of frequency shows the same behavior as that of Z' with frequency. However, the variation in peak broadening is seen with increasing temperature, indicating the electrical relaxation at a particular frequency [120]. The steady species at low temperatures and defects at higher temperatures are mainly responsible for the relaxation process in the material.

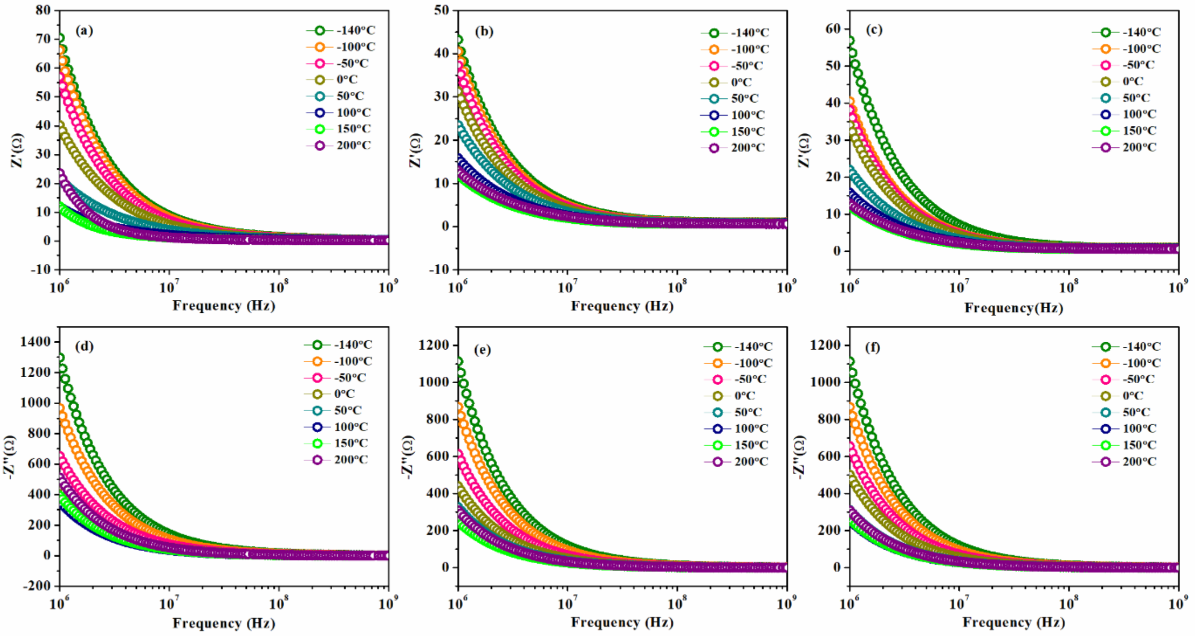

Figure 3. 5: Variation of real impedance (Z') with frequency for (a) BTBF1, (b) BTBF2, and (c) BTBF3 ceramics at a selected temperature from RT to 200°C in the high-frequency range from 1 MHz to 1 GHz and (d), (e) and (f) represents the corresponding variation of the imaginary part of impedance (Z") with frequency.

Figure 3. 6 represents the impedance spectra plotted at different temperatures and presented on the complex plane of *Z″* and *Z′* for BTBF1 ceramic in a high-frequency range (1 MHz to 1GHz). The inset shows the equivalent modeled circuits. This plot helps to study the impact of grain, grain boundary effect, and their electrode contributions to the electric properties of materials using various circuit elements (resistors, capacitors). The number of semicircle arcs determines the types of contribution of the electric process present in the material. For an ideal Debye-type relaxation, a perfect single semicircle with a center lying at

the *Z′* axis is observed [121]. An asymmetrical distorted semicircle suggests the presence of non-Debye-type relaxation in the sample.

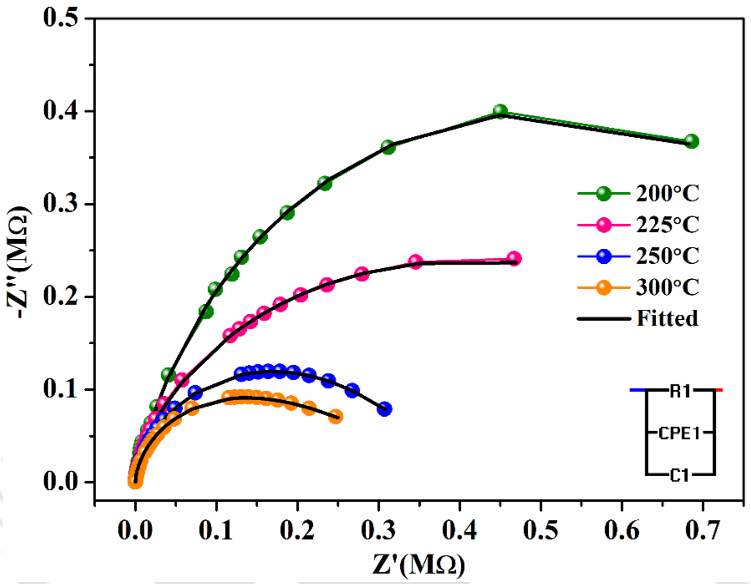

Figure 3. 6: Nyquist plot of BTBF1 ceramic for temperatures 200 ºC, 225 ºC, 250 ºC and 300 ºC. The solid line (black color) denotes the fitting with the RQC equivalent electronic circuit obtained from the fitting. The equivalent circuit model is represented in the inset.

Table 3. 3: Fitted parameters for Nyquist plots for BTBF1 solid solution sample.

Temperature (ºC)	***Model***	***R(kΩ)***	***C(pF)***	***Q***	***n***	***Relaxation Time(τ sec)***
200	RQC	823.27	336.41	2.5118×10^{-09}	0.8562	276.53
225	RQC	505.53	365.16	4.6638×10^{-08}	0.4659	184.32
250	RQC	407.13	323.24	3.5029×10^{-08}	0.4900	131.46
300	RQC	329.07	360.57	1.2246×10^{-07}	0.3825	118.65

A *Z′* and *Z″* plot for BTBF1 ceramics at high temperatures is fitted with an RQC equivalent circuit, where C is capacitance, Q is constant phase angle (CPE), and R is resistance.

The equivalent circuit is modeled by EIS (Electrochemical Impedance Spectroscopy) [125] for 200 ºC, 225 ºC, 250 ºC, and 300 ºC temperatures. The single arc represents the only effect of grain contribution to the conduction [126]. The nature of semi-circle arcs varies with temperature, and their radii increase with a decrease in temperature. With increasing temperature, the resistance and relaxation time decrease, indicating the rise in conductivity. The value of fitted parameters for the Nyquist plot is given in **Table 3. 3**.

A typically frequency-dependent spectrum comprises two distinct regions: frequency-independent dc-conductivity (low-frequency dispersion) and highly dispersive frequency-dependent ac-conductivity (an extended dispersion at high frequency) [120]. The frequency-dependent conductivity is related by the simple expression given by Jonscher's power law [127]:

$$\sigma(\omega) = \sigma_0 + A\omega^s \qquad (3.6)$$

where A is the pre-exponential constant, $\omega=2\pi f$ is the angular frequency, and s is the power-law exponent lies between 0<s<1, σ_α is dc conductivity, and $\sigma(\omega)$ is ac-conductivity, [128]. The conductivity for any ceramic is calculated by empirical formula [122]:

$$\sigma_{ac}(\omega) = \omega\varepsilon_0\varepsilon_r tan\delta \qquad (3.7)$$

The frequency-dependent study of conductivity explains the mechanism of charge carrier hopping. The plot between ln σ_{ac} versus ln(f) in the high-frequency region from 1 MHz to 1 GHz at constant temperature for BTBF1 ceramic has been represented in **Figure 3. 7(a)**. The ac conductivity rises with an increase in frequency, indicating conductivity dispersion with frequency. The conductivity is frequency-dependent and increases linearly for all the temperatures. **Figure 3. 7(b)** displays the ln (σ_{ac}) versus 10^3/T at selected frequencies for BTBF1 composite ceramics. It shows a linear relationship between ln (σ_{ac}) and the inverse temperature. The thermal activation energy of the charge carrier is estimated by the Arrhenius equation given by [36][129]:

$$\sigma_{ac} = \sigma_0 \exp\left(\frac{-E_a}{k_\beta T}\right) \qquad (3.8)$$

where E_a represents activation energy, k_β is the Boltzmann constant, σ_0 is the pre-exponential factor, and σ_{ac} is ac conductivity. The estimated activation energy at high-temperature regions for 1 MHz, 10 MHz, 100 MHz, and 1 GHz is 0.020 eV, 0.025 eV, 0.044 eV, and 0.031 eV, respectively. The value of activation energy is found to be increasing with frequency in higher temperature regions.

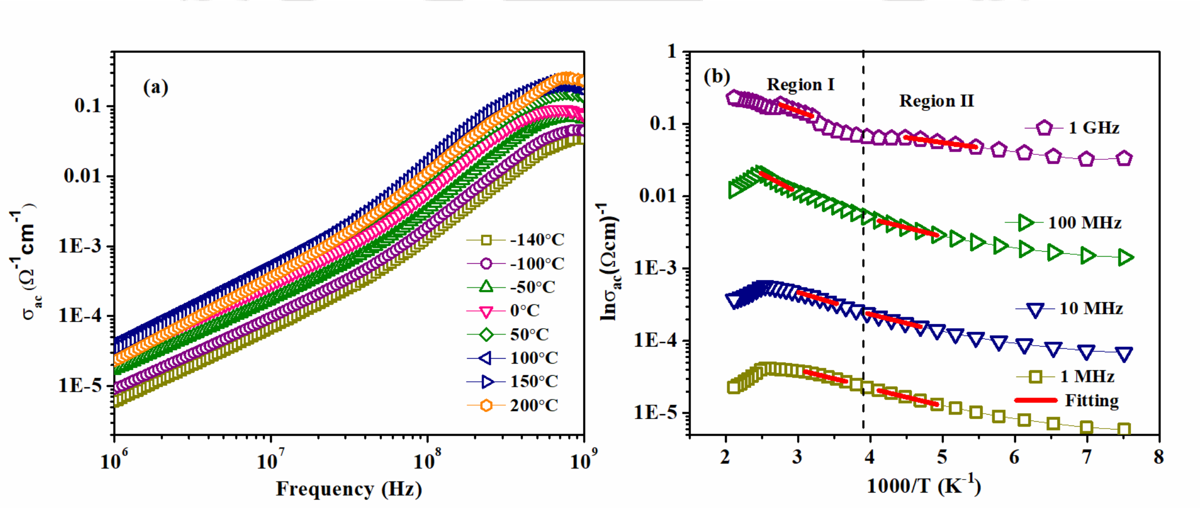

Figure 3. 7: Frequency-dependent conductivity at a selected frequency and (b) Temperature-dependent ln (σ_{ac}) at various selected frequencies for BTBF1 ceramics.

The polarization as a function of the electric field (P-E) is studied at RT to examine the ferroelectric features of the prepared specimens. The P-E hysteresis loop measurement is carried out in the presence of different applied voltages at 10 Hz for each sample, as shown in **Figure 3. 8(a-c)**. A well-shaped hysteresis loop can be seen with increasing applied fields for each sample. However, a well-saturated loop is not observed for any composition due to the application of low electric fields to avoid the breakdown of samples during measurement. The nature of the loops obtained is ferroelectric loops with considerable remnant polarization and coercive fields. The enhanced maximum polarization and better ferroelectric P-E loops are obtained for the prepared ceramics as compared to earlier reports [130]. The values of the hysteresis loop and the energy storage parameters for BTBF1 ceramics are tabulated in **Table 3. 4**.

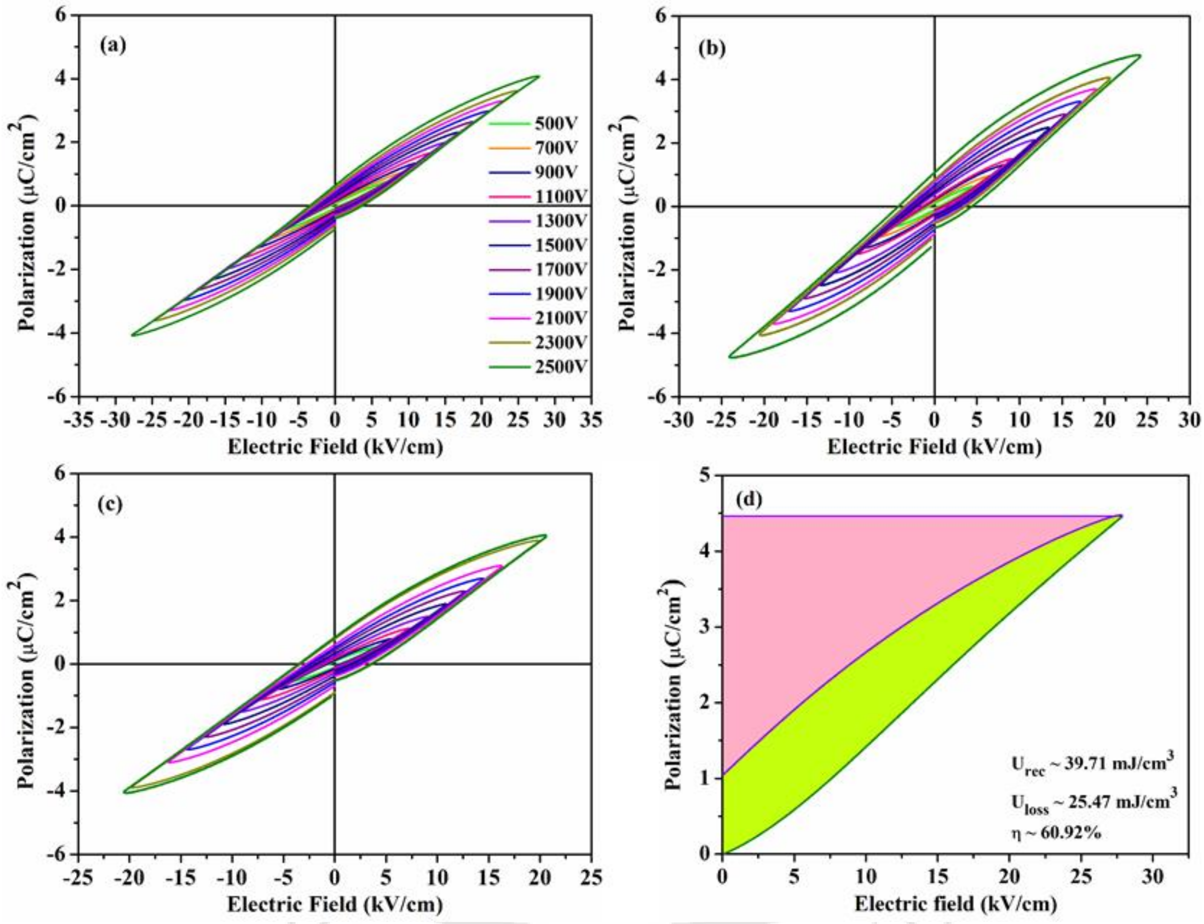

Figure 3. 8: PE loops obtained for (a) BTBF1, (b) BTBF2, (c) BTBF3 ceramics, and (d) represents the recoverable energy density and hysteresis loss of BTBF1 ceramics.

From an energy storage application point of view, the following key parameters must be taken care of large stored and recoverable energy density, high energy efficiency, large breakdown fields, and thermal stability [8]. In the present study, the required parameters for energy storage performance are evaluated and obtained from the P-E hysteresis loops. The recoverable energy density (W_{rec}) is obtained by integrating the area between the polarization axis and the discharge curve of the polarization curve of the P-E hysteresis loop illustrated in (**equation 3.10**) [131]. The energy stored density (W) and energy efficiency (η) are mathematically expressed using **equations (3.9)** and (**3.11**), respectively [41][42]:

$$W = \int_0^{Pmax} EdP \qquad (3.9)$$

$$Wrec = -\int_{Pmax}^{Pr} EdP \qquad (3.10)$$

$$\eta = \frac{Wrec}{W} \times 100\% \qquad (3.11)$$

where P_{max} represents maximum polarization, and P_r indicates remnant polarization.

Table 3. 4: BTBF1, BTBF2, and BTBF3 Polarization parameters.

Composition	P_r (μC/cm^2)	E_c (kV/cm)	P_{max} (μC/cm^2)	Energy density (mJ/cm^3)	Efficiency η (%)	Electric field (kV/cm)
BTBF1	0.64	3.66	4.07	39.71	60.92	25 kV/cm
BFBT2	0.81	3.70	4.04	27.03	52.52	24 kV/cm
BTBF3	0.84	3.62	4.03	26.98	52.48	20 kV/cm

The W_{rec} and η (%) for BTBF1, BTBF2, and BTBF3 ceramic composite have been calculated using the monopolar P-E loops. The W_{rec} and η (%) for BTBF1 ceramics are highlighted in pink and light green color, respectively, as depicted in **Figure 3. 8(d)**. The BTBF1 ceramic showed a higher energy density among all the ceramics, i.e., ~ 40 (mJ/cm^3) at an applied field of 25 kV/cm. The obtained value of recoverable energy density is comparable to the earlier reported value [132]. However, much effort is needed to get a higher magnitude of W_{rec} to serve the purpose of the energy storage application. Energy efficiency is another important parameter for evaluating energy storage performance. It suggests better reliability, low heat loss, and a longer lifespan of physical integrity (capacitors) [8]. The η (%) for BTBF1 is 60.92%, higher among the prepared samples.

3.4 Results and discussion: BT-BZNT solid-solution

The structural analysis is carried out via an X-ray diffractometer scanned in the 2θ range between 20-80° to check the phase formation and crystal structure. **Figure 3. 9(a)** shows the obtained XRD pattern of the prepared BT-BZNT ceramics, sintered at 1250°C for 2 hrs without any secondary phases. All the obtained diffraction patterns of the compositions are indexed with a JCPDS card no 01-074-9807 related to pure BT having a tetragonal structure. No separate phase for BZNT composition is observed, suggesting that the dopants have thoroughly diffused into the host lattice (BTO). For the lower concentration of BZNT ceramics (i.e., x = 0.05, 0.10, and 0.15), no prominent peak splitting is observed for the peak at (110). However, a slight peak splitting can be seen for the peak at the (200) plane, which signifies the characteristic of tetragonal symmetry [133].

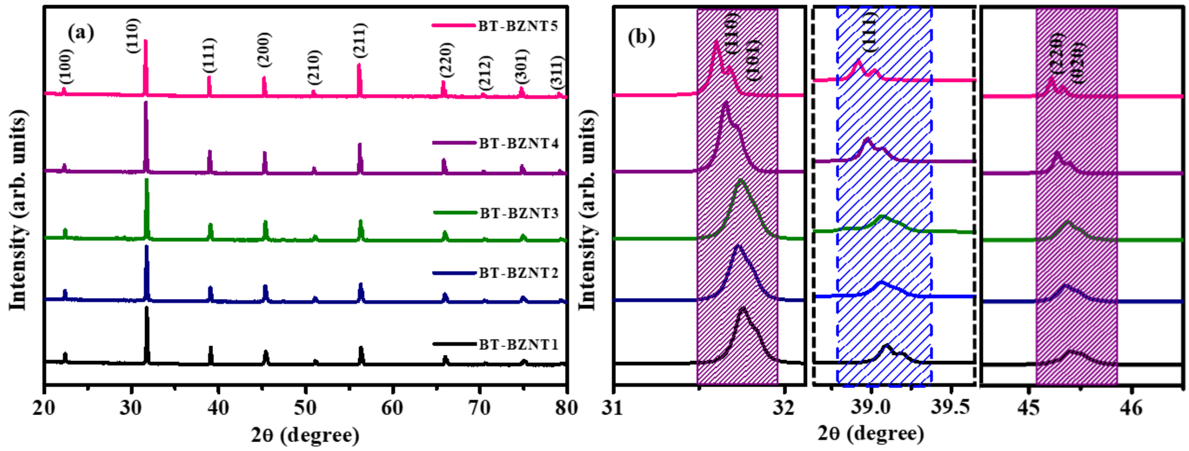

Figure 3. 9: (a) XRD pattern of BT-BZNT ceramics, (b) Enlarged portion of diffraction peaks at 2θ~31.76°, 39.2° and 45.45°.

With the further addition of BZNT ceramic, a remarkable peak splitting (110/101), (220/020) is observed for (110/200) planes indicating the structural transformation. The orthorhombic phase is characterized by 220/020 splitting at ~45° [103]. It is also observed from **Figure 3. 9(b)** that the splitting of the (111) plane along with the shoulder peak at the (200) plane gives evidence of rhombohedral symmetry in all synthesized ceramics [134]. **Figure 3. 9(b)** depicts the shifting of the diffraction peaks with the composition modification. The diffraction peaks shift toward the left, indicating the crystal lattice's expansion. The expansion in the lattice is caused by the substitution of bigger ionic radii [Zn^{2+} (0.74Å), Nb^{5+} (0.64Å), and Ta^{5+} (0.64Å)] [135][105][136] ions with comparable smaller ionic radii [Ti^{4+} (0.605Å)] in B-site [44]. The crystal structure expansion indicates that B-O_6 octahedral is dominant in unit cell volume [45], although the ionic radii of Ba^{2+} (1.61Å) are larger than the Bi^{3+} (1.36Å) in A-site.

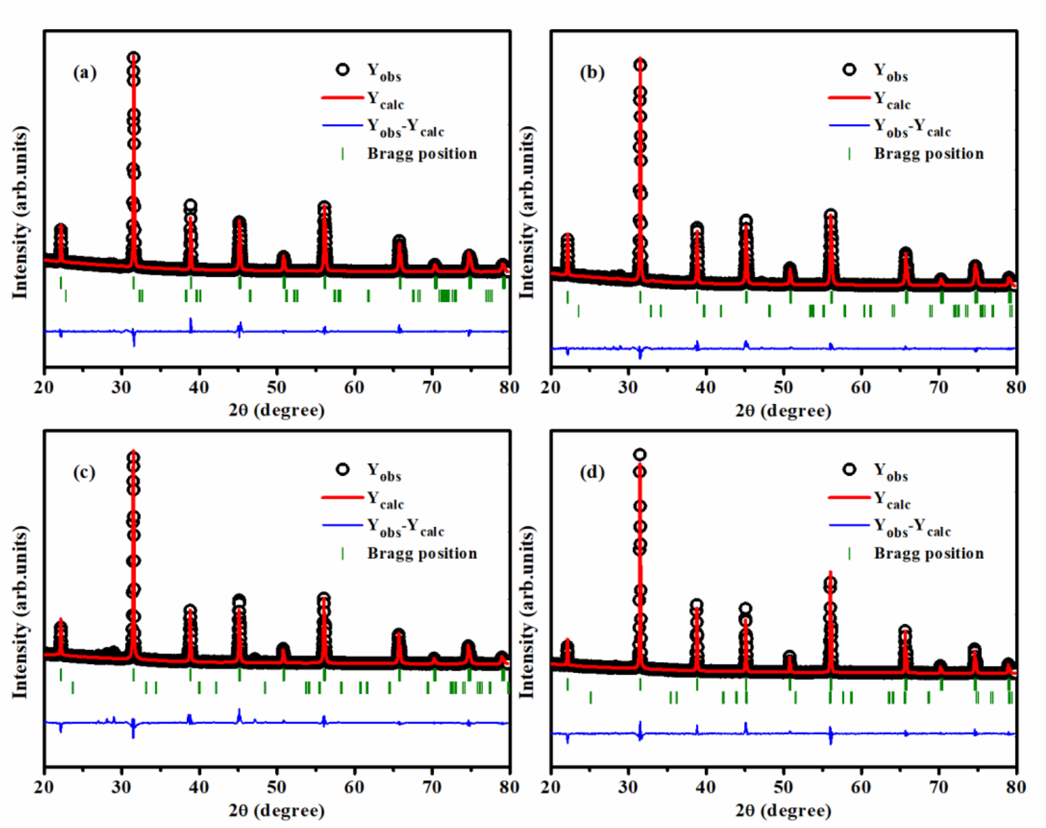

Figure 3. 10: Rietveld refined XRD pattern of (a) BT-BZNT1, (b) BT-BZNT2, (c) BT-BZNT3, and (d) BT-BZNT4 ceramics.

The crystal symmetry of BT-BZNT ceramics seems quite complex when analyzed using the XRD pattern alone. Further, the experimentally obtained XRD pattern is refined using the FullProf Suite software to confirm the phase assemblage. The refinement fitting results confirmed that the XRD pattern of the BT-BZNT ceramics is best fitted with the two-phase model using tetragonal and rhombohedral symmetries. Therefore, a two-phase refinement method is carried out considering tetragonal and rhombohedral structures (*p4mm+R3c*). The observed pattern is well matched with the calculated patterns, as shown in **Figure 3. 10** for all fitted samples. The extracted goodness of fitting (χ^2) and lattice parameters from the refinement are listed in **Table 3. 5**.

Table 3. 5: χ^2 and lattice parameters deduced from Rietveld refined XRD pattern.

Compositions	χ^2	*Crystalltite size (nm)*	*Lattice strain (10^{-3})*	*Tetragonal phase*			*Rhombohedral Phase*			*Grain size (µm)*	*Relative density (%)*
				a=b (Å)	*c (Å)*	*Volume fraction (%)*	*a=b (Å)*	*c (Å)*	*Volume fraction (%)*		
BT-BZNT1	4.65	165	1.90	4.014 (0)	4.008 (0)	96.17	5.496 (9)	13.646 (4)	3.83	0.64 ± 0.01	93.2
BT-BZNT2	4.42	148	1.83	4.017 (0)	4.012 (0)	91.35	5.249 (3)	13.613 (4)	8.65	1.30 ± 0.03	93.7
BT-BZNT3	4.89	134	1.65	4.018 (0)	4.014 (0)	84.58	5.220 (9)	13.532 (6)	15.42	1.72 ± 0.03	95.8
BT-BZNT4	4.71	118	1.62	4.020 (0)	4.018 (0)	79.63	5.070 (11)	12.045 (9)	20.37	2.91 ± 0.05	96.4
BT-BZNT5	4.58	112	1.53	4.025 (0)	4.023 (0)	76.04	4.368 (8)	13.678 (7)	23.96	4.65 ± 0.08	94.3

Further, the crystal structure of pure BTO and BZNT is illustrated in **Figure 3. 11(a)** and **(b),** generated from Vesta software. The presence of respective elements in the respective positions in the BTO and BZNT ceramics unit cell is well visualized. Likewise, the dual phases can be observed for multiphase refined BT-BZNT4 ceramic, illustrating the mixed crystal structures consisting of BTO and BZNT phases as shown in **Figure 3. 11(c)**. Therefore, the formation of homogeneous perovskite binary solid-solution of BT-BZNT ceramics with dual phase is confirmed [103].

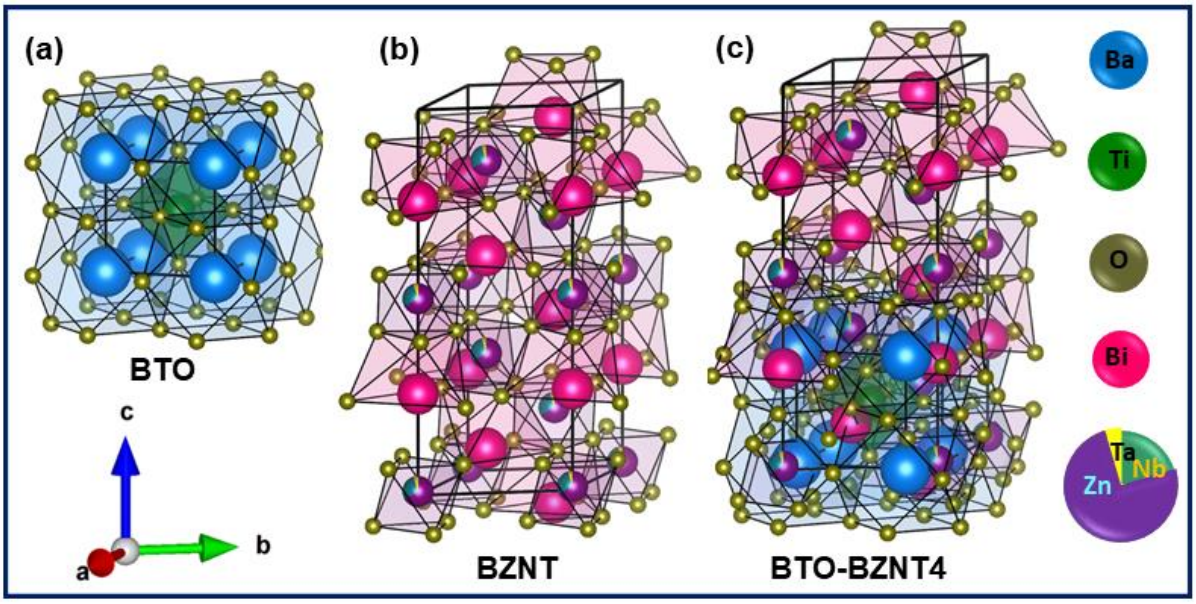

Figure 3. 11: Vesta generated crystal structure of (a) BTO, (b) BZNT, and (c) BTO-BZNT4 ceramics.

The crystallite size and lattice strain of the synthesized ceramics are calculated utilizing the Williamson Hall (W-H) analysis method using the equation as follows [102]:

$$\beta cos\theta = \frac{k\lambda}{D} + 4\varepsilon sin\theta \qquad (3.12)$$

here, β represents full width at half maxima, k denotes the shape factor, and λ equal to 1.5406 Å, which is the wavelength of X-ray radiation. D and ε represent crystallite size and lattice strain, respectively, and are deduced from the y-intercept and slope of the fitted line from the

$\beta cos\theta$ and $4sin\theta$ as shown in **Figure 3. 12(a-d)**. The extracted values of crystallite size and lattice strain are listed in **Table 3. 5**. With BZNT concentration, the crystallite size diminishes, suggesting the crystal lattice's expansion. Besides increased lattice parameters and shifting of diffraction peaks towards a lower angle with BZNT substitution, the coexistence of tetragonal and rhombohedral symmetry is evident from the XRD analysis for all the ceramics.

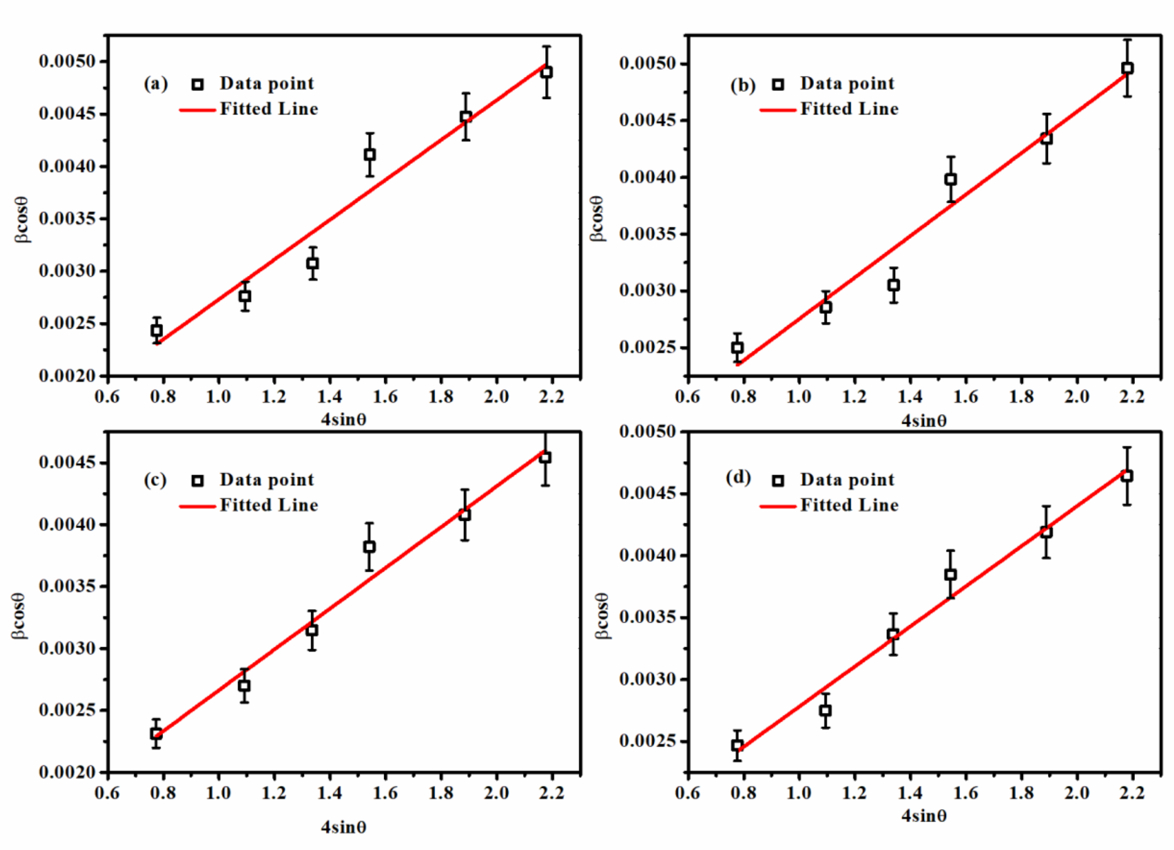

Figure 3. 12: W-H plot for (a) BT-BZNT1, (b) BT-BZNT2, (c) BT-BZNT3, and (d) BT-BZNT4 ceramics.

Raman spectra of the BT-BZNT ceramics are analyzed to complement the XRD analysis to verify the crystal structure and phase formation. **Figure 3. 13(a)** depicts the Raman spectra for all samples in the 100-800 cm^{-1} wavenumber range. The tetragonal BTO consists of eight Raman active phonon modes comprised of $3[A_1(TO) + A_1(LO)] + 4[E(TO) + E(LO)] + B_1$. The asymmetric mode around 111 cm^{-1} is assigned to $E(TO_1)$, whereas the strong peak at 178 cm^{-1} is assigned to the $A_1(TO_1)$ mode corresponding to Ba^{2+} ions for TiO_6 octahedra. Two broad bands approximately located at 267 and 524 cm^{-1} correspond to $A_1(TO_2)$ mode and $A_1(TO_3)$ modes, respectively [137]. The sharp mode present at 305 and 720 cm^{-1} is the signature peak indicating the tetragonal distortion in $BaTiO_3$ [138].

Table 3. 6: Raman shift (cm^{-1}) of the modes for BT-BZNT ceramics.

Composition	***1***	***2***	***3***	***4***	***5***	***6***	***7***	***8***
BT-BZNT1	111.6	151.1	178.9	267.4	305.7	524.8	721.1	769.8
BT-BZNT2	111.5	149.7	176.1	270.5	307.7	524.7	704.8	760.4
BT-BZNT3	111.9	149.3	182.8	261.3	309.3	524.4	720.0	765.6
BT-BZNT4	112.2	146.9	177.6	264.2	314.7	524.9	724.3	771.7
BT-BZNT5	111.9	150.7	185.4	238.6	312.4	525.0	715.5	766.3

All the Raman modes assigned in **Figure 3. 13(a)** are consistent with the earlier investigation on $BaZr_{0.05}Ti_{0.95}O_3$ ceramic [139]. It is evident from **Figure 3. 13(a)** that the tetragonality is reduced as the concentration of BZNT is raised, which is confirmed by the intensity of the 305 and 720 cm^{-1} peaks assigned for ETO_2 and A_1LO_3 mode diminishes for higher BZNT substituted samples. With BZNT substitution, the broadband detected around 770 cm^{-1} (A_1LO_4) further broadened may result from the B-site substitution. Hence, a stable binary solid solution is formed by introducing BZNT [140][141]. **Figure 3. 13(b-f)** illustrates the fitted Raman spectra using the Gaussian-Lorentzian distribution function, revealing the prominent peak positioning of the synthesized samples. The broadening and the shifting of several peak positions are observed, suggesting the coexistence of dual phase (tetragonal + rhombohedral) in BT-BZNT ceramics. All detected and fitted vibrational modes for BT-BZNT ceramics are listed in **Table 3. 6**.

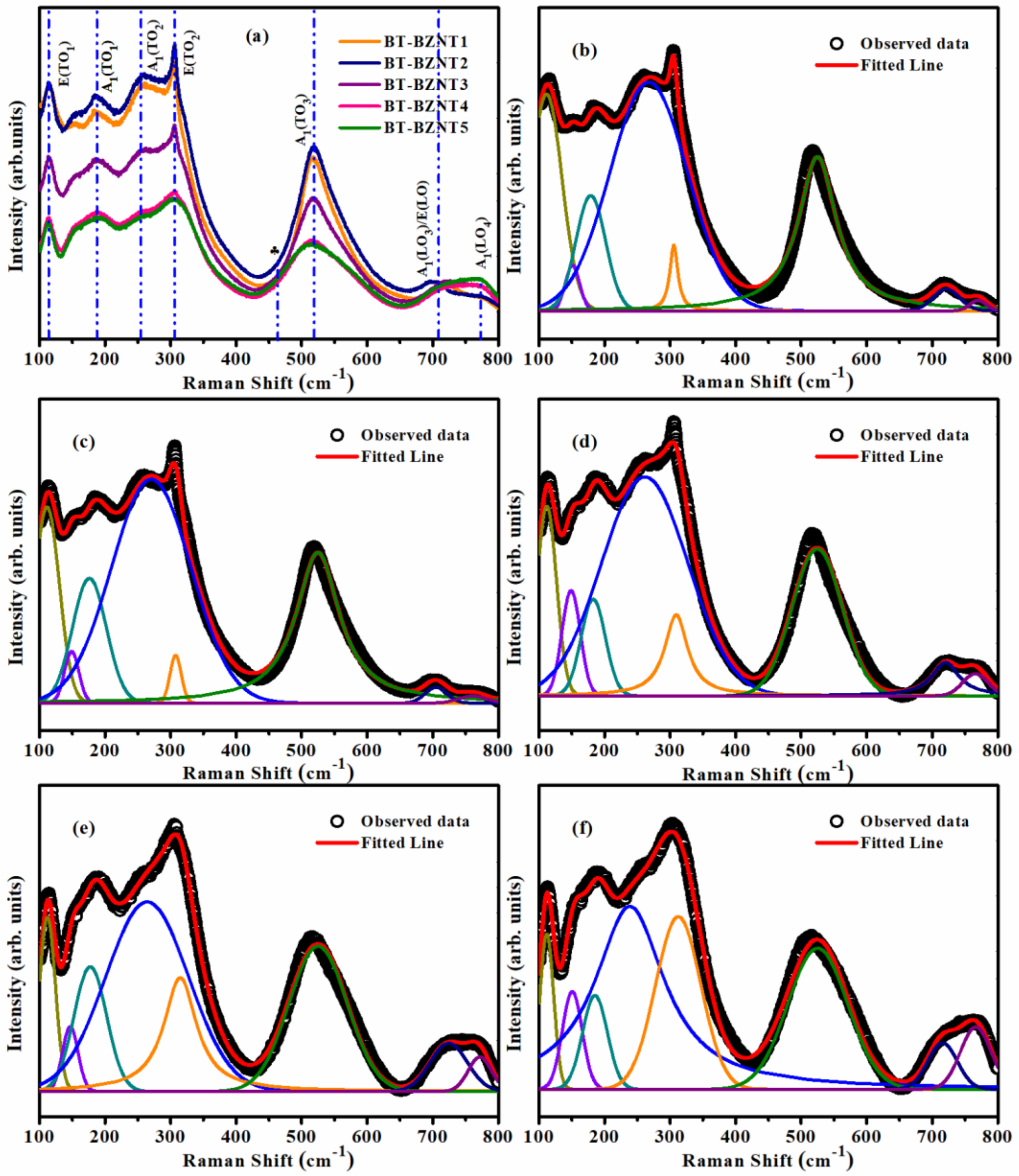

Figure 3. 13: (a) Raman spectra and (b-f) fitted experimental Raman spectrum of BT-BZNT ceramics.

Figure 3. 14 shows the FESEM micrograph of BT-BZNT ceramics and the corresponding grain size histogram. For all BT-BZNT compositions, both irregular and cuboidal-shaped grains are observed. The tiny irregular grains belong to BTO, whereas BZNT ceramics displays cuboidal-shaped grains. A mixture of tiny irregular and cuboidal-shaped grains is observed for BT-BZNT1 ceramics, which systematically grows with further BZNT substitution. The grain growth in the ceramics observed may be due to the expansion in the crystal lattice with the

addition of BZNT into the BTO matrix, which agrees well with the XRD and Raman interpretations.

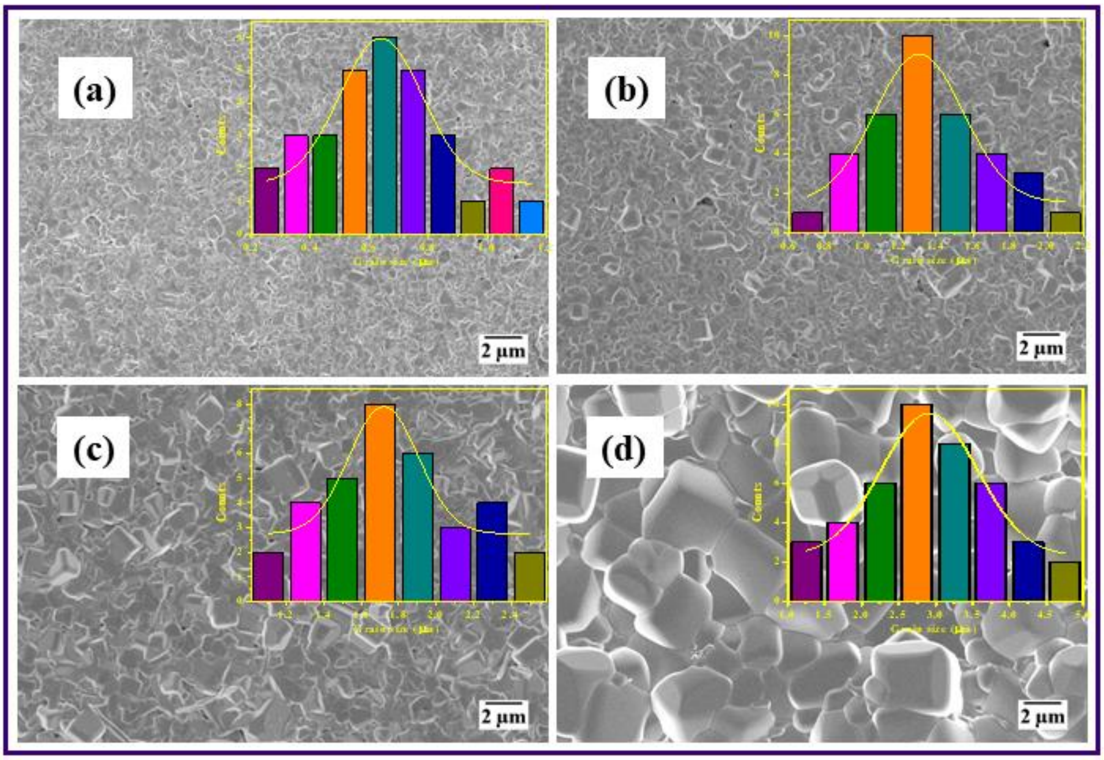

Figure 3. 14: FESEM microstructure with grain size histogram in the inset for (a) BT-BZNT1, (b) BT-BZNT2, (c) BT-BZNT3, and (d) BT-BZNT4 ceramics.

The addition of BZNT ceramic in which A-site element Bi volatilizes, as a result, oxygen vacancies are generated to maintain overall charge neutrality that facilitates the mass transportation during the sintering, which accelerates the grain growth [40][142]. Similar grain growth is likewise observed in solid solutions with higher substitution concentrations [143][43]. With increasing BZNT substitution, the number of irregular grains reduced, and the concentration of cuboidal-shaped grains appeared. The average grain size estimated from ImageJ software is found to be 0.64 (BT-BZNT1), 1.30 (BT-BZNT2), 1.72 (BT-BZNT3), 2.91 (BT-BZNT4), and 4.65 μm (BT-BZNT5). The calculated average grain size of the compositions is listed in **Table 3. 5**, along with the relative density of BT-BZNT ceramics. It is found that with BZNT addition, the relative density of the ceramics improved from 93.2%

(BT-BZNT1) to 96.4% for BT-BZNT4 and reduced to 94.3% for BT-BZNT5. With BZNT substitution, the surface of the ceramic becomes dense with negligible voids, and clear grain boundaries appear, implying that the optimum concentration substitution can appreciably improve the microstructure. The dense morphology for BT-BZNT4 ceramic may be attributed to the better crystallinity and the maximum relative density. The presence of all the elements and the formation of synthesized ceramics in the stoichiometric ratio is examined through EDAX analysis. **Figure 3. 15(a)** and **(b)** show the FESEM images and the corresponding elements in the BT-BZNT1 and BT-BZNT4 ceramics. The EDAX spectra represent the elemental peaks corresponding to the elements present in the sample. The presence of elements in the stoichiometric ratio is confirmed by the experimentally obtained atomic weight % of the elements compared to the theoretical calculation as presented in the inset of **Figure 3. 15(a)** and **(b).**

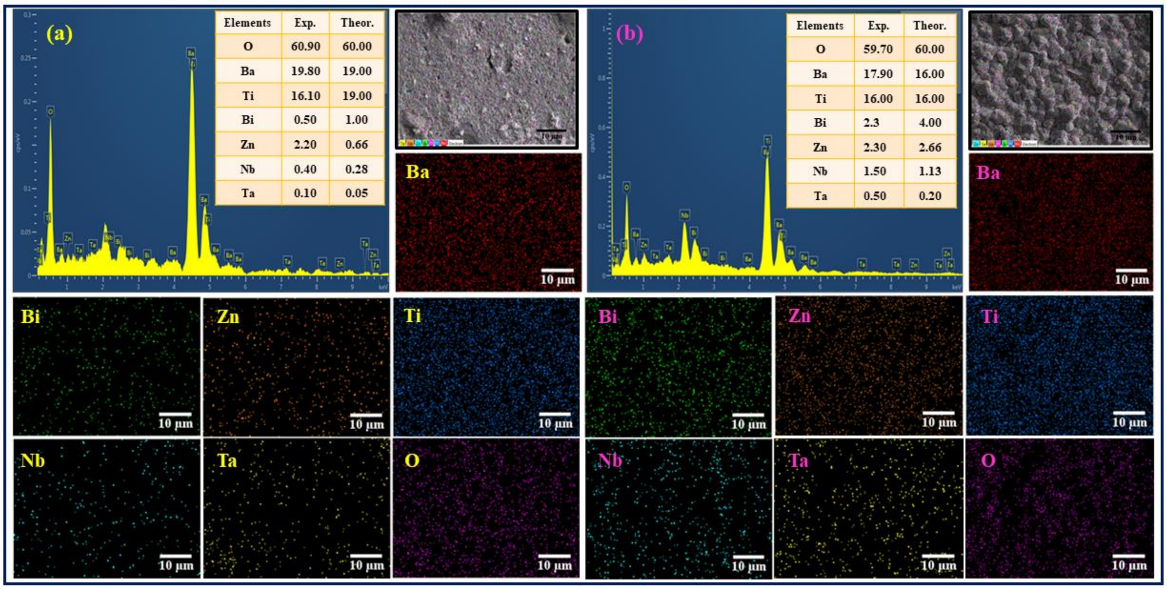

(a)

Elements	Exp.	Theor.
O	60.90	60.00
Ba	19.80	19.00
Ti	16.10	19.00
Bi	0.50	1.00
Zn	2.20	0.66
Nb	0.40	0.28
Ta	0.10	0.05

(b)

Elements	Exp.	Theor.
O	59.70	60.00
Ba	17.90	16.00
Ti	16.00	16.00
Bi	2.3	4.00
Zn	2.30	2.66
Nb	1.50	1.13
Ta	0.50	0.20

Figure 3. 15: EDAX spectra and elemental mapping of (a) BT-BZNT1 and (b) BT-BZNT4 ceramics with their respective elements.

The elemental mapping at the same scanned area revealed that the corresponding elements are uniformly distributed, demonstrating good chemical homogeneity. For BT-

BZNT4 ceramic, the elemental distribution of the substituted BZNT compositions, such as Bi, Zn, Nb, and Ta elements, appears dense compared to the BT-BZNT1 composition. The experimentally obtained atomic weight % of the BT-BZNT4 ceramic is close to the theoretically calculated At. % values that display the better formation of the sample in the stoichiometric ratio and the substitution of BZNT compositions are well incorporated in the BTO matrix. The X-ray photoelectron spectroscopy **(**XPS) analysis is further carried out for BT-BZNT ceramics to validate the elemental compositions.

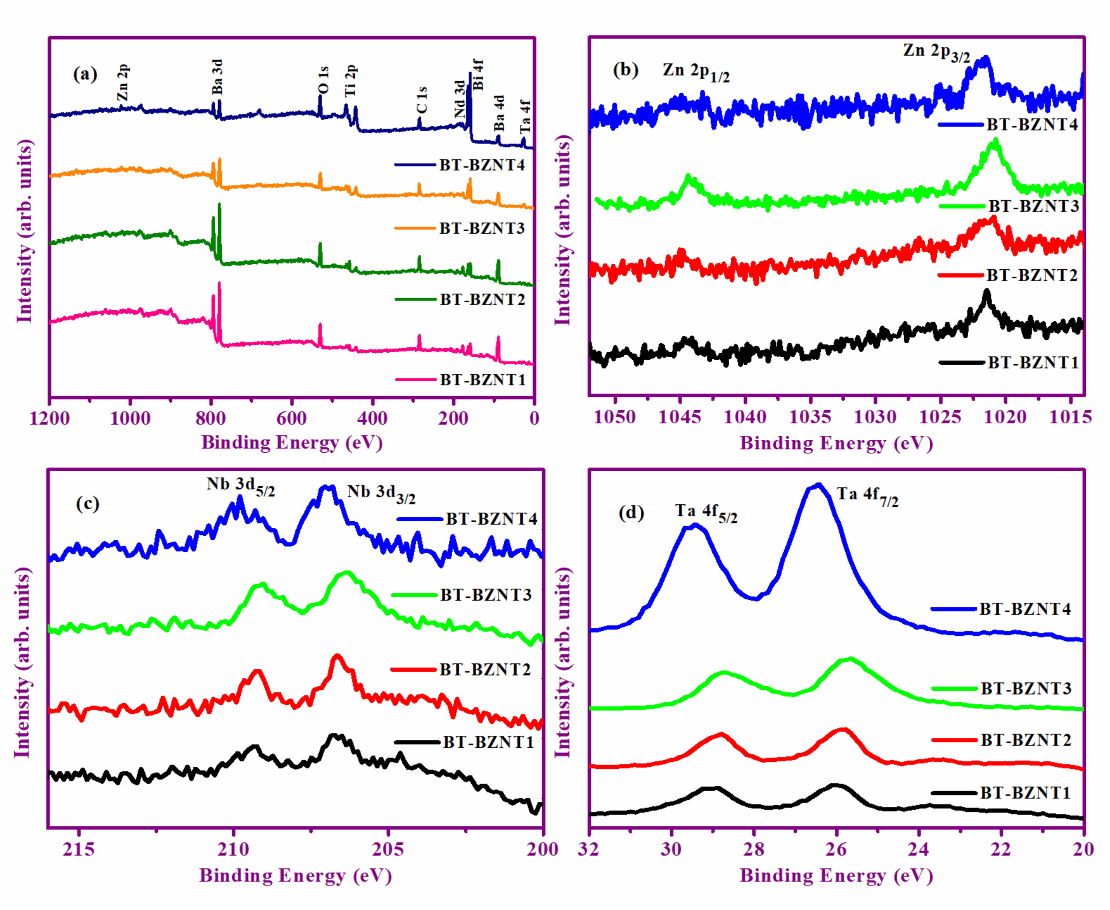

Figure 3. 16: (a) XPS full scan spectra and high-resolution XPS spectra for (b) Zn 2p, (c) Nb 3d, and (d) Ta 4f states of BT-BZNT ceramics.

Figure 3. 16(a) shows the XPS full spectra of BT-BZNT ceramics obtained for different samples (i.e., BT-BZNT1, BT-BZNT2, BT-BZNT3, and BT-BZNT4). The core level

peaks of all elements constituting the BT-BZNT ceramics (Ba 3d, Ti 2p, Bi 4f, Zn 2p, Nb 3d, and O 1s) are significantly observed in the spectra. The intensity of the BT characteristic peaks "Ba 3d" and "Ba 4d" gradually weaken for higher BZNT substituents (BT-BZNT4 sample). Additionally, Bi 4f, Zn 2p, Nb 3d, and Ta 4f peaks of BZNT composition become prominent with higher BZNT substitution. The high-resolution (HR) spectrum of Zn 2p, Nb 3d, and Ta 4f are depicted in **Figure 3. 16(b-d).** Similarly, the higher intensity of the fine spectrum is found for higher BZNT substituent samples.

To determine the oxidation states of the elements present in the samples, the HRXPS spectra for Ba 3d, Ti 2p, O 1s, and Bi 4f states are plotted and shown in **Figure 3. 17(a-d)**. In the synthesized ceramics, a significant change in chemical state is observed for major substituted elements. Two peaks with binding energies around 779.59 and 794.93 eV are assigned to Ba $3d_{5/2}$ and Ba $3d_{3/2}$ with spin-orbit separation (SOS) energy difference of 15.34 eV suggests the presence of Ba in the Ba^{2+} state in all samples. However, the prominent peak spectra of Ba 3d become less significant with higher BZNT addition, as shown in **Figure 3. 17(a)**. Similarly, for Ti 2p, two peaks located approximately at 458.12 and 464.18 eV belong to Ti $2p_{3/2}$ and Ti $2p_{1/2}$, displayed in **Figure 3. 17(b),** indicating the presence of Ti 2p in the Ti^{4+} state. With further BZNT substitution, the prominent peak shifting is noticed for the Ti $2p_{1/2}$ peak due to the low concentration of Ti in higher substituted samples. **Figure 3. 17(c)** depicts the O 1s spectra. Two sub-components at binding energies ~529 and 531 eV appeared, indicating the lattice oxygen and oxygen vacancies/defects. However, with further addition of BZNT, the oxygen vacancies/defects are expected to be less dominant. The peak at higher binding energy (531 eV) seems to be reduced with the composition variation, indicating the low amount of oxygen vacancies in the higher substituted samples. As can be seen from **Figure 3. 17(d)**, the Bi 4f spectra consist of two deconvoluted peaks at 164.8 and 158.5 eV for Bi $4f_{5/2}$ and Bi $4f_{7/2}$, with SOS of 5.3 eV confirming the presence of bismuth in +3 state. Meanwhile, two less prominent peaks appeared at lower binding energies for Bi $4f_{5/2}$ and Bi $4f_{7/2}$ around 162.1 and 156.5 eV for lower BZNT substituted samples, validating the existence of Bi in a lower oxidation state (Bi^{2+}) [144]. The presence of oxygen vacancies (V_0^{2+}) resulted in a transition of the $Bi^{3+} \rightarrow Bi^{2+}$ state to maintain the charge neutrality in the sample. Thus, the Kroger–Vink notation can be described as follows [145][146]:

$$2Bi^{3+} + 3O^{2-} \rightarrow 2V_{Bi}^{3-} + 3V_0^{2+} + Bi_2O_3 \qquad (3.13)$$

For the BT-BZNT4 sample, the presence of lower binding peaks for Bi $4f_{5/2}$ and Bi $4f_{7/2}$ disappeared, suggesting the lower oxygen vacancies within the sample.

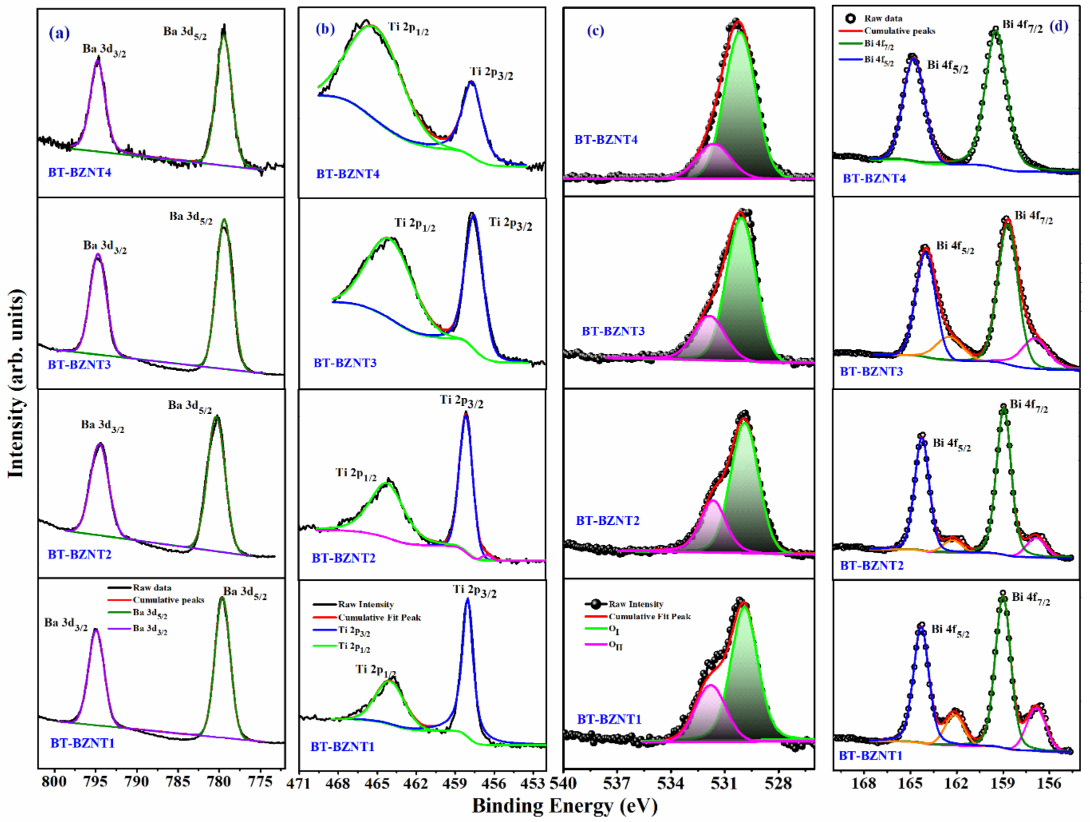

Figure 3. 17: Fitted HRXPS spectra of (a) Ba 3d, (b) Ti 2p, (c) O 1s, and (d) Bi 4f states of BT-BZNT ceramics.

Figure 3. 18(a) and **(b)** show the dielectric response of the BT-BZNT ceramics as a function of temperature from RT to 500 °C, measured at 1 MHz frequency. With the

substitution of BZNT, the subsequent dielectric behavior is noticed in the synthesized samples. (i) It is to be noted that BT-BZNT1 ceramics exhibited two peaks at ~95°C (T_{m1}) and ~155°C (T_{m2}) in the measured temperature range. Whereas the other compositions with higher BZNT substitution showed only one diffused peak. Two characteristic dielectric peaks (T_{m1} and T_{m2}) appeared for BT-BZNT1 ceramic and may be associated with the particular structure of the grain. A similar dielectric response is observed for $BaTiO_3$–$Bi(Zn_{0.5}Zr_{0.5})O_3$ and BT@(0.3BZT-0.7BT) core-shell structure systems [103][147]. The lower substituent sample (BT-BZNT1) showed a prominent sharp peak at 155 °C corresponding to the tetragonal-cubic phase transition often referred to as the Curie temperature (T_c) of pure BTO ceramic, which gradually shifted to a higher temperature (170°C) with a compositional variation. (ii) With the further addition of BZNT, the T_c gradually broadens, manifesting diffused behavior [148]. (iii) The value of dielectric permittivity (ε_r) of the ceramics is observed to be decreasing with BZNT substitution. The reduced ε_r with compositional variation may be due to the difference in ionic radii between Ti^{4+} (0.605Å) and $(Zn_{0.667}Nb_{0.283}Ta_{0.05})^{3+}$ (0.674Å). Adding a bigger cation is expected to compress the oxygen octahedra and restrict the area available for B-site cations to migrate, consequently lowering the permittivity and reducing polarization [45].

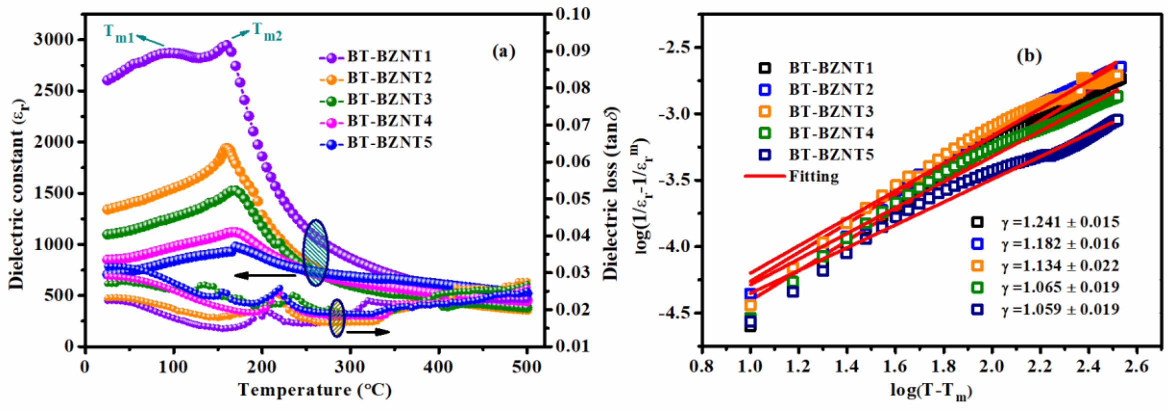

Figure 3. 18: (a) Temperature-dependent dielectric response and (b) diffusivity analysis of BT-BZNT ceramics measured at 1 MHz.

With BZNT content, the curves exhibited diffused behavior with decreased ε_r, which may indicate the existence of nanodomain structures. Besides, the dielectric loss curve resembles the dielectric permittivity curve trend. The dielectric loss hump above 200 °C is found for BT-BZNT1 ceramic which further shifted to a higher temperature for higher BZNT substitute samples. The influence of diffuse phase transition in BT-BZNT ceramics is further examined using the diffusivity analysis. The modified Curie-Weiss law fitting is used to investigate the effects of diffuse phase transition in BZNT-substituted BTO ceramics. The material with $\gamma = 1$ indicates the ferroelectric nature of the sample. When $\gamma = 2$, the material is expected to show complete relaxor behavior. And if the γ value is between 1 and 2, the material exhibits ferroelectric diffuse characteristics [138].

$$\frac{1}{\varepsilon}-\frac{1}{\varepsilon_m}=\frac{(T-T_m)^\gamma}{C} \qquad (3.14)$$

here, ε is the dielectric constant, and ε_m is the maximum dielectric constant in the given temperature range. T is the temperature, and T_m is the corresponding temperature at the maximum dielectric constant. C and γ are constants, termed as the Curie-Weiss constant and diffusivity constant, respectively. **Figure 3. 18(b)** depicts the relation between $\ln(1/\varepsilon - 1/\varepsilon_m)$ versus $\ln(T-T_m)$ for all BT-BZNT ceramics. The diffusivity constant in the current study is between 1 and 2 for samples up to $x = 0.15$ composition. Above this, the sample behaves like a normal ferroelectric material, exhibiting a diffused phase transition behavior, as shown in **Figure 3. 18(a)**.

Figure 3. 19(a) shows the dependence of conductivity with frequency in the range of 100 Hz to 0.5 MHz for the BT-BZNT ceramics measured at 250 °C. The observed decrease in conductivity with increasing BZNT substitution shows that the samples have resistive insulation characteristics, which enhances the electric breakdown strength. **Figure 3. 19(b)** represents the frequency-dependent conductivity for BT-BZNT4 ceramic in the temperature

range from 210-250 °C. An increase in conductivity with temperature in the sample suggests a negative temperature coefficient of resistance (NTCR) behavior [40]. In both cases, the conductivity curve shows three distinct frequency regions indicated as Region I, Region II, and Region III in the graph. Lower frequency conductivity (Region I) is almost frequency-independent and equal to direct conductivity (dc conductivity) caused by charge carrier displacement, extending progressively with frequency [149]. In the intermediate frequency range (Region II), the conductivity rises with frequency, increasing linearly at higher frequency regions (Region III). Therefore, electrical conductivity can be expressed as dc and ac conductivity as **equation 3.6**. The ω (2πf) and S (0<S<1) are angular frequency and power-law exponent, respectively. The fitting parameter "S" is less than or equal to unity, representing the measure of interaction between the mobile ions and their surrounding lattices.

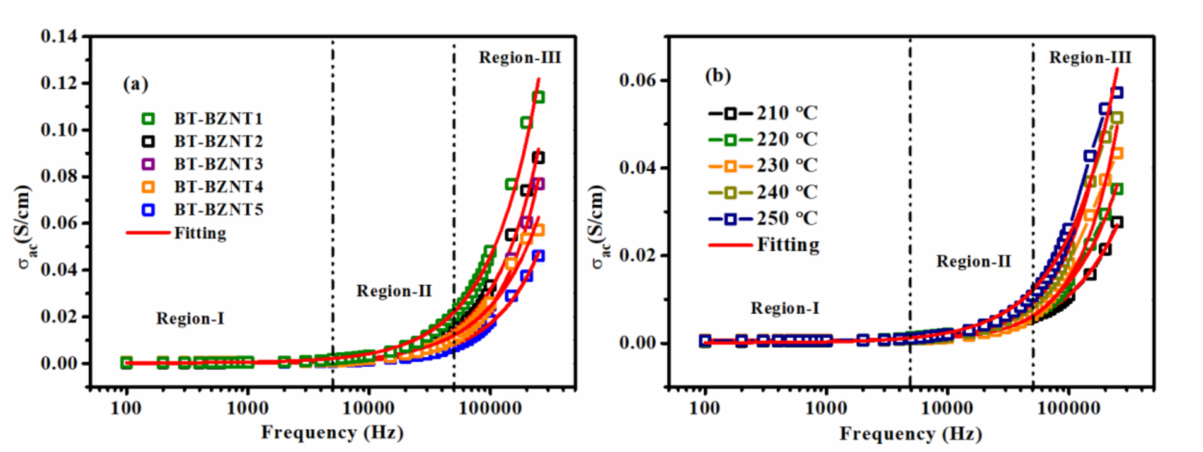

Figure 3. 19: (a) Conductivity versus frequency at 100 kHz frequency for (a) all BT-BZNT ceramics, (b) at different temperatures for BT-BZNT4 ceramics.

The thermal activation energy (E_A) of the synthesized ceramics is estimated using the Arrhenius equation following the relation below:

$$\sigma_{ac} = \sigma_0 exp(\frac{-E_A}{k_B T}) \quad (3.15)$$

here, σ_0 is the pre-exponential factor, T represents the absolute temperature and k_B is the Boltzmann constant. The Arrhenius equation in terms of resistivity (since $\sigma_{ac} = 1/\rho_{ac}$) can be expressed as:

$$\rho_{ac} = \rho_0 exp(\frac{E_A}{k_B T}) \tag{3.16}$$

Figure 3. 20(a-d) shows the ln(ρ_{ac}) versus 1000/T plots for BT-BZNT ceramics in the measuring temperature regime (210-250 °C). Using **equation 3.16**, the value of E_A of the charge carriers is found to be 0.37, 0.42, 0.43, 0.46, and 0.61 eV for BT-BZNT1, BT-BZNT2, BT-BZNT3, BT-BZNT4, and BT-BZNT5 ceramics respectively. With the addition of BZNT, the activation energy of the composition is observed to be increasing at the measured 100 kHz frequency. This suggests the existence of oxygen vacancies and defects in the samples with higher BZNT substitution reduced, further supporting the XPS finding. These activation energy values are similar to the $LiCrP_2O_7$ compound studied below 550 K [149]. However, the estimated activation energy values are less than 1 eV implying the presence of oxygen vacancies due to the relaxation of charge carriers or defects of ions in complexes. At the same time, oxygen vacancies are unavoidable in perovskite oxides under high-temperature sintering conditions. Generally, the charge carriers are not free to contribute band-to-band conduction process at low temperatures, despite hopping from one state to another energetically favored state within the band. This hopping-like conduction may be limited to nearest neighbor hopping (NNH) or variable range hopping (VRH). According to the VRH model proposed by Mott [150], the hopping conduction of the charge carriers follows the relation with the measuring temperature as expressed:

$$\rho_{ac} = \rho_0 \exp(\frac{T_0}{T})^{1/4} \tag{3.17}$$

here, ρ_0 is the pre-exponential factor, and T_0 (equals $16\alpha^3/k_B N(E_F)$) is the characteristic temperature coefficient calculated from the slope following the relation ln(ρ_{ac})

versus $T^{-1/4}$. **Figure 3. 20(a-d)** illustrates the variation of $\ln(\rho_{ac})$ versus $T^{-1/4}$ for BT-BZNT ceramics measured at 100 kHz. The linear straight-line fitting ($R^2 > 0.9$) suggests the validation of the VRH conduction mechanism present in the synthesized samples.

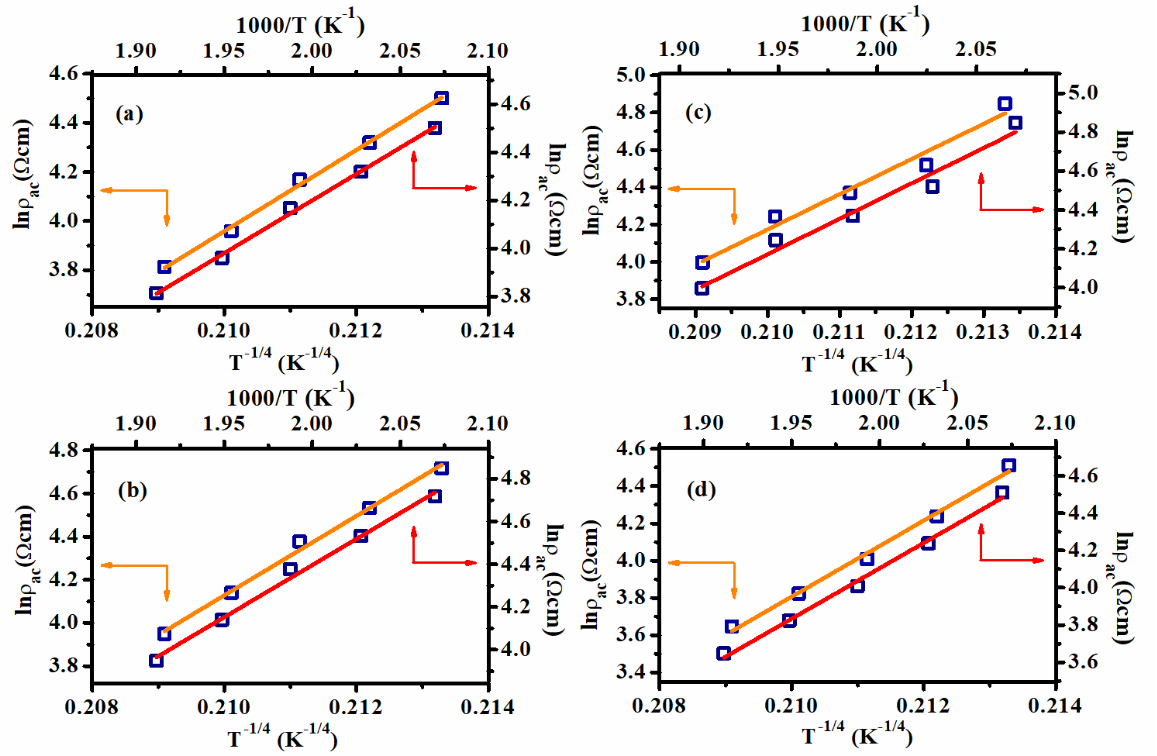

Figure 3. 20: Temperature-dependent electrical resistivity for (a) BT-BZNT1, (b) BT-BNT2, (c) BT-BNT3, and (d) BT-BZNT4 samples with respect to 1/T and $T^{-1/4}$, respectively.

Following **equation (3.17)**, the slope of the $[\ln(\rho_{ac}/\rho_0)]$ vs. lnT curve fitted linearly should be equal to ~ 1/4. Hence, the obtained values of the slope for the BT-BZNT ceramics are nearly found to be -0.25, as shown in **Figure 3. 21(a-d)**, indicating that Mott's VRH model is obeyed in this temperature regime. Again, the density of the localized states at the Fermi level using temperature coefficient (T0) and the inverse localized length of localized states (α) can be expressed by:

$$N(E_F) = \frac{16\alpha^3}{K_B T_0} \tag{3.18}$$

The decay length, ξ (ξ =1/α), can be taken as the distance between the nearest Ti ions and equals 0.40 nm in the case of BTO [151][152]. Hence, the obtained $N(E_F)$ are 3.91×10^{18}, 2.53×10^{18}, 2.27×10^{18}, 1.67×10^{18}, and 1.28×10^{18} eV^{-1} cm^{-3} for BT-BZNT1, BT-BZNT2, BT-BZNT3, BT-BZNT4 and BT-BZNT5 ceramics respectively. The density of states decreased from 3.91×10^{18} to 1.28×10^{18} eV^{-1} cm^{-3} with BZNT substitution from BT-BZNT1 to BT-BZNT5 ceramics and is well agreed with the observed increment of activation energy with BZNT concentration. The similar magnitude of $N(E_F)$ as BT-BZNT ceramics is also seen in Cu and Nb-doped $BaTiO_3$ ceramics [152].

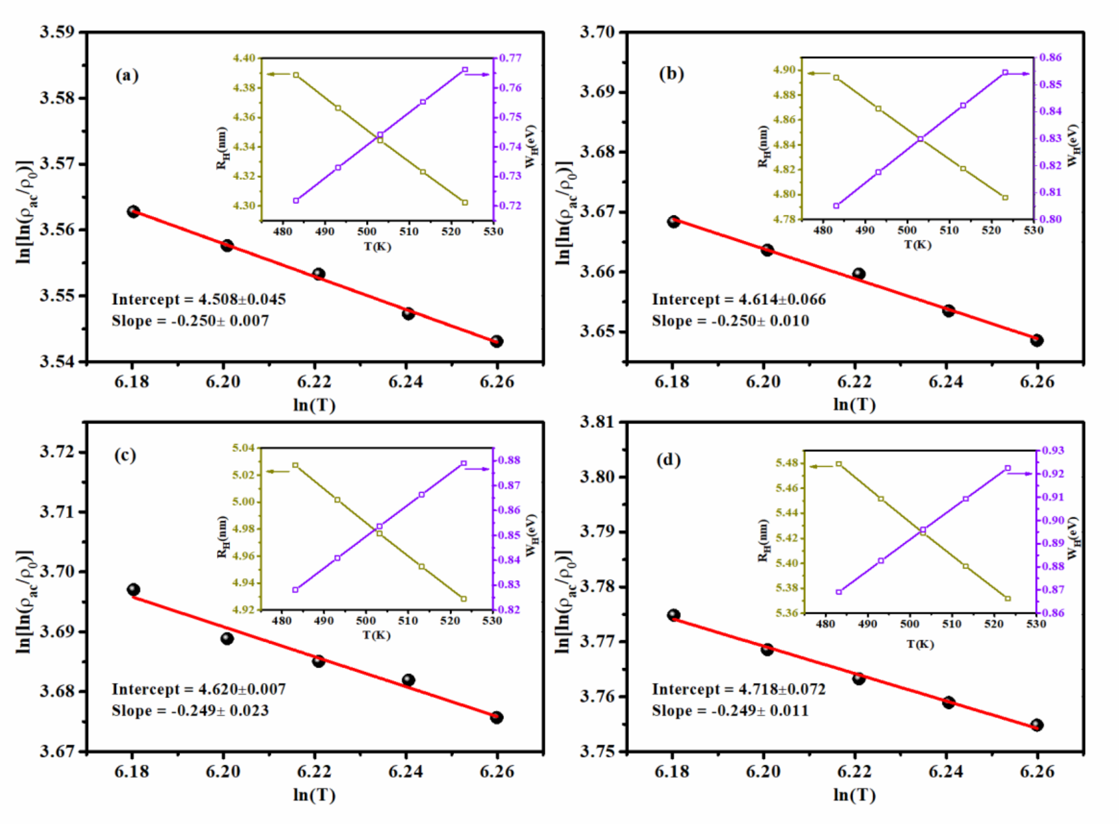

Figure 3. 21: $\ln[\ln(\rho_{ac}/\rho_0)]$ vs. ln(T) and the inset shows the variation of average R_H and average W_H with temperature for (a) BT-BZNT1, (b) BT-BZNT2, (c) BT-BZNT3, and (d) BT-BZNT4 ceramics.

According to Mott's VRH, the average hopping length (R_H) and average hopping energy (W_H) can be expressed as follows:

$$R_H = 0.75 \times [3/(2\pi\alpha N(E_F)K_BT)]^{1/4} \quad (3.19)$$

and

$$W_H = [3/4\pi R_H^3 N(E_F)] \quad (3.20)$$

The R_H and W_H as a function of temperature are depicted in the inset of **Figure 3. 21(a-d)**. With the rising temperature, the average hopping length is found to be decreasing, whereas the average hopping energy is found to be increasing. The estimated R_H value for the BT-BZNT ceramics is almost 10 times larger than the lattice constant, validating the system's VRH transport in the systems [152].

Room temperature ferroelectric hysteresis loop measurements for BT-BZNT ceramics are performed at 10 Hz, and are shown in **Figure 3. 22(a)**. All the samples exhibited well-shaped ferroelectric hysteresis loops up to composition $x = 0.15$, and beyond this composition, the samples exhibited extremely slim hysteresis loops. At the same time, both maximum saturation polarization and remnant polarization drastically reduced with the BZNT substitution. The BT-BZNT1 ceramics can achieve higher maximum polarization up to 30.36 μC/cm^2, which declines to 19.40 μC/cm^2 for BT-BZNT5 samples. The recoverable energy storage density (W_{rec}) and energy efficiency (η) are calculated from the ferroelectric hysteresis curves measured to further reveal the energy storage performance. The achieved W_{rec} and η(%) values for the BT-BZNT ceramics are shown in **Figure 3. 22(b)**. The W_{rec} acquired is 1.48, 1.64, 2.06, 1.82, and 1.70 J/cm^3 for BT-BZNT1, BT-BZNT2, BT-BZNT3, BT-BZNT4, and BT-BZNT5 respectively. Similarly, the obtained η(%) is 60.01, 62.70, 78.21, 94.79, and 96.27% at applied field of 140, 160, 180, 180 and 180 kV/cm respectively. The ultrahigh energy efficiency in the ceramics is attributed to the extremely thin hysteresis loops (low remnant polarization) for higher substituted BZNT samples. The W_{rec} is directly dependent on breakdown strength (E_{BDS}), whereas η(%) is only dependent on the shape of the hysteresis loop and completely independent of E_{BDS} for all investigated ceramics. In the current investigation, the BT-BZNT3 sample exhibited a high W_{rec} of 2.06 J/cm^3 with an energy efficiency of 78% at 180 kV/cm. Still, the BT-BZNT4 ceramic demonstrated excellent energy storage performance among all synthesized samples by achieving a W_{rec} of 1.82 J/cm^3 with extremely high energy efficiency of 95% at 180 kV/cm.

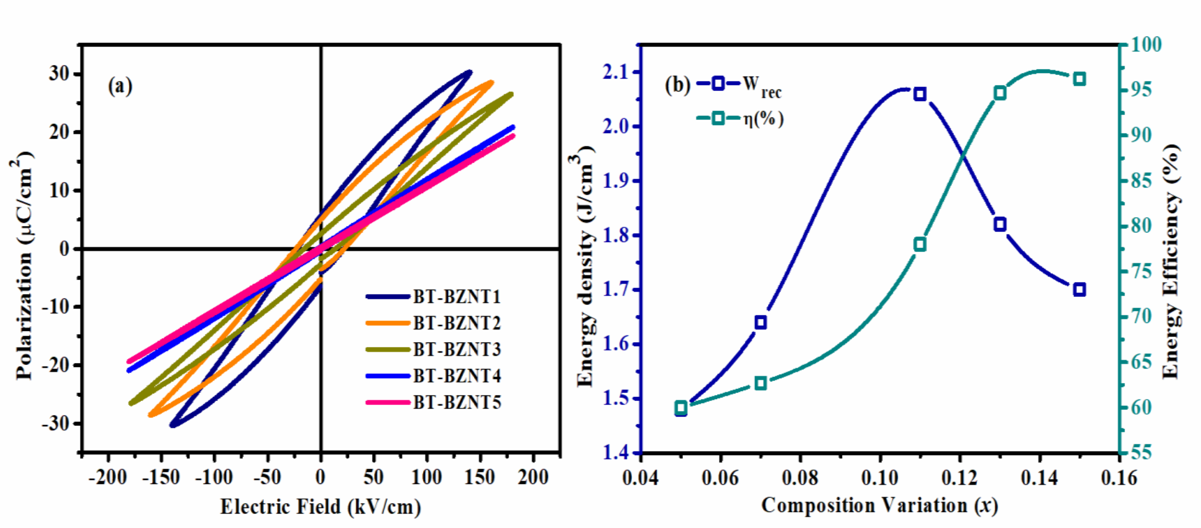

Figure 3. 22: (a) Ferroelectric hysteresis loops measured at RT, and (b) Energy density and energy efficiency for BT-BZNT ceramics.

A detailed comparison of energy storage performance of the $BaTiO_3$-$BiMeO_3$ family with the present study. **Table 3. 7** shows that the listed $BaTiO_3$-$BiMeO_3$ ceramics exhibited quite interesting energy storage performance. It is worth noting that some reports display higher recoverable energy density and efficiency at higher applied fields than the present study. The highly applied field strongly influences the performance of the devices, affecting the supporting insulation of electronic devices, making them unsuitable for general applications in integrated miniaturized portable equipment and wearable electronic device applications [153]. In the present study, BT-BZNT3 and BT-BZNT4 ceramics achieved comparable energy storage performance at a low applied field of 180 kV/cm, demonstrating the excellence of BT-BZNT ceramics over other $BaTiO_3$-$BiMeO_3$ counterparts listed in **Table 3. 7**.

Table 3. 7: Comparison of energy storage performance between the $BaTiO_3$-$BiMeO_3$ family and the current work.

Compositions	***W_{rec} (J/cm^3)***	***η (%)***	***E_{BDS} (kV/cm)***	***Ref.***
BT-0.125BMN	1.89	83	240	[35]
$0.7[0.88BT-0.12Bi(Zn_{2/3}Nb_{1/3})O_3]$-$0.3Bi_{0.5}Na_{0.5}TiO_3$	3.82	94.4	265	[36]
$0.95BaTiO_3$-$0.05Bi(Ni_{2/3}Ta_{1/3})O_3$	0.55	87.15	117	[37]
$0.93BaTiO_3 - 0.07YNbO_4$	0.61	86.8	170	[38]
$0.85BaTiO_3$–$0.15Bi(Mg_{1/2}Zr_{1/2})O_3$	1.25	95.4	185	[39]
$0.85BaTiO_3$–$0.15Bi(Zn_{2/3}Nb_{1/3})O_3$	0.79	93.5	131	[73]
$0.92BaTiO_3$–$0.08Bi(Mg_{1/2}Ce_{1/2})O_3$	1.26	68.5	250	[40]
$0.9BaTiO_3$–$0.1Bi(Mg_{2/3}Nb_{1/3})O_3$	1.13	90	144	[41]
$0.86BaTiO_3$–$0.14Bi(Zn_{1/2}Ti_{1/2})O_3$	0.81	94	120	[42]
0.88BST-0.12BZN	1.62	99.8	225	[43]
$0.85BaTiO_3$-$0.15Bi(Mg_{0.5}Sn_{0.5})O_3$	3.05	95	220	[44]
0.9BT-0.1BMH	3.38	87	240	[45]
$(1-x)BaTiO_3$-$xBi(Mg_{0.5}Zr_{0.5})O_3$	2.9	86.8	220	[46]
0.6BT-0.4BMT	4.49	93	290	[47]
0.85BT-0.15BZS	2.41	91.6	280	[48]
0.85BT-0.15BZNT	2.06	78	180	***This work***
0.80BT-0.20BZNT	1.82	95	180	***This work***

3.5 Conclusions

- Two series (BTBF and BT-BZNT solid solutions) of the $BaTiO_3$-$BiMeO_3$ family have been synthesized using a solid-state reaction route.

- The crystalline phase, microstructure, dielectric, ferroelectric, and energy storage properties are systematically investigated.
- The XRD pattern, the Rietveld refinement, and the Raman analysis confirmed the tetragonal phase for pure BTO, and the phase gradually changes to pseudo-cubic with the addition of BFO for BTBF ceramics. Whereas, the BT-BZNT ceramics displayed a dual phase symmetry with tetragonal (*p4mm*) and rhombohedral (*R3c*) crystal structure.
- The binary solid solutions BTBF and BT-BZNT displayed both types of grains (smaller and larger) resembling a mixture of two different phases. An average grain growth is slightly suppressed with BFO substitution for BTBF ceramics, however, a significant grain growth with dense microstructure is found with the BZNT substitution in BT-BZNT solid solution.
- In the case of BTBF composition: two dielectric peaks around 60 ℃ and 150 ℃ are observed for BTBF1 ceramics, which are believed to be the phase transition peaks for $T_{O\text{-}T}$ and T_C phases. For the other two specimens with higher BFO concentrations, the peaks at a lower temperature almost disappeared. Only the T_C is observed to be shifted from 150 ℃ to 180 ℃ with increasing BFO content. Similarly, for BT-BZNT ceramics, two peaks at ~95°C (T_{m1}) and ~155°C (T_{m2}) are found for the BT-BZNT1 sample, whereas only one diffused peak at higher temperature is observed for higher BZNT concentrations with slight peak shifting towards higher temperature. In both compositions, the dielectric permittivity is found to be the highest for a lower concentration of BFO and BZNT concentrations.
- Further, the ferroelectric studies for both compositions are analyzed to evaluate energy storage performance. The BTBF composition displayed a W_{rec} and η (%) of ~ 40mJ/cm^3 and 60.92% respectively at 25 kV/cm applied field, which is sufficiently lower as compared to other $BaTiO_3$-$BiMeO_3$ systems. However, a significant improvement in energy storage performance is observed in BT-BZNT ceramics. A remarkably high W_{rec} of 2.06 J/cm^3 with

an η(%) of 78% is achieved for BT-BZNT3 ceramics at an applied field of 180 kV/cm. The ultrahigh-energy efficiency of up to 96% is observed for higher concentrations in BT-BZNT ceramics. This improvement in energy storage performance is attributed to the lower oxygen vacancies/defects in the higher BZNT substituted ceramics confirmed through XPS analysis. Therefore, the BT-BZNT ceramics can have potential applications in advanced pulsed power capacitors.

Chapter 4

The development of BLFO thin films for energy storage capacitor applications

The synthesis of BFO ceramic is highly challenging when prepared through a solid-state synthesis route. Hence, this chapter deals with the optimization of pure-phase BFO ceramics. After obtaining the single-phase BLFO bulk ceramics, the BLFO thin films are grown to investigate the energy storage performance at different oxygen partial pressures (OPPs).

4 Optimization of pure phase BFO and development of BLFO thin films

4.1 Introduction

Multiferroic materials belong to the class of materials known for having more than one ferroic property [154]. They simultaneously show ferroelectric and antiferromagnetic behavior in the same phase [155][156][157]. The electric polarization can be reversed with the application of a magnetic field and vice versa in these materials due to coupling between the ferroic orders [155]. The category of material having perovskite structure includes $BiMnO_3$, $TbMnO_3$, $YMnO_3$, and $BiFeO_3$ [158]. $BiFeO_3$ (BFO) is a single-phase multiferroic material known to have the highest T_C (Curie temperature), i.e., 1103 K, and the highest T_N (Neel temperature), around 643 K [159]. It has a rhombohedral distorted perovskite structure with an *R3c* space group [160]. The coexistence of magnetic and electric ordering at room temperature gained the interest of researchers in BFO compounds for their wide range of applications in the field of multifunctional devices such as in spintronics, data storage, and electromagnetic devices [26][27][161]. However, despite having promising properties at room temperature, BFO limits its potential in device application due to high leakage current and secondary phase formation during sintering at high temperatures. This happens because of the volatile nature of Bi, fluctuation of the valence of Fe element, and oxygen vacancies created during the high-temperature sintering process. Therefore, numerous efforts have been made to overcome these limitations and eliminate secondary phase formation such as $Bi_2Fe_4O_9$, $Bi_{25}FeO_{39}$ [162], and $Bi_{25}FeO_{40}$ [163]. Rare-earth ions doping is considered the most effective approach to improve the magnetic and photocatalytic properties of BFO. Lanthanide rare earth elements have similar ionic radii as that of Bi^{3+} ion. Therefore, the dopant is more likely to occupy the A-site replacing Bi^{3+} causing the lattice distortion which effectively tunes the multiferroic properties of BFO [154]. The earlier report suggests that the doping with La^{3+} in the A site of BFO nanoparticles can easily cause the lattice distortion (due to compressive stress) with La (La^{3+} = 1.03Å) substitution in BFO (Bi^{3+} = 1.17Å) [164]. Because of this lattice distortion, there is a change in canting angle between FeO_6 in the octahedral accompanying the structural changes [165]. The substitution of La^{3+} in place of Bi^{3+} improves the crystallinity of the BLFO system and helps reduce the Bi loss during high-temperature sintering [166]. Excess Bi is also added to account for the loss of Bi to suppress the formation of Bi-deficient secondary phases.

Thin films show different exciting properties to their bulk counterparts. In thin films, the surface-to-volume ratio increases, which alters the properties of bulk ceramics. Achieving high-quality thin film is difficult as maintaining stoichiometric is challenging in the BFO system. The deposition pressure, oxygen partial pressures (OPPs), and deposition temperature also play an important role in acquiring the desired properties in thin films [167][168][144]. These parameters influence the film growth rate, stoichiometry, and crystallinity. Introducing the gas (O_2) in the vacuum may lead to the lower kinetic energy of the target material particles resulting in the growth of higher crystalline films. The presence of oxygen in the deposition chamber is necessary for depositing the oxide films using the pulsed laser deposition technique [169]. Acquiring smooth and uniform growth of ZnO film in the presence of an oxygen atmosphere is studied by Hasabeldaim, et al. [170]. The authors have also observed the films grown in Ar and vacuum are rougher than the films grown in an O_2 atmosphere. The plume particles that arrive onto the substrates are expected to have higher energy in the absence of gas, resulting in re-sputtering of the previous film layer, hence the film deposited in a vacuum seems rougher. Another group of researchers found oxygen deficiency in SiO_2 films grown in a vacuum [171]. The substrate temperature may also greatly influences the growth of the thin films as it may affect the aggregation and atomic motion of the crystal [172].

The current study describes the optimization to achieve pure phase bismuth ferrite (BFO) with doping with lanthanum. The optimized $B_{0.993}L_{0.007}FeO_3$ composition is used further to fabricate the monolayer thin films on quartz substrates, and n-type Si, and Pt/Ti/SiO_2/Si (Pt-Si) substrates using the PLD technique. The deposition of BLFO thin films is optimized at different oxygen partial pressures (OPPs) under 15, 20, 25, and 30 SCCM. The effect of OPPs is then studied to observe the multiferroic behavior.

4.2 Bulk ceramic preparation (target preparation) and film deposition:

Analytical grade reagents from M/s Sigma Aldrich, USA (Bi_2O_3, La_2O_3) and M/s JiangXiHaiTe Advance Material, China (Fe_2O_3) are used to prepare $Bi_{0.993}La_{0.007}FeO_3$ (BLFO) composition. The preparation route discussed in **Chapter 2** (section 2.1) is followed to obtain the BLFO powders. Initially, the preparation of BFO is optimized with Bi (0% to 15%) excess addition. Subsequently, the La-doped BFO powders are prepared with an excess 5% Bi addition to compensate for the Bi-loss during the high-temperature sintering process. In this study, a trace amount of La is substituted in the A-site to obtain the pure phase BFO composition and to reduce the effect of secondary phases. Eventually, 0.7% La-doped samples exhibited a single phase, hence, this composition is used for the BLFO target preparation. Using this BLFO target, the thin films are deposited at different OPPs on quartz and the n-type silicon substrate via PLD. The BLFO thin films are deposited at the substrate temperature of 500 °C and kept in a vacuum (~10^{-2} mbar) for 1hr at the same temperature to induce crystallinity. The deposition conditions of the BLFO thin films are listed in **Table 4. 1**.

Table 4. 1: Deposition conditions for BLFO thin film growth by the pulsed laser deposition technique at various OPPs.

Deposition condition	***15 SCCM***	***20 SCCM***	***25 SCCM***	***30 SCCM***
OPPs (SCCM)	15	20	25	30
Base pressure	4×10^{-6} mbar	4×10^{-6} mbar	4×10^{-6} mbar	4×10^{-6} mbar
Deposition pressure	1×10^{-2} mbar	1×10^{-2} mbar	1×10^{-2} mbar	1×10^{-2} mbar
Deposition time	20 min	20 min	20 min	20 min
Laser Energy (Fluence)	80 mJ	80 mJ	80 mJ	80 mJ
Pulse repetition rate	10 Hz	10 Hz	10 Hz	10 Hz
A substrate to target distance	5 cm	5 cm	5 cm	5 cm
Laser Type	Nd: YAG	Nd: YAG	Nd: YAG	Nd: YAG
wavelength	355 nm	355 nm	355 nm	355 nm

4.3 Results and Discussion:

Figure 4. 1(a) shows the XRD spectra for all La-doped BFO ceramics prepared with the addition of excess Bi from 0% to 15%. The experimentally recorded XRD pattern of the samples is scanned in the range of 2θ varies from 20º to 80º with Cu-Kα radiation (λ = 1.5406 Å). As Bismuth oxide is volatile, extra Bi_2O_3 is added to the sample to compensate for the loss of Bi. To optimize the addition of excess Bi, the ceramic with various Bi_2O_3 concentrations (x = 0%, 5%, 10%, 15% excess Bi) is added to the composition. The Bi deficient secondary phases such as $Bi_2Fe_4O_9$ (assigned ♠) and $Bi_{25}FeO_{40}$ (assigned ♣) are observed for 0% excess Bi_2O_3 added BFO ceramics due to Bi loss during high-temperature sintering. The sample with 5%

excess Bi_2O_3 showed a single phase with a trace amount of impurity phase. After the addition of 10% and above excess Bi_2O_3, the extra weak reflection corresponding to Bi-rich secondary phase Bi_2O_3 (assigned ♥) indicates the phase segregation at the grain boundaries [173]. Therefore, 5% excess Bi has been added to prepare La-doped $BiFeO_3$ ceramics to compensate for Bi loss during the sintering.

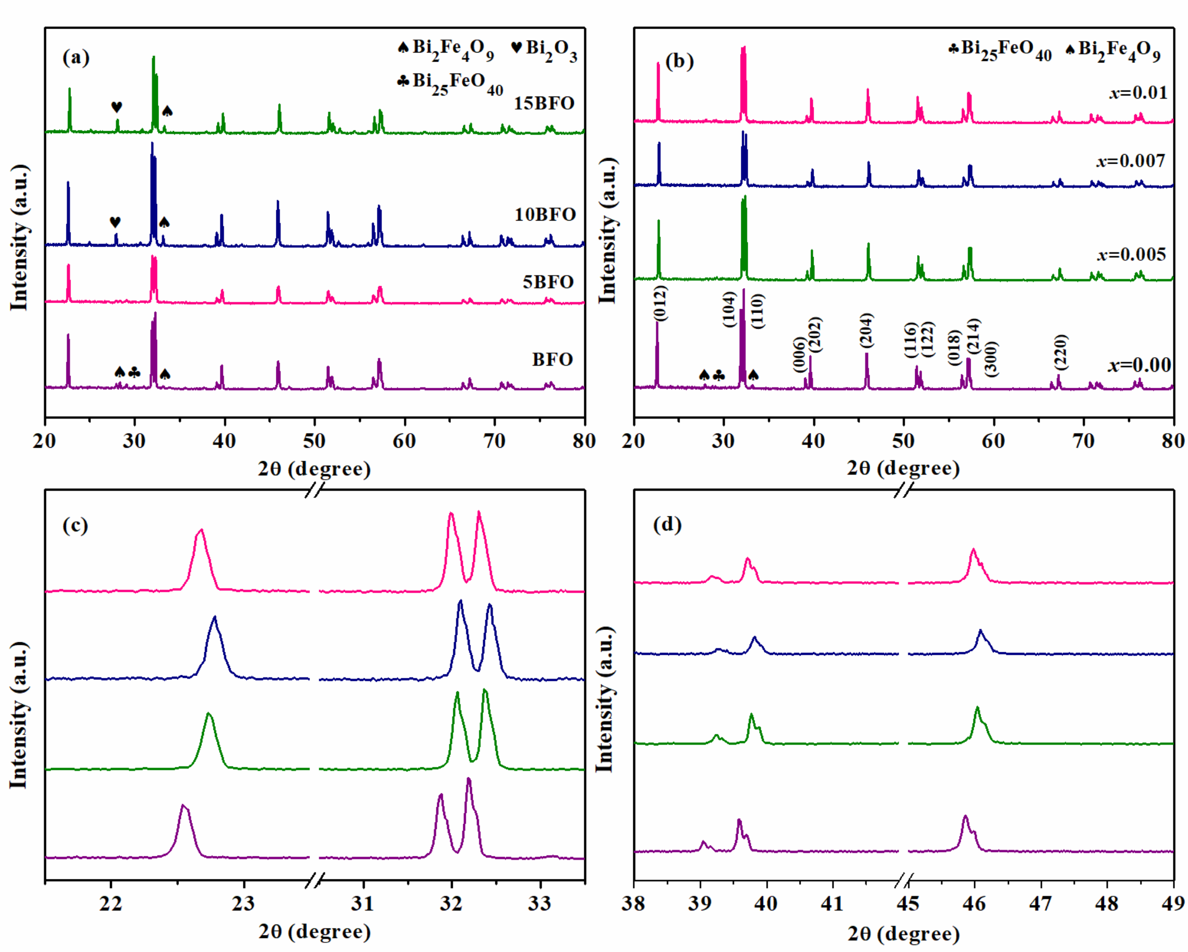

Figure 4. 1: (a) XRD pattern with varying excess Bi content (0%, 5%, 10%, and 15%) (b) XRD patterns of La-doped $BiFeO_3$, sintered at 800°C for 30 minutes (c) Zoomed region corresponding to diffraction angle 2θ ~22° and 32° and (d) 2θ ~39° and 45°showing peak shifting.

The room temperature XRD patterns are recorded to obtain the structural information of La-doped $BiFeO_3$ ceramics shown in **Figure 4. 1(b)**. All significant peaks are indexed by characteristics peaks of BFO (JCPDS No. 00-066-0439) with distorted rhombohedral phase with *R3c* space group. The corresponding peak also matches with the values of reflection reported for JCPDS card No. 71-2494 [159]. A minute amount of the secondary phase of $Bi_2Fe_4O_9$ and $Bi_{25}FeO_{40}$ along with the primary phase is observed for $BiFeO_3$ ceramics [174]. The major diffraction peaks with La-doped samples at 2θ ~32°, 39°, and 45° shifted to a higher angle for x= 0.00 to 0.007. Then these peaks are shifted to the left (lower angle) for $x = 0.01$ and $x = 0.03$, as shown in **Figure 4. 1(c-d)**. The shifting of diffraction peaks to a higher Bragg angle is a consequence of the difference in ionic radii of La^{3+} (1.03 Å) and Bi^{3+} (1.17 Å). The difference in ionic radii creates the (compressive stress/strain) lattice distortion in the rhombohedral structure of BFO with the substitution of La ion [175]. However, in the samples with concentration $x = 0.01$ and above, the impurity phase of La_2O_3 appears. The appreciable shifting of diffraction peaks toward the lower angle indicates the induced stress attributed to increasing La content. Furthermore, no phase transition is observed for all the ceramics.

The XRD patterns of the BLFO films deposited at different OPP variations are shown in **Figure 4. 2(a)**. All films show a pure perovskite phase with no trace of an impurity phase. There is a slight difference in thin films with the OPP variation. Only the intense diffraction peak is observed for the film deposited for 20 SCCM. The diffraction peak of the films is matched with the JCPDS card no 00-066-0439 and indexed with the rhombohedral structure with the *R3c* space group. Furthermore, the Rietveld refinement of the XRD pattern is performed using FullProf software, and the diffraction peak profiles are fitted with a pseudo-Voight function. **Figure 4. 2(b)** represents the refined pattern for the film deposited at 20 SCCM, and the inset figure represents the crystal structure of the BLFO system. The inset image represents all the atoms in the system in stoichiometric ratio and occupying the respective positions. **Figure 4. 2(b)** presents the lattice parameters obtained after refinement.

Figure 4. 2(c-d) shows the TEM-analyzed micrographs of BLFO thin films deposited at 20 SCCM OPP.

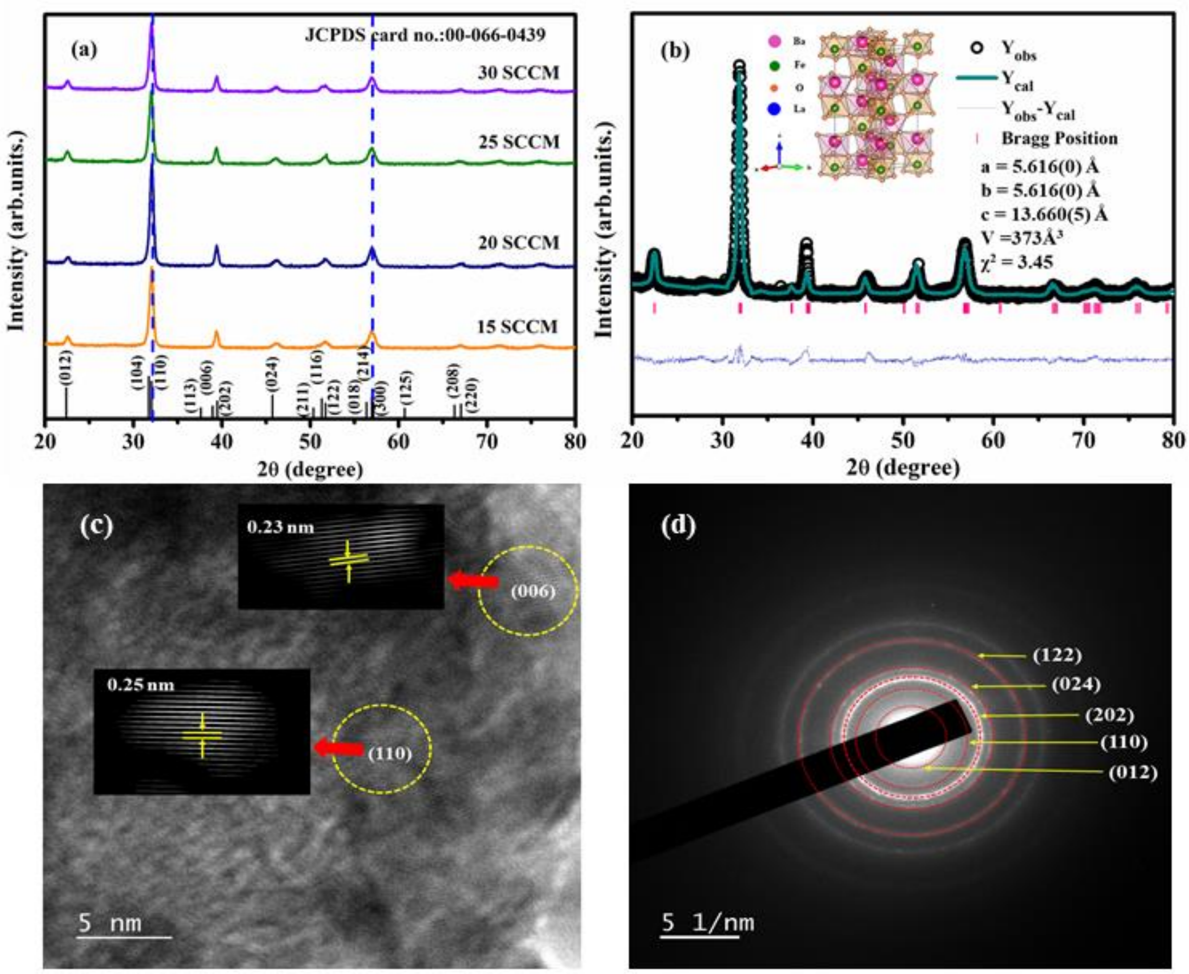

Figure 4. 2: (a) Experimentally obtained XRD pattern for BLFO thin films at different OPPs, (b) The XRD Rietveld refinement results of the BLFO thin films deposited at 20 SCCM. The inset illustration presents the generated crystal structure of the BLFO system, (c) an HRTEM image confirming the crystal planes, and (d) the SAED pattern obtained from FETEM analysis.

Figure 4. 2(c) shows a high-resolution TEM image of the BLFO crystallites. The inset image in **Figure 4. 2(c)** shows the inverse Fast Fourier transform (FFT) of BLFO crystallites. Using ImageJ software, the inverse FFT is used to plot the profile to estimate the interplanar

distance. An atomic plane with an inter-planar distance of 0.25 nm and 0.23 nm is estimated and is indexed to (110) and (066) planes, respectively. **Figure 4. 2(d)** represents the (selected area electron diffraction) SAED pattern for the same film. The image shows bright fringes representing each of the lattice plane characteristics of the BFO crystal structure. Bright concentric fringes reveal that the film is well crystalline, with prominent fringes representing the corresponding plane of the BLFO system. The d-spacing and the crystal planes obtained via SAED analysis well match the d-spacing and plane obtained via HRTEM analysis. The d-spacing and crystal plane estimated using HRTEM and SAED pattern is verified with the JCPDS card assigned to rhombohedral BFO with space group *R3c*.

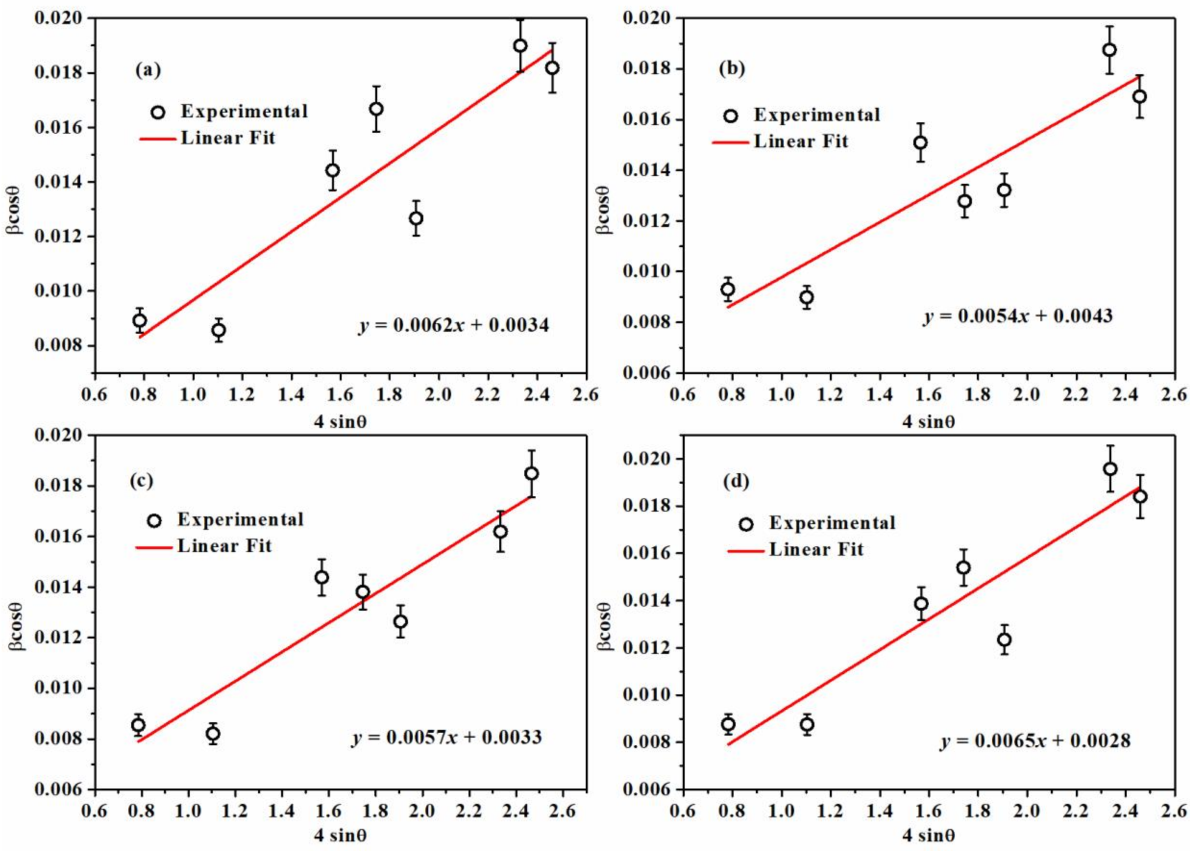

Figure 4. 3: Williamson-Hall plots of BLFO thin films, deposited at different OPPs.

The Williamson-Hall (W-H) method is used to calculate the crystallite size and strain in the deposited films at different OPPs [176]. The crystallite size and microstrain of the films are deduced from **equation 3.12**. The W-H plot with straight lines with Y-intercept (kλ/D) and slope (ε) are shown in The crystallite size and microstrain have been estimated from intercept and slope and are presented in **Table 4. 2**. It is worth noting that the film deposited at 20 SCCM has the minimal strain; further, the strain is found to be improved for 30 SCCM deposited films. Similarly, the crystallite size for the same film is found to be the lowest among the deposited films. However, an improvement in crystallite size is observed with the increasing OPPs. After crystal structure verification and lattice parameter information, the surface morphology and topology of the films are examined using FESEM micrograph and atomic-force microscopy (AFM) imaging. The correlation between RMS roughness and grain growth with the OPPs variation is studied further.

Table 4. 2: Lattice parameters, lattice volume crystallite size, and microstrain of BLFO films.

OPPs	*a=b (Å)*	*c (Å)*	*V(Å³)*	*Crystallite size (nm)*	*Strain*
15 SCCM	5.612(0)	13.655(0)	372.53(16)	42.46	6.2×10^{-3}
20 SCCM	5.616(0)	13.660(4)	373.15(13)	33.29	5.4×10^{-3}
25 SCCM	5.615(0)	13.685(6)	373.69(16)	43.10	5.7×10^{-3}
30 SCCM	5.617(0)	13.704(6)	374.49(17)	51.17	6.5×10^{-3}

Figure 4. 4(a-d) represents the FESEM images of BLFO thin films deposited at different OPPs. All the deposited films exhibited spherical grains with homogeneous microstructure. It can be noticed that the increase in oxygen content amount facilitates grain growth in the films. Enhanced grain growth with increasing oxygen pressure is observed for the films deposited at different deposition conditions. The film deposited at 20 SCCM showed uniform, compact, and dense morphology. To check the surface morphology and roughness, the AFM image of BLFO thin film has been imaged for an area of 2×2 μm. The 3D pictorial

representation for the atomic forced microscopy images has been shown in the inset of **Figure 4. 4(a-d)**.

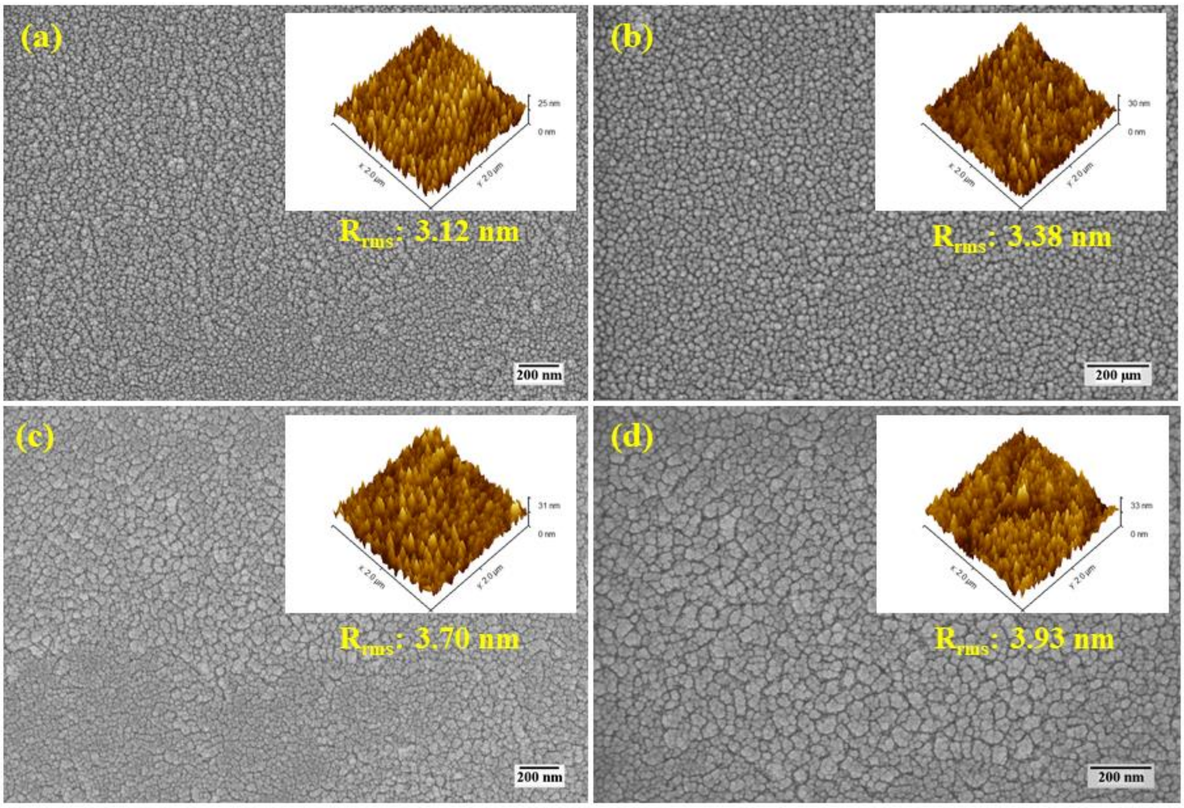

Figure 4. 4: FESEM micrograph of (a) 15 SCCM, (b) 20 SCCM, (c) 25 SCCM, and (d) 30 SCCM deposited BLFO thin films. Insets of **(a)**, **(b)**, **(c)**, and **(d)** represent the respective AFM 3D images.

The images show the uniform growth of all the films for all the deposited conditions. The films' RMS roughness of the films is calculated using the Gwyddion software. The RMS roughness for all the films is 3.12, 3.38, 3.70, and 3.93 nm, respectively. The measured roughness of the films is well-matched with the profilometer-obtained results, which are nearly 5 nm average roughness. It can be inferred that the grain growth and roughness in the films are improved with increasing OPPs. It is worth correlating the grain growth and surface roughness with OPPs. On the other hand, it can be inferred that a rough surface develops more nucleation sites resulting in grain growth [87].

With increasing OPPS, the film's thickness enhancement is also observed and confirmed through FESEM cross-section images. The cross-sectional FESEM images of BLFO thin films with OPPs variation are presented in **Figure 4. 5(a-d)**. The films' estimated thickness is approximately 200 ± 10 nm, which agrees well with the thickness measured using a profilometer. In addition, a relatively compact and dense microstructure in depth is revealed for 20 SCCM films.

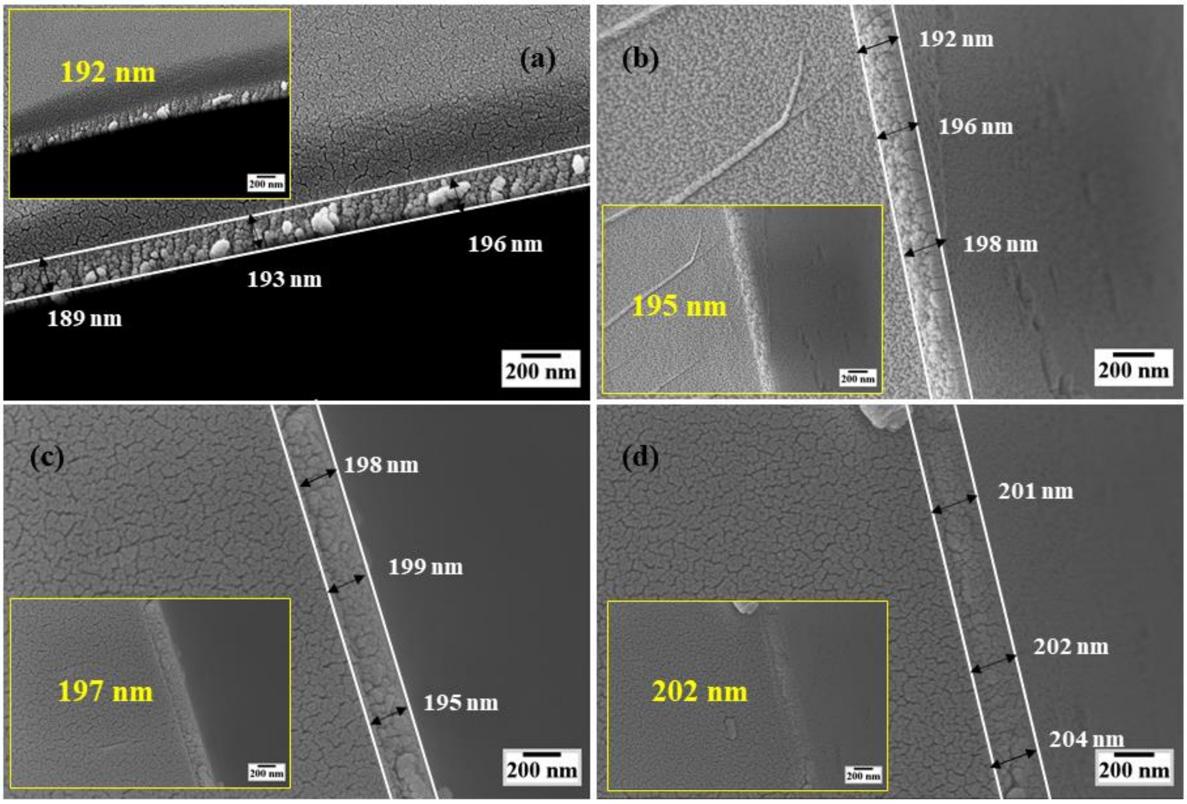

Figure 4. 5: Cross-sectional FESEM images of (a) 15 SCCM, (b) 20 SCCM, (c) 25 SCCM, and (d) 30 SCCM deposited BLFO thin film with well distinct and smooth grain growth of each film with nearly 200 nm.

After crystal structure and microstructural analysis, the electronic structure of BLFO film deposited at 20 SCCM is analyzed via X-ray photoelectron spectroscopy (XPS). This technique is used mainly to determine the surface chemical state of the elements present in the film. XPS measurement mainly studies the thin surface's Bi and Fe chemical state. The binding energy of the XPS spectra is calibrated using the C1s (285.44eV). **Figure 4. 6(a-d)** shows the fitted high-resolution spectra of Bi 4f, La 3d, Fe 2p, and O 1s core level state for BLFO thin film. **Figure 4. 6(a)** displays the XPS Bi 4f spectrum representing two peaks at 163.04 eV and 157.74 eV corresponding to Bi $4f_{5/2}$ and Bi $4f_{7/2}$ assigned to Bi-O bonds. The spin-orbit splitting between these two peaks is estimated to be approximately 5.3 eV, confirming the trivalent oxidation state of Bi ion [177]. The peak positions of Bi $4f_{7/2}$ and Bi $4f_{5/2}$ and their difference between the BEs agree with the earlier study [178]. **Figure 4. 6(b)** shows the La 3d peaks with minute intensity due to the low content of the La element in BLFO film. However, the La 3d core energy level is deconvoluted to see the sub-peaks at 836.85 and 833.20 eV belonging to the La $3d_{5/2}$ peak [179]. The other two peaks that appear at 844.79 and 842.01 eV are assigned to the satellite peak of La $3d_{5/2}$ peak. Meanwhile, the peak at higher binding energy corresponding to $La3d_{3/2}$ peaks is undetected. Further, the Fe2p peaks are deconvoluted by two sets of sub-peaks assigned to Fe^{2+} and Fe^{3+}, as shown in **Figure 4. 6(c)** An oxygen deficiency is responsible for the combination of Fe^{3+} and Fe^{2+} ions. The presence of oxygen vacancies results in the transition of $Fe^{3+} \rightarrow Fe^{2+}$ described with equation [145][180][181]:

$$2Fe^{3+} + O^{2-} \rightarrow 2Fe^{2+} + V_O^{2+} + \frac{1}{2} O_2 \qquad (4.1)$$

The appearance of oxygen vacancies and Fe^{2+} ions simultaneously occurs for charge compensation in the BFO system [182]. Fe^{2+} components are indexed at 708.74 and 721.65 eV, whereas Fe^{3+} components appeared at peak positions at 710.10 and 722.56 eV. The component of Fe^{2+} and Fe^{3+} belonging to $Fe2p_{3/2}$ peak and $Fe2p_{1/2}$ appears at (708.74, 710.10 eV) and (721.65, 722.56 eV), respectively. A pair of satellite peaks belonging to Fe^{2+} and Fe^{3+} are observed to appear at 716.75 and 717.58 eV [183]. The Fe peak spectra fitted for Fe 2p core level reveal that Fe exists in Fe^{2+} and Fe^{3+} in BLFO thin film. For O1s, two peaks are observed at 529.87 and 531.98 eV. One peak corresponds to cation-oxygen (lattice oxygen) bonding indicated by dark cyan color, and the other peak corresponds to oxygen vacancies (O defects) [183] shown in orange color in **Figure 4. 6(d)**. Hence, the existence of Fe^{2+} with oxygen vacancies/defects is confirmed via XPS analysis.

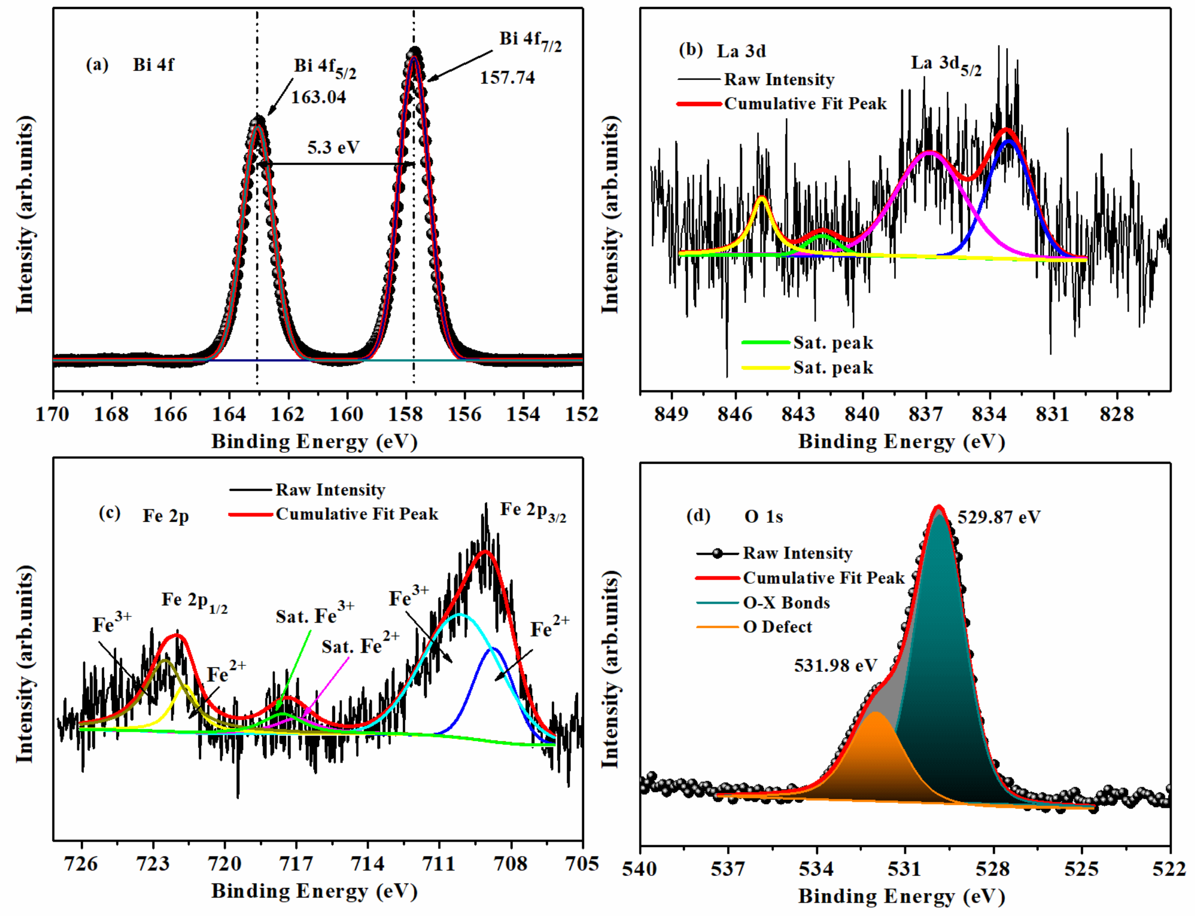

Figure 4. 6: High-resolution fitted XPS spectra for (a) Bi 4f, (b) La 3d, (c) Fe 2p, and (d) O 1s core level state for BLFO thin film, deposited at 20 SCCM.

The dielectric behavior with varying frequencies of the films is displayed in **Figure 4. 7(a-b)**. The dielectric response of the films is measured as a function of frequency (10^3–10^6 Hz) at RT to see the behavior of the film deposited at different oxygen ambiances. There is a slight variation of dielectric constant and tanδ with variation in OPPs. As expected, the dielectric constant and tanδ are observed to decrease with frequency for all films. The BLFO films deposited at 20 SCCM revealed a higher dielectric constant of 447 and lower tanδ of 0.202 at 1 kHz among the deposited films, as summarized in **Table 4. 3**.

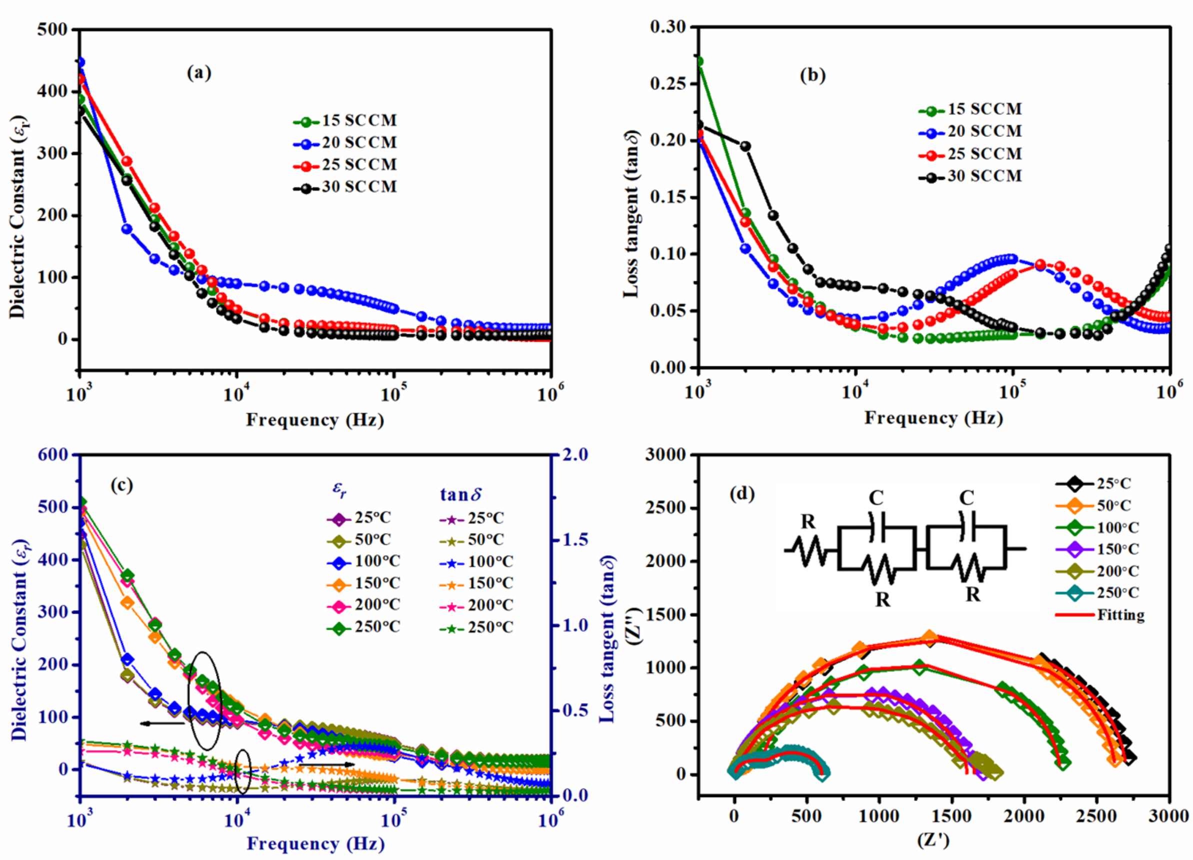

Figure 4. 7: (a) Dielectric permittivity and (b) dielectric loss of BLFO films as a function of frequency at different OPPs, (c) temperature-dependent dielectric plots, and (d) Nquist plot for 20 SCCM deposited BLFO thin films.

The RT value obtained for dielectric permittivity for BLFO films is much higher than those reported in the literature [145][184]. It is worth noting the value of the dielectric permittivity at low-frequency regions is higher than that at relatively higher frequencies. Generally, the dielectric permittivity is high at low frequencies due to the potential barrier from the space charge polarization at the grain boundaries. Accumulating charges at grain boundaries leads to high dielectric permittivity in the material. Reducing space charge polarization at high frequency results in low dielectric permittivity values. At the same time, a high value of tanδ at low frequency is observed, which may be due to space charges in the interface of the films. Herein, for each film, the decrease in tanδ is observed up to 10^4 Hz, and then it increases when the frequency exceeds 10^4 Hz. Beyond 10^5 Hz, the rise in tanδ is significant again. In the present study, the tanδ includes three parts: polarization, conduction, and resonance loss. The leakage current dominates in lower frequencies, whereas polarization relaxation governs in higher frequency regions [185]. The dielectric studies obtained for BLFO thin films are superior to the values reported in earlier studies [186][187].

Table 4. 3: Dielectric response of all the deposited films at room temperature and measured at 1 kHz.

Deposition condition	***Dielectric constant (ε_r)***	***Dielectric loss (tanδ)***
15 SCCM	387	0.269
20 SCCM	447	0.202
25 SCCM	420	0.206
30 SCCM	368	0.214

Figure 4. 7(c) displays the temperature-dependent dielectric response of 20 SCCM deposited film from RT to 250°C at a frequency range of 10^3–10^6 Hz. The dielectric permittivity is expected to rise with an increment in temperature up to the phase transition temperature known as Curie temperature. As BFO systems are known to have higher Neel temperature (T_c ~ 370 °C) and Curie temperature (T_c ~ 830 °C), the dielectric constant is observed to rise with temperature in the plotted curve. Furthermore, tanδ first appears to decrease up to 10^4 Hz for all temperature differences. Beyond 10^4 Hz, the rise in tanδ is observed again as the film's charge carriers cannot follow the rapidly varying external electric field. **Figure 4. 7(d)** depicts the complex impedance spectrum (Z" vs. Z') for wide temperature

differences from 25 to 250 °C. The Debye type relaxation governs the relaxation process if the impedance spectra are a perfect semi-circle. On the other hand, if the impedance spectra exhibit asymmetric and depressed semi-circle plots indicates the existence of non-Debye-type relaxation in the material. The spectra of Z" vs. Z' with frequency is fitted with ZSimpWin software. The thin film's dielectric response is modeled with an equivalent circuit comprising two parallel RC circuits in series followed by an additional resistance, R. The simulated data are well-fitted with the experimental data implying the contributions from grain, grain boundaries, and electrodes. The first (R_g, C_g) circuit describes the grain contribution, while the second (R_{gb}, C_{gb}) circuit corresponds to the grain boundary contribution [188]. The R represents the electrode resistance and is comparatively small. The equivalent modeled circuit is shown in the inset of **Figure 4. 7(d)**, and the expression of the total impedance can be given as follows

$$Z_{tot} = Z_g + Z_{gb} + R \tag{4.2}$$

The low-frequency response can be seen from grain boundaries and electrode contribution, while the high-frequency response corresponds to grain contribution in the sample. The fitted parameters for the Nyquist plot at different temperatures are obtained from the modeled series RC circuit in **Table 4. 4**.

Table 4. 4: The obtained parameters for Cole-Cole plots measured at different temperatures.

Parameters	**C_g (F)**	**R_g (Ω)**	**C_{gb} (F)**	**R_{gb} (Ω)**	**R (Ω)**
25 °C	3.008E-8	2590	6.932E-9	192	4.18
50 °C	3.072E-8	2518	6.964E-9	182	4.45
100 °C	6.213E-9	2137	5.400E-8	106	4.22
150 °C	5.979E-9	2050	3.486E-8	103	5.42
200 °C	8.808E-9	1588	1.546E-8	92	6.62
250 °C	9.348E-9	1502	1.422E-8	56	7.94

Room temperature ferroelectric hysteresis studies are obtained at 100 Hz by varying the applied electric field. With the application of an electric field, the maximum polarization tends to increase for all deposited films and is depicted in **Figure 4. 8(a-d)**. The curves obtained for the different fields at room temperature showed well-shaped ferroelectric hysteresis loops for all films. Slim hysteresis loops with maximum polarization are obtained for the film deposited at 20 SCCM. Considering the obtained hysteresis loop parameters, the energy storage performance of the thin films is evaluated following the equations mentioned in **equations (3.10)** and **(3.11)**. The energy stored density (W), the recoverable energy storage density (W_{rec}), and energy efficiency (η) can be calculated using **equations (3.9)**, **(3.10)**, and **(3.11)** from the polarization-electric field (P-E) hysteresis loops curve [131][189].

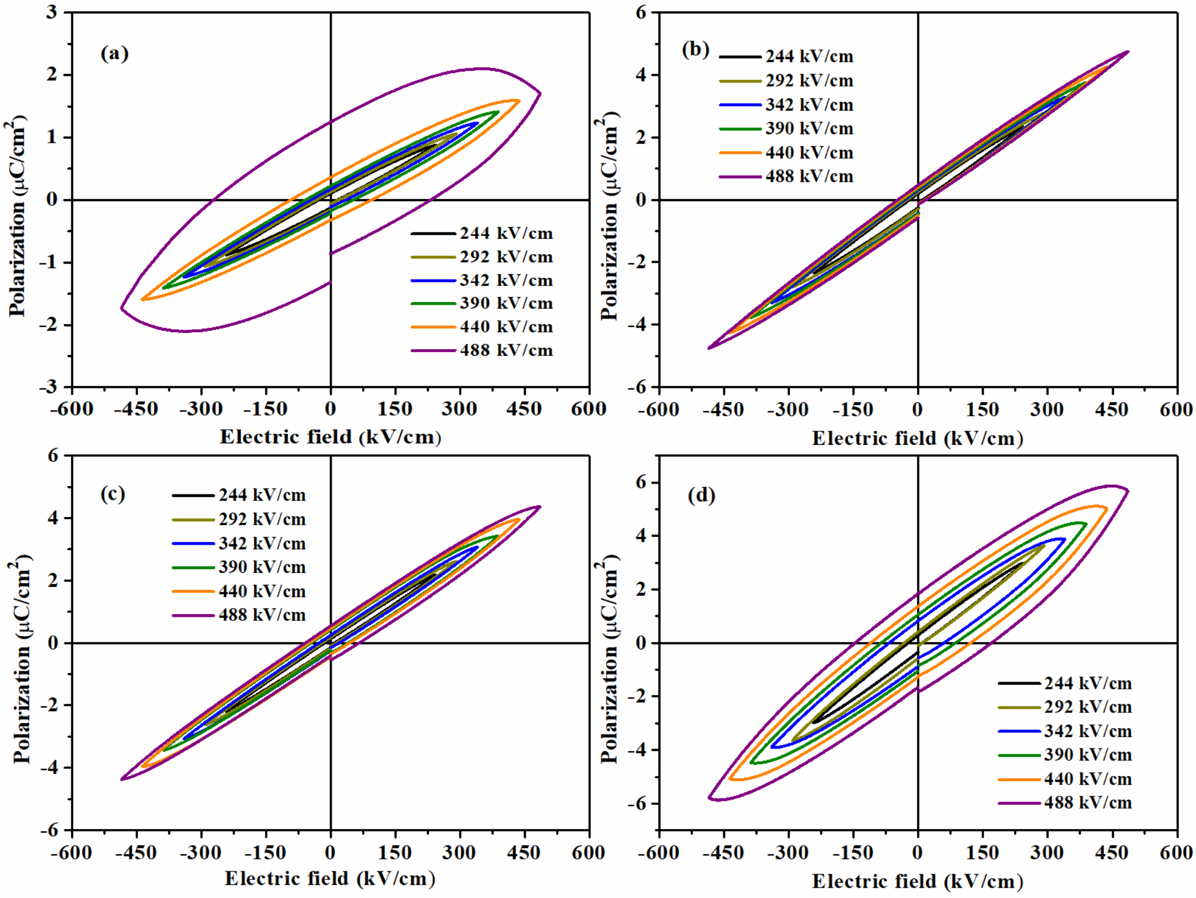

Figure 4. 8: Ferroelectric hysteresis loops for (a) 15 SCCM, (b) 20 SCCM, (c) 25 SCCM, and (d) 30 SCCM measured at RT.

Values obtained from ferroelectric hysteresis loops, energy storage density, and energy efficiency calculated from P-E loops for the films have been summarized in **Table 4. 5**. The values obtained from P-E hysteresis loops for BLFO films are superior to those reported in the previous studies [176][190]. The film's improvement in energy storage performance is also observed compared to reported studies on energy storage performance [87].

Table 4. 5: Key parameters obtained from ferroelectric hysteresis loops.

OPPs	P_{max} ($\mu C/cm^2$)	P_r ($\mu C/cm^2$)	E_{BDS} (kV/cm)	W_{rec} (J/cm^3)	η (%)
15 SCCM	1.7	1.26	488	0.22	21.08
20 SCCM	4.8	0.51	488	2.09	78.42
25 SCCM	4.4	0.56	488	1.85	64.24
30 SCCM	5.7	1.85	488	1.87	47.40

The absorption spectra and bandgap energy estimated for BLFO thin films grown on an amorphous SiO_2 substrate are shown in **Figure 4. 9(a-b)**. According to the inter-band absorption theory, the optical band gap of the films can be calculated using Tauc's equation [191][180][192]:

$$\alpha h\nu = A(h\nu - E_g)^n \tag{4.3}$$

where α is the adsorption coefficient, hν is photon energy, A is constant, E_g denotes bandgap energy, and n represents the transition coefficient with values 1/2 and 2 for direct and indirect, respectively [191].

Figure 4. 9(b) shows the direct bandgap curve extrapolated from the linear portion of $(\alpha h\nu)^2$ versus photon energy ($h\nu$). The values of bandgap energies obtained for BLFO thin films match well with the earlier reported values of bandgap energy of ~2.8 eV of BFO films [191][192][193][194]. It is observed that the bandgap for the film deposited at 20 SCCM showed a low value of 2.74 eV, and it rises with further increasing OPPs. **Figure 4. 9(c)** shows

the films' corresponding optical transmission spectra. The films exhibited the optical spectra of around 70-96% of transmission in the visible region. The observed transmission is relatively high, confirming the films' low roughness and homogeneous growth. **Figure 4. 9(d)** represents the refractive index of the films derived from transmission spectra using the envelope methods of Swanepoel as discussed in **Chapter 2**.

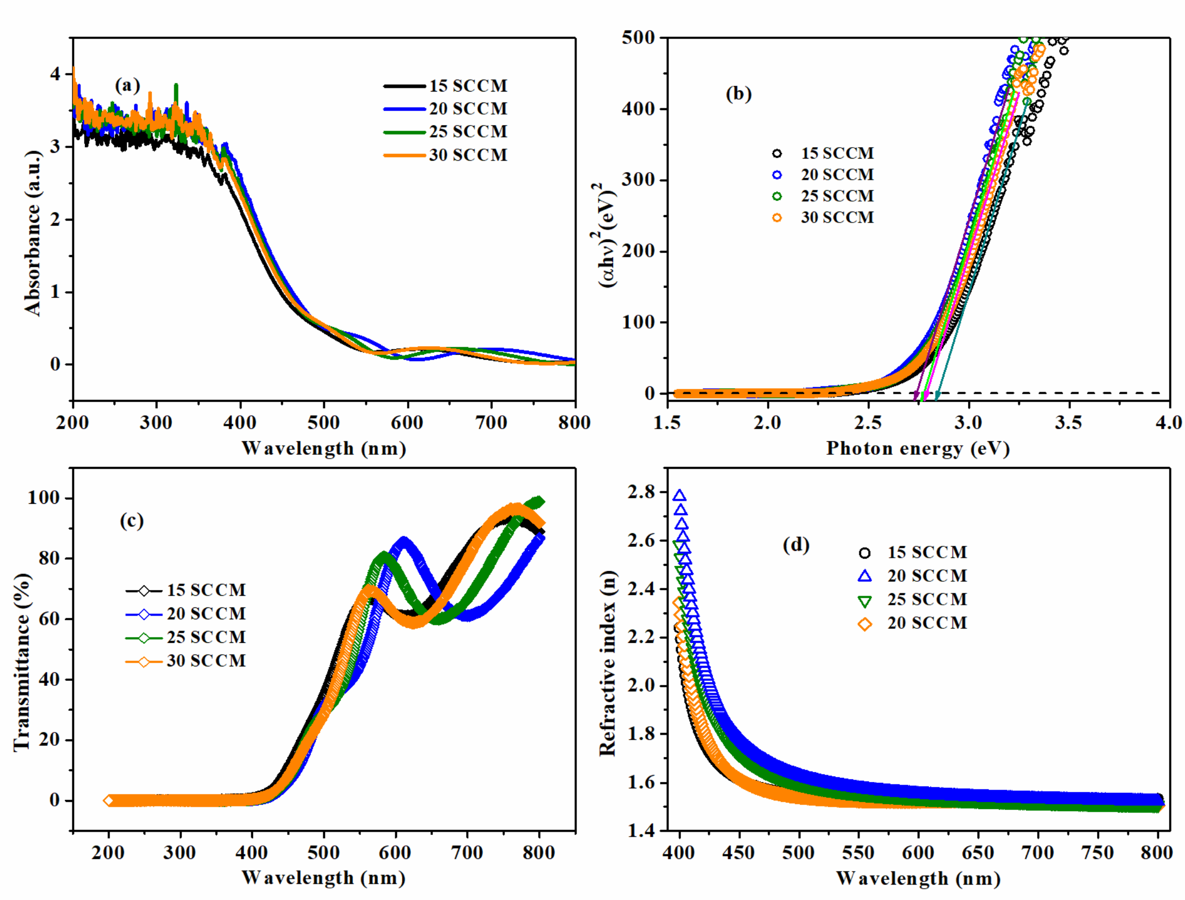

Figure 4. 9: Optical properties of BLFO thin films (a) absorption spectrum and (b) Tauc plots, (c) transmission spectra, and (d) refractive index for BLFO films at various deposition conditions.

The estimated film thickness, refractive index, and bandgap energy for the film are presented in **Table 4. 6**. The thickness of the films calculated is approximately 200 nm for all deposition conditions and agrees well with the results obtained from the profilometer. The refractive index value of the film deposited at 20 SCCM is 2.78 at 450 nm, and it starts declining with the increase in OPPs. The high value of the refractive index for 20 SCCM film indicates the increase in the material density of the film as the material density is proportional to the refractive index [191]. The refractive index of the BLFO films is comparable to those reported in earlier studies [195] but smaller than the values reported by L. Bi et al. [196]. The lower bandgap energy and higher refractive index for the 20 SCCM film indicate the better crystallinity of film among the deposited films [195]. Hence, the relatively high value of the refractive index may be correlated with higher crystallinity (high intense diffraction peaks) and dense microstructure, as suggested by the XRD pattern and AFM images.

Table 4. 6: Thickness, $n_{f,}$ and bandgap energy estimated using optical spectra

OPPs	*Thickness (nm)*	*(n_f) at 450 nm*	*Bandgap energy (eV)*
15 SCCM	202	2.24	2.81
20 SCCM	188	2.78	2.74
25 SCCM	196	2.58	2.77
30 SCCM	210	2.34	2.79

The leakage current density (J) of BLFO thin films deposited at different OPPs as a function of the electric field measured at RT is shown in **Figure 4. 10(a)**. All deposited films exhibited almost symmetric behavior under positive and negative electric fields (±500 kV/cm). The rise in J value is observed with the increasing applied field; still, the saturation is not achieved even at the higher applied electric field of 500 kV/cm. The leakage current density of the deposited BLFO thin film at 15 SCCM is ~8.34×10^{-7} A/cm^2 at 100 kV/cm electric field. Interestingly, leakage current density decreases substantially to 1.08×10^{-7} A/cm^2 for 20 SCCM deposited films. With a further increase in oxygen ambiance (for 25 and 30 SCCM deposited films), a significant rise in leakage current density is observed. It is intriguing to note that the leakage current density of 20 SCCM deposited films exhibited lower J values of ~1.08×10^{-7},

2.20×10^{-6}, and 3×10^{-5} A/cm^2 at an applied field of 100, 250, and 500 kV/cm respectively among the deposited films.

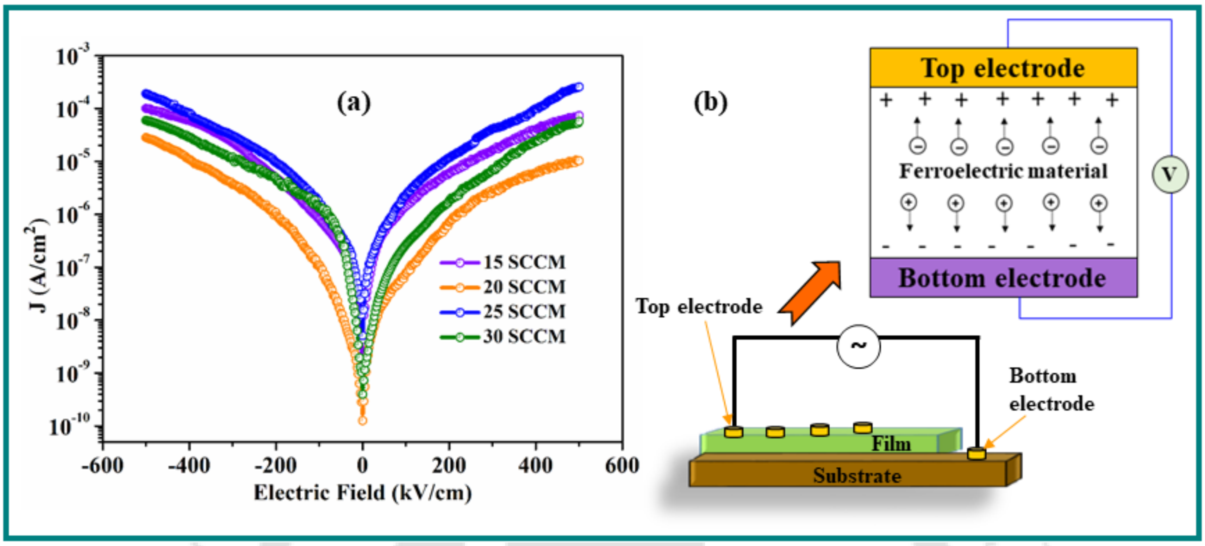

Figure 4. 10: (a) Current density and electric field characteristics of BLFO thin films deposited at various OPPs, (b) Schematic illustration of the MFM capacitor configuration of Al/BLFO/Al.

Table 4. 7: The value of leakage current density at different applied fields.

OPPs	***@± 100 kV/cm (A/cm²)***	***@± 250 kV/cm (A/cm²)***	***@± 500 kV/cm (A/cm²)***
15 SCCM	8.34×10^{-7}	1.14×10^{-5}	8.87×10^{-5}
20 SCCM	1.08×10^{-7}	2.20×10^{-6}	2.99×10^{-5}
25 SCM	1.88×10^{-6}	1.85×10^{-5}	1.94×10^{-4}
30 SCCM	1.46×10^{-6}	7.29×10^{-6}	6.08×10^{-5}

The lower value of leakage current density for 20 SCCM film may be attributed to the higher crystallinity and homogeneous, smooth, and dense microstructure [197]. The leakage current studies display a comparatively excellent value of leakage current density than earlier reports on BFO films [162][198]. The value of current density at different applied electric fields is summarized in **Table 4. 7**. **Figure 4. 10(b)** represents the simplified graphical illustration of the MFM capacitor for the Al/BLFO/Al structure.

4.4 Conclusions

- La-doped BFO ceramics are effectively synthesized via a solid-state reaction route without any impurity phase. Utilizing this BLFO target, a series of BLFO films varying the OPPs is grown using the pulsed laser deposition technique on n-type silicon and quartz substrates.
- A rhombohedral phase structure with space group *R3c* is confirmed via XRD, and the crystal planes (110) and (006) are revealed for the same film and are correlated with the high-resolution HRTEM image and SAED pattern. A microstructural and topological study found improved grain size and surface roughness with increased OPP concentration. The existence of mixed-phase of Fe^{2+} and Fe^{3+} was analyzed with the XPS spectrum.
- The improved dielectric and ferroelectric response were observed for 20 SCCM deposited films. The high dielectric constant (447) with minimum loss tangent (0.202) and enhanced energy storage density of 2.09 $J/cm^{3,}$ having an energy efficiency of 78.42% at 488 kV/cm, are achieved for BLFO thin films.
- The low bandgap energy of 2.74 eV and relatively higher refractive index of 2.78 are observed for the same film. The optical spectra of the films exhibited > 70% transmission in the visible region, and the estimated refractive index declined with increasing OPPs after 20 SCCM deposited film.
- The thickness of the films determined by optical studies is approximately 200 nm, well matches the cross-sectional FESEM images and profilometer-obtained results. The lower leakage current density of $\sim 1.08\times 10^{-7}$ is estimated for 20 SCCM film attributing to dense microstructure and favorable oxygen ambiance. Hence, the BLFO films can be studied for memory, visible light response photocatalysts, and energy storage capacitor applications.

Chapter 5

Investigation of $BiMeO_3/BaTiO_3$ bilayer and multilayer thin films

This chapter describes the fabrication of BLFO/BTO bilayer hetero-structures and explores the induced interfacial effect in enhancing the energy storage of thin films. This also discusses the development of multilayer BZNT/BTO hetero-structures to observe the dominance of alternate interfacial effect in enhancing the breakdown strength and reducing the leakage current density to obtain improved energy storage response in alternatively stacked multilayer thin films.

5 Investigation of $BaTiO_3/BiMeO_3$ bilayer and multilayer thin film

5.1 Introduction

The growth and success of the electronic industry, particularly in automotive, mobile, photovoltaic, and pulse power technologies, motivate researchers to develop exceptional energy storage devices. The rapid development of miniaturization, lightness, and integration has increased interest in thin film capacitors for energy storage. The concept of combining multiple material properties into a single system is gaining popularity in the fields of science and engineering. This is the case with so-called multifunctional materials (MF), which can perform multiple functions within a system due to their unique properties. Barium titanate (BTO) is a typical ferroelectric material with ferroelectric, dielectric, piezoelectric, electro-optical, and non-linear optical effects. BTO is among the multifunctional materials with broad applications in multilayer ceramic capacitors, energy storage devices, and PTC (Positive temperature coefficient) thermistors, owing to its exceptional physical properties [199][200].

The superiority of the superlattice structure as a lead-free film capacitor has caused current research to concentrate on BTO-based multilayer films [199]. Because of its abundant structural defects like pores, voids, and impurities, bulk ceramic has an extremely low energy density and electric breakdown strength [201]. The inherent limitations of individual compositions and a single nanostructured material cannot practically obtain a fast charging/discharging rate, high energy density, large breakdown strength, and long cycle performance. However, in a single dielectric material, it is highly challenging to satisfy these requirements. Therefore, to find a suitable design for high energy density pulse power capacitors, bilayer, and multilayer film capacitors have come into being. Nanoscale structure design involving the fabrication of bilayer or multilayer thin films results in a subtler microscopic change than ion-scale doping modification. Meanwhile, several studies on energy storage performance have been reported on BFO/BTO bilayer films. The BFO/BTO film on $SrRuO_3$ (SRO)-coated (100) $SrTiO_3$ (SRO/STO) substrate deposited by RF sputtering is reported to achieve a high W_{rec} of 51 J/cm^3 with η of 73% at an applied field of 2600 kV/cm [80]. Likewise Mn-doped $BiFeO_3$–$BaTiO_3$ thin films deposited on conductive Nb-doped $SrTiO_3$ (STO) (100) substrates using PLD record an enhanced W_{rec} of 80 J/cm^3 with $\eta > 90\%$ at 3100 kV/cm [202]. A single layer of BTBF films fabricated by PLD on $Pt/Ti/SiO_2/Si$ substrate displayed a W_{rec} of 19 J/cm^3 with η of 51% at 900 kV/cm [203]. On the other hand, BFO/BTO films deposited on $Pt/Ti/SiO_2/Si$ substrates showed a significantly low value of W_{rec} in order of 10^{-2} in magnitude [204], [205]. Multilayer thin films are expected to display significantly superior performance compared to single-layer thin films. Designing a multilayer structure is a very effective way to address and resolve the above-discussed limitations with single-layer or bulk ceramics. Multilayer-structure arrangements preserve structural integrity and restrict volume expansion. Additionally, it can also protect the inner materials from being affected by the outside environment and promotes the rapid transport of electrons and ions. In addition, multilayer arrangement improves the BDS and possesses high polarization facilitating improved energy storage performance [206]. Likewise, $[(Ba_{0.9}Sr_{0.1})Zr_{0.4}Ti_{0.6}O_3/SrZr0.1Ti0.9O_3]_N$ (BSZT/SZT) multilayer films achieved a high Wrec of 107.3 J/cm^3 with an energy efficiency of 84%, investigated recently by Nguyen [207]. Localized space charges near the BSZT/SZT interfacial layers prevent charge carrier propagation under the externally applied field between the alternative stacking of BSZT and SZT layers. It is responsible for improving energy storage performance in BSZT/SZT multilayer films. A similar study on BCT/BZT heterostructures via interface engineering displayed a large W_{rec} of 42.1 J/cm^3 conducted by Sharma, et al. [206].

In this chapter, bilayer BLFO/BTO structures and BZNT/BTO multilayer films are reported to observe the interfacial phenomenon occurring at heterostructure interfaces. Both the series of bilayer (BLFO/BTO) and multilayer (BZNT/BTO) films are deposited on SiO_2/Si (100) and Pt/Ti/SiO_2/Si substrates using a pulsed deposition technique. The **first section** of this chapter includes BLFO/BTO thin films with varying thicknesses of the BLFO (top) layer, mainly to overcome the leakage current. The bottom layer BTO (200 nm) is fixed with the growth of different nanoscale thicknesses of the BLFO layer on top of it, 200, 250, and 300 nm. This investigation emphasizes the impact of top-layer variation on structural, morphological, dielectric, magnetic, and ferroelectric behavior. In the **second section**, two excellent ferroelectric materials (BTO and BZNT) with the same structure (perovskite structure: ABO_3), have been used to enhance the multifunctional properties of the BZNT/BTO multilayered structures. A comprehensive study has been performed on the structural, electrical, ferroelectric, and leakage characteristics of the BZNT/BTO multilayered system. This study also aims to study the leakage current properties with the number of alternate stacking layers associated with evaluating the energy storage performance of multi-layered thin films.

5.2 Materials and method of film deposition:

BTO, BLFO, and BZNT powders prepared from solid-state reaction routes are used for target preparation. The powders of BTO, BLFO, and BZNT are pressed in the form of cylindrical discs of 20 mm diameter and 4 mm thickness. The BTO disc is sintered at 1250 °C for 2 hr while the BLFO and BZNT discs are sintered at 800 °C for 30 minutes. Using these targets, bilayer (BLFO/BTO) and multilayer (BZNT/BTO) films are deposited. The deposition procedure of bi-layer and multi-layer is the same as discussed in **Chapter 4** for the deposition of BLFO films. Here, the bilayer films are deposited at 20 SCCM varying the BLFO (top layer) thickness. For multi-layer stacking, the number of stacking layers (alternate stacking of two different layers; BTO and BZNT) is varied forming bi-layer, tri-layer, and tetra-layer arrangements. The BLFO/BTO and BZNT/BTO heterostructures are deposited at the substrate temperature of 600°C and kept at the same temperature for 1 hr under vacuum ($\sim 10^{-2}$) to achieve crystallinity.

5.3 Results and Discussions: BLFO/BTO bilayer films:

Figure 5. 1(a) depicts the obtained XRD pattern of the bilayer films grown on n-type Si. The thickness of the BTO bottom layer is kept constant at 200 nm, and the deposition time is varied for the BLFO layer to get different film thicknesses of 200 nm, 250 nm, and 300 nm. The XRD patterns of single layers; BTO, and BLFO layers are also included in the XRD pattern to show the BTO and BLFO phases and their contribution to phase formation for bilayer films. The nomenclature of the deposited bilayer films is kept as BLFO/BTO1, BLFO/BTO2, and BLFO/BTO3 for the sake of simplicity. The pure phase for BTO and BLFO layers are achieved at a deposition temperature of 700 °C and 500 °C, respectively. The bilayer thin films are optimized, and the crystalline phase is obtained at 600 °C deposition temperature. The corresponding peak profiles of BTO and BLFO are indexed with JCPDS card no 01-083-1880 and 00-066-0439. Both tetragonal (T) and rhombohedral phases (R) are observed for bilayer

films in the XRD pattern without the appearance of any satellite peaks suggesting that the individual ferroelectric and ferromagnetic phases are retained in the double-layered thin films [208].

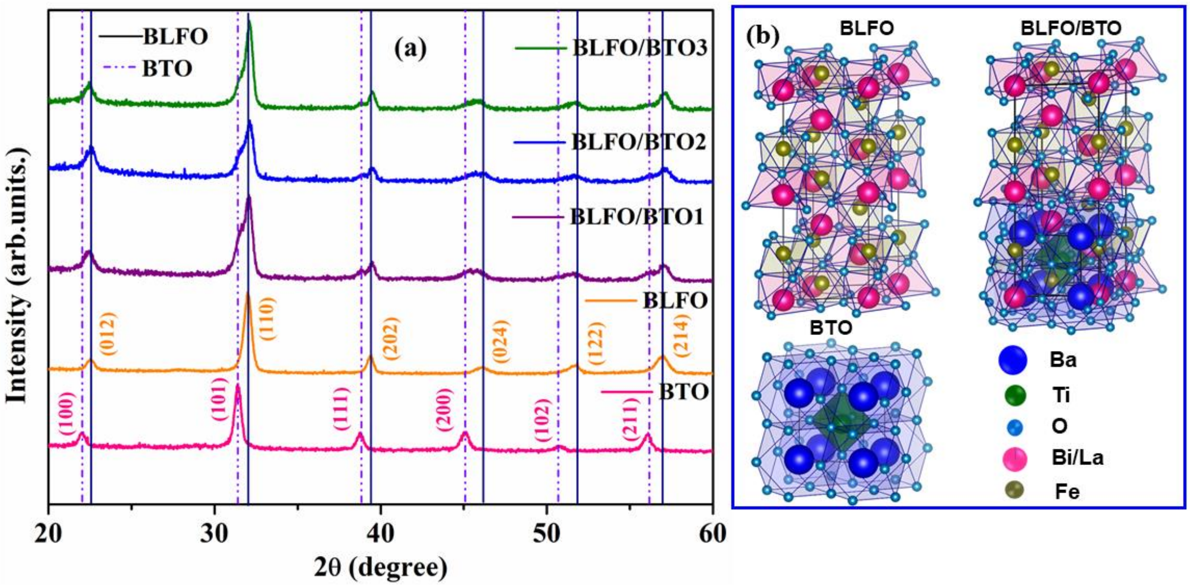

Figure 5. 1: (a) Experimentally obtained XRD pattern of single layer BTO and BLFO with their bilayer thin films, (b) represents the 3D crystal structure of upper layer (BLFO), bottom layer (BTO), and bilayer heterostructure (BLFO/BTO).

It is worth noticing the intensity of the BTO (101) peak reduced with increasing BLFO thickness with an increase in the (110) peak corresponding to BLFO. It is evident from the XRD pattern that the BLFO layer is well-grown over the BTO layer. The Rietveld refinement of the films is performed to gather further information regarding the phases and the crystal system. FullProf software has been employed for the experimentally obtained XRD pattern for bilayer films to estimate the contribution of both phases. The peak profile of the obtained XRD pattern is fitted with the pseudo-Voight function. The XRD pattern for the monolayer films, BTO and BLFO, is refined considering the T and R phases. The multiphase refinement with T and R phases for bilayer films revealed the presence of both layers. **Figure 5. 1(b)** shows the respective 3D crystal structure of BLFO, BTO and their bilayer heterostructures generated from

Vesta software. The upper layer BLFO with rhombohedral crystal structure having R3c space group is represented with pink and dark yellow color indicating A-site (Bi) and B-site (Fe) atoms with O in sky blue color. It is to be noted that the La atom in the A-site is not visible in the BLFO crystal structure illustrated in Figure due to the trace amounts of La in the BLFO composition. Similarly, the crystal structure of the bottom layer (BTO) is shown with the respective atoms present in respective positions. Likewise, the blue and green color represents A site (Ba) and B site (Ti) atoms with sky-blue oxygen atoms. The 3D representation of the BLFO/BTO bilayer is illustrated on the right side of **Figure 5. 1(b)** shows both the contribution of BLFO and BTO layers in the heterostructure. Hence, the presence of both phases in bilayer films is well depicted by the Vesta-generated illustrations.

Figure 5. 2(a-d) shows the Rietveld refined XRD pattern for BTO single layer and BLFO/BTO bilayer films. The obtained χ^2 values signify the good fitting ranging between 1-2 in the present study. The presence of each layer in the bilayer films is quantified with volumetric fraction percentages for BTO and BLFO layers. The enhancement in the top layer in heterostructures increased the volumetric fraction percentages of the R phase, whereas the T phase declined. All other refined parameters for all the deposited films are presented in **Table 5. 1**. The lattice mismatch between the intermediate and top layers significantly impacts the heterostructure; therefore, the lattice mismatch of the BTO and BLFO is examined. The expression of the lattice mismatch concerning film is as follows [209]:

$$S = \frac{a_f - a_s}{a_f} \qquad (5.1)$$

here, S is the lattice mismatch of the two materials; a_f is the lattice constant of the top layer and a_s is the lattice constant of the substrate. The differences in lattice parameters of Si (a = b = c = 5.43 Å), BTO (a = b = c = 3.999 Å), and BLFO (a = b = 5.593 Å and c = 13.778 Å) would lead to stresses (tensile or compressive strain) on deposited film as a result of lattice mismatch (S). The calculated lattice mismatch according to expression (1) is summarized in **Table 5. 1**.

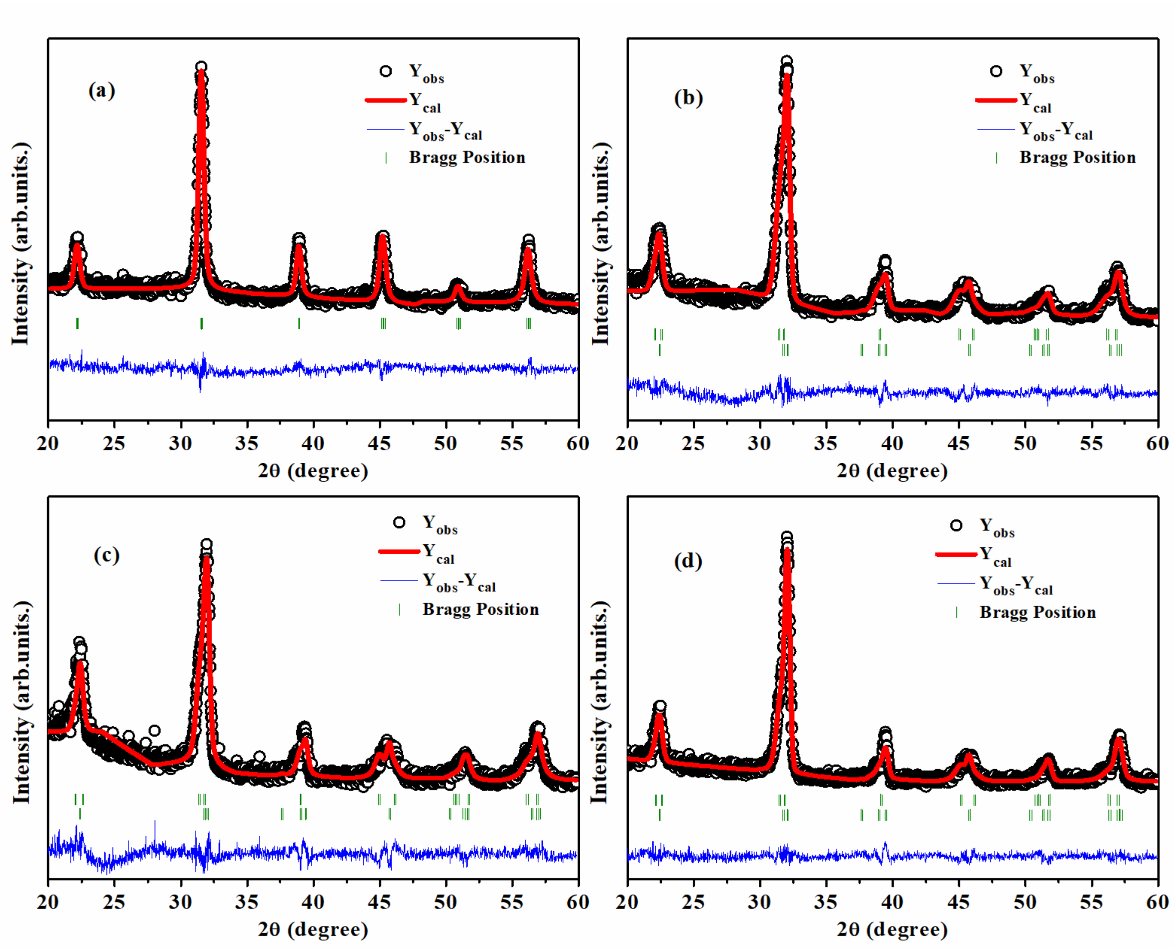

Figure 5. 2: Rietveld refinement XRD pattern for (a) BTO monolayers and (c-d) BLFO/BTO bilayers.

The lattice mismatch between the BTO and BLFO layers causes strain in the thin films. Here, the lattice mismatch occurred due to the difference in lattice constant between BTO and BLFO films. The monolayer BTO and BLFO films deposited on Si have lattice mismatches of -35.78% and 2.91%, respectively. The lattice mismatch of bilayer films is found to be around 29.5%. A large lattice mismatch between the two layers is also observed for the bilayer films [209], [210].

Table 5. 1: The obtained refined parameter for BTO, BLFO/BTO, and BLFO films.

Films	χ^2	**Tetragonal Phase**		**Rhombohedral Phase**			***S (lattice misfit)***
		Volume Fraction (%)	a=b=c (Å)	Volume Fraction (%)	a=b (Å)	c (Å)	
BTO	1.48	100%	3.999(1)	-	-	-	-35.78%
BLFO/BTO1	1.88	52.87%	3.939(4)	47.13%	5.583(1)	13.873(16)	29.44%
BLFO/BTO2	1.80	39.61%	3.934(3)	60.39%	5.593(1)	13.841(9)	29.66%
BLFO/BTO3	1.38	34.31%	3.931(3)	65.69%	5.581(0)	13.877(14)	29.56%
BLFO	1.59	-	-	100%	5.593(1)	13.778(2)	2.91%

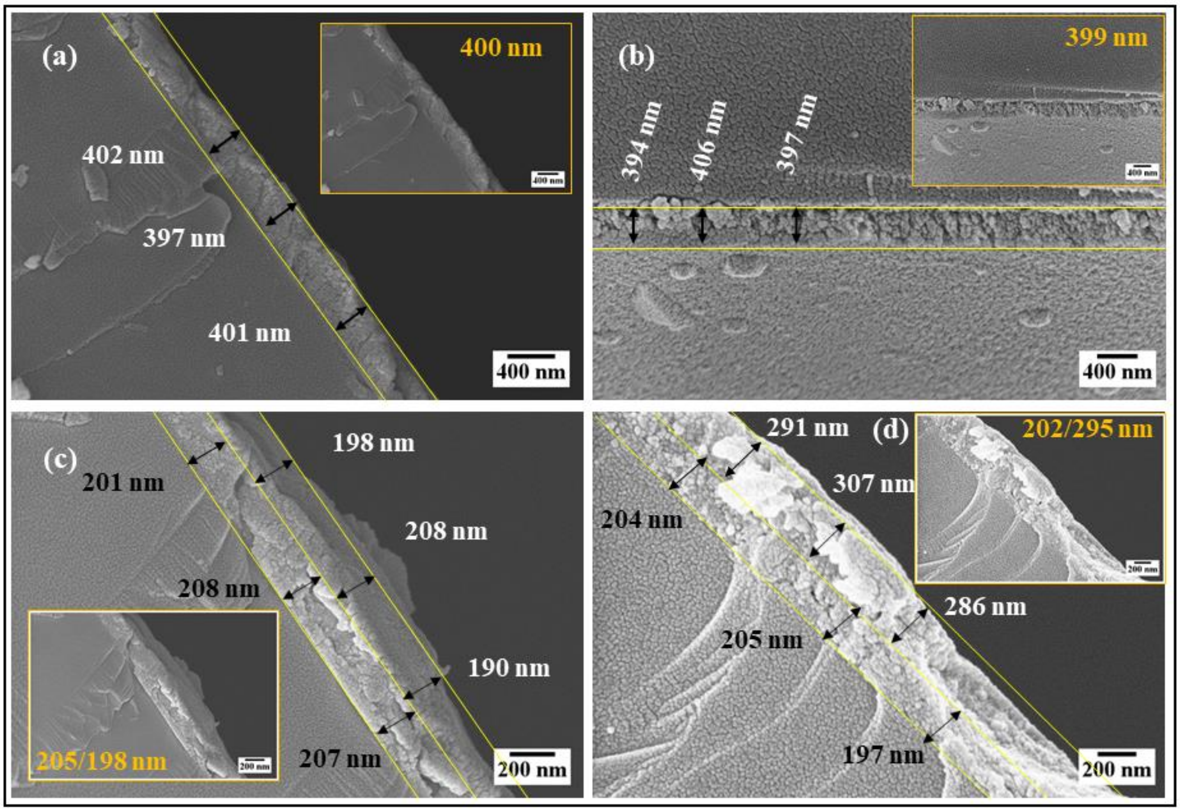

Figure 5. 3: FESEM cross-section showing the thickness of (a) BTO, (b) BLFO thin films, (c) BLFO/BTO1, and (d) BLFO/BTO3 bilayer films.

Figure 5. 3(a) and **(b)** illustrate the cross-section FESEM images of the single layer, BTO, and BLFO thin films. The thickness estimated for the monolayers BTO and BLFO films is 400 and 399 nm, respectively. Similarly, the thickness of the bilayers is calculated using the cross-section FESEM images and found to be approximately 205/198, 201/247, and 202/295 nm for BLFO/BTO1, BLFO/BTO2, and BLFO/BTO3, respectively, and is summarized in **Table 5. 2**. The cross-section image for BLFO/BTO1 and BLFO/BTO3 heterostructure with distinct interfaces is observed in **Figure 5. 3(c)** and **(d)**.

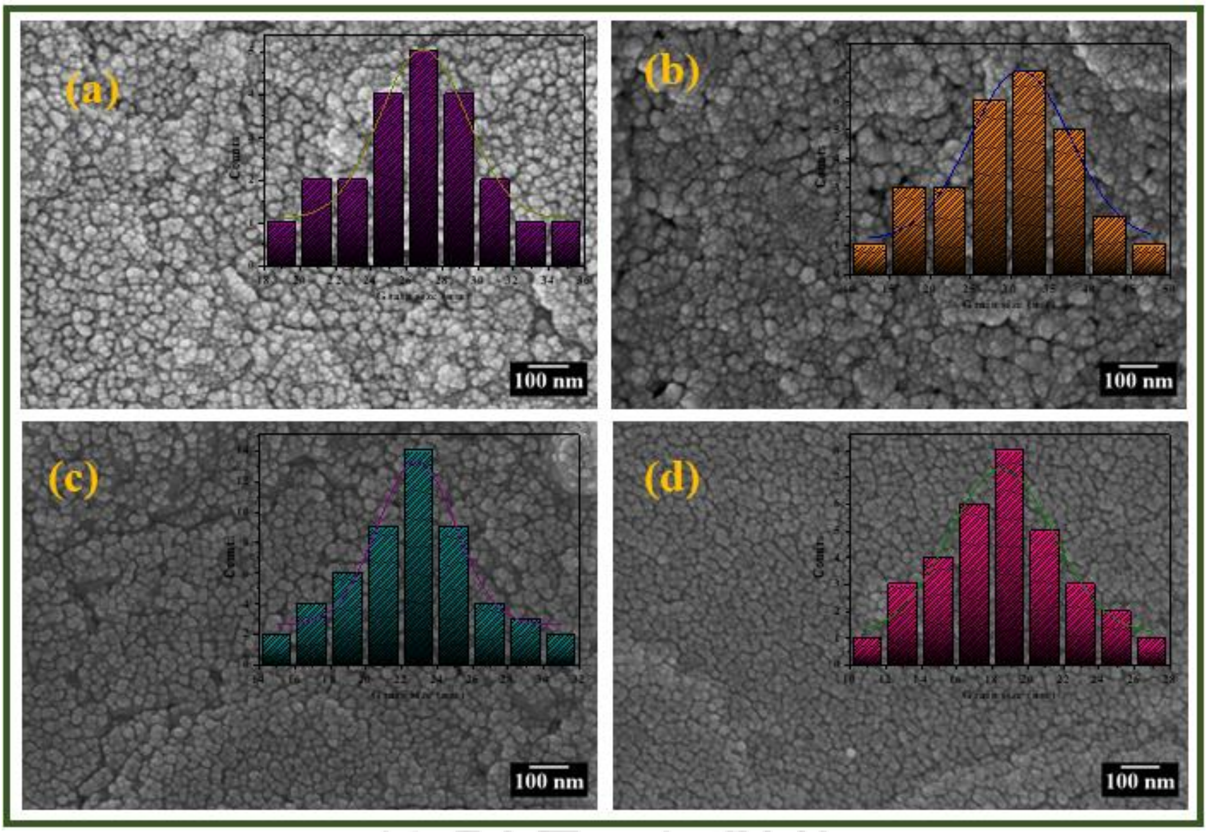

Figure 5. 4: FESEM images of (a) BTO, (b) BLFO/BTO1, (c) BLFO/BTO2, and (d) BLFO/BTO3 bilayer thin films.

The microstructure of the BTO and BLFO/BTO bilayers is presented in **Figure 5. 4(a-d)**. The corresponding average grain size histogram is depicted in the inset. The microstructure of the BTO single layer seems to be rough, with an average grain size of 27 nm and is estimated using ImageJ software. With stacking of the BLFO layer over BTO, the microstructure seems rougher, and significant grain growth is observed for BLFO/BTO1 bilayer film. With the further enhancement in thickness of the top layer, the suppression in grain growth for BLFO/BTO2 and BLFO/BTO3 bilayer films with an average grain size of 22.84 and 18.51 nm is observed. The inhibition of grain growth with uniform microstructure is achieved for BLFO/BTO3 bilayer films indicating the good stacking of each layer and improved crystallization. A well-grown BLFO layer over the BTO layer is also quite evident from the structural analysis.

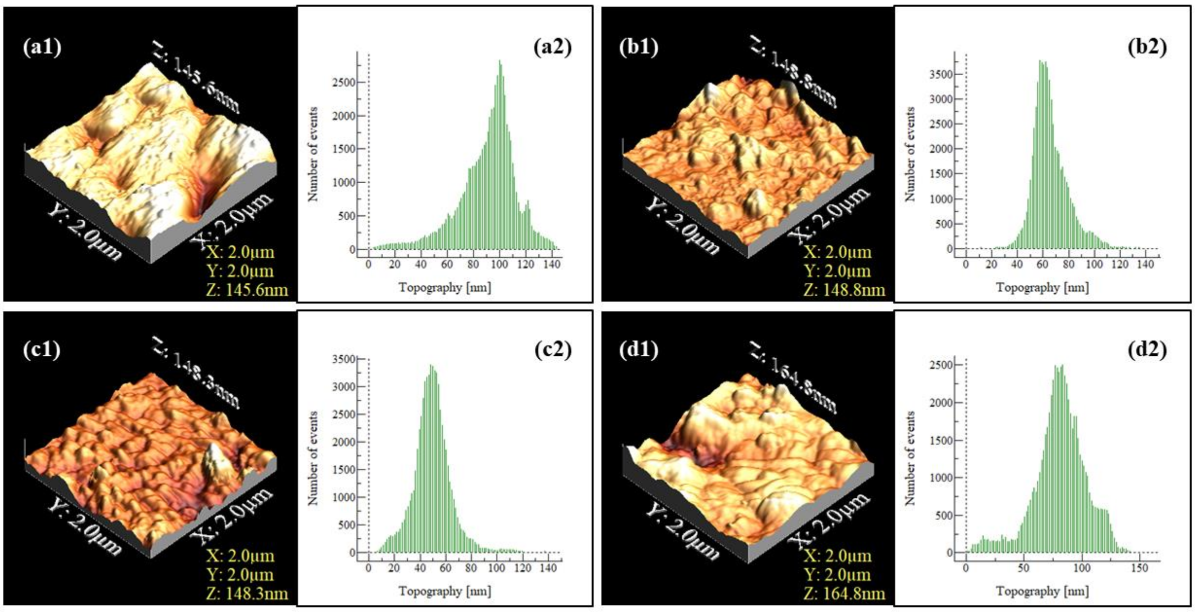

Figure 5. 5: AFM 3D topological representation of (a) BTO, (b) BLFO/BTO1, (c) BLFO/BTO2, and (d) BLFO/BTO3 with their corresponding particle size distributions.

The surface topology of bilayer thin films with BTO monolayer is examined using the AFM analysis to study the nature of the deposited film. The images are scanned at a 2×2 µm area to observe the roughness and topology of the films. The corresponding particle size distribution is shown along the 3D AFM images determined with the help of WSxM software, as illustrated in **Figure 5. 5(a-d)**. The RMS roughness (R_{rms}) of the single layer BTO is 22 nm, whereas uniform and smooth topography is achieved for BLFO monolayers with R_{rms} of 3.73

nm for the same film thickness of 400 nm. Interestingly, the bilayer film with 200/200 nm thickness (BLFO/BTO1) showed a lower roughness of 14.56 nm compared to the BTO monolayer. The possible reason could be the higher roughness of the BTO (bottom) layer is suppressed by the BLFO layer with lower roughness. Another reason for the reduced roughness could be the lower bottom layer thickness of BTO (200 nm) compared to monolayer BTO of 400 nm thickness. Similarly, for BLFO/BTO2 and BLFO/BTO3, the RMS roughness is 15.66 and 22.92 nm, respectively, as summarized in **Table 5. 2**. The increase in roughness is noticed with the further enhancement in thickness of the top BLFO layer. The improvement in RMS roughness in bilayer films is due to an increment in the average thickness of the films.

Table 5. 2: FESEM and AFM analyzed parameters.

Films	***Thickness (nm) cross-section***	***Grain size (nm)***	***RMS Roughness (nm)***
BTO	400±2.65	26.93±0.21	22.12
BLFO/BTO1	205.33±3.79/198.67±9.02	31.26±0.75	14.56
BLFO/BTO2	201.33±3.51/247.33±1.53	22.84±0.21	15.66
BLFO/BTO3	202±4.36/294.67±10.99	18.51±0.26	22.92
BLFO	399±6.24	21.31±0.31	3.73

The dielectric studies of the deposited films from RT to 250 °C as a function of frequency are measured for monolayer BTO and BLFO/BTO3 bilayer films. The effective dielectric permittivity of the heterostructure can be calculated by introducing a series capacitor model [211]. Suppose ε_1 and ε_2 are the dielectric permittivity of the two films with thickness t_1 and t_2, respectively. In that case, the effective dielectric constant of the bilayer films can be deduced using the following relation [212]:

$$\varepsilon_{eff} = \frac{\varepsilon_1 \varepsilon_2 (t_1 + t_2)}{t_1 \varepsilon_2 + t_2 \varepsilon_1} \tag{5.2}$$

here, ε_1 and ε_2 represent the dielectric permittivity of the BTO and BLFO layer, and t_1 and t_2 are the corresponding thickness.

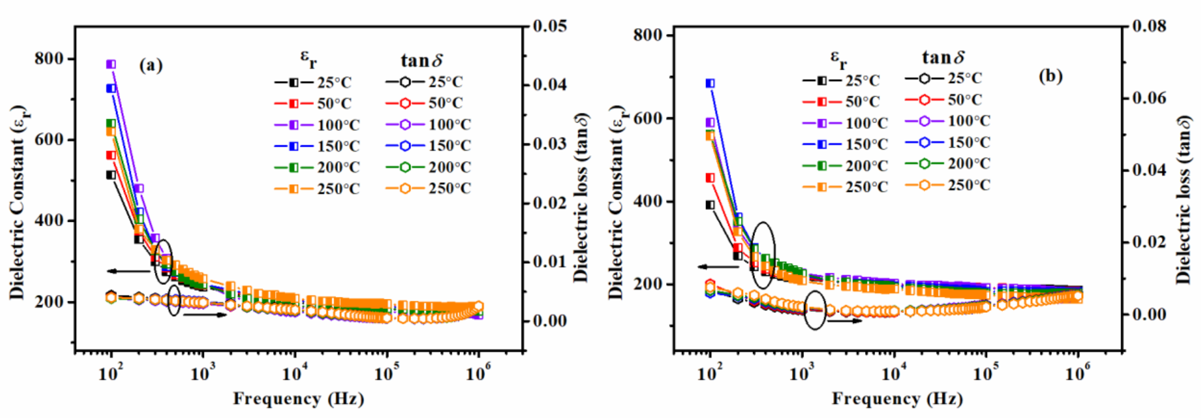

Figure 5. 6: Dielectric permittivity and dielectric loss as a function of frequency for (a) BTO and (b) BLFO/BTO3 bilayer thin films.

Figure 5. 6(a-b) depicts the dielectric permittivity and tangent loss (tan*δ*) for BTO and BLFO/BTO3 bilayer thin films as a function of frequency. At RT, the 'ε_r' at 100 Hz is about 514 for BTO monolayer films, which drops to 388 for bilayer films. The slight reduction in ε_r for BLFO/BTO3 bilayer film compared to BTO monolayer film is due to adding a low dielectric constant (BLFO) layer. Therefore, adding the BLFO layer slightly lowers the dielectric permittivity of the bilayer films. At the same time, the dielectric permittivity for both the BTO monolayer and BLFO/BTO3 heterostructure declines with the rise in frequency. At lower frequencies, mainly the space charge polarization is responsible for the elevated values of dielectric permittivity, and this behavior also agrees with the Maxwell-Wagner model [213]. After attaining a certain frequency (10^3 Hz), both films exhibited a steady dielectric permittivity behavior. The slight variation in permittivity with frequency in the higher frequency regions may be due to the release of space charge polarization. **Figure 5. 6** shows the dielectric loss (tan*δ*) for both films stabilizes low values for the measured frequency, indicating the high quality of the films. However, the rising trend in tan*δ* beyond a particular

frequency (i.e., 10^5 for BTO films and 10^4 for BLFO/BTO3 heterostructure) may be due to the insufficient response of the charge carriers to the external electric field [214].

Complex impedance analysis helps to investigate the electroactive regions in the fabricated thin films. The electrical response due to various contributions to impedance depends on the film's microstructure [215]. The complex impedance can be described as follows in **equation 3.1**. **Figure 5. 7** illustrates the real and imaginary part of the complex impedance plotted for monolayer BTO and bilayer BLFO/BTO3 films.

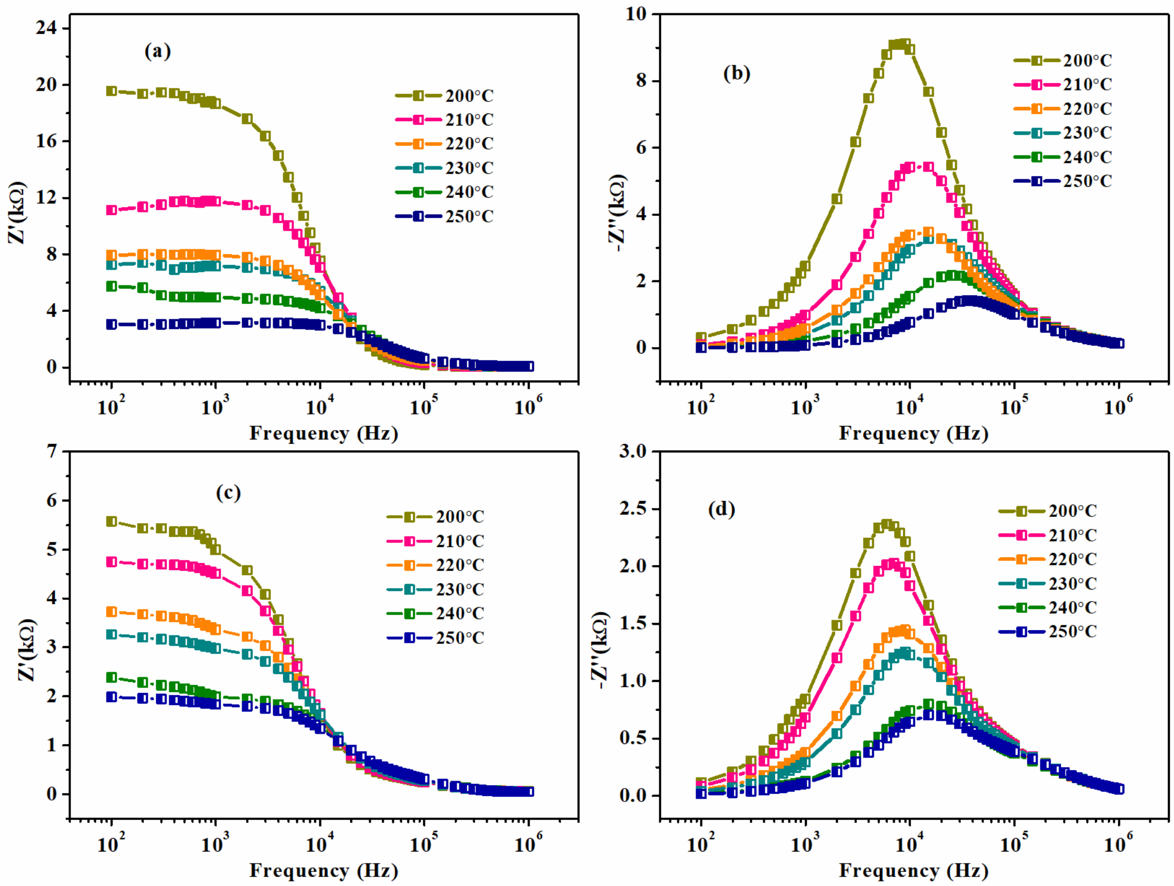

Figure 5. 7: Real part and imaginary part of impedance with varying frequency for (a-b) BTO and (c-d) BLFO/BTO3 bilayer thin films.

Figure 5. 7(a) and **(c)** depict the real part of the impedance for BTO and BLFO/BTO3 films showing the decreasing trend of Z' with the rise in frequency and temperature. At lower

frequencies (10^2 - 10^4 Hz), the decrease in the magnitude of Z' with the temperature rise suggests the negative resistance temperature coefficient (NTCR) behavior [216]. At higher frequencies, the values of Z' seem to merge for all temperatures mainly due to the release of space charge. The imaginary part of impedance for both the films showed the maximum peak around the mid-frequency region for the lowest temperature (200 °C), which then decreased with a temperature rise. These peaks observed for the imaginary part of impedance are mainly attributed to the relaxation process resulting from the contribution of immobile charges [213]. From **Figure 5. 7(b)** and **(d)**, the peak shifting towards the higher frequency regions is also observed with the rise in temperature for both films. The broadening with asymmetry of the peaks with increasing temperature is attributed to the increase in relaxation time [215].

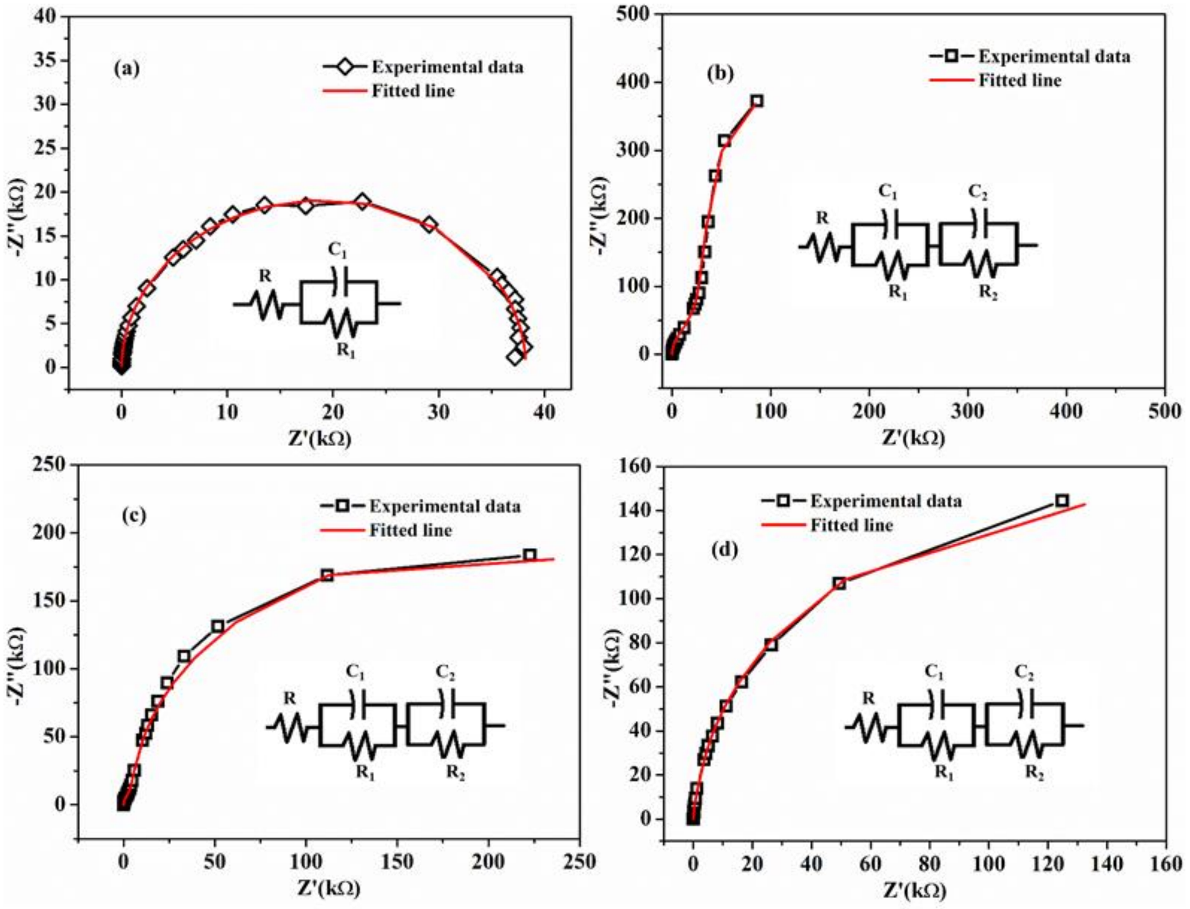

Figure 5. 8: Room temperature Nyquist plot for (a) BTO, (b) BLFO/BTO1, (c) BLFO/BTO2, and (d) BLFO/BTO3 thin films.

To see the effect of different contributions to impedance, such as grain, grain boundaries, and electrode/sample interfaces, a Nyquist plot is plotted between the real and imaginary impedance parts. A room-temperature Nyquist plot for monolayer and bilayer films is shown in **Figure 5. 8(a-d).** The correlation between the spectrum and morphology of the film is shown with the help of the corresponding electrical circuit shown in the inset of **Figure 5. 8(a-d)**. The semicircle at low frequency arises due to the grain boundary and electrode/ sample interface, and the high-frequency semicircle represents the grain contributions. In the current study, the Z' versus Z" curves are fitted with different circuit models using ZSimWin software for all the deposited films at RT. In the monolayer film BTO, only one semicircular arc is found, indicating only the grain effect is predominated [217]. An equivalent model with a single RC circuit with additional R in series well fitted confirms the only grain contributions shown in **Figure 5. 8(a)**. For BLFO/BTO bilayer films, grain and grain boundary contribution is observed with two parallel RC circuits in series with additional R. The obtained resistance and capacitance values are summarized in **Table 5. 3**.

Table 5. 3: Equivalent circuit model fitting parameters for BTO and BLFO/BTO heterostructures measured at RT.

Films	***R(Ω)***	***C_g(F)***	***R_g (Ω)***	***C_{gb} (F)***	***R_{gb} (Ω)***
BTO	24.9	1.11E-11	3.82E4	-	-
BLFO/BTO1	38.1	2.91E-9	2739	3.21E-9	4.08E6
BLFO/BTO2	46.3	6.28E-10	4154	3.34E-9	3.72E5
BLFO/BTO3	58.7	6.06E-9	6753	8.32E-9	2.86E5

Similarly, to know the effect of temperature on microstructure, the Nyquist plot for BTO and BLFO/BTO3 films are plotted in the temperature range of 200-250 °C shown in

Figure 5. 9(a-b). Likewise, the BTO film showed semicircles fitted with two parallel RC circuits with additional R, as shown in **Figure 5. 9(a)**.

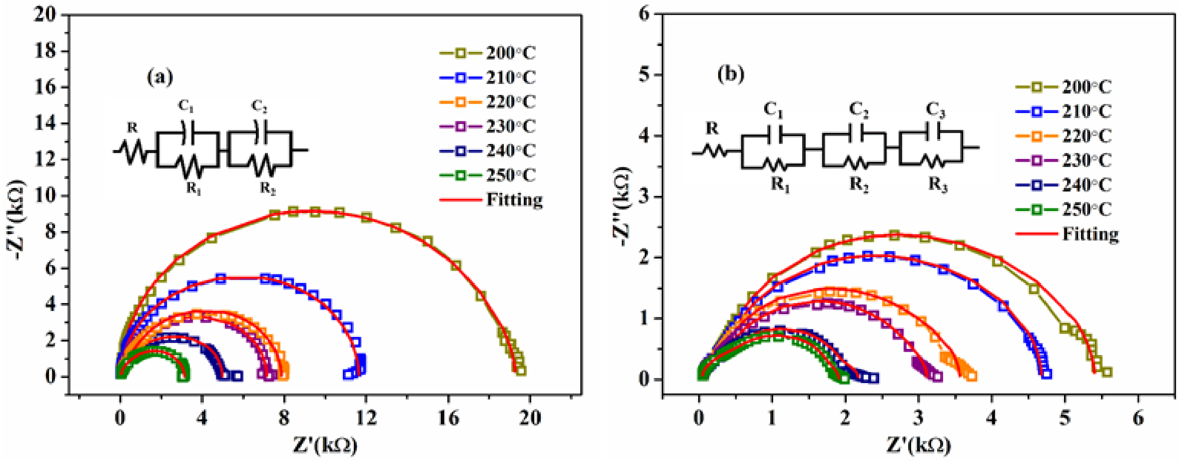

Figure 5. 9: Nyquist plot in the temperature range of 200 - 250 °C for (a) BTO and (b) BLFO/BTO3 bilayer thin films.

Interestingly, for BLFO/BTO3 films, the Z' versus -Z" curves are fitted with three parallel RC circuits connected in series with additional R illustrated in **Figure 5. 9(b)** inset. As discussed earlier, the third RC circuit indicates the presence of a polarization effect at the material–electrode interface at high temperatures [218]. The contribution of the films' resistance, capacitance, and polarization effect (α) are tabulated in **Table 5. 4**.

Table 5. 4: Equivalent circuit model fitting parameters for BTO and BLFO/BTO3 thin films measured at 250 °C.

Films	*R(Ω)*	*C_g (F)*	*R_g (Ω)*	*C_{gb} (F)*	*R_{gb} (Ω)*	*$C_α$ (F)*	*$R_α$ (Ω)*
BTO	21.8	1.83E-9	477	2.76E-9	2.593E5	-	-
BLFO/BTO3	14.3	8.28E-9	876	8.77E-8	1.64E5	3.456E-9	407.1

To study the role of oxygen vacancies/defects and the effect of the change in valence state in the films, the X-ray photoelectron spectroscopy (XPS) spectra with different BLFO layer thicknesses are measured. The core level spectra of Ti 2p, Fe 2p, and O1s for the BTO and BLFO/BTO thin films are displayed in **Figure 5. 10** using the high-resolution XPS (HRXPS) spectrum. **Figure 5. 10(a)** depicts the full scan of the XPS spectra for BTO and BLFO/BTO hetero-structures suggesting that all the elements are present in the fabricated film.

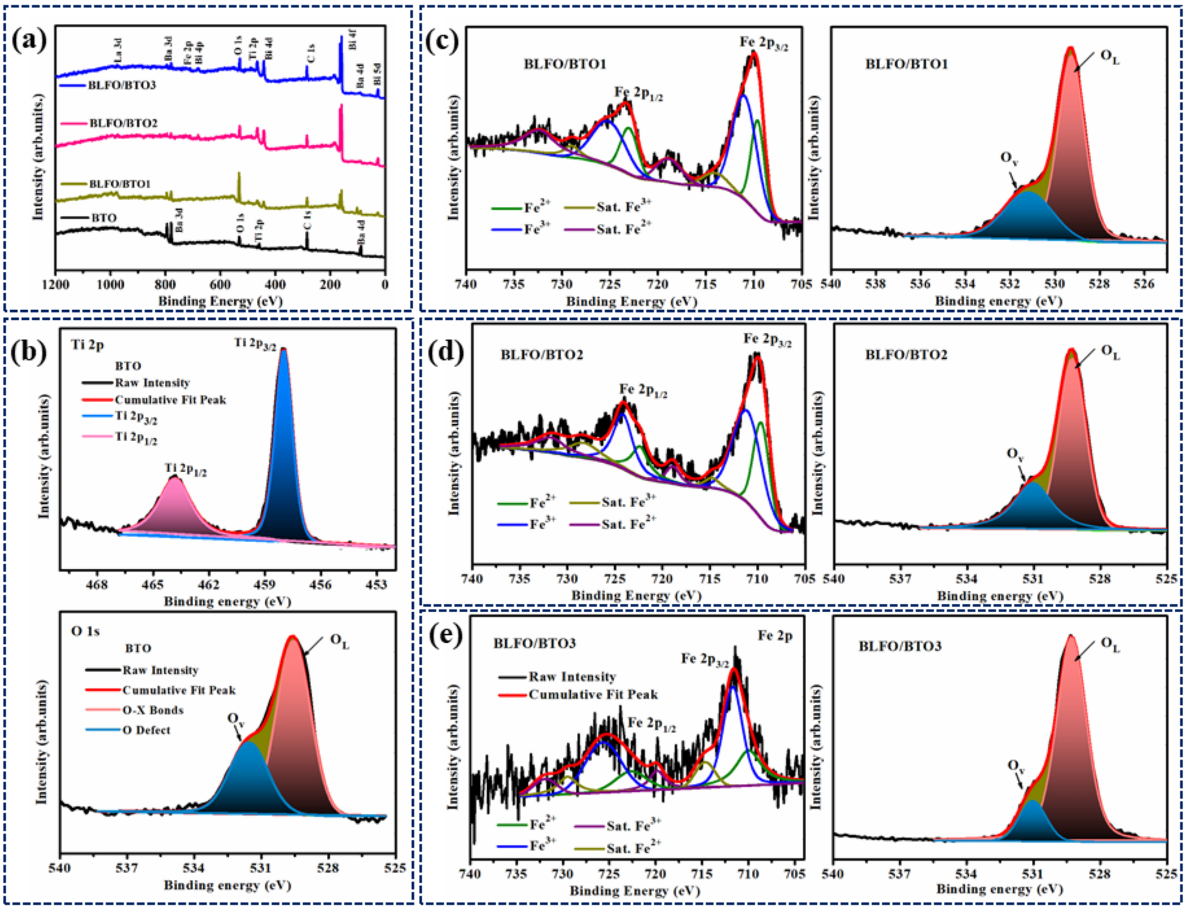

Figure 5. 10: (a) Full scan of XPS spectra for BTO and BLFO/BTO films, (b) HRXPS fitting of Ti 2p and O1s spectrum for BTO monolayer film, (c) depicts the HRXPS fitting of Fe 2p and O1s spectrum for BLFO/BTO1 film, similarly (d) and (e) represents Fe 2p and O1s spectra for BLFO/BTO2 and BLFO/BTO3 films, respectively.

Figure 5. 10(b) illustrates the HRXPS Ti 2p and O1s spectra of BTO monolayer film. The Ti 2p spectrum is resolved into two peaks at 458.04 and 463.85 eV belonging to Ti $2p_{3/2}$ and Ti $2p_{1/2}$ respectively, well agreeing with the Ti $2p_{3/2}$ and Ti $2p_{1/2}$ components of Ti^{4+} in BTO

[219], [220]. Similarly, **Figure 5. 10(c), (d),** and **(e)** show the Fe 2p and corresponding O1s spectra for all bilayer films. Further, the Fe 2p core levels are de-convoluted by two components assigned to Fe^{2+} (green) and Fe^{3+} (blue) components. The satellite peaks appearing for Fe^{2+} and Fe^{3+} are indicated with dark yellow and purple colors. Fe^{2+} peaks around 709.8, 715.1, 722.5, and 728.9 eV are assigned to Fe $2p_{3/2}$, a satellite, Fe $2p_{1/2}$, and a satellite peak, respectively. Likewise, the peaks approximately at 711.4, 719.1, 724.8, and 731.8 eV belong to Fe^{3+} [178]. These values of Fe 2p core level binding energies agree with the previous work [178]. The ratio of Fe^{3+}/Fe^{2+} determined by XPS spectra fitting for BLFO/BTO1, BLFO/BTO2, and BLFO/BTO3 improves from 1.7 to 2.1. Accordingly, the existence of both Fe^{2+} and Fe^{3+} is confirmed by the presence of oxygen vacancies in the bilayer heterostructures. The slight oxygen deficiency is reported to result in the combination of Fe^{2+} and Fe^{3+} ions.

To support the existence of Fe^{2+} and Fe^{3+} in bilayer films, a series of O 1s spectra is fitted with Gaussian/Lorentz distribution as depicted in **Figure 5. 10(c)**, **(d)**, and **(e)**. The fitted profile of O 1s spectra displays de-convoluted sub-peaks found approximately at 529 and 531 eV. The peak at lower binding energies (BEs) is attributed to the lattice oxygen, and the peak at higher BEs is ascribed to oxygen defects and vacancies [221]. It is believed that the BE of Bi_2O_3 appears at 529.8 eV [222], and the oxygen atoms corresponding to the Ba-O-Ti bond appear at 529.5 eV [223]. The BE at 531 eV appears due to the adsorbed oxygen species present on the surface of the sample. It is noticed that the peak at higher BE corresponding to defects and vacancies decreases significantly for BLFO/BTO3 hetero-structures. It is found that with increasing thickness of the top layer of the films, the Fe^3+/Fe^{2+} ratio rises with a lowering of oxygen defect percentages, summarized in **Table 5. 5**. It can be well expressed that with increasing thickness of the top layer of the films, the leakage current in the system can be significantly reduced. In the current study, the interface of the two layers plays a major role in bridging and enhancing the film quality.

Table 5. 5: Fe^{3+}/Fe^{2+} ratio in 2p core level spectrum and the contribution of lattice oxygen and oxygen vacancies in O 1s for BLFO/BTO bilayer thin films.

Films	***Fe 2p core level***	***O 1s percentages***	
	Fe^{3+}/Fe^{2+}	***O-X***	***O defect***
BTO	-	67.16	32.84
BLFO/BTO1	1.7	68.61	31.39
BLFO/BTO2	1.9	72.51	27.49
BLFO/BTO3	2.1	86.75	13.25

The isothermal magnetization versus magnetic field for bilayer BLFO/BTO heterostructures and BLFO thin film measured at room temperature are shown in **Figure 5. 11**. It can be noticed from **Figure 5. 11(a)** that the BLFO films showed a relatively low value of magnetization among the deposited films. A BFO is a G-type canted antiferromagnetic material with weak ferromagnetic ordering [224]. Pure BFO thin films generally possess small saturation magnetization (M_s) as the spiral spin structure cancels the net magnetization [225]. In the current study, for BLFO thin films, La-substitution enhanced the magnetic property as La suppresses the spiral spin structure, improving the magnetic response [186]. In heterostructure films, the M_s is enhanced compared to BLFO films. Here, the ferroelectric BTO buffer layer is anticipated to induce ferromagnetism, which is attributed to the interface diffusion next to the lattice constraint, where strong hybridization of Ti-O and Bi-O leads to the corresponding mechanism for stabilizing the distorted structure [226]. The bilayer film (BLFO/BTO1) with lower top layer thickness showed the highest magnetization of 35.9 emu/cm^3 at 2.5 kOe applied field with a broad hysteresis loop. With the enhancement in BLFO top layer thickness, the magnetization of the films is reduced with slimmer hysteresis loops. The enhancement in top layer thickness increased the total thickness of the bilayer films. Hence the decrease in magnetization is found for bilayer films with higher BLFO thickness. The lower magnetization with increasing film thickness is believed to be due to the particle size effect [224].

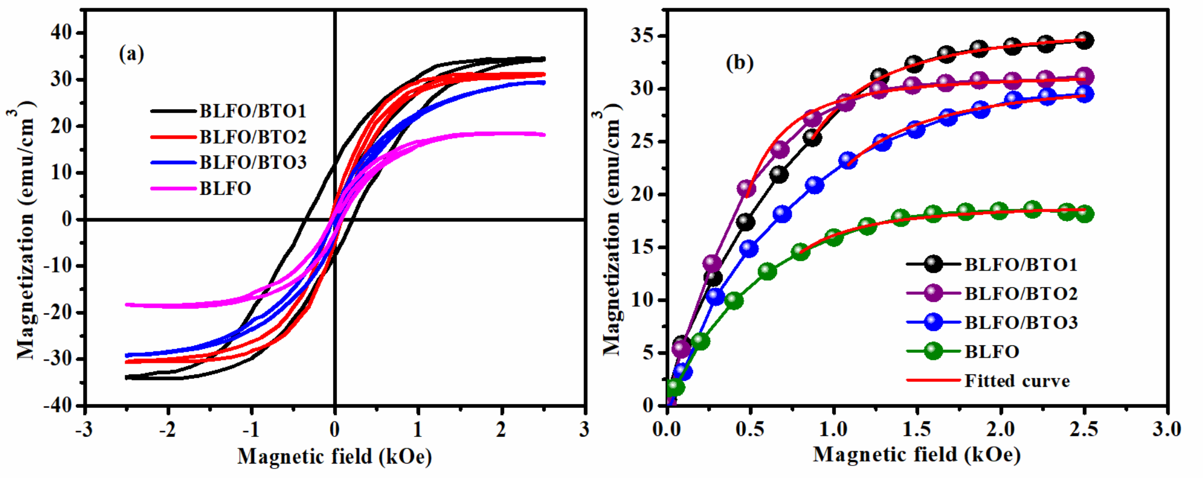

Figure 5. 11: Magnetic studies of BLFO/BTO bilayer films with varying BLFO thickness and monolayer BLFO thin films.

Table 5. 6: Magnetic parameters for BLFO/BTO heterostructures and BLFO monolayer films.

Film	***H_c (k Oe)***	***M_r (emu/cm^3)***	***M_s (emu/cm^3)***	***b (Oe^2) *10^6***
BLFO/BTO1	0.277	9.54	35.9 (0)	8.0 (1)
BLFO/BTO2	0.065	4.10	31.3 (2)	2.6 (1)
BLFO/BTO3	0.051	2.46	30.8 (2)	9.4 (5)
BLFO	0.056	2.14	19.0 (1)	2.9 (1)

Figure 5. 11(b) depicts the M_s of the films determined by fitting the law of approach to saturation (LAS). The value of M_s of all the films is listed in **Table 5. 6**, expressing LAS as follows [227]:

$$M(H) = M_s\left(1 - \frac{b}{H^2}\right) + \chi H \qquad (5.3)$$

where $M(H)$ and M_s represents magnetization at applied field H and saturation magnetization respectively. b is a factor proportional to K_1^2 (K_1 anisotropy constant) and χ is magnetic susceptibility obtained by fitting parameters.

Figure 5. 12 depicts the typical RT polarization versus electric field loops of BTO and BLFO/BTO heterostructures fabricated on Pt-Si substrates. Well-defined hysteresis loops are observed for all the films. A strong ferroelectric nature of loops is seen for BTO thin film, whereas the shape of loops becomes slimmer for bilayer films with comparatively low remnant polarization. Since the ferroelectric properties are mainly dependent on structural modification and change in microstructure. The oxygen vacancies and defects also affect the ferroelectric response of the films. The bilayer film (BLFO/BTO3) significantly showed lower oxygen vacancies as compared with other films when analyzed with high-resolution XPS spectra for O1s. It suggests that the contribution of lattice oxygen is the majority, i.e., 86.75% of the total O1s element present in the film, and nearly 13.25% of the contribution comes from oxygen vacancies and defects. At the same time, microstructure also plays a vital role in enhancing ferroelectric properties. The heterostructure with higher top layer thickness showing uniform and comparatively dense microstructure could be the possible reason for higher ferroelectricity in the film. The other reason for improved ferroelectricity is the addition of a BTO buffer layer in the BLFO/BTO system. Further, the energy storage performance of thin films, such as total energy storage density (W), recoverable energy storage density (W_{rec}), and energy efficiency (η), is determined for all the deposited bilayer films. The mathematical expression for evaluating the energy storage parameters is described elsewhere [228]. **Table 5. 7** presents the obtained ferroelectric loop values for all films. The maximum polarization (P_{max}) and electrical breakdown strength (E_{BDS}) of heterostructure films improved with the higher BLFO thickness. At the same time, the reduction in remnant polarization is observed for bilayer films with higher BLFO thickness attributing to the better energy efficiency of 85% for BLFO/BTO3 films.

Additionally, a complete ferroelectric loop is observed for BLFO/BTO3 films, indicating a shallow leakage current in the film.

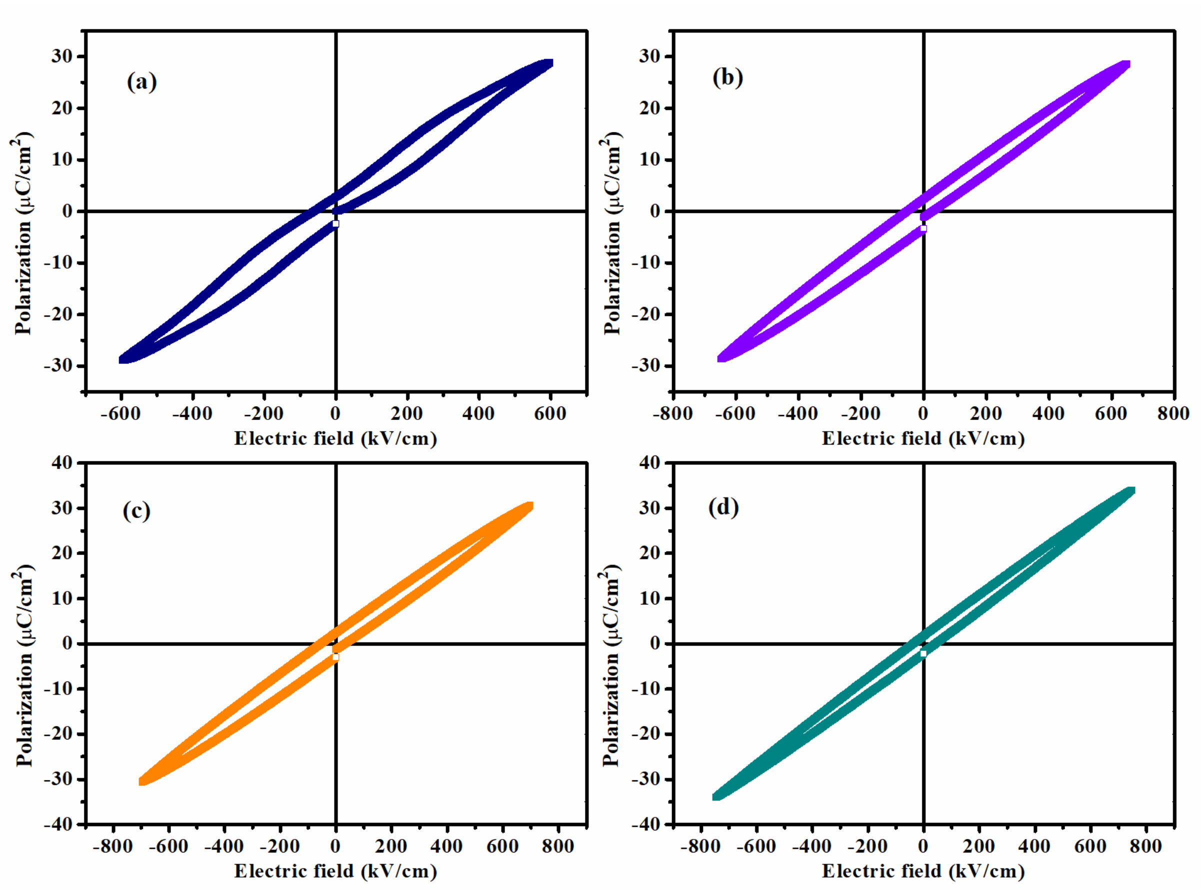

Figure 5. 12: Ferroelectric hysteresis curve (a) BTO, (b) BLFO/BTO1, (c) BLFO/BTO2, and (d) BLFO/BTO3 heterostructures.

Table 5. 7: Ferroelectric properties and energy storage parameters for BLFO/BTO heterostructures.

Films	P_{max} *(μC/cm²)*	P_r *(μC/cm²)*	E_{BDS} **(kV/cm)**	W_{rec} *(J/cm³)*	*η(%)*
BTO	28.84	2.74	596	6.84	74.67
BLFO/BTO1	28.85	2.58	646	8.01	79.86
BLFO/BTO2	30.54	2.42	696	9.32	80.55
BLFO/BTO3	34.00	1.50	746	11.65	85.04

Electrical breakdown strength (E_{BDS}) is one of the critical factors in obtaining better energy storage performance in determining a large W_{rec} and operating the electric field of dielectrics for practical applications. The improved E_{BDS} observed for the heterostructures are listed in **Table 5. 7** may be attributed to the influence of the interfacial layer. **Figure 5. 13** illustrates the interfacial layer between the BTO and BLFO layers preventing the formation of conducting filament. **Figure 5. 13(a)** shows the BTO single-layer films with Pt atoms and oxygen-deficient BTO interface. When high voltage is applied to the electrodes (Pt), there is a formation of the conducting filaments in series with the induced BTO/Pt interface. With the further application of the electric field, the formed conduction filament becomes thicker with more and more oxygen vacancies resulting in lower electric resistance, finally leading to the electrical breakdown as shown in **Figure 5. 13(b)**. In the case of bilayer thin films, the E_{BDS} can be increased to some extent by preventing the formation of conducting filament by interfacial layer between BTO and BLFO layers, as illustrated in **Figure 5. 13(c)**. Therefore, the large E_{BDS} is attributed to the enhanced W_{rec} of 11.65 J/cm^3 at 746 kV/cm applied field in the bilayer films. With this, the acquired ferroelectric response and energy storage performance of BLFO/BTO thin films are superior to the earlier studies for multilayer films [204], [229].

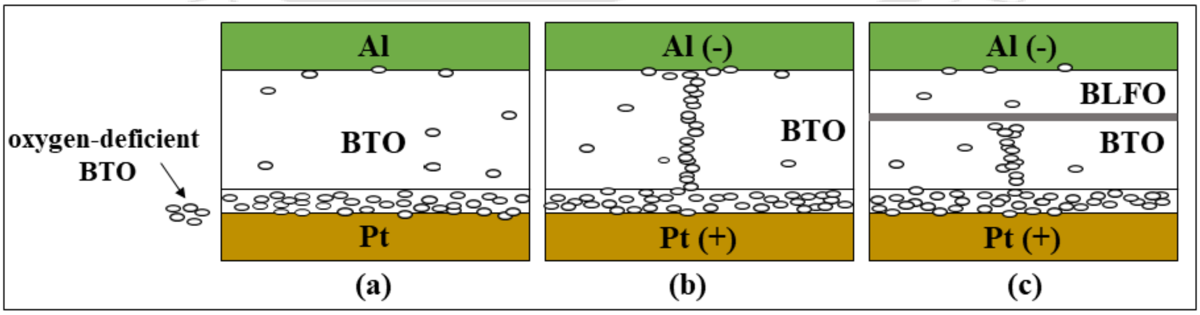

Figure 5. 13: Schematic diagram of conducting filament formation (a) before an electric breakdown, (b) after the electrical breakdown of monolayer BTO films, and (c) heterostructure thin films [230].

The power density of BTO and BLFO/BTO3 films are further evaluated to see the performance of the capacitors. Power density possessing a capacitance, C can be estimated based on a theory of Ragone plots as follows [229], [230]:

$$P = \frac{W_{rec}}{2 \times ESR \times C} \tag{5.4}$$

where W_{rec} denotes recoverable energy density, and equivalent series resistance (ESR) represents equivalent series resistance and is the product of dielectric loss ($\tan\delta$) and capacitive reactance (X_c). Hence, the ESR can be written as:

$$\text{ESR} = \tan\delta \times X_c = \frac{\tan\delta}{2\pi f C} \tag{5.5}$$

Therefore, the maximum power density can be estimated as follows :

$$P_{max} = \frac{\pi f W_{rec}}{\tan\delta} \tag{5.6}$$

here, it is observed from **equation 5.6** that the maximum power density depends on energy storage density and the dielectric loss of the material. Using the above relations, the power density of the BTO and BLFO/BTO3 bilayer films obtained is 0.5 and 0.9 MW/cm^3 at 100 Hz frequency.

Figure 5. 14(a) depicts the leakage current density (J) versus the electric field (E) for BTO and BLFO/BTO bilayer thin films with varying BLFO thicknesses. The current leakage characteristics curves of the films are asymmetric for positive and negative bias electric fields. The asymmetry in the leakage curves is due to the metal-ferroelectric-metal configuration [231]. It is evident from **Figure 5. 14(a)** that the bilayer films displayed a lower magnitude of leakage current densities than the monolayer BTO film. **Table 5. 8** lists the values of leakage current density and slopes at different field regions. A leakage current density of 1.69×10^{-4} A/cm^2 at 500 kV/cm is achieved for BTO films, whereas a significant decline in values is

observed for BLFO/BTO1, BLFO/BTO2, and BLFO/BTO3 heterostructures with 2.77×10^{-5}, 1.07×10^{-5}, and 5.99×10^{-6} A/cm^2, respectively. As the interface barriers exist at the interface of bilayer films, the movement of the free charge carriers is prevented in the heterostructure showing lower leakage current characteristics in the bilayer thin films [230]. An appreciable lower leakage current density in BLFO/BTO3 thin films can also be correlated with the lower oxygen vacancies and defects confirmed with the XPS analysis. The ferroelectric studies also supported the acquired low leakage current density for BLFO/BTO3 films.

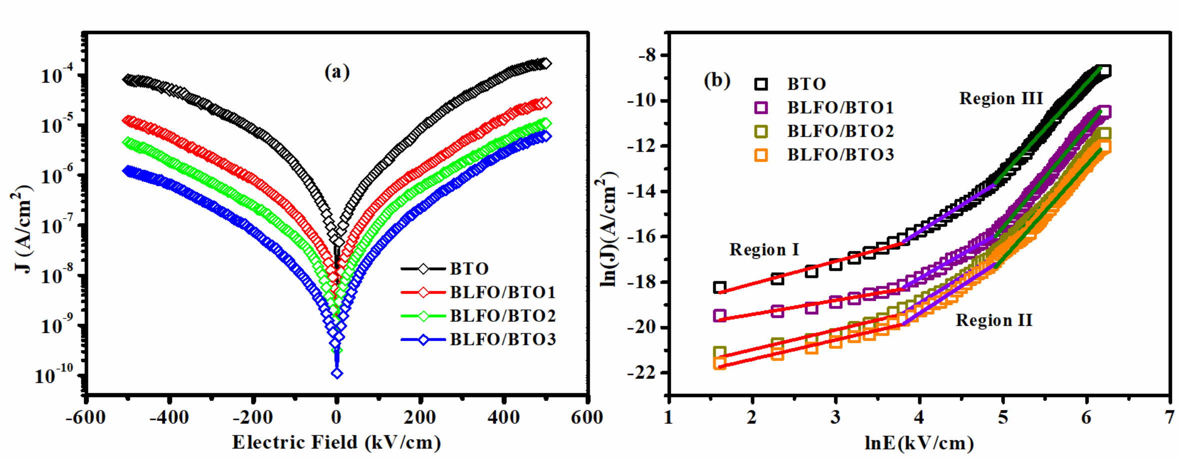

Figure 5. 14: (a) Leakage characteristics, and (b) log(J)-log(E) curves with slopes fitted at different field regimes for BTO monolayer and BTO/BLFO bilayer thin films.

The positive bias leakage current curves are fitted with the different leakage mechanisms to understand the conduction mechanism of the heterostructure thin films. It is found that the leakage current curves are well fitted with the space-charge-limited conduction (SCLC mechanism) using the power law relationship log(J)-log(E) shown by three straight lines in **Figure 5. 14(b)** for all the films. Three distinct electric field regions can be observed for each film. The fitting lines with different slopes (S) indicated the dominating conduction mechanism in the different field regions. In the lower field region (region I), the slope (S1) of the curve is almost 1, indicating the Ohmic behavior [208]. In region II, the slope (S2) values are around 2 suggesting the SCLC mechanism dominating in this field region. In the high field region (region III), an abrupt increase in the slope is observed (nearly S3~3.5) and can be explained by the trap-filled-limit (TFL) law. In this region, the contribution to the conduction mechanism is mainly attributed to all available traps filled by the injected electrons. The values of slopes at different field regimes are listed in **Table 5. 8** for all the films. Hence, the other conduction mechanisms ruling in different field region for the deposited films is explained through Ohmic, SCLC, and TFL mechanisms.

Table 5. 8: Leakage characteristics at a positive and negative bias (±500 kV/cm) and the SCLC fitted values at different field regions

Thin Film	***J(A/cm²)@ -500 kV/cm***	***J(A/cm²)@ +500 kV/cm***	***Region I (slope=S1)***	***Region II (slope=S2)***	***Region III (slope=S3)***
BTO	8.08×10^{-5}	1.69×10^{-4}	0.97	2.12	3.50
BLFO/BTO1	1.23×10^{-5}	2.77×10^{-5}	1.21	2.03	3.56
BLFO/BTO2	4.47×10^{-6}	1.07×10^{-5}	1.01	2.31	3.23
BLFO/BTO3	1.21×10^{-6}	5.99×10^{-6}	1.24	2.30	3.76

Table 5. 9 presents the comparison of the energy storage performance of the bilayer BLFO/BTO films with earlier values reported on BFO/BTO systems. The present study shows a relatively lower value of recoverable energy density as compared with the previous reports. It is worth noting that the energy storage performance of the BLFO/BTO films is achieved at the comparatively lower values of the applied field. So, it is promising for those devices that operate at lower applied fields. Further, it is also important to mention that the BLFO/BTO films are deposited on the cost-effective SiO_2/Si (100) and Pt-Si substrates compatible with the Si technology.

Table 5. 9: Comparison of the present work with earlier reported BFO/BTO heterostructures.

Films	**Deposition method**	**Substrate used**	W_{rec} **(J/cm^3)**	η**(%)**	E_{BDS} **(kV/cm)**	**Ref.**
BFO/BTO bilayer	RF sputtering	SRO/STO	51	73	2600	[80]
Mn -doped $BiFeO_3$–$BaTiO_3$ thin films	PLD	Conductive Nb-doped SrTiO3 (STO) (100) substrates	80	90	3100	[202]
BFBT single layer	PLD	$Pt/Ti/SiO_2/Si$	19	51	900	[203]
BFO/BTO multilayer	Spin coating	$Pt/Ti/SiO_2/Si$	121×10^{-3}	59	-	[204]
BFO/BTO bilayer	RF sputtering	$Pt/Ti/SiO_2/Si$	920×10^{-3}	79.7	330	[205]
BLFO/BTO bilayer	PLD	$Pt/Ti/SiO_2/Si$	11.65	85	746	Present work

In the former section of this chapter, the effect of top layer thickness in bilayer films is investigated successfully. The later section discusses the influence of a number of alternating interfacial layers on the energy storage performance of the fabricated multilayer films.

5.4 Results and discussions: BZNT/BTO multi-layer thin films:

The 3D surface topology of the films obtained using WSxM software over a scanned area of 2×2 μm^2 is depicted in **Figure 5. 15**(**a1**, **b1**, **c1**, **d1**, **e1**, and **f1**). The corresponding particle size distribution of the films is shown in **Figure 5. 15**(**a2**, **b2**, **c2**, **d2**, **e2**, and **f2**), which revealed the uniform particle size distribution of all hetero-structures. Further, the RMS roughness (R_{rms}) of the films is extracted from WSxM-generated parameters. R_{rms} estimated for a bare substrate is 0.23 nm in the scanned area of 2×2 μm^2. The BZNT films showed a low R_{rms} value of 5.13 nm among the deposited films, whereas BTO exhibited a moderate R_{rms} value of 22.51 nm. For hetero-structured films, the highest roughness of ~ 32.01 nm is observed for the tri-layered films (BZNT/BTO2) in which BTO is present in the top layer. As compared to tri-layered films (BZNT/BTO2), a relatively lower roughness is found for bi-layered (BZNT/BTO1) and tetra-layered films (BZNT/BTO3) with BZNT in the top layer. For BZNT/BTO1 and BZNT/BTO3 films, the roughness of 30.23 nm and 11.41 nm is estimated, and is worth noting that with an increasing number of alternate stacking layers, the roughness of the film is declined.

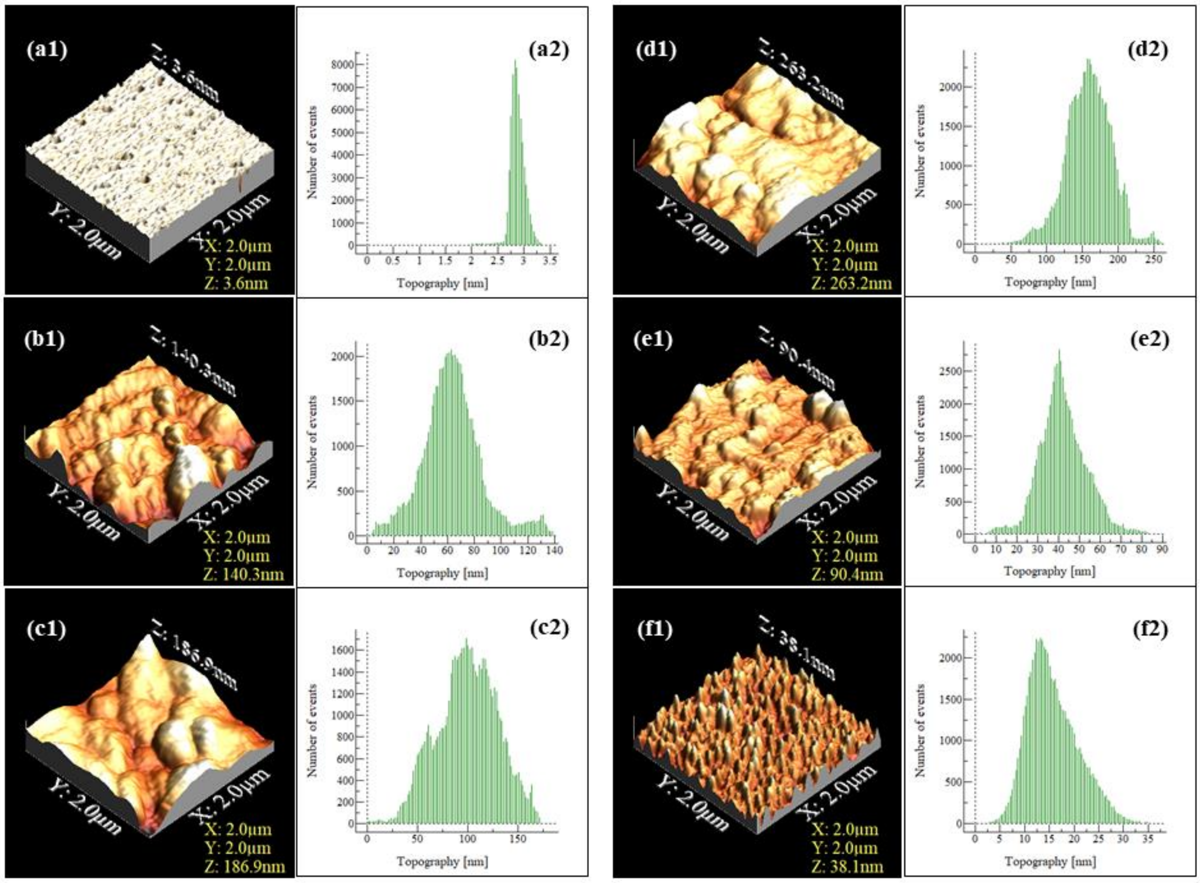

Figure 5. 15: Topological 3D representation and corresponding particle size histogram for (a) bare Si substrate, (b) BTO, (c) BZNT/BTO1, (d) BZNT/BTO2, (e) BZNT/BTO3 and (f) BZNT thin films.

The reduction in the roughness of the films with the stacking of alternate layers indicates the improved crystallization properties of the films. Therefore, the AFM analysis for alternately stacked hetero-structures strongly agreed with the expected stacking assumption. Generally, the film's roughness variation is correlated with the grain size. The roughness is expected to increase with improvement in grain size and increase in grain size leading to enhancement in structural properties [232]. Further, structural and morphological studies are carried out to see the effect of the stacking sequence of the deposited films.

The crystal structure of the deposited bi-layer, tri-layer, and tetra-layer structures is confirmed using an X-ray diffraction pattern and is depicted in **Figure 5. 16(a)**. The XRD patterns of monolayer BTO and BZNT thin films fabricated under the same deposition conditions have also been shown in the XRD plot for comparison. The monolayers BTO and BZNT are indexed with tetragonal (*P4mm*) and cubic symmetry (*Fd-3m*), referring to the JCPDS card no. 01-083-1880 and 01-079-6718, respectively. There is a slight peak shifting for BZNT diffraction peaks because the XRD pattern is indexed with the JCPDS card no 01-079-6718 for $Bi_3Zn_2Ta_3O_{14}$ composition. The XRD pattern of the multilayered thin films revealed that all the peaks correspond to either BTO (depicted by the "♣" symbol) or BZNT (depicted by the "♦" symbol) only. The absence of parasitic XRD peaks, except the presence of Si substrate peak (indicated by the "♥" symbol), is observed for tri-layered and tetra-layered films confirming the pure phase formation of the deposited films. It is also noticed that the bi-layer (BZNT/BTO1) films showed both the BTO and BZNT diffraction peaks with high-intensity BZNT peaks due to the deposition of BZNT on top of the BTO layer. Similarly, the tri-layer film resembles tetragonal and cubic phases with decreasing BZNT peaks and higher-intensity BTO diffraction peaks. Likewise, the growth of the tetra layers is also confirmed by the rise in intensity of diffraction peaks of the top layer (BZNT) in the BZNT/BTO3 film. Hence, well-grown bi-layer, tri-layer, and tetra-layer films with the stacking of each layer are evident in the deposited multilayer films.

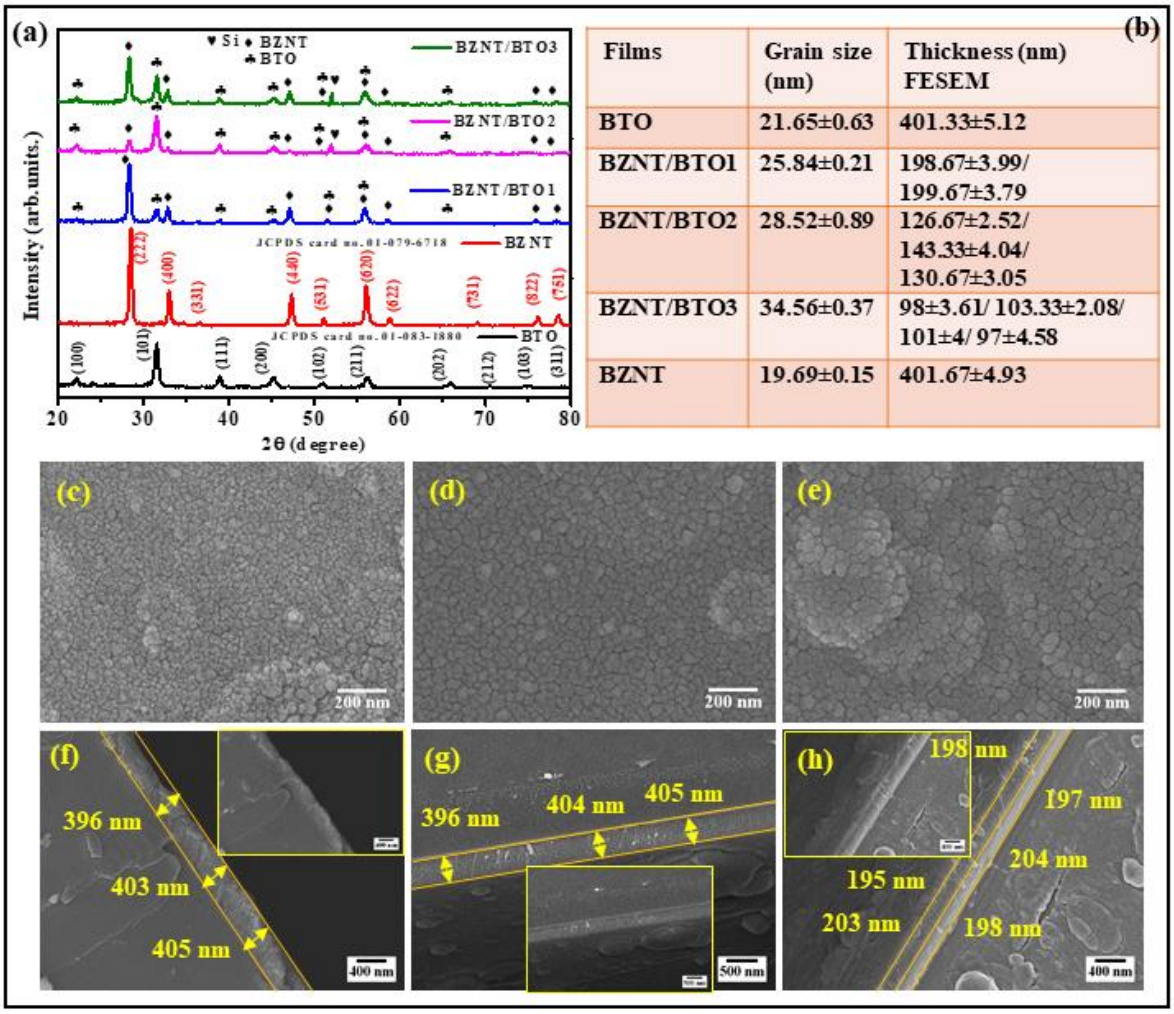

Films	Grain size (nm)	Thickness (nm) FESEM
BTO	21.65±0.63	401.33±5.12
BZNT/BTO1	25.84±0.21	198.67±3.99/ 199.67±3.79
BZNT/BTO2	28.52±0.89	126.67±2.52/ 143.33±4.04/ 130.67±3.05
BZNT/BTO3	34.56±0.37	98±3.61/ 103.33±2.08/ 101±4/ 97±4.58
BZNT	19.69±0.15	401.67±4.93

Figure 5. 16: Crystal structure representation using (a) XRD pattern, (b) Grain size and thickness estimation of all films using FESEM, (c-e) depict the microstructure of bi-layer (BZNT/BTO1), tri-layer (BZNT/BTO2), and tetra-layer (BZNT/BTO3) heterostructures, and (f-h) represents the FESEM cross-sectional micrograph of BTO monolayer, BZNT monolayer, and BZNT/BTO1 bi-layer films.

The estimated average grain size and film thickness using FESEM are shown in **Figure 5. 16(b)**. **Figure 5. 16(c-e)** depicts the morphology of the deposited multilayer films. The microstructure of the films showed uniform grain distributions with dense morphology. The average grain size is evaluated and found to be ~ 26, 28, and 35 nm for bi-layer, tri-layer, and tetra-layered films, respectively. The improvement in grain growth is observed with the number of stacking layers. The improvement in grain size with a number of stacking layers may be due to the higher crystallinity of the films. **Figure 5. 16(f-h)** illustrates the cross-section images of BTO and BZNT monolayer films along with BZNT/BTO1 bilayer film. The inset of **Figure 5. 16(f)** and **(g)** depict a well-grown monolayer of each film while the inset of **Figure 5. 16(h)** shows two distinct layers of bi-layer film. Each layer of BTO and BZNT of nearly 201 nm is estimated using ImageJ software. Likewise, the aggregate tri-layer and four-layered film's thickness is estimated to be 401 nm and 399 nm having each stacking layer of 134 and 100 nm, respectively.

XPS is a successful spectroscopic technique for revealing surface information, such as elemental composition, chemical status, and electronic states. The XPS survey spectrum for all films is presented in **Figure 5. 17(a)** with high-resolution XPS O1s spectra. The full scan of the XPS spectrum reveals all the elements in the fabricated films. It also suggests that the deposited alternate BTO and BZNT surface layers are well-grown in the hetero-structured films. Similar to XRD analysis, the XPS spectrum consisting of the BZNT top layer (BZNT/BTO1 and BZNT/BTO3 films) displays BZNT peaks sharply as compared to BTO top layer (BZNT/BTO2) films. In the case of BZNT/BTO2 film, Ba 3d, and Ti 2p peaks appear more prominently than that of Bi 4f, Zn 2p, Nb 3d, and Ta 4f peaks with the appearance of BTO on the top surface. XPS is a surface-sensitive technique that can identify the elemental chemical state, defects, and impurities within the material or covering on its surface. Therefore, it is more obvious to determine the surface profile of the top layer of the deposited films. Hence, the intensity of the top layer (BTO or BZNT) is prominently visible depending on the stacking order. HRXPS spectrum of the O1s state for all samples showed asymmetric peaks, indicating the presence of various bonds of oxygen in the deposited films. The peak profile of O1s spectra is fitted employing the Shirley background to observe two sub-peaks approximately at 529 and 531 eV for all the films. The peak at lower binding energy is mainly ascribed to the lattice oxygen, and the peak at higher binding energy is responsible for oxygen defects in the specimen. The decrease in oxygen vacancies/defects can be seen with several stacking layers indicating the lower imperfection and defect in the higher number of alternately stacked films (BZNT/BTO3) and is ascribed to the better quality of the deposited films.

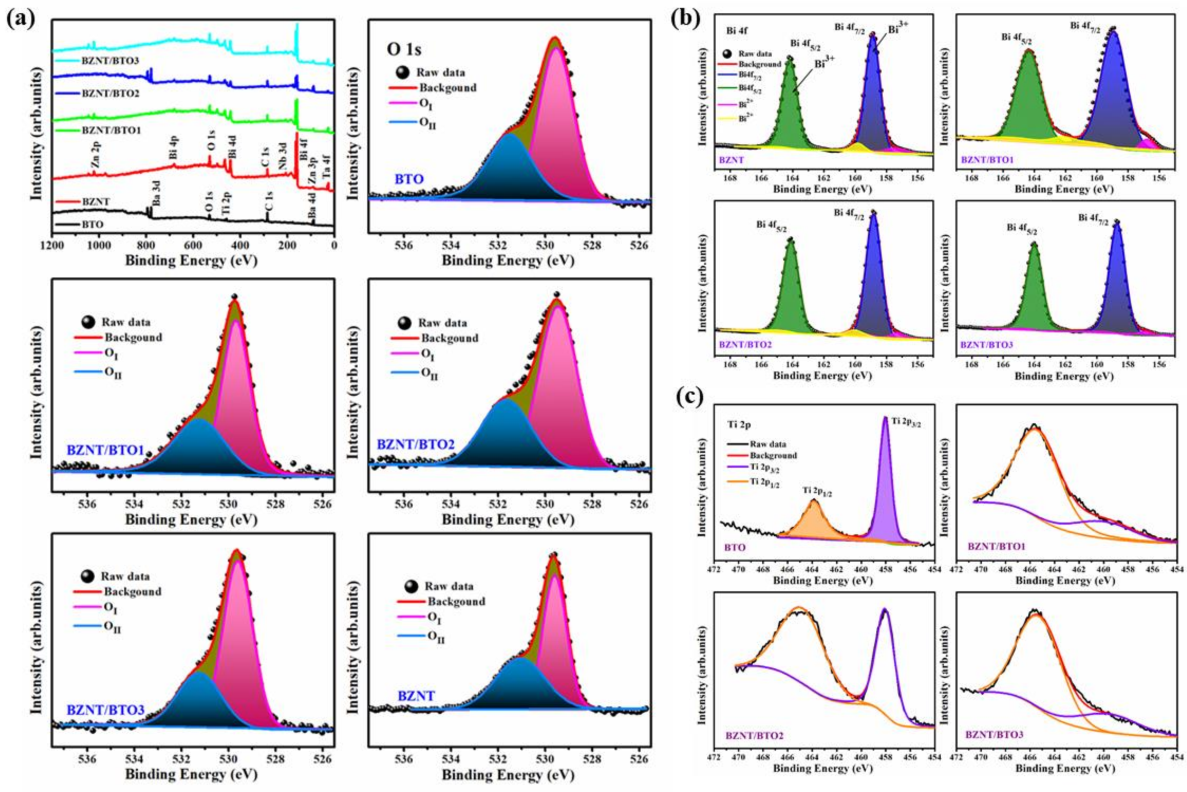

Figure 5. 17: (a) Full range XPS survey and High-resolution XPS O 1s spectra of all films, (b) Core level HRXPS spectra of Bi 4f state for BZNT monolayer and BZNT/BTO hetero-structured films, (c) Ti 2p state for BTO monolayer and BZNT/BTO hetero-structured films.

The quantitative contribution of lattice oxygen and oxygen defects obtained from the fitted area is listed in **Table 5. 10**, along with the peak positions of O 1s, Bi 4f, and Ti 2p states. The appearance/generation of oxygen defect and vacancies are inevitable in the fabricated oxide films owing to the volatilization of Bi and the reduction of Ti^{4+} to Ti^{3+} state (charge neutralization of multiple ionic state elements such as Bi and Ti) is explained further.

Table 5. 10: Quantitative contributions of lattice oxygen and oxygen vacancies and the peak positions of core level O 1s, Bi 4f, and Ti 2p states.

Films	***O_I* (eV)**	***O_{II}* (eV)**	***O_I (%)***	***O_{II} (%)***	***Bi $4f_{5/2}$* (eV)**	***Bi $4f_{7/2}$* (eV)**	***Ti $2p_{1/2}$* (eV)**	***Ti $2p_{3/2}$* (eV)**
BTO	529.5	531.5	67.16	32.84	-	-	458.0	463.8
BZNT/BTO1	529.6	531.2	68.66	31.34	158.8	164.1	459.9	465.3
BZNT/BTO2	529.4	531.6	69.64	30.36	158.7	164.0	458.0	464.7
BZNT/BTO3	529.6	531.2	71.00	29.00	158.6	163.9	459.5	465.2
BZNT	529.6	531.0	53.51	46.49	158.8	164.1	-	-

The diminishing of oxygen vacancies with many alternate stacking numbers can also be further verified by Bi 4f and Ti 2p states. **Figure 5. 17(b)** depicts the Bi 4f states for the BZNT monolayer and BZNT/BTO hetero-structures. For each film, two sub-peaks appeared nearly at 158.8 and 164.1 eV corresponding to Bi $4f_{5/2}$ and Bi $4f_{7/2}$ peaks with spin-orbit splitting (SOS) energy of ~5.3 eV validating the existence of Bi in 3+ state. Along with these peaks, the other two shoulder peaks appeared at lower binding energy, approximately at 157.4 and 159.8 eV for BZNT, BZNT/BTO1, and BZNT/BTO2 films. For tetra-layered (BZNT/BTO3) films, one peak at lower binding energy disappeared while the other is visible at 156.9 eV giving evidence of Bi in lower oxidation states. The existence of Bi in more than one chemical state (Bi^{3+} and Bi^{2+}) validates the existence of oxygen vacancies [144] in all the films that reduce with the stacking number of layers.

Additionally, **Table 5. 10** presents the Ti 2p states of BTO monolayer and BZNT/BTO hetero-structures depicting two peaks nearly at 458.0 and 463.8 eV corresponding to Ti $2p_{3/2}$ and Ti $2p_{1/2}$ peaks. For BTO monolayer film, two peaks are prominently visible for Ti $2p_{3/2}$ and Ti $2p_{1/2}$ states that are further broadened for BZNT/BTO2 bilayer film for which the BTO stacking is on the top surface. For the other two films with BZNT on the top surface, the peak intensity at lower binding energy (Ti $2p_{3/2}$) is almost diminished. Oxygen defects/vacancies are inherent for oxide thin films and hence cannot be avoidable. Therefore, the evidence of oxygen defects/vacancies is simultaneously observed for all the fabricated films, which can only be reduced to a certain amount for obtaining the higher quality films showing the better response. Controlled surface defect engineering is essential for tuning surface properties in enhancing ferroelectric as well as leakage conduction characteristics.

The dielectric permittivity is generally considered to be one of the key elements affecting energy storage performance. Hence, the dielectric properties of the multi-layered thin films are studied from 100 Hz to 1 MHz frequency range with varying temperatures from RT to 250 °C. **Figure 5. 18(a-d)** shows the dielectric permittivity (ε_r) and dielectric loss (tanδ) with frequency variation for all the fabricated thin films. It is observed from the graphs that both ε_r and tanδ decreased with a rise in frequency exhibiting normal dielectric behavior. Initially, a rapid drop in (ε_r) is seen up to 10^3 Hz frequency for all films which stabilizes with a rise in frequency. In general, there are different types of polarizations associated with the dielectric response, including dipolar, interfacial, ionic, and electronic polarizations. All of these polarizations are effective at low frequencies, whereas electronic and ionic polarizations are active at higher frequencies. Mainly, at lower frequencies dipoles are easily oriented in the direction of the applied field which contributes to the total polarization leading to high dielectric permittivity. As the frequency rises, these dipoles are no longer able to follow the rapidly varying applied field as a result oscillation begins to lag behind the applied field, and a decrease in permittivity is observed in the sample [233][234].

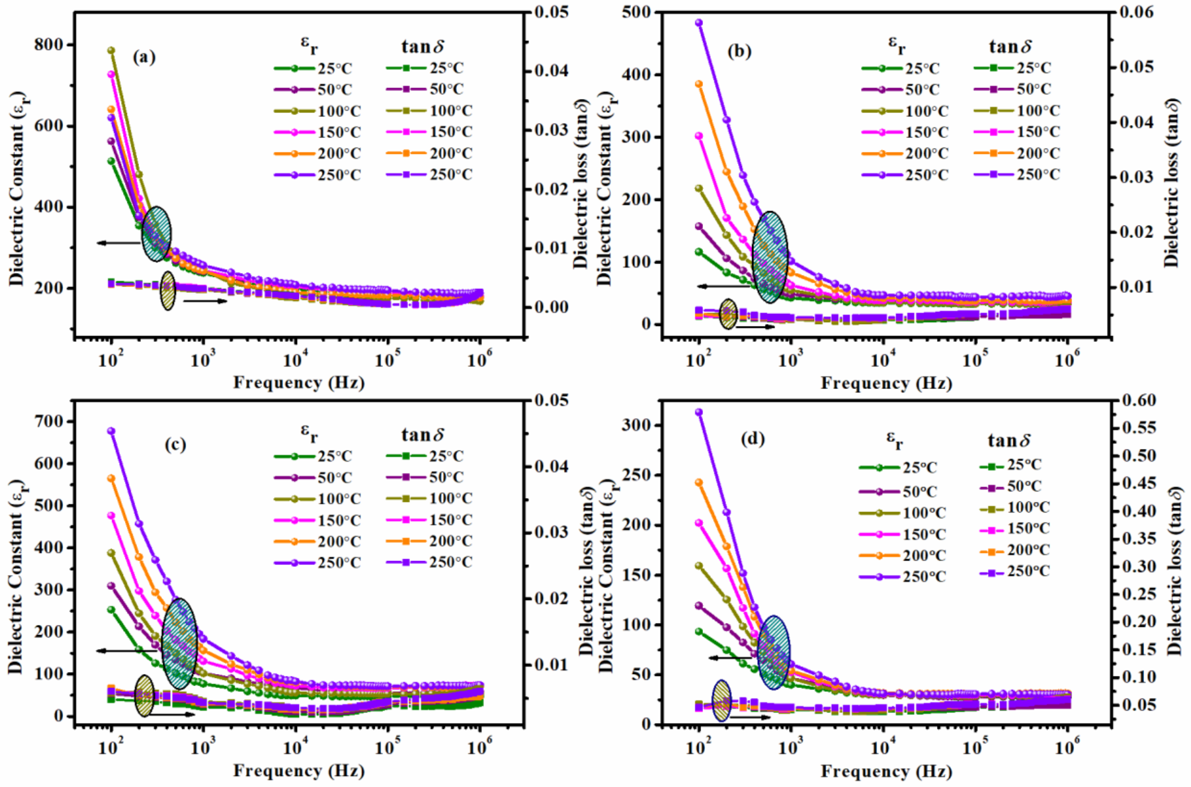

Figure 5. 18: Frequency-dependent of the dielectric response of (a) BTO, (b) BZNT/BTO1, (c) BZNT/BTO3, and (d) BZNT hetero-structured thin films.

All the films exhibited large dielectric dispersion with frequency indicating the existence of interfacial states due to space charge polarization [234]. Several models, including inhomogeneity and the electrode barrier effect present in the dielectric film, have been proposed to describe the dispersion in dielectric constant at lower frequencies [235]. In agreement with Koop's phenomenological theory, the higher dielectric dispersion at lower frequencies can be explained by the Maxwell-Wagner (MW) two-layer model [236]. The specimen, according to the MW two-layered model, is composed of two layers that include grains and grain boundaries, in which the conducting grains are separated by higher resistive grain boundaries [236][237][238]. The grain boundaries are more effective at lower frequencies, whereas the grains become active at higher frequencies [239]. The hopping of the electrons causes them to approach the grain boundary, where if the resistance is high enough, they will build up and produce polarization. This mechanism describes the polarization of grain boundaries at low-frequency regions and is more applicable for inhomogeneous structures like structural heterogeneity, multiphase materials, and materials with large amounts of interfaces and defects [240][241].

Given temperature-dependent dielectric behavior, **Figure 5. 18(a)** shows the dielectric response of BTO monolayer film at 100 Hz frequency, which attains the maximum dielectric permittivity (788 at 100 °C) close to the Curie temperature (T_c ~120-130°C) [242][228][229] of bulk BTO ceramics and declines again for the higher temperatures. At 100 Hz, BZNT/BTO1 and BZNT/BTO3 films displayed lower ε_r at RT in comparison to BTO monolayer film (ε_r ~ 514), which may be due to the introduction of a low dielectric constant layer (BZNT) in the hetero-structures [243]. However, among the hetero-structure films, BZNT/BTO3 displayed enhanced dielectric response (ε_r ~253 and tanδ ~10^{-3} at RT and 100 Hz frequency) may be attributed to the presence of a heterostructure interface. At the same time, the ε_r continues to rise sharply with temperature for BZNT/BTO1, BZNT/BTO3, and BZNT films, indicating that the transition temperature lies quite above the measured temperatures. Indeed, ε_r is relatively constant over an extensive range of frequencies at low temperatures. At the same time, it displays high values at lower frequencies at increasing temperatures may be explained by the Maxwell-Wagner effect [244]. This effect is common in oxide heterostructures due to the space charge polarization at the interface between film and electrode.

Likewise, the tanδ also followed a trend similar to dielectric permittivity, which declines with rising frequency. The tanδ shows a weak dependence on the frequency at lower frequencies for all the films. Beyond 100 kHz, the slight rising trend in tanδ with frequency is noticed, indicating the failure of the polarization mechanism of defective dipoles leading to a rise in dielectric loss [245]. The dielectric loss for the BZNT/BTO3 film is the lowest of the order of 10^{-3} among the deposited film expressing the quality and low defects. The growth condition, orientation, the type of electrode used, and interfaces between the films, however, all significantly impact the ε_r and tanδ in the case of thin films [246]. Hence, different dielectric responses can be expected from their bulk counterparts.

The Impedance spectroscopy (IS) investigation has been carried out to study the impact of various temperatures on the dielectric behavior of the heterostructured thin films. **Figure 5. 19(a-d)** displays the Nyquist plots of all thin films in the frequency range of 100 Hz-1 MHz and at various temperatures from 200-250 °C. The Nyquist diagrams illustrate that the diameter of a semi-circle is substantially influenced by measured temperature. The decrease in semicircular diameters as temperature rises results in a decrease in resistance, which is caused by the thermal activation energy of the charge carriers [247][248]. For all thin films, a depressed semicircle is observed, which reveals a non-Debye-type relaxation mechanism of the charge carriers [215]. For both BTO and BZNT monolayer films, the semi-circular curves are well-fitted with the two parallel RC circuits in series with additional resistance R, as shown in **Figure 5. 19(a)** and **(d)**. Here, R and C represent the resistance and capacitance. The first RC circuit (R_1C_1) contributes resistance and capacitance from grain and generally in high-frequency regions. The second RC (R_2C_2) circuit indicates the grain boundary contribution, which is at a lower frequency [249][250]. The additional resistance R suggests the contribution of electrode resistance, which is generally a lower value. The inset of **Figure 5. 19** shows the fitted electrical equivalent modeled circuit. In the case of bilayer and tetra-layered films, an additional RC circuit (R_3C_3) in series is observed (three RC circuits), indicating the interfacial polarization effect in hetero-structures [218]. The fitted parameters obtained from ZSimpWin software for grain, grain boundaries, and polarization effect for the films are listed in **Table 5.**

11. It can be concluded that the simulated data are very well-matched with the experimental data.

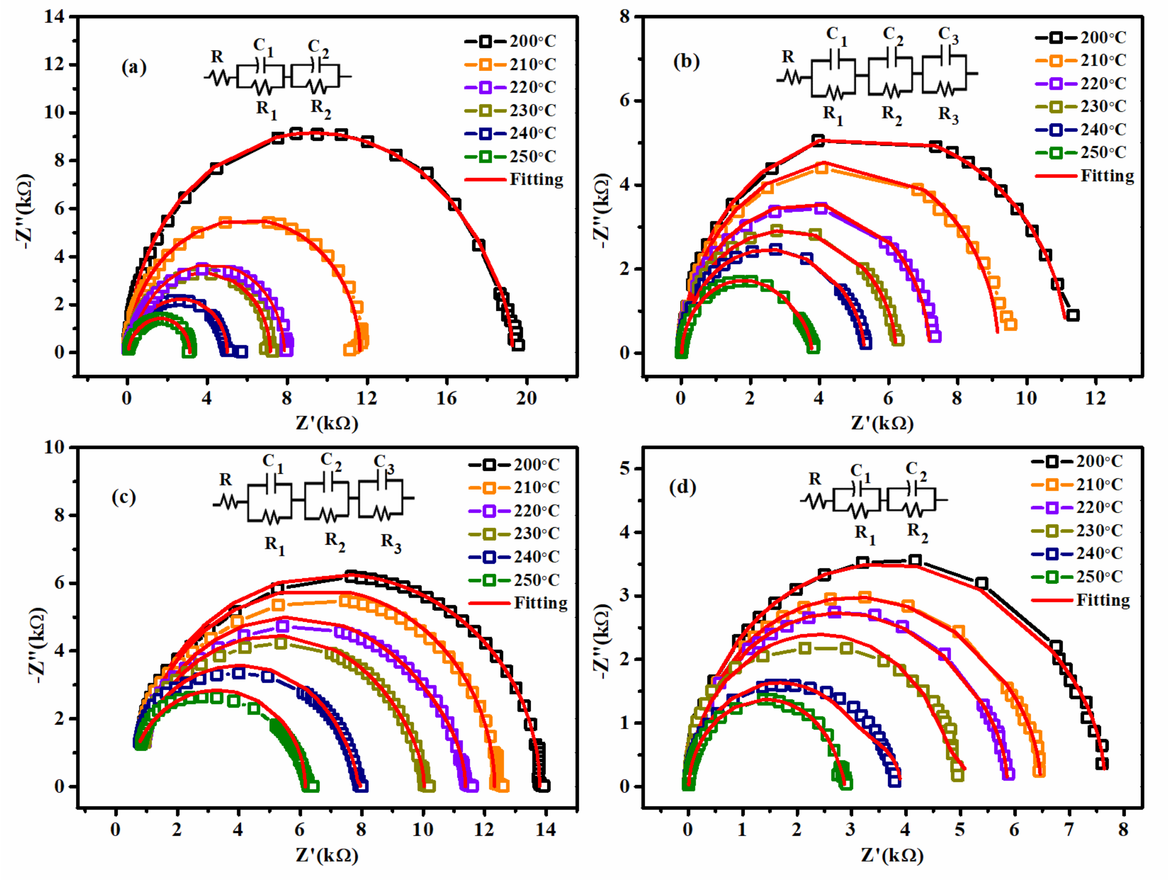

Figure 5. 19: Cole-Cole plots for (a) BTO, (b) BZNT/BTO1, (c) BZNT/BTO3, and (d) BZNT hetero-structured thin films.

Table 5. 11: The fitted parameters of the equivalent circuit elements measured at 250 °C

Elements	**R (Ω)**	**C_g (F)**	**R_g (Ω)**	**C_{gb} (F)**	**R_{gb} (Ω)**	**C_α (F)**	**R_α (Ω)**
BTO	21.8	1.89E-9	477	2.76E-9	2.59E5	-	-
BZNT/BTO1	17.83	2.24E-9	1911	1.94E-8	1.47E4	8.51E-8	13.74
BZNT/BTO3	62.41	2.76E-9	282	2.4E-8	4219	3.72E-7	27.97
BZNT	29.56	2.03E-9	285	1.77E-8	8093	-	-

Figure 5. 20(a-c) represents the ferroelectric hysteresis loops of multilayered thin films measured at 100 Hz frequency and 10 V applied bias voltage. When compared to bi-layer (BZNT/BTO1) and tri-layer (BZNT/BTO2) films, the tetra-layered (BZNT/BTO3) film displayed large maximum polarization (P_{max}) and low remnant polarization (P_r) with higher E_{BDS}, as shown in **Figure 5. 20(d)**, which is the essential criteria for the enhanced energy storage performance. In the case of heterostructure films, the lattice coupling between BTO and BZNT plays a major role in this evolution. Here, interfacial lattice induces lattice stretching, electron transfer, and domain segmenting effect. The first two effects give rise to polyhedral dipole polarization and interfacial polarization whereas the segment effect depresses the saturation polarization. With a rise in the number of layers, the P_{max} increases due to the interfacial lattice coupling owing to the contributions from polyhedral dipole polarization and interfacial polarization. Similarly, the decrease in P_r and coercive field (E_c) indicates the depression of the interaction between domains due to the segmenting effect [251]. It is worth noting that the multilayered structures exhibited enhanced ferroelectric properties with a greater number of stacking layers. Tetra layered films (Al/BTO/BZNT/BTO/BZNT/Si) exhibited a large P_{max} of 42.46 μC/cm^2 with comparable low P_r of 1.58 μC/cm^2 at an applied field of 2.58 MV/cm. The enhanced ferroelectric response of BZNT/BTO3 (tetra-layered) film may be due to the interfacial polarization acting a crucial role besides the other polarizations. A significant amount of space charge is generated at the multiple interfaces (Al/BTO/BZNT/BTO/BZNT/Si). These interfacial charges act as an effective charge trap for mobile electrons from metal electrodes under highly applied electric fields resulting in high electrical resistivity which further improves the electrical insulation, the breakdown field strength, and polarization [206]. Therefore, the current study unveils that the hetero-structured films having multiple interfaces improved the electrical insulation as well as boosted the polarization.

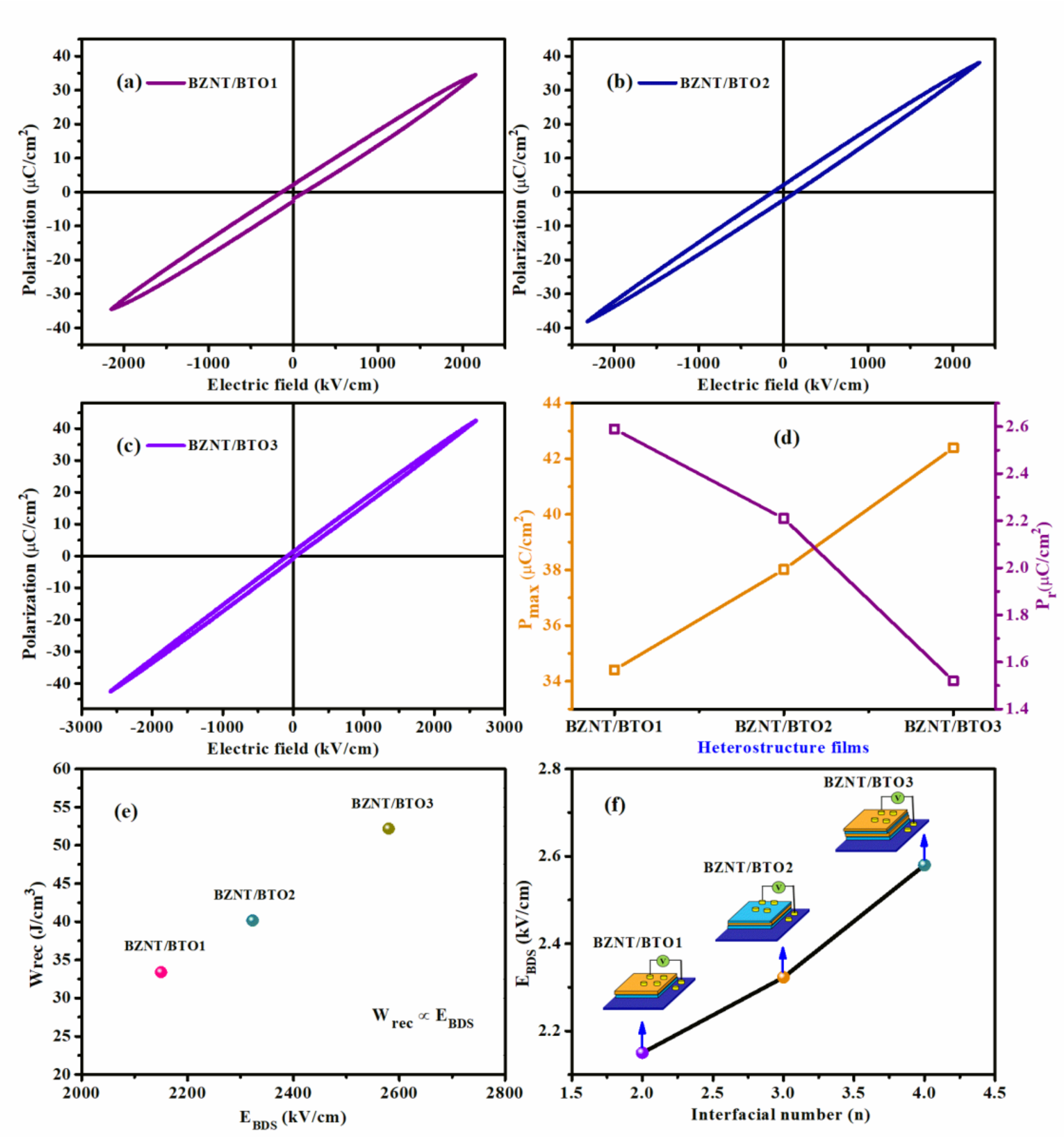

Figure 5. 20: (a-c) Ferroelectric loops measured at RT for fabricated heterostructure films, (d) maximum polarization and remnant polarization, (e) recoverable energy density with breakdown strength, and (f) breakdown strength with an interfacial number.

The ferroelectric loops are further employed to calculate the electrical storage properties. The formula to compute the charging, and discharging energy densities and energy efficiencies of the heterostructure capacitors is described in detail elsewhere [252]. The BZNT/BTO3 film exhibited a maximum value of W_{rec} and energy efficiency of 52.19 J/cm^3 and 92.21%, respectively at an applied field of 2.58 MV/cm as shown in **Figure 5. 20(e)**. The higher value of W_{rec} is attributed to a larger difference between P_{max} and P_r ($\Delta P = P_{max} - P_r$)

with high E_{BDS}. Similarly, the high energy efficiency (η) is ascribed to lower remnant polarization of the hetero-structured film. **Figure 5. 20(e)** also indicates that the recoverable energy density of the fabricated films is highly dependent on the breakdown strength. Likewise, **Figure 5. 20(f)** depicts the enhancement in breakdown strength with the number of interfacial layers.

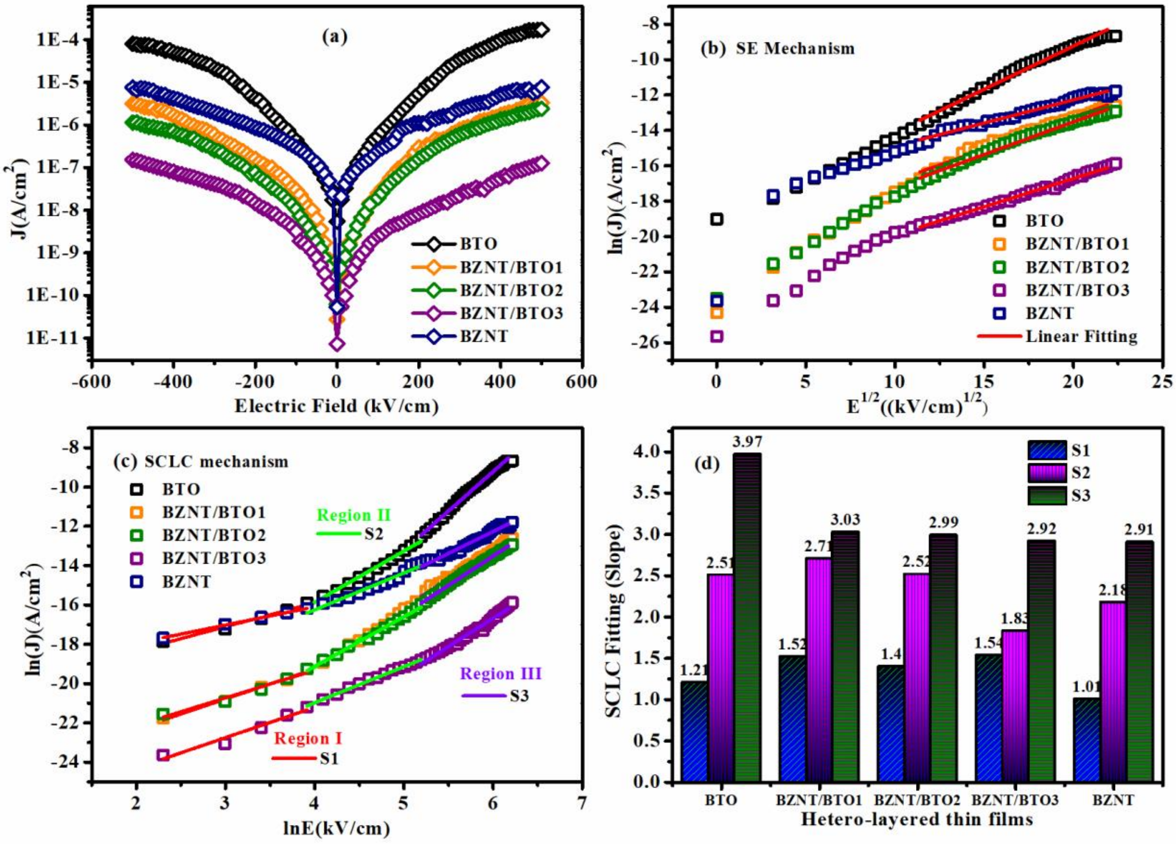

Figure 5. 21: (a) Leakage current characteristics and different types of leakage conduction model (b) SE mechanism, (c) SCLC mechanism fitted for BZNT/BTO multilayer thin films, and (d) shows the values of slope at different field regimes fitted linearly for log(J) versus log(E) plots.

Apart from the improved dielectric response, leakage current characteristic is another crucial parameter to understand the reliability of the films. **Figure 5. 21(a)** depicts the leakage current density of the multilayer thin films recorded at an applied field of ±500 kV/cm at room temperature. The J-E curve seems unsaturated even at a higher electric field (±500 kV/cm). All films displayed slight asymmetric current density curves for the positive and negative electric field, indicating the metal-ferroelectric-metal configuration [231], which is due to the difference in the work function of the electrode-film interface. Mainly, the leakage current density of the BZNT/BTO3 film is observed to be three orders of magnitude lower than the individual BTO and BZNT monolayer film, which is remarkably low compared to other deposited films. It is also evident that the lower leakage current density assisted in achieving higher polarization and a larger breakdown field [206], as can be seen for BZNT/BTO3 films. The lower leakage current density (~1.27×10^{-7} A/cm^2) in the BZNT/BTO3 film may result from a higher potential barrier of charge carriers gathered at the interface between the film and the electrode. Hence, stacking two different ferroelectric layers effectively reduces the leakage current density, significantly improving the E_{BDS}.

The leakage current mechanism includes Ohmic conduction, space charge limited conduction (SCLC), Schottky emission (SE), Poole-Frenkel emission (PF), and Fowler-Nordheim tunneling (FN) mechanism. Out of these conduction mechanisms, the SE and FN tunneling mechanism belongs to the electrode-limited conduction mechanism category, and the other belongs to the bulk-limited conduction mechanism [233]. The relation between the above conduction mechanism with the applied electric field is described in detail elsewhere [253]. Following the discussed relations, the different conduction models are fitted linearly to the experimental data to determine the dominant leakage mechanism in the fabricated multilayered films. Schottky Emission barrier mainly comes from the Fermi-level difference between the metal electrode and the films [254]. The linear fit in high electric field regions between ln(J) and $E^{0.5}$ curves is illustrated in **Figure 5. 21(b)** for all the films exhibited a well-fitted curve, implying that the SE mechanism is followed in the high electric field regions. Meanwhile, the possibility of the PF mechanism is ruled out for all the films as no linear behavior is observed between ln(*J/E*) and $E^{0.5}$ curves. In principle, both SE and PF mechanisms can be expressed as ln(*J*) proportional to $E^{0.5}$; however, only the SE mechanism appeared in the deposited films due to the formation of interfacial barrier layers between films and electrodes [255]. The profile of the log(J) versus log(*E*) plots for all films is shown in **Figure 5. 21(c)** indicates three regimes (I, II, and III regimes) with different slopes (S1, S2, and S3). The slope (S1) of regime I is approximately 1 for all films indicating the typical Ohmic behavior in low-frequency regions. Similarly, the slope in the intermediate regions is ~2, suggesting the SCLC mechanism is dominant in Regime II. When the electric field continues to increase, some of the injected electrons are trapped in the defects or voids, which slowly increases the density of electrons [256]. These trapped electrons are emitted at a particular electric field, giving rise to a trapped-filled conduction mechanism in that field regime. As a result, a sudden increase in conductivity is observed for these higher frequency regions reaching the value of slope ~3 in Regime III, featuring the trap-filled limited voltage is obeyed where J is proportional to E^n (with n>2) [257]. **Figure 5. 21(d)** gives the fitted value of slopes (S1, S2, and S3) in different field regimes (regime I, II, and III) from log(*J*) versus log(*E*) curves. Here, in the present study, the FN leakage-conduction mechanism can be excluded because the thickness of the as-prepared film is about 400 nm, much larger than 50 nm for the possible tunneling depth [254]. The non-existence of the FN mechanism in the films is also verified by a no-linear fitting of $\ln(J/E^2)$ vs. 1/E curves. Hence, the dominant mechanism in the fabricated films is typical Ohmic conduction behavior in low field regime while in high field regime, the conduction mechanism is governed by SCLC and SE mechanisms.

Table 5. 12 presents the comparison of the energy storage performance of the fabricated film to that of other recently reported multi-structure systems. It shows that the energy storage properties of this work achieved a relatively better response in terms of energy efficiency and recoverable energy density at a comparatively lower applied field of 2.58 MV/cm.

Table 5. 12: Comparison of the present work with multilayer films.

Multi-structures	**W_{rec} (J/cm^3)**	**η(%)**	**E_{BDS} (MV/cm)**	**Ref.**
$Ba_2Bi_{3.97}Pr_{0.03}Ti_5O_{18}/BiFeO_3$	79.3	75	4.22	[258]
$BaSn_{0.15}Ti_{0.85}O_3/Ba_{0.6}Sr_{0.4}TiO_3$	43.28	84.91	2.37	[259]
$0.5(Bi_{0.5}Na_{0.5})TiO_3$-$0.5Bi(Zn_{0.5}Zr_{0.5})O_3$	40.8	64.1	1.50	[260]
0.89NBT-0.06BT-0.05BFO	42.9	65.7	1.72	[261]
BFO/NBT/LSMO	37.0	47.8	2.68	[262]
$Na_{0.5}Bi_{0.5}(Ti_{0.97}Fe_{0.03})O_3/Ba_{(1-x)}Sr_xTiO_3$	67.18	75.65	3.17	[263]
$PbZrO_3/Al_2O_3$	32.6	88.1	4.76	[264]
0.8STO-0.8BFO	65	75	4.90	[265]
$Bi[Zn_{2/3}(Nb_{0.85}Ta_{0.15})_{1/3}]O_3/$ $BaTiO_3$ (tetra-layer)	52.19	92.2	2.58	Present work

5.5 Conclusions:

- The bi-layer and multi-layer films deposited on n-type and Pt Si substrates using a pulsed laser deposition technique have been reported. The bi-layer (BLFO/BTO) thin films with different top layer thicknesses, and multi-layered (BZNT/BTO) thin films with different numbers of stacking of alternate layers are fabricated.
- The bilayer (BLFO/BTO3) with higher top layer thickness and multilayered system with more stacking layers exhibited improved crystallinity, dense microstructure, enhanced ferroelectric response, and lower leakage current density.
- A significantly lower dielectric loss tangent of the order of 10^{-2} for BLFO/BTO3 and BZNT/BTO3 films suggests the better quality of the deposited films.
- The interfacial layer between BLFO and BTO enhances the energy density and efficiency ascribed to the enhancement of E_{BDS} induced via the interfacial barrier effect on the

conducting filaments. Hence, the heterostructure with BLFO/BTO3 displays an improved W_{rec} of 11.65 J/cm^3 with η of 85% at 746 kV/cm. A remarkably improved recoverable energy density of 52.19 J/cm^3 with an energy efficiency of 92.21% at 2.58 MV/cm is obtained for the higher number of stacking layered films. The enhanced energy storage performance may be attributed to the intervening ferroelectric BTO and BZNT layers in the multilayered BZNT/BTO3 films.

- The low value of leakage current density in the order of 10^{-6} A/cm^2 is also observed for BLFO/BTO3 films at an applied field of ±500 kV/cm. The experimental results achieved for BLFO/BTO heterostructures demonstrate that the interfacial layer is a very effective way of improving the energy storage performance of the films. Similarly, the lower leakage current value (~10^{-7} A/cm^2 at ±500 kV/cm) in the deposited tetra-layered BZNT/BTO multilayer structure assures its appropriateness for the device applications. Ohmic, SCLC, and SE mechanisms are dominant leakage mechanisms observed in all films at different field regimes. Hence, the fabricated multilayered structures are promising for energy storage applications.

Chapter 6

Conclusion and Future Scope

This chapter highlights the important findings and discussions of BTO-BFO and BTO-BZNT solid solutions, BLFO thin films, BLFO/BTO bilayer films, and BZNT/BTO multilayer heterostructures.

6 Summary

This thesis work is mainly focused on lead-free dielectric ceramics and thin films for energy storage applications. The fundamental aspects of dielectric ceramics, their applications in pulsed power devices, evaluation of energy storage parameters, $BaTiO_3$-$BiMeO_3$ solid solution family, and thin films are presented in **Chapter 1**. A detailed synthesis route and characterization techniques are discussed in **Chapter 2**. Successful efforts have been made to enhance the structural, morphological, electrical, and ferroelectric properties of dielectric ceramics through compositional modification and forming solid solutions as presented in **Chapter 3**. Optimization of pure phase BFO, excess Bi addition, and substitution with La-rare earth element to obtain single-phase bismuth ferrite and to reduce the leakage current density in BLFO ceramics. Subsequently, the BLFO thin films are deposited by the PLD technique to investigate the ferroelectric response presented in **Chapter 4**. Further, the effect of interfacial layers on bi-layer and multi-layer thin films in improving the energy storage performance is discussed in **Chapter 5**. A summary of important findings of the thesis work is concluded in **Chapter 6** as follows.

6.1 Conclusions

- A detailed investigation of two systems (BTBF and BT-BZNT) from $BaTiO_3$-Bi*Me*O_3 solid solution has been reported. The crystal symmetry, morphology, dielectric behavior, and ferroelectric properties are studied. The BTBF and BT-BZNT crystallize into dual phases of pseudo-cubic and tetragonal-rhombohedral crystal structures respectively.
- The binary solution (BTBF1) exhibited two dielectric anomalies around 60 °C and 150 °C corresponding to phase transition peaks for $T_{O\text{-}T}$ and T_C phases. Similarly, the BT-BZNT1 sample displayed two peaks at ~95°C (T_{m1}) and ~155°C (T_{m2}) associated with the two particular structures of the grains. The peak at higher temperatures is around ~155°C (T_{m2}) is the T_C for the BT-BZNT sample. In both series, the T_C slightly shifted to a higher temperature with higher substitution. The BTBF1 ceramic showed enhanced dielectric properties with a large dielectric constant (ε_r =1555) and low loss tangent ($tan\delta$ = 0.08) at 1MHz among the prepared BTBF ceramics.
- The ferroelectric studies for both compositions are analyzed to evaluate energy storage performance. The BTBF composition displayed a W_{rec} and η (%) of ~ 40mJ/cm^3 and 60.92% respectively at 25 kV/cm applied field, which is sufficiently lower as compared to other $BaTiO_3$-$BiMeO_3$ systems. However, a significant improvement in energy storage performance is observed in BT-BZNT ceramics. A remarkably high W_{rec} of 2.06 J/cm^3 with an η(%) of 78% is achieved for BT-BZNT3 ceramics at an applied field of 180 kV/cm. The ultrahigh-energy efficiency of up to 96% is observed for higher concentrations in BT-BZNT ceramics. In this study, BT-BZNT3 and BT-BZNT4 ceramics exhibited a comparable energy storage performance at a lower applied field of 180 kV/cm demonstrating the excellence of BT-BZNT ceramics over other $BaTiO_3$-$BiMeO_3$ family.
- A BLFO ceramics is initially optimized to obtain the single-phase to reduce leakage current density. As bismuth is highly volatile, it facilitates the formation of impurity phases like

$Bi_2Fe_4O_9$, $Bi_{25}FeO_{39}$, and $Bi_{25}FeO_{40}$, and the preparation of a phase pure BFO is challenging, especially in realizing as a thin film. A highly crystalline and pure phase $Bi_{0.993}La_{0.007}FeO_3$ (BLFO) thin films have been grown using a pulsed laser deposition technique at different oxygen partial pressures (OPPs) on n-type silicon and quartz substrates.

- The film deposited at 20 SCCM OPPs at 500 °C under 10^{-2} mbar pressure exhibited a higher intensity diffraction pattern. The XRD pattern revealed a rhombohedral phase structure with an *R3c* space group, which is further confirmed by the crystal planes (110), and (066) found by the high-resolution HRTEM image and SAED patterns. An improvement in grain size and surface roughness with increased OPP concentration is observed by microstructural and topological investigation. An improvement in dielectric constant (447) with minimum loss tangent (0.202) at RT is found for 20 SCCM deposited films. At the same time, the existence of mixed-phase of Fe^{2+} and Fe^{3+} along with oxygen vacancies is validated with the XPS spectra.
- Further, the ferroelectric behavior for all films is analyzed using ferroelectric hysteresis loops for all deposited films. Among all, 20 SCCM deposited films exhibited an enhanced energy storage density of 2.09 J/cm^3, having an energy efficiency of 78.42% at the applied field of 488 kV/cm. The lower leakage current density of ~1.08×10^{-7} is estimated for 20 SCCM film attributing to dense microstructure and favorable oxygen ambiance. Hence, the BLFO thin films can be used for energy storage capacitor applications.
- Several different types of interfaces, such as asymmetric top and bottom film-electrode interfaces and ferroelectrics/ non-ferroelectrics heterogeneous interfaces, are formed in the ferroelectrics/non-ferroelectrics heterogeneous bi-layered and multi-layered films. It is well known that the physical properties of ferroelectric thin films are very sensitive to the presence of interfaces. These interfaces will inevitably influence the electrical properties

and parameters of ferroelectric devices. The BLFO/BTO bi-layer thin films with varying top layer thicknesses and BZNT/BTO multi-layer heterostructures with a number of stacking layers are deposited on n-type and Pt Si substrate using a pulsed laser deposition technique.

- The structural stability, dielectric, ferroelectric, magnetic, and leakage current characteristics based on top layer variation (for BLFO/BTO) and a number of stacking layers (BZNT/BTO) are investigated. The higher top layer thickness film (BLFO/BTO3) and higher number of stacking films (BZNT/BTO3; tetra-layer) exhibited improved crystallinity, dense microstructure, enhanced ferroelectric response, and lower leakage current density.
- The interfacial layer between BLFO and BTO enhances the energy density and efficiency ascribed to the enhancement of E_{BDS} induced via the interfacial barrier effect on the conducting filaments. Hence, the heterostructure with BLFO/BTO3 displays an improved W_{rec} of 11.65 J/cm^3 with η of 85% at 746 kV/cm. At the same time, a remarkable enhancement in recoverable energy density (W_{rec}) of 52.19 J/cm^3 with energy efficiency (η) of 92.21% at 2.58 MV/cm is achieved for the higher number of stacking layered films among the BZNT/BTO multi-layer films. This enhancement in energy storage performance may be attributed to the intervening ferroelectric BTO and BZNT layers in the multilayered BZNT/BTO3 films. In both cases, a low value of leakage current density in the order of ~10^{-6} A/cm^2 and ~10^{-7} A/cm^2 is also observed for BLFO/BTO3 and tetra-layer BZNT/BTO films at an applied field of ±500 kV/cm respectively. Hence, a small leakage current value in the deposited bi-layer (BLFO/BTO) and multi-layer (BZNT/BTO) films assures their appropriateness for energy storage device applications.

6.2 Future scope:

- In particular, dielectric ceramic films demonstrating energy densities of 50–300 J cm^{-3}, storage efficiencies of 60–90%, breakdown fields of 1–6 MV cm^{-1}, fatigue life of 10^6–10^9 cycles, and stability in the temperature range of -50 to 200 °C have a huge potential for implementation in real device applications.
- Some effective approaches that have been adopted for enhancing the energy storage properties of dielectric ceramic films include fabrication of films with compositionally graded layers, formation of solid solutions of ceramics, control of crystallographic orientation of the films, domain engineering via lattice mismatch and misfit strain between the film and the substrate, and manipulation of composition and charge transport across the film/electrode interface.
- Despite the progress accomplished through these approaches, there is plenty of room for further improvement as several issues remain to be addressed. The conduction losses and polarization fatigue in energy storage dielectrics under high electric fields and at high temperatures are concerning. The temperature-dependent ferroelectric response to investigate the temperature stability of dielectric ceramics and thin films needs to be further studied. Likewise, the frequency dependence of energy storage properties of the dielectrics has not been given enough attention and should be explored further.

For practical implementation of the dielectric ceramic films in pulsed power capacitors, it is necessary to consider the aspects of device design and operating conditions. Although significantly large volume-specific energy storage densities have been obtained in dielectric ceramic films, the absolute energy stored in them is rather small due to their thickness/volume limitations. Therefore, the corresponding devices must be designed with configurations involving series and parallel connections. For the long-term operation of the dielectric capacitors, the intrinsic energy storage characteristics must be retained after the capacitor is assembled with other electronic components for its final application. The capacitor must be reliable regardless of the exposure to derated voltages, temperatures, and a variety of operating conditions. To expedite the implementation of energy storage dielectric capacitors in practical applications, future research and development activities should focus on

i) Improving the fundamental understanding of complex structure–property relationships,

ii) Using high-throughput computational screening Combined with experimental synthesis and testing,

iii) Simple and scalable synthesis and processing approaches for fabrication of large-area (wafer-scale) and freestanding dielectric ceramic films,

iv) Developing a set of standard practices for energy storage performance evaluation, and

v) Establishing a consensus of typical property requirements for energy storage dielectric capacitors used in real pulsed power electronic devices.

References

[1] A. Jain, Y. G. Wang, and L. N. Shi, “Recent developments in $BaTiO_3$ based lead-free materials for energy storage applications,” *J. Alloys Compd.*, vol. 928, p. 167066, 2022, doi: 10.1016/j.jallcom.2022.167066.

[2] L. Yang *et al.*, “Perovskite lead-free dielectrics for energy storage applications,” *Prog. Mater. Sci.*, vol. 102, no. December 2018, pp. 72–108, 2019, doi: 10.1016/j.pmatsci.2018.12.005.

[3] U.S. Department of Energy, “Energy Storage Grand Challenge Energy Storage Market Report 2020,” *U.S. Dep. Energy*, vol. Technical, no. December, p. 65, 2020.

[4] K. Zou *et al.*, “Recent advances in lead-free dielectric materials for energy storage,” *Mater. Res. Bull.*, vol. 113, no. January, pp. 190–201, 2019, doi: 10.1016/j.materresbull.2019.02.002.

[5] H. Zhang *et al.*, “A review on the development of lead-free ferroelectric energy-storage ceramics and multilayer capacitors,” *J. Mater. Chem. C*, vol. 8, no. 47, pp. 16648–16667, 2020, doi: 10.1039/d0tc04381h.

[6] L. Yang *et al.*, “Perovskite lead-free dielectrics for energy storage applications,” *Prog. Mater. Sci.*, vol. 102, no. May 2018, pp. 72–108, 2019, doi: 10.1016/j.pmatsci.2018.12.005.

[7] M. Peddigari, H. Palneedi, G. T. Hwang, and J. Ryu, “Linear and nonlinear dielectric ceramics for high-power energy storage capacitor applications,” *J. Korean Ceram. Soc.*, vol. 56, no. 1, pp. 1–23, 2019, doi: 10.4191/kcers.2019.56.1.02.

[8] H. Palneedi, M. Peddigari, G. T. Hwang, D. Y. Jeong, and J. Ryu, “High-Performance Dielectric Ceramic Films for Energy Storage Capacitors: Progress and Outlook,” *Adv. Funct. Mater.*, vol. 28, no. 42, pp. 1–33, 2018, doi: 10.1002/adfm.201803665.

[9] M. S. Whittingham, “History, evolution, and future status of energy storage,” *Proc. IEEE*, vol. 100, no. SPL CONTENT, pp. 1518–1534, 2012, doi: 10.1109/JPROC.2012.2190170.

[10] A. Z. AL Shaqsi, K. Sopian, and A. Al-Hinai, “Review of energy storage services, applications, limitations, and benefits,” *Energy Reports*, vol. 6, pp. 288–306, 2020, doi: 10.1016/j.egyr.2020.07.028.

[11] K. Laadjal and A. J. M. Cardoso, “Multilayer Ceramic Capacitors: An Overview of Failure Mechanisms, Perspectives, and Challenges,” *Electron.*, vol. 12, no. 6, 2023, doi: 10.3390/electronics12061297.

[12] W. Zhu *et al.*, “A review: $(Bi,Na)TiO_3$ (BNT)-based energy storage ceramics,” *J. Mater.*, vol.

3, no. xxxx, 2023, doi: 10.1016/j.jmat.2023.05.002.

[13] S. Liu and B. Shen, "energy density and ultra-fast discharge speed for," pp. 15118–15135, 2019, doi: 10.1039/c9tc05253d.

[14] A. R. Jayakrishnan *et al.*, "Are lead-free relaxor ferroelectric materials the most promising candidates for energy storage capacitors?," *Prog. Mater. Sci.*, vol. 132, no. November 2022, 2023, doi: 10.1016/j.pmatsci.2022.101046.

[15] Z. Yang, H. Du, L. Jin, and D. Poelman, "High-performance lead-free bulk ceramics for electrical energy storage applications: design strategies and challenges," *J. Mater. Chem. A*, vol. 9, no. 34, pp. 18026–18085, 2021, doi: 10.1039/d1ta04504k.

[16] K. Reichmann, A. Feteira, and M. Li, "Bismuth Sodium Titanate based materials for piezoelectric actuators," *Materials (Basel).*, vol. 8, no. 12, pp. 8467–8495, 2015, doi: 10.3390/ma8125469.

[17] B. Wang, L. Luo, X. Jiang, W. Li, and H. Chen, "Energy-storage properties of (1-x)$Bi_{0.47}Na_{0.47}Ba_{0.06}TiO_3$-x$KNbO_3$ lead-free ceramics," *J. Alloys Compd.*, vol. 585, pp. 14–18, 2014, doi: 10.1016/j.jallcom.2013.09.052.

[18] L. Luo, B. Wang, X. Jiang, and W. Li, "Energy storage properties of (1-x)$(Bi_{0.5}Na_{0.5})TiO_3$-x$KNbO_3$ lead-free ceramics," *J. Mater. Sci.*, vol. 49, no. 4, pp. 1659–1665, 2014, doi: 10.1007/s10853-013-7849-9.

[19] Q. Li, J. Wang, Y. Ma, L. Ma, G. Dong, and H. Fan, "Enhanced energy-storage performance and dielectric characterization of $0.94Bi_{0.5}Na_{0.5}TiO_3$-$0.06BaTiO_3$ modified by $CaZrO_3$," *J. Alloys Compd.*, vol. 663, pp. 701–707, 2016, doi: 10.1016/j.jallcom.2015.12.194.

[20] X. Zhou *et al.*, "Energy storage properties and electrical behavior of lead-free $(1-x)$ $Ba_{0.04}Bi_{0.48}Na_{0.48}TiO_3$–x$SrZrO_3$ ceramics," *J. Mater. Sci. Mater. Electron.*, vol. 27, no. 4, pp. 3948–3956, 2016, doi: 10.1007/s10854-015-4247-x.

[21] M. Yao, Y. Pu, H. Zheng, L. Zhang, M. Chen, and Y. Cui, "Improved energy storage density in 0.475BNT-0.525BCTZ with MgO addition," *Ceram. Int.*, vol. 42, no. 7, pp. 8974–8979, 2016, doi: 10.1016/j.ceramint.2016.02.155.

[22] P. Kumar, M. Pattanaik, and Sonia, "Synthesis and characterizations of KNN ferroelectric ceramics near 50/50 MPB," *Ceram. Int.*, vol. 39, no. 1, pp. 65–69, 2013, doi: 10.1016/j.ceramint.2012.05.093.

[23] J. F. Li, K. Wang, B. P. Zhang, and L. M. Zhang, "Ferroelectric and piezoelectric properties of fine-grained $Na_{0.5}K_{0.5}NbO_3$ lead-free piezoelectric ceramics prepared by spark plasma

sintering," *J. Am. Ceram. Soc.*, vol. 89, no. 2, pp. 706–709, 2006, doi: 10.1111/j.1551-2916.2005.00743.x.

[24] H. Gu, K. Zhu, X. Pang, B. Shao, J. Qiu, and H. Ji, "Synthesis of (K, Na) (Nb, Ta)O_3 lead-free piezoelectric ceramic powders by high temperature mixing method under hydrothermal conditions," *Ceram. Int.*, vol. 38, no. 3, pp. 1807–1813, 2012, doi: 10.1016/j.ceramint.2011.10.003.

[25] B. Mohanty, S. Bhattacharjee, N. C. Nayak, R. K. Parida, and B. N. Parida, "Dielectric, magnetic and optical study of La- doped BFO-BST ceramic for multifunctional applications," *Mater. Sci. Semicond. Process.*, vol. 128, no. November 2020, p. 105720, 2021, doi: 10.1016/j.mssp.2021.105720.

[26] F. Zhang, X. Zeng, D. Bi, K. Guo, Y. Yao, and S. Lu, "Dielectric, ferroelectric, and magnetic properties of Sm-Doped $BiFeO_3$ ceramics prepared by a modified solid-state-reaction method," *Materials (Basel).*, vol. 11, no. 11, 2018, doi: 10.3390/ma11112208.

[27] H. Maleki, "Characterization and photocatalytic activity of Y-doped $BiFeO_3$ ceramics prepared by solid-state reaction method," *Adv. Powder Technol.*, no. September, pp. 1–9, 2019, doi: 10.1016/j.apt.2019.08.031.

[28] S. P. Balmuchu and P. Dobbidi, "The effect of La doping on multiferroic $BiFeO_3$ ceramic through structural, dielectric, magnetic, ferroelectric, and optical studies," *Phys. B Condens. Matter*, vol. 638, no. March, p. 413937, 2022, doi: 10.1016/j.physb.2022.413937.

[29] M. Acosta *et al.*, "$BaTiO_3$-based piezoelectrics: Fundamentals, current status, and perspectives," *Appl. Phys. Rev.*, vol. 4, no. 4, 2017, doi: 10.1063/1.4990046.

[30] J. J. Wang, F. Y. Meng, X. Q. Ma, M. X. Xu, and L. Q. Chen, "Lattice, elastic, polarization, and electrostrictive properties of $BaTiO_3$ from first-principles," *J. Appl. Phys.*, vol. 108, no. 3, pp. 0–6, 2010, doi: 10.1063/1.3462441.

[31] A. R. Jayakrishnan *et al.*, "Are lead-free relaxor ferroelectric materials the most promising candidates for energy storage capacitors?," *Prog. Mater. Sci.*, vol. 132, no. November 2022, p. 101046, 2023, doi: 10.1016/j.pmatsci.2022.101046.

[32] W. Wang *et al.*, "Modified relaxor ferroelectrics in $BiFeO_3$-(Ba,Sr)TiO_3-$BiScO_3$ ceramics for energy storage applications," *Sustain. Mater. Technol.*, vol. 32, no. February, pp. 1–10, 2022, doi: 10.1016/j.susmat.2022.e00428.

[33] H. Tang *et al.*, "Enhancement of energy-storage properties in $BiFeO_3$-based lead-free bulk ferroelectrics," *Ceram. Int.*, vol. 48, no. 12, pp. 16792–16799, 2022, doi:

10.1016/j.ceramint.2022.02.229.

[34] D. Zheng, R. Zuo, D. Zhang, and Y. Li, “Novel $BiFeO_3$-$BaTiO_3$-$Ba(Mg_{1/3}Nb_{2/3})O_3$ Lead-Free Relaxor Ferroelectric Ceramics for Energy-Storage Capacitors,” *J. Am. Ceram. Soc.*, vol. 98, no. 9, pp. 2692–2695, 2015, doi: 10.1111/jace.13737.

[35] G. Liu *et al.*, “An investigation of the dielectric energy storage performance of $Bi(Mg_{2/3}Nb_{1/3})O_3$-modifed $BaTiO_3$ Pb-free bulk ceramics with improved temperature/frequency stability,” *Ceram. Int.*, vol. 45, no. 15, pp. 19189–19196, 2019, doi: 10.1016/j.ceramint.2019.06.166.

[36] Y. Yan *et al.*, “Enhanced energy storage in temperature stable $Bi_{0.5}Na_{0.5}TiO_3$-modified $BaTiO_3$-$Bi(Zn_{2/3}Nb_{1/3})O_3$ ceramics,” *Ceram. Int.*, vol. 48, no. 24, pp. 36478–36489, 2022, doi: 10.1016/j.ceramint.2022.08.208.

[37] H. Zhao, X. Yang, D. Pang, and X. Long, “Enhanced energy storage efficiency by modulating field-induced strain in $BaTiO_3$-$Bi(Ni_{2/3}Ta_{1/3})O_3$ lead-free ceramics,” *Ceram. Int.*, vol. 47, no. 16, pp. 22734–22740, 2021, doi: 10.1016/j.ceramint.2021.04.290.

[38] X. Dong, H. Chen, M. Wei, K. Wu, and J. Zhang, “Structure, dielectric and energy storage properties of $BaTiO_3$ ceramics doped with $YNbO_4$,” *J. Alloys Compd.*, vol. 744, pp. 721–727, 2018, doi: 10.1016/j.jallcom.2018.01.276.

[39] X. Jiang *et al.*, “Enhanced energy storage and fast discharge properties of $BaTiO_3$ based ceramics modified by $Bi(Mg_{1/2}Zr_{1/2})O_3$,” *J. Eur. Ceram. Soc.*, vol. 39, no. 4, pp. 1103–1109, 2019, doi: 10.1016/j.jeurceramsoc.2018.11.025.

[40] M. U. Rehman, A. Manan, A. Ullah, Y. Iqbal, M. A. Khan, and R. Muhammad, “Structural, dielectric and complex impedance analysis of Pb-free $BaTiO_3$-$Bi(Mg_{0.5}Ce_{0.5})O_3$ ceramics,” *J. Alloys Compd.*, vol. 947, p. 169575, 2023, doi: 10.1016/j.jallcom.2023.169575.

[41] T. Wang, L. Jin, C. Li, Q. Hu, and X. Wei, “Relaxor ferroelectric $BaTiO_3$-$Bi(Mg_{2/3}Nb_{1/3})O_3$ ceramics for energy storage application,” *J. Am. Ceram. Soc.*, vol. 98, no. 2, pp. 559–566, 2014, doi: 10.1111/jace.13325.

[42] X. Zhao, Z. Zhou, R. Liang, F. Liu, and X. Dong, “High-energy storage performance in lead-free $(1-x)BaTiO_3$-$xBi(Zn_{0.5}Ti_{0.5})O_3$ relaxor ceramics for temperature stability applications,” *Ceram. Int.*, vol. 43, no. 12, pp. 9060–9066, 2017, doi: 10.1016/j.ceramint.2017.04.051.

[43] L. Zhang, L. X. Pang, W. B. Li, and D. Zhou, “Extreme high energy storage efficiency in perovskite structured $(1-x)(Ba_{0.8}Sr_{0.2})TiO_3$-$xBi(Zn_{2/3}Nb_{1/3})O_3$ $(0.04 \leq x \leq 0.16)$ ceramics,” *J. Eur. Ceram. Soc.*, vol. 40, no. 8, pp. 3343–3347, 2020, doi:

10.1016/j.jeurceramsoc.2020.03.015.

[44] X. Dong *et al.*, "Effective strategy to realise excellent energy storage performances in lead-free barium titanate-based relaxor ferroelectric," *Ceram. Int.*, vol. 47, no. 5, pp. 6077–6083, 2021, doi: 10.1016/j.ceramint.2020.10.183.

[45] Z. G. Liu, M. D. Li, Z. H. Tang, and X. G. Tang, "Enhanced energy storage density and efficiency in lead-free Bi($Mg_{1/2}Hf_{1/2}$)O_3-modified $BaTiO_3$ ceramics," *Chem. Eng. J.*, vol. 418, no. March, p. 129379, 2021, doi: 10.1016/j.cej.2021.129379.

[46] Q. Yuan *et al.*, "Simultaneously achieved temperature-insensitive high energy density and efficiency in domain engineered $BaTiO_3$-Bi($Mg_{0.5}Zr_{0.5}$)O_3 lead-free relaxor ferroelectrics," *Nano Energy*, vol. 52, no. June, pp. 203–210, 2018, doi: 10.1016/j.nanoen.2018.07.055.

[47] Q. Hu *et al.*, "Achieve ultrahigh energy storage performance in $BaTiO_3$–Bi($Mg_{1/2}Ti_{1/2}$)O_3 relaxor ferroelectric ceramics via nano-scale polarization mismatch and reconstruction," *Nano Energy*, vol. 67, no. November 2019, p. 104264, 2020, doi: 10.1016/j.nanoen.2019.104264.

[48] M. Zhou, R. Liang, Z. Zhou, and X. Dong, "Novel $BaTiO_3$-based lead-free ceramic capacitors featuring high energy storage density, high power density, and excellent stability," *J. Mater. Chem. C*, vol. 6, no. 31, pp. 8528–8537, 2018, doi: 10.1039/c8tc03003k.

[49] C. Zhu, Z. Cai, L. Li, and X. Wang, "High energy density, high efficiency and excellent temperature stability of lead free Mn–doped $BaTiO_3$–Bi($Mg_{1/2}Zr_{1/2}$)O_3 ceramics sintered in a reducing atmosphere," *J. Alloys Compd.*, vol. 816, p. 152498, 2020, doi: 10.1016/j.jallcom.2019.152498.

[50] N. Buatip *et al.*, "Comparison of conventional and reactive sintering techniques for Lead–Free BCZT ferroelectric ceramics," *Radiat. Phys. Chem.*, vol. 172, no. January, p. 108770, 2020, doi: 10.1016/j.radphyschem.2020.108770.

[51] L. M. Wang, Q. X. Liu, and D. Zhou, "Dielectric and energy storage properties of the (1-x)$BaTiO_3$-xBi($Li_{1/3}Hf_{2/3}$)O_3 ($0.08 \leq \times \leq 0.14$) ceramics," *Mater. Lett.*, vol. 283, p. 128823, 2021, doi: 10.1016/j.matlet.2020.128823.

[52] H. Yang *et al.*, "Novel $BaTiO_3$-based, Ag/Pd-compatible lead-free relaxors with superior energy storage performance," *ACS Appl. Mater. Interfaces*, vol. 12, no. 39, pp. 43942–43949, 2020, doi: 10.1021/acsami.0c13057.

[53] Q. Hu, L. Jin, T. Wang, C. Li, Z. Xing, and X. Wei, "Dielectric and temperature stable energy storage properties of 0.88$BaTiO_3$-0.12Bi($Mg_{1/2}Ti_{1/2}$)O_3 bulk ceramics," *J. Alloys Compd.*, vol. 640, pp. 416–420, 2015, doi: 10.1016/j.jallcom.2015.02.225.

[54] "Journal of the American Ceramic Society - 2009 - Ogihara - High-Energy Density Capacitors Utilizing 0 7 $BaTiO_3$ 0 3 $BiScO_3$.pdf." .

[55] H. Yang, F. Yan, Y. Lin, T. Wang, L. He, and F. Wang, "A lead free relaxation and high energy storage efficiency ceramics for energy storage applications," *J. Alloys Compd.*, vol. 710, pp. 436–445, 2017, doi: 10.1016/j.jallcom.2017.03.261.

[56] Y. Lin *et al.*, "Excellent Energy-Storage Properties Achieved in $BaTiO_3$-Based Lead-Free Relaxor Ferroelectric Ceramics via Domain Engineering on the Nanoscale," *ACS Appl. Mater. Interfaces*, vol. 11, no. 40, pp. 36824–36830, 2019, doi: 10.1021/acsami.9b10819.

[57] W. B. Li, D. Zhou, R. Xu, L. X. Pang, and I. M. Reaney, "$BaTiO_3$-$Bi(Li_{0.5}Ta_{0.5})O_3$, Lead-Free Ceramics, and Multilayers with High Energy Storage Density and Efficiency," *ACS Appl. Energy Mater.*, vol. 1, no. 9, pp. 5016–5023, 2018, doi: 10.1021/acsaem.8b01001.

[58] F. Li, M. Zhou, J. Zhai, B. Shen, and H. Zeng, "Novel barium titanate based ferroelectric relaxor ceramics with superior charge-discharge performance," *J. Eur. Ceram. Soc.*, vol. 38, no. 14, pp. 4646–4652, 2018, doi: 10.1016/j.jeurceramsoc.2018.06.038.

[59] Q. Hu *et al.*, "Achieve ultrahigh energy storage performance in $BaTiO_3$–$Bi(Mg_{1/2}Ti_{1/2})O_3$ relaxor ferroelectric ceramics via nano-scale polarization mismatch and reconstruction," *Nano Energy*, vol. 67, no. October 2019, p. 104264, 2020, doi: 10.1016/j.nanoen.2019.104264.

[60] Q. Yuan, F. Yao, Y. Wang, R. Ma, and H. Wang, "Relaxor ferroelectric 0.9$BaTiO_3$-0.1$Bi(Zn_{0.5}Zr_{0.5})O_3$ ceramic capacitors with high energy density and temperature stable energy storage properties," *J. Mater. Chem. C*, vol. 5, no. 37, pp. 9552–9558, 2017, doi: 10.1039/c7tc02478a.

[61] D. Wang, A. Khesro, S. Murakami, A. Feteira, Q. Zhao, and I. M. Reaney, "Temperature dependent, large electromechanical strain in Nd-doped $BiFeO_3$-$BaTiO_3$ lead-free ceramics," *J. Eur. Ceram. Soc.*, vol. 37, no. 4, pp. 1857–1860, 2017, doi: 10.1016/j.jeurceramsoc.2016.10.027.

[62] A. Pakalniškis *et al.*, "Nanoscale ferroelectricity in pseudo-cubic sol-gel derived barium titanate - bismuth ferrite ($BaTiO_3$– $BiFeO_3$) solid solutions," *J. Alloys Compd.*, vol. 830, 2020, doi: 10.1016/j.jallcom.2020.154632.

[63] C. Ji *et al.*, "Influence of sintering method on microstructure, electrical and magnetic properties of $BiFeO_3$–$BaTiO_3$ solid solution ceramics," *Mater. Today Chem.*, vol. 20, pp. 2–11, 2021, doi: 10.1016/j.mtchem.2020.100419.

[64] K. Meng, W. Li, X. G. Tang, Q. X. Liu, and Y. P. Jiang, "A Review of a Good Binary

Ferroelectric Ceramic: $BaTiO_3$-$BiFeO_3$," *ACS Appl. Electron. Mater.*, 2021, doi: 10.1021/acsaelm.1c00109.

[65] H. Tang *et al.*, "Enhancement of energy-storage properties in $BiFeO_3$-based lead-free bulk ferroelectrics," *Ceram. Int.*, vol. 48, no. 12, pp. 16792–16799, 2022, doi: 10.1016/j.ceramint.2022.02.229.

[66] S. O. Leontsev and R. E. Eitel, "Dielectric and piezoelectric properties in Mn-modified (1-x)$BiFeO_3$-x$BaTiO_3$ ceramics," *J. Am. Ceram. Soc.*, vol. 92, no. 12, pp. 2957–2961, 2009, doi: 10.1111/j.1551-2916.2009.03313.x.

[67] J. Chen *et al.*, "Excellent thermal stability and aging behaviors in $BiFeO_3$-$BaTiO_3$ piezoelectric ceramics with rhombohedral phase," *J. Am. Ceram. Soc.*, vol. 103, no. 1, pp. 374–381, 2020, doi: 10.1111/jace.16755.

[68] Q. Fan *et al.*, "Normal-to-relaxor ferroelectric phase transition and electrical properties in Nb-modified 0.72$BiFeO_3$-0.28$BaTiO_3$ ceramics," *J. Electroceramics*, vol. 36, no. 1–4, pp. 1–7, 2016, doi: 10.1007/s10832-015-0008-8.

[69] X. Wu, M. Tian, Y. Guo, Q. Zheng, L. Luo, and D. Lin, "Phase transition, dielectric, ferroelectric and ferromagnetic properties of La-doped $BiFeO_3$–$BaTiO_3$ multiferroic ceramics," *J. Mater. Sci. Mater. Electron.*, vol. 26, no. 2, pp. 978–984, 2015, doi: 10.1007/s10854-014-2492-z.

[70] Q. Fan *et al.*, "Normal-to-relaxor ferroelectric phase transition and electrical properties in Nb-modified 0.72$BiFeO_3$-0.28$BaTiO_3$ ceramics," *J. Electroceramics*, vol. 36, no. 1–4, pp. 1–7, 2016, doi: 10.1007/s10832-015-0008-8.

[71] I. Calisir, A. A. Amirov, A. K. Kleppe, and D. A. Hall, "Optimisation of functional properties in lead-free $BiFeO_3$-$BaTiO_3$ ceramics through La3+ substitution strategy," *J. Mater. Chem. A*, vol. 6, no. 13, pp. 5378–5397, 2018, doi: 10.1039/c7ta09497c.

[72] D. Wang *et al.*, "Bismuth ferrite-based lead-free ceramics and multilayers with high recoverable energy density," *J. Mater. Chem. A*, vol. 6, no. 9, pp. 4133–4144, 2018, doi: 10.1039/c7ta09857j.

[73] L. Wu, X. Wang, and L. Li, "Lead-free $BaTiO_3$-$Bi(Zn_{2/3}Nb_{1/3})O_3$ weakly coupled relaxor ferroelectric materials for energy storage," *RSC Adv.*, vol. 6, no. 17, pp. 14273–14282, 2016, doi: 10.1039/c5ra21261h.

[74] P. Zhao *et al.*, "High-Performance Relaxor Ferroelectric Materials for Energy Storage Applications," *Adv. Energy Mater.*, vol. 9, no. 17, pp. 1–7, 2019, doi: 10.1002/aenm.201803048.

[75] "Adv Funct Materials - 2018 - Palneedi - High-Performance Dielectric Ceramic Films for Energy Storage Capacitors Progress.pdf" .

[76] S. Li *et al.*, “Ferroelectric thin films: performance modulation and application,” *Mater. Adv.*, vol. 3, no. 14, pp. 5735–5752, 2022, doi: 10.1039/d2ma00381c.

[77] Y. X. Zhang, C. H. Yang, Y. C. Guo, J. H. Song, Q. Yao, and Z. D. Yi, “The microstructure, energy storage and dielectric behaviours of (Ti,Zn)-doped $Bi_{0.97}Nd_{0.03}FeO_3$ thin films,” *Mater. Technol.*, vol. 33, no. 1, pp. 10–15, 2018, doi: 10.1080/10667857.2017.1370816.

[78] B. Xu, J. Íñiguez, and L. Bellaiche, “Designing lead-free antiferroelectrics for energy storage,” *Nat. Commun.*, vol. 8, no. May, 2017, doi: 10.1038/ncomms15682.

[79] T. Chen, J. Wang, X. Zhong, F. Wang, B. Li, and Y. Zhou, “High energy density capacitors based on $0.88BaTiO_3$-0. $12Bi(Mg_{0.5}, Ti_{0.5})O_3/PbZrO_3$ multilayered thin films,” *Ceram. Int.*, vol. 40, no. 4, pp. 5327–5332, 2014, doi: 10.1016/j.ceramint.2013.10.110.

[80] H. Zhu, M. Liu, Y. Zhang, Z. Yu, J. Ouyang, and W. Pan, “Increasing energy storage capabilities of space-charge dominated ferroelectric thin films using interlayer coupling,” *Acta Mater.*, vol. 122, pp. 252–258, 2017, doi: 10.1016/j.actamat.2016.09.051.

[81] S. Chao and F. Dogan, “$BaTiO_3$-$SrTiO_3$ layered dielectrics for energy storage,” *Mater. Lett.*, vol. 65, no. 6, pp. 978–981, 2011, doi: 10.1016/j.matlet.2010.12.043.

[82] M. Liu, H. Zhu, Y. Zhang, C. Xue, and J. Ouyang, “Energy storage characteristics of $BiFeO_3/BaTiO_3$ Bi-layers integrated on Si,” *Materials (Basel).*, vol. 9, no. 11, 2016, doi: 10.3390/ma9110935.

[83] T. Zhang, W. Li, Y. Zhao, Y. Yu, and W. Fei, “High Energy Storage Performance of Opposite Double-Heterojunction Ferroelectricity–Insulators,” *Adv. Funct. Mater.*, vol. 28, no. 10, pp. 1–9, 2018, doi: 10.1002/adfm.201706211.

[84] B. B. Yang *et al.*, “Ultrahigh energy storage in lead-free $BiFeO_3/Bi_{3.25}La_{0.75}Ti_3O_{12}$ thin film capacitors by solution processing,” *Appl. Phys. Lett.*, vol. 112, no. 3, pp. 0–5, 2018, doi: 10.1063/1.5002143.

[85] Z. Sun *et al.*, “Ultrahigh Energy Storage Performance of Lead-Free Oxide Multilayer Film Capacitors via Interface Engineering,” *Adv. Mater.*, vol. 29, no. 5, pp. 4–9, 2017, doi: 10.1002/adma.201604427.

[86] N. Ortega *et al.*, “Relaxor-ferroelectric superlattices: High energy density capacitors,” *J. Phys. Condens. Matter*, vol. 24, no. 44, 2012, doi: 10.1088/0953-8984/24/44/445901.

[87] S. Lamichhane, S. Sharma, M. Tomar, A. Kumar, and V. Gupta, “Influence of laser fluence in modifying energy storage property of $BiFeO_3$ thin film capacitor,” *J. Energy Storage*, vol. 32, no. July, 2020, doi: 10.1016/j.est.2020.101769.

[88] T. Zhang *et al.*, “High-energy storage density and excellent temperature stability in antiferroelectric/ferroelectric bilayer thin films,” *J. Am. Ceram. Soc.*, vol. 100, no. 7, pp. 3080–3087, 2017, doi: 10.1111/jace.14876.

[89] H. H. W. Stanjek, “3-Basics of X-Ray Diffraction,” pp. 107–119, 2004.

[90] S. Nandi, “Raman spectroscopy,” no. September, pp. 0–11, 2021, doi: 10.13140/RG.2.2.24191.33445.

[91] G. Greczynski and L. Hultman, “A step-by-step guide to perform x-ray photoelectron spectroscopy,” *J. Appl. Phys.*, vol. 132, no. 1, 2022, doi: 10.1063/5.0086359.

[92] G. Greczynski and L. Hultman, “Referencing to adventitious carbon in X-ray photoelectron spectroscopy: Can differential charging explain C 1s peak shifts?,” *Appl. Surf. Sci.*, vol. 606, no. September, p. 154855, 2022, doi: 10.1016/j.apsusc.2022.154855.

[93] Z. Xu, Y. Tanushi, M. Suzuki, K. Wakushima, and S. Yokoyama, “Optical properties of amorphous $Ba_{0.7}Sr_{0.3}TiO_3$ thin films obtained by metal organic decomposition technique,” *Thin Solid Films*, vol. 515, no. 4, pp. 2326–2331, 2006, doi: 10.1016/j.tsf.2006.03.051.

[94] M. J. Haque, M. S. Mostari, S. B. R. Ankur, and M. S. Rahman, “Enhanced dielectric, ferroelectric and optical properties of $Ba(Zr_{0.15}Ti_{0.85})O_3$ ceramics incorporated with MgO,” *Results Mater.*, vol. 10, no. February, p. 100176, 2021, doi: 10.1016/j.rinma.2021.100176.

[95] K. S. K. R. C. Sekhar *et al.*, “Energy storage, electrocaloric and optical property studies in Ho-modified NBT – BT lead-free ferroelectric ceramics,” *Ceram. Int.*, vol. 49, no. 5, pp. 8313–8324, 2023, doi: 10.1016/j.ceramint.2022.10.363.

[96] T. Zhang, H. Gu, and J. Liu, “Structural and optical properties of BST thin films prepared by the sol-gel process,” *Microelectron. Eng.*, vol. 66, no. 1–4, pp. 860–864, 2003, doi: 10.1016/S0167-9317(02)01012-2.

[97] T. Zhang, J. Wang, B. Zhang, R. Pan, and N. Wan, “The effect of Ho doping on the microstructure and optical properties of $Ba_{0.65}Sr_{0.35}TiO_3$ thin films,” *Microelectron. Eng.*, vol. 83, no. 11–12, pp. 2446–2451, 2006, doi: 10.1016/j.mee.2006.05.005.

[98] Z. Quan *et al.*, “Effect of annealing temperature on microstructure, optical and electrical properties of sputtered $Ba_{0.9}Sr_{0.1}TiO_3$ thin films,” *Appl. Surf. Sci.*, vol. 255, no. 22, pp. 9045–9053, 2009, doi: 10.1016/j.apsusc.2009.06.096.

[99] J. Wang, J. Xiang, L. Bai, T. Liu, G. Yang, and T. J. Zhang, “Microstructure, dielectric and optical properties of compositionally graded $Ba_{1-x}Sr_xTiO_3$ thin film,” *Mater. Chem. Phys.*, vol. 112, no. 2, pp. 542–545, 2008, doi: 10.1016/j.matchemphys.2008.05.095.

[100] S. Pattipaka, P. Dobbidi, J. Pundareekam Goud, K. C. James Raju, G. Pradhan, and V. Sridhar, "Investigation of surface scaling, optical and microwave dielectric studies of $Bi_{0.5}Na_{0.5}TiO_3$ thin films," *J. Mater. Sci. Mater. Electron.*, vol. 33, no. 11, pp. 8893–8905, 2022, doi: 10.1007/s10854-021-06970-8.

[101] K. Venkata Saravanan, K. Sudheendran, M. Ghanashyam Krishna, K. C. James Raju, and A. K. Bhatnagar, "Effect of process parameters and post deposition annealing on the optical, structural and microwave dielectric properties of RF magnetron sputtered $(Ba_{0.5},Sr_{0.5})TiO_3$ thin films," *Vacuum*, vol. 81, no. 3, pp. 307–316, 2006, doi: 10.1016/j.vacuum.2006.05.002.

[102] L. Yu, H. Deng, W. Zhou, P. Yang, and J. Chu, "Structural characteristics and optical properties of lead-free $Bi(Zn_{1/2}Ti_{1/2})O_3$-$BaTiO_3$ ceramics," *Ceram. Int.*, vol. 43, no. 8, pp. 6175–6179, 2017, doi: 10.1016/j.ceramint.2017.02.014.

[103] Y. Wang, X. Chen, H. Zhou, L. Fang, L. Liu, and H. Zhang, "Evolution of phase transformation behavior and dielectric temperature stability of $BaTiO_3$-$Bi(Zn_{0.5}Zr_{0.5})O_3$ ceramics system," *J. Alloys Compd.*, vol. 551, pp. 365–369, 2013, doi: 10.1016/j.jallcom.2012.09.127.

[104] X. Li, X. Chen, J. Sun, M. Zhou, and H. Zhou, "Novel lead-free ceramic capacitors with high energy density and fast discharge performance," *Ceram. Int.*, vol. 46, no. 3, pp. 3426–3432, 2020, doi: 10.1016/j.ceramint.2019.10.055.

[105] W. Qin *et al.*, "High energy storage and thermal stability under low electric field in $Bi_{0.5}Na_{0.5}TiO_3$-modified $BaTiO_3$-$Bi(Zn_{0.25}Ta_{0.5})O_3$ ceramics," *Chem. Eng. J.*, vol. 443, no. April, p. 136505, 2022, doi: 10.1016/j.cej.2022.136505.

[106] P. Yadav, S. Sharma, and N. P. Lalla, "Effect of magnetic ion (Mn) doping on structural, ferroelectric and magnetic properties of $Ba_{0.90}Mn_{0.10}TiO_3$," *Ceram. Int.*, vol. 43, no. 16, pp. 13339–13344, 2017, doi: 10.1016/j.ceramint.2017.07.032.

[107] W. Jia *et al.*, "Advances in lead-free high-temperature dielectric materials for ceramic capacitor application," *IET Nanodielectrics*, vol. 1, no. 1, pp. 3–16, 2018, doi: 10.1049/iet-nde.2017.0003.

[108] B. Zn *et al.*, "Enhanced energy storage in temperature stable $Bi_{0.5}Na_{0.5}TiO_3$ -modified," *Ceram. Int.*, vol. 48, no. 24, pp. 36478–36489, 2022, doi: 10.1016/j.ceramint.2022.08.208.

[109] Z. Shen, X. Wang, B. Luo, and L. Li, "$BaTiO_3$-$BiYbO_3$ perovskite materials for energy storage applications," *J. Mater. Chem. A*, vol. 3, no. 35, pp. 18146–18153, 2015, doi: 10.1039/c5ta03614c.

[110] H. Ogihara, C. A. Randall, and S. Trolier-Mckinstry, "High-energy density capacitors utilizing 0.7 $baTiO_3$-0.3 $BiScO_3$ ceramics," *J. Am. Ceram. Soc.*, vol. 92, no. 8, pp. 1719–1724, 2009, doi:

10.1111/j.1551-2916.2009.03104.x.

[111] X. Chen, J. Chen, D. Ma, L. Fang, and H. Zhou, “High relative permittivity, low dielectric loss and good thermal stability of $BaTiO_3$-bi($Mg_{0.5}Zr_{0.5}$)O_3 solid solution,” *Ceram. Int.*, vol. 41, no. 2, pp. 2081–2088, 2015, doi: 10.1016/j.ceramint.2014.10.003.

[112] A. Zeb and S. J. Milne, “Temperature-stable dielectric properties from -20°C to 430°C in the system $BaTiO_3$-Bi($Mg_{0.5}Zr_{0.5}$)O_3,” *J. Eur. Ceram. Soc.*, vol. 34, no. 13, pp. 3159–3166, 2014, doi: 10.1016/j.jeurceramsoc.2014.04.047.

[113] R. Muhammad, Y. Iqbal, I. M. Reaney, and C. Randall, “$BaTiO_3$-Bi($Mg_{2/3}Nb_{1/3}$)O_3 Ceramics for High-Temperature Capacitor Applications,” *J. Am. Ceram. Soc.*, vol. 99, no. 6, pp. 2089–2095, 2016, doi: 10.1111/jace.14212.

[114] X. Chen, J. Chen, D. Ma, L. Fang, and H. Zhou, “Thermally stable $BaTiO_3$-Bi($Mg_{2/3}Nb_{1/3}$)O_3 solid solution with high relative permittivity in a broad temperature usage range,” *J. Am. Ceram. Soc.*, vol. 98, no. 3, pp. 804–810, 2015, doi: 10.1111/jace.13357.

[115] Q. Hu *et al.*, “Achieve ultrahigh energy storage performance in $BaTiO_3$–Bi($Mg_{1/2}Ti_{1/2}$)O_3 relaxor ferroelectric ceramics via nano-scale polarization mismatch and reconstruction,” *Nano Energy*, vol. 67, no. November, 2020, doi: 10.1016/j.nanoen.2019.104264.

[116] M. Zhang *et al.*, “Effects of sintering temperature and composition on dielectric , ferroelectric , and magnetoelectric properties of $BaTiO_3$ – $BiFeO_3$ solid solutions E ff ects of sintering temperature and composition on dielectric , ferroelectric , and magnetoelectric pro,” *Ceram. Int.*, vol. 43, no. 18, pp. 16957–16964, 2017, doi: 10.1016/j.ceramint.2017.09.101.

[117] W. Huang *et al.*, “Ultrahigh recoverable energy storage density and efficiency in barium strontium titanate-based lead-free relaxor ferroelectric ceramics,” *Appl. Phys. Lett.*, vol. 113, no. 20, pp. 0–5, 2018, doi: 10.1063/1.5054000.

[118] C. Behera, R. N. P. Choudhary, and P. R. Das, “Structural and electrical properties of La-modified,” vol. 3, pp. 2086–2095, 2014, doi: 10.1007/s10854-014-1844-z.

[119] D. P. Dutta, M. Roy, N. Maiti, and A. K. Tyagi, “Phase evolution in sonochemically synthesized Fe^{3+} doped $BaTiO_3$ nanocrystallites: Structural, magnetic and ferroelectric characterisation,” *Phys. Chem. Chem. Phys.*, vol. 18, no. 14, pp. 9758–9769, 2016, doi: 10.1039/c5cp07736b.

[120] N. Kumar, A. Shukla, N. Kumar, R. N. P. Choudhary, and A. Kumar, “Structural, electrical, and multiferroic characteristics of lead-free multiferroic: Bi($Co_{0.5}Ti_{0.5}$)O_3–$BiFeO_3$ solid solution,” *RSC Adv.*, vol. 8, no. November, pp. 36939–36950, 2018, doi: 10.1039/C8RA02306A.

[121] S. Pattanayak, B. N. P. Piyush, and R. N. P. Choudhary, “Impedance spectroscopy of Gd-doped

BiFeO 3 multiferroics,” pp. 387–395, 2013, doi: 10.1007/s00339-012-7412-6.

[122] P. Fe, “Dielectric , impedance and transport characteristics,” *J. Mater. Sci. Mater. Electron.*, vol. 26, no. 12, pp. 10012–10019, 2015, doi: 10.1007/s10854-015-3681-0.

[123] S. T. Dadami, S. Matteppanavar, I. Shivaraja, and S. Rayaprol, “solid solution,” vol. 43, no. August, pp. 16684–16692, 2017, doi: 10.1016/j.ceramint.2017.09.059.

[124] Y. Wang, Y. Pu, and P. Zhang, “Investigation of dielectric relaxation in $BaTiO_3$ ceramics modified with $BiYO_3$ by impedance spectroscopy,” *J. Alloys Compd.*, vol. 653, pp. 596–603, 2015, doi: 10.1016/j.jallcom.2015.09.012.

[125] R. G. A. Bondarenko A. S., “Inverse problem in potentiodynamic electrochemical impedance spectroscopy,” *Prog. Chemom. Res.*, pp. 89–102, 2005.

[126] V. Purohit, R. Padhee, and R. N. P. Choudhary, “Structural and electrical properties of $Bi(Mg_{0.5}Ti_{0.5})O_3$ ceramic,” *J. Mater. Sci. Mater. Electron.*, vol. 29, no. 6, pp. 5224–5232, 2018, doi: 10.1007/s10854-017-8487-9.

[127] M. Atif, M. Nadeem, W. Khalid, and Z. Ali, “Structural, magnetic and impedance spectroscopy analysis of $(0.7)CoFe_2O_4$+$(0.3)BaTiO_3$ magnetoelectric composite,” *Mater. Res. Bull.*, vol. 107, no. July 2017, pp. 171–179, 2018, doi: 10.1016/j.materresbull.2018.07.026.

[128] S. Selvasekarapandian and M. Vijayakumar, “The ac impedance spectroscopy studies on $LiDyO_2$,” vol. 80, pp. 29–33, 2003.

[129] H. Zhao, X. Yang, D. Pang, and X. Long, “Enhanced energy storage efficiency by modulating field-induced strain in,” *Ceram. Int.*, vol. 47, no. 16, pp. 22734–22740, 2021, doi: 10.1016/j.ceramint.2021.04.290.

[130] N. Wang *et al.*, “Investigation of structural, ferroelectric and magnetic properties of Ca modified $BiFeO_3$–$BaTiO_3$ ceramics,” *Ceram. Int.*, vol. 46, no. 3, pp. 3855–3860, 2020, doi: 10.1016/j.ceramint.2019.10.110.

[131] Y. Huang, F. Li, H. Hao, F. Xia, H. Liu, and S. Zhang, “and ef fi ciency,” vol. 5, pp. 385–393, 2019, doi: 10.1016/j.jmat.2019.03.006.

[132] J. Gao *et al.*, “Enhancing dielectric permittivity for energy-storage devices through tricritical phenomenon,” *Sci. Rep.*, vol. 7, no. January, pp. 1–10, 2017, doi: 10.1038/srep40916.

[133] M. Ganguly, S. K. Rout, W. S. Woo, C. W. Ahn, and I. W. Kim, “Characterization of A-site deficient samarium doped barium titanate,” *Phys. B Condens. Matter*, vol. 411, pp. 26–34, 2013, doi: 10.1016/j.physb.2012.11.006.

[134] A. Paterson, H. T. Wong, Z. Liu, W. Ren, and Z. G. Ye, “Synthesis, structure and electric properties of a new lead-free ferroelectric solid solution of (1-x)$BaTiO_3$-x$Bi(Zn_{2/3}Nb_{1/3})O_3$,” *Ceram. Int.*, vol. 41, no. S1, pp. S57–S62, 2015, doi: 10.1016/j.ceramint.2015.03.305.

[135] M. Zhang, H. Yang, Y. Yu, and Y. Lin, “Energy storage performance of $K_{0.5}Na_{0.5}NbO_3$-based ceramics modified by $Bi(Zn_{2/3}(Nb_{0.85}Ta_{0.15})_{1/3})O_3$,” *Chem. Eng. J.*, vol. 425, no. August, p. 131465, 2021, doi: 10.1016/j.cej.2021.131465.

[136] L. Wu, X. Wang, Z. Shen, L. Li, and A. Feteira, “Ferroelectric to Relaxor Transition in $BaTiO_3$–$Bi(Zn_{2/3}Nb_{1/3})O_3$ Ceramics,” *J. Am. Ceram. Soc.*, vol. 100, no. 1, pp. 265–275, 2017, doi: 10.1111/jace.14564.

[137] X. Wang, Y. Fan, G. Luo, R. Tu, Q. Shen, and L. Zhang, “Effect of yttrium (Y) substitution on the structure and dielectric properties of $BaTiO_3$,” *Ceram. Int.*, vol. 49, no. 6, pp. 9042–9051, 2023, doi: 10.1016/j.ceramint.2022.11.060.

[138] M. Arshad *et al.*, “Fabrication, structure, and frequency-dependent electrical and dielectric properties of Sr-doped $BaTiO_3$ ceramics,” *Ceram. Int.*, vol. 46, no. 2, pp. 2238–2246, 2020, doi: 10.1016/j.ceramint.2019.09.208.

[139] T. Badapanda *et al.*, “Structural refinement, optical and ferroelectric properties of microcrystalline $Ba(Zr_{0.05}Ti_{0.95})O_3$ perovskite,” *Curr. Appl. Phys.*, vol. 14, no. 5, pp. 708–715, 2014, doi: 10.1016/j.cap.2014.02.015.

[140] M. Zeng, J. Liu, H. Li, S. Zhang, and W. Zhang, “High energy storage efficiency and fast discharge property of temperature stabilized $Ba_{0.4}Sr_{0.6}TiO_3$–$Bi(Mg_{0.5}Ti_{0.5})O_3$ ceramics,” *Ceram. Int.*, vol. 48, no. 16, pp. 23518–23526, 2022, doi: 10.1016/j.ceramint.2022.04.348.

[141] J. Xie, Q. Qin, Y. Li, P. Zhao, A. Chang, and H. Zhang, “ceramics by composition design and bandgap engineering,” vol. 49, no. March, pp. 19682–19690, 2023.

[142] Q. Xu *et al.*, “A new energy-storage ceramic system based on $Bi_{0.5}Na_{0.5}TiO_3$ ternary solid solution,” *J. Mater. Sci. Mater. Electron.*, vol. 27, no. 1, pp. 322–329, 2016, doi: 10.1007/s10854-015-3757-x.

[143] B. Yan, K. Chen, and L. An, “Design and energy storage performance of $(Bi_{0.4}K_{0.2}Na_{0.2}Ba_{0.2})TiO_3$- $Sr(Mg_{1/3}Ta_{2/3})O_3$ high-entropy Relaxor ceramics,” *Mater. Res. Bull.*, vol. 167, no. April, p. 112392, 2023, doi: 10.1016/j.materresbull.2023.112392.

[144] D. Janardhana, S. N. Jayaramu, W. D. Roos, W. Purcell, and H. C. Swart, “Influences of substrate temperatures and oxygen partial pressures on the crystal structure, morphology and luminescence properties of pulsed laser deposited bi_2o_3:Ho^{3+} thin films,” *Coatings*, vol. 10, no.

12, pp. 1–29, 2020, doi: 10.3390/coatings10121168.

[145] J. P. Liu *et al.*, “Substantial reduction of leakage currents in La/Er/Zn/Ti multielement-doped $BiFeO_3$ multiferroic thin films,” *Ceram. Int.*, vol. 48, no. 12, pp. 17328–17334, 2022, doi: 10.1016/j.ceramint.2022.02.295.

[146] R. Das, S. Sharma, and K. Mandal, “Aliovalent Ba^{2+} doping: A way to reduce oxygen vacancy in multiferroic $BiFeO_3$,” *J. Magn. Magn. Mater.*, vol. 401, pp. 129–137, 2016, doi: 10.1016/j.jmmm.2015.10.022.

[147] C. Chen *et al.*, “The role of diffusion behavior on the formation and evolution of the core-shell structure in $BaTiO_3$-based ceramics,” *J. Am. Ceram. Soc.*, vol. 103, no. 1, pp. 304–314, 2020, doi: 10.1111/jace.16735.

[148] M. S. Alkathy, A. Rahaman, V. R. Mastelaro, F. L. Zabotto, F. P. Milton, and J. A. Eiras, “Achieving high energy storage density simultaneously with large efficiency and excellent thermal stability by defect dipole, and microstructural engineering in modified-$BaTiO_3$ ceramics,” *J. Alloys Compd.*, vol. 934, p. 167887, 2023, doi: 10.1016/j.jallcom.2022.167887.

[149] M. Sassi, A. Bettaibi, A. Oueslati, K. Khirouni, and M. Gargouri, “Electrical conduction mechanism and transport properties of $LiCrP_2O_7$ compound,” *J. Alloys Compd.*, vol. 649, pp. 642–648, 2015, doi: 10.1016/j.jallcom.2015.07.148.

[150] S. Pattipaka, A. R. James, and P. Dobbidi, “Enhanced dielectric and piezoelectric properties of BNT-KNNG piezoelectric ceramics,” *J. Alloys Compd.*, vol. 765, pp. 1195–1208, 2018, doi: 10.1016/j.jallcom.2018.06.138.

[151] H. Han, C. Davis, and J. C. Nino, “Variable range hopping conduction in $BaTiO_3$ ceramics exhibiting colossal permittivity,” *J. Phys. Chem. C*, vol. 118, no. 17, pp. 9137–9142, 2014, doi: 10.1021/jp502314r.

[152] J. Liu, Q. Liu, W. Wang, Y. Liang, D. Lu, and P. Zhu, “Variable-range-hopping conduction and polaron dielectric relaxation in Cu and Nb co-doped $BaTiO_3$,” *J. Phys. Chem. Solids*, vol. 129, no. July 2018, pp. 111–121, 2019, doi: 10.1016/j.jpcs.2018.12.036.

[153] R. L. Nayak, Y. Zhang, S. S. Dash, and M. P. K. Sahoo, “Intermediate ferroelectric phase driven ferroelectric-relaxor crossover and superior storage properties in phase boundary engineered BCZT ceramics,” *Ceram. Int.*, vol. 48, no. 8, pp. 10803–10816, 2022, doi: 10.1016/j.ceramint.2021.12.296.

[154] D. V. Karpinsky *et al.*, “Peculiarities of the crystal structure evolution of $Bifeo_3$-$batio_3$ ceramics across structural phase transitions,” *Nanomaterials*, vol. 10, no. 4, 2020, doi:

10.3390/nano10040801.

[155] T. D. Rao and S. Asthana, “Evidence of improved ferroelectric phase stabilization in Nd and Sc co-substituted,” vol. 164102, no. July 2014, 2018, doi: 10.1063/1.4898805.

[156] S. Jangid, S. K. Barbar, I. Bala, and M. Roy, “Structural, thermal, electrical and magnetic properties of pure and 50% la doped $BiFeO_3$ ceramics,” *Phys. B Condens. Matter*, vol. 407, no. 18, pp. 3694–3699, 2012, doi: 10.1016/j.physb.2012.05.013.

[157] P. Kum-onsa, N. Chanlek, P. Thongbai, and P. Srepusharawoot, “Effect of complex defects on the origin of giant dielectric properties of Mg^{2+}–doped $BiFeO_3$ ceramics prepared by a precipitation method,” *Ceram. Int.*, vol. 46, no. 16, pp. 25017–25023, 2020, doi: 10.1016/j.ceramint.2020.06.287.

[158] B. Yotburut, P. Thongbai, T. Yamwong, and S. Maensiri, “Synthesis and characterization of multiferroic Sm-doped $BiFeO_3$ nanopowders and their bulk dielectric properties,” *J. Magn. Magn. Mater.*, vol. 437, pp. 51–61, 2017, doi: 10.1016/j.jmmm.2017.04.041.

[159] T. Durga Rao, R. Ranjith, and S. Asthana, “Enhanced magnetization and improved insulating character in Eu substituted $BiFeO_3$,” *J. Appl. Phys.*, vol. 115, no. 12, 2014, doi: 10.1063/1.4869775.

[160] A. A. Zatsiupa *et al.*, “Magnetization, magnetic susceptibility, effective magnetic moment of Fe^{3+} ions in $Bi_{25}FeO_{39}$ ferrite,” *J. Solid State Chem.*, vol. 212, pp. 147–150, 2014, doi: 10.1016/j.jssc.2014.01.019.

[161] Y. S. Lu and J. Q. Dai, “Enhanced electrical properties of (Zn, Mn)-modified $BiFeO_3$–$BaTiO_3$ lead-free ceramics prepared via sol–gel method and two-step sintering,” *J. Alloys Compd.*, vol. 899, p. 163387, 2022, doi: 10.1016/j.jallcom.2021.163387.

[162] X. L. Liang, J. Q. Dai, and C. C. Zhang, “Effect of (Zn, Mn) co-doping on the structure and ferroelectric properties of $BiFeO_3$ thin films,” *Ceram. Int.*, vol. 48, no. 5, pp. 6347–6355, 2022, doi: 10.1016/j.ceramint.2021.11.177.

[163] P. Suresh and S. Srinath, “Effect of Gd substitution on structure and magnetic properties of $BiFeO_3$,” *IOP Conf. Ser. Mater. Sci. Eng.*, vol. 73, no. 1, pp. 5–8, 2015, doi: 10.1088/1757-899X/73/1/012082.

[164] P. Suresh and S. Srinath, “Study of structure and magnetic properties of rare earth doped $BiFeO_3$,” *Phys. B Phys. Condens. Matter*, vol. 448, pp. 281–284, 2014, doi: 10.1016/j.physb.2014.03.040.

[165] P. Suresh, P. D. Babu, and S. Srinath, “Role of (La, Gd) co-doping on the enhanced dielectric

and magnetic properties of $BiFeO_3$ ceramics," *Ceramics International*, vol. 42, no. 3. pp. 4176–4184, 2016, doi: 10.1016/j.ceramint.2015.11.091.

[166] J. Y. Lee *et al.*, "The role of intermediate S-polymorph towards high piezoelectricity in La-doped $BiFeO_3$ epitaxial thin films," *Acta Mater.*, vol. 207, p. 116683, 2021, doi: 10.1016/j.actamat.2021.116683.

[167] R. Gupta, V. Gupta, and M. Tomar, "Structural and dielectric properties of PLD grown BST thin films," *Vacuum*, vol. 159, no. September 2018, pp. 69–75, 2019, doi: 10.1016/j.vacuum.2018.10.010.

[168] Y. Wang *et al.*, "First-principles investigation of structural, electronic, and energetic properties of $BaSnO_3$ (001) surfaces," *Vacuum*, vol. 212, no. March, p. 111977, 2023, doi: 10.1016/j.vacuum.2023.111977.

[169] K. Trzciński *et al.*, "Pulsed laser deposition of bismuth vanadate thin films-the effect of oxygen pressure on the morphology, composition, and photoelectrochemical performance," *Materials (Basel).*, vol. 13, no. 6, 2020, doi: 10.3390/ma13061360.

[170] E. Hasabeldaim, O. M. Ntwaeaborwa, R. E. Kroon, D. E. Motaung, E. Coetsee, and H. C. Swart, "Effect of PLD growth atmosphere on the physical properties of ZnO:Zn thin films," *Opt. Mater. (Amst).*, vol. 74, pp. 76–85, 2017, doi: 10.1016/j.optmat.2017.04.061.

[171] B. D. Jackson and P. R. Herman, "Vacuum-ultraviolet pulsed-laser deposition of silicon dioxide thin films," *Appl. Surf. Sci.*, vol. 127–129, pp. 595–600, 1998, doi: 10.1016/S0169-4332(97)00712-5.

[172] K. Wang, M. Zhang, T. Zeng, F. He, and W. Wen, "Lattice-matched heteroepitaxial preparation of InSb/CdTe on Si (111) substrate by magnetron sputtering," *Vacuum*, vol. 212, no. 1, p. 112010, 2023, doi: 10.1016/j.vacuum.2023.112010.

[173] S. Gupta *et al.*, "Optimization of excess Bi doping to enhance ferroic orders of spin casted $BiFeO_3$ thin film," *J. Appl. Phys.*, vol. 115, no. 23, 2014, doi: 10.1063/1.4884680.

[174] W. Liu and X. Ren, "Large piezoelectric effect in Pb-free ceramics," *Phys. Rev. Lett.*, vol. 103, no. 25, pp. 1–4, 2009, doi: 10.1103/PhysRevLett.103.257602.

[175] B. Yotburut, P. Thongbai, T. Yamwong, and S. Maensiri, "Electrical and nonlinear current-voltage characteristics of La-doped $BiFeO_3$ ceramics," *Ceram. Int.*, vol. 43, no. 7, pp. 5616–5627, 2017, doi: 10.1016/j.ceramint.2017.01.094.

[176] S. Kossar *et al.*, "Study on ferroelectric polarization induced resistive switching characteristics of neodymium-doped bismuth ferrite thin films for random access memory applications," *Curr.*

Appl. Phys., vol. 39, no. October 2021, pp. 221–229, 2022, doi: 10.1016/j.cap.2022.04.013.

[177] T. M. Pan, Y. C. Chou, and J. L. Her, “Effect of Yb-doping on structural and electrical properties of $BiFeO_3$ thin films,” *Mater. Chem. Phys.*, vol. 278, no. December 2021, p. 125699, 2022, doi: 10.1016/j.matchemphys.2022.125699.

[178] A. Bougoffa *et al.*, “Investigation of temperature and frequency dependence of the dielectric properties of multiferroic $(La_{0.8}Ca_{0.2})_{0.4}Bi_{0.6}FeO_3$ nanoparticles for energy storage application,” *RSC Adv.*, vol. 12, no. 11, pp. 6907–6917, 2022, doi: 10.1039/d1ra08975g.

[179] K. Yi, Q. Tang, Z. Wu, and X. Zhu, “Unraveling the Structural , Dielectric , Magnetic , and Optical Characteristics of Nanostructured La_2NiMnO_6 Double Perovskites,” pp. 1–20, 2022.

[180] X. Deng *et al.*, “Study of structural, optical and enhanced multiferroic properties of Ni doped BFO thin films synthesized by sol-gel method,” *J. Alloys Compd.*, vol. 831, p. 154857, 2020, doi: 10.1016/j.jallcom.2020.154857.

[181] W. Ahmad Wani, H. Renuka, S. Kundu, S. Goel, H. Venkataraman, and K. Ramaswamy, “What ails the photovoltaic performance in single-layered unpoled BFO? – The role of oxygen annealing in improving the photovoltaic efficiency,” *Sol. Energy*, vol. 236, no. March, pp. 822–831, 2022, doi: 10.1016/j.solener.2022.03.058.

[182] Y. Li, M. S. Cao, D. W. Wang, and J. Yuan, “High-efficiency and dynamic stable electromagnetic wave attenuation for la doped bismuth ferrite at elevated temperature and gigahertz frequency,” *RSC Adv.*, vol. 5, no. 94, pp. 77184–77191, 2015, doi: 10.1039/c5ra15458h.

[183] Y. Zhang *et al.*, “Enhanced magnetic properties of $BiFeO_3$ thin films by doping: Analysis of structure and morphology,” *Nanomaterials*, vol. 8, no. 9, pp. 1–13, 2018, doi: 10.3390/nano8090711.

[184] X. Deng, J. Huang, Y. Sun, K. Liu, and R. Gao, “Effect of processing parameters on the structural , electrical and magnetic properties of BFO thin fi lm synthesized via RF magnetron sputtering,” *J. Alloys Compd.*, vol. 684, pp. 510–515, 2016, doi: 10.1016/j.jallcom.2016.05.114.

[185] X. L. Liang, J. Q. Dai, and G. dong Zhang, “Great ferroelectric properties and narrow bandgaps of $BiFeO_3$ thin films by (Mg, Mn) modifying,” *Appl. Surf. Sci.*, vol. 586, no. January, p. 152751, 2022, doi: 10.1016/j.apsusc.2022.152751.

[186] Y. Zhang *et al.*, “Microstructures and multiferroic properties of textured $Bi_{0.8}La_{0.2}FeO_3$ thin films,” *Appl. Surf. Sci.*, vol. 254, no. 21, pp. 6762–6765, 2008, doi: 10.1016/j.apsusc.2008.04.082.

[187] A. K. Sinha *et al.*, “Enhanced dielectric, magnetic and optical properties of Cr-doped $BiFeO_3$ multiferroic nanoparticles synthesized by sol-gel route,” *Results Phys.*, vol. 13, no. April, p. 102299, 2019, doi: 10.1016/j.rinp.2019.102299.

[188] Y. Liu *et al.*, “Multiferroic properties of La/Er/Mn/Co multi-doped $BiFeO_3$ thin films,” *Ceram. Int.*, vol. 45, no. 9, pp. 11765–11775, 2019, doi: 10.1016/j.ceramint.2019.03.053.

[189] H. Yang *et al.*, “Novel $BaTiO_3$-Based, Ag/Pd-Compatible Lead-Free Relaxors with Superior Energy Storage Performance,” *ACS Appl. Mater. Interfaces*, vol. 12, no. 39, pp. 43942–43949, 2020, doi: 10.1021/acsami.0c13057.

[190] A. Ravalia *et al.*, “Role of oxygen in multiferroic behavior of $BiFeO_3$ films grown on 0.2% Nb doped $SrTiO_3$,” *Solid State Commun.*, vol. 169, pp. 10–13, 2013, doi: 10.1016/j.ssc.2013.06.020.

[191] A. Gaur *et al.*, “Structural, optical and magnetic properties of Nd-doped $BiFeO_3$ thin films prepared by pulsed laser deposition,” *Phys. B Condens. Matter*, vol. 406, no. 10, pp. 1877–1882, 2011, doi: 10.1016/j.physb.2011.02.046.

[192] A. Singh, Z. R. Khan, P. M. Vilarinho, V. Gupta, and R. S. Katiyar, “Influence of thickness on optical and structural properties of $BiFeO_3$ thin films: PLD grown,” *Mater. Res. Bull.*, vol. 49, no. 1, pp. 531–536, 2014, doi: 10.1016/j.materresbull.2013.08.050.

[193] X. Yao *et al.*, “Growth and physical properties of $BiFeO_3$ thin films directly on Si substrate,” *J. Cryst. Growth*, vol. 522, no. April, pp. 110–116, 2019, doi: 10.1016/j.jcrysgro.2019.06.017.

[194] H. Wang, F. Khatkhatay, J. Jian, J. Huang, M. Fan, and H. Wang, “Strain tuning of ferroelectric and optical properties of rhombohedral-like $BiFeO_3$ thin films on $SrRuO_3$-buffered substrates,” *Mater. Res. Bull.*, vol. 110, no. July 2018, pp. 120–125, 2019, doi: 10.1016/j.materresbull.2018.10.016.

[195] B. S. Soram, B. S. Ngangom, and H. B. Sharma, “Effect of annealing temperatures on the structural and optical properties of sol-gel processed nanocrystalline $BiFeO_3$ thin films,” *Thin Solid Films*, vol. 524, pp. 57–61, 2012, doi: 10.1016/j.tsf.2012.09.015.

[196] L. Bi *et al.*, “Structural , magnetic , and optical properties of $BiFeO_3$ and Bi_2FeMnO_6 epitaxial thin films : An experimental and first-principles study,” pp. 1–10, 2008, doi: 10.1103/PhysRevB.78.104106.

[197] S. Hussain, S. K. Hasanain, G. Hassnain Jaffari, and S. I. Shah, “Thickness dependent magnetic and ferroelectric properties of $LaNiO_3$ buffered $BiFeO_3$ thin films,” *Curr. Appl. Phys.*, vol. 15, no. 3, pp. 194–200, 2015, doi: 10.1016/j.cap.2014.12.012.

[198] A. Kumar, A. Kumar, S. Tyagi, R. Chandra, and D. Kaur, “Room temperature tunability of

ferroelectricity and dielectricity in La and Mn codoped $BiFeO_3$ nanoflakes: Implications for electronic devices applications," *Ceram. Int.*, vol. 49, no. 2, pp. 1960–1969, 2022, doi: 10.1016/j.ceramint.2022.09.161.

[199] X. Zhang *et al.*, "Dielectric property and tunability of multilayer BST-BTO thin film in the terahertz range," vol. 155, no. June, pp. 4–8, 2022, doi: 10.1016/j.optlastec.2022.108366.

[200] C. A. Vasilescu *et al.*, "Structure, morphology and optical properties of multilayered sol-gel $BaTi_{0.85}Zr_{0.15}O_3$ thin films," *Appl. Surf. Sci.*, vol. 265, pp. 510–518, 2013, doi: 10.1016/j.apsusc.2012.11.036.

[201] H. Liu, M. Yao, W. Gao, Z. Su, and X. Yao, "Dual interfacial modification via anodizing method for achieving enhanced breakdown strength in multi-layer anodized alumina/$Sr_{0.85}Bi_{0.1}TiO_3$ films," *J. Alloys Compd.*, vol. 817, p. 152783, 2020, doi: 10.1016/j.jallcom.2019.152783.

[202] A. Kursumovic, W. W. Li, S. Cho, P. J. Curran, D. H. L. Tjhe, and J. L. MacManus-Driscoll, "Lead-free relaxor thin films with huge energy density and low loss for high temperature applications," *Nano Energy*, vol. 71, 2020, doi: 10.1016/j.nanoen.2020.104536.

[203] Y. Hu *et al.*, "High energy storage performance in lead-free $BiFeO_3$-$BaTiO_3$ ferroelectric thin film fabricated by pulsed laser deposition," *AIP Adv.*, vol. 9, no. 8, pp. 1–6, 2019, doi: 10.1063/1.5100928.

[204] S. Sharma, M. Tomar, A. Kumar, N. K. Puri, and V. Gupta, "Stress induced enhanced polarization in multilayer $BiFeO_3$/$BaTiO_3$ structure with improved energy storage properties," *AIP Adv.*, vol. 5, no. 10, 2015, doi: 10.1063/1.4934578.

[205] C. Lien *et al.*, "The Investigation for Thickness-Dependent Electrical Performance on $BaTiO_3$ /$BiFeO_3$ Bilayer Ferromagnetic Capacitors," *IEEE Trans. Electron Devices*, vol. 67, no. 8, pp. 3417–3423, 2020, doi: 10.1109/TED.2020.2998450.

[206] A. P. Sharma, D. K. Pradhan, S. K. Pradhan, and M. Bahoura, "Large energy storage density performance of epitaxial BCT/BZT heterostructures via interface engineering," *Sci. Rep.*, vol. 9, no. 1, pp. 1–8, 2019, doi: 10.1038/s41598-019-53358-0.

[207] M. D. Nguyen, "Energy storage properties of multilayer thin films based on relaxor-ferroelectric $(Ba_{0.9}Sr_{0.1})(Zr_{0.4}Ti_{0.6})O_3$ and paraelectric $Sr(Zr_{0.1}Ti_{0.9})O_3$ layers," *Mater. Res. Bull.*, vol. 168, no. August, p. 112472, 2023, doi: 10.1016/j.materresbull.2023.112472.

[208] L. G. Wang, G. B. Yu, C. M. Zhu, M. W. Yao, F. C. Liu, and W. J. Kong, "Synthesis and room-temperature multiferroic properties of lead-free $Bi_4Ti_3O_{12}$/$NiFe_2O_4$ nanocomposite films," *Ceram. Int.*, vol. 46, no. 10, pp. 16973–16978, 2020, doi: 10.1016/j.ceramint.2020.03.281.

[209] X. Zhao *et al.*, “Effect of the thickness of $Sr_2Bi_4Ti_5O_{18}$ transition layer on the properties of BiFeO3/Sr2Bi4Ti5O18 bilayer composite thin films,” *Ceram. Int.*, vol. 46, no. 8, pp. 10536–10544, 2020, doi: 10.1016/j.ceramint.2020.01.055.

[210] J. Ding, H. Chen, X. Wang, H. Fu, and L. Ma, “Unusual enhanced photoluminescence from highly lattice mismatched ZnO/Cu_3N multilayer films,” *Mater. Res. Bull.*, vol. 96, pp. 40–46, 2017, doi: 10.1016/j.materresbull.2016.12.040.

[211] S. Yu, C. Zhang, M. Wu, H. Dong, and L. Li, “Ultra-high energy density thin-film capacitors with high power density using $BaSn_{0.15}Ti_{0.85}O_3/Ba_{0.6}Sr_{0.4}TiO_3$ heterostructure thin films,” *J. Power Sources*, vol. 412, no. November 2018, pp. 648–654, 2019, doi: 10.1016/j.jpowsour.2018.12.012.

[212] S. K. Sahoo *et al.*, “Improved dielectric properties and their temperature insensitivity in multilayered $Ba_{0.8}Sr_{0.2}TiO_3/ZrO_2$ thin films,” *J. Appl. Phys.*, vol. 109, no. 6, pp. 0–6, 2011, doi: 10.1063/1.3563576.

[213] S. Khan *et al.*, “Role of Ca doping on oxygen vacancy production in modulating dielectric, ferroelectric and magnetic polarization in $BaTiO_3$ thin films,” *J. Mater. Res. Technol.*, vol. 16, pp. 993–1007, 2022, doi: 10.1016/j.jmrt.2021.11.148.

[214] C. Diao, H. Liu, H. Hao, M. Cao, Z. Yao, and H. Zheng, “Dielectric, ferroelectric properties and photoconductivity effect of sol-gel grown $SrTiO_3/BaTiO_3$ thin film heterostructure,” *Ceram. Int.*, vol. 44, no. 11, pp. 12157–12161, 2018, doi: 10.1016/j.ceramint.2018.03.265.

[215] M. K. Adak, A. Mukherjee, A. Chowdhury, J. Khatun, U. K. Ghorai, and D. Dhak, “Electrical and energy storage properties of nickel substituted barium bismuth niobate nano-ceramics prepared by chemical route,” *J. Mater. Sci. Mater. Electron.*, vol. 29, no. 18, pp. 15847–15858, 2018, doi: 10.1007/s10854-018-9671-2.

[216] F. M. Pontes *et al.*, “Materials Science & Engineering B Electrical transport properties and complex impedance investigation of Fe^{3+} and La^{3+} co-doping (Pb , Sr)TiO_3 thin films,” *Mater. Sci. Eng. B*, vol. 236–237, no. November, pp. 179–188, 2018, doi: 10.1016/j.mseb.2018.11.013.

[217] M. K. Adak, A. Mukherjee, A. Chowdhury, U. K. Ghorai, and D. Dhak, “Structure-property correlation of $Ba_{1-x}Cu_xBi_2(Nb_{1-x}Ta_x)_2O_9$ ferroelectric nano ceramics prepared by chemical route,” *J. Alloys Compd.*, vol. 740, pp. 203–211, 2018, doi: 10.1016/j.jallcom.2018.01.025.

[218] S. Brahma, R. N. P. Choudhary, and A. K. Thakur, “AC impedance analysis of $LaLiMo_2O_8$ electroceramics,” *Phys. B Condens. Matter*, vol. 355, no. 1–4, pp. 188–201, 2005, doi: 10.1016/j.physb.2004.10.091.

[219] D. R. Arunkumar, S. Anjelin Ursula Portia, and K. Ramamoorthy, "Design and fabrication of novel Tb doped $BaTiO_3$ thin film with superior light-harvesting characteristics for dye sensitized solar cells," *Surfaces and Interfaces*, vol. 22, no. August 2020, p. 100853, 2021, doi: 10.1016/j.surfin.2020.100853.

[220] K. Siemek, A. Olejniczak, L. N. Korotkov, P. Konieczny, and A. V. Belushkin, "Investigation of surface defects in $BaTiO_3$ nanopowders studied by XPS and positron annihilation lifetime spectroscopy," *Appl. Surf. Sci.*, vol. 578, no. October 2021, p. 151807, 2022, doi: 10.1016/j.apsusc.2021.151807.

[221] Y. Mei *et al.*, "Enhanced multiferroic properties of $Bi_4Ti_{3-x}Co_xO_{12}/La_{0.67}Sr_{0.33}MnO_3$ layered composite thin films," *Ceram. Int.*, vol. 48, no. 15, pp. 21769–21779, 2022, doi: 10.1016/j.ceramint.2022.04.154.

[222] X. Zhao *et al.*, "Effect of the thickness of $Sr_2Bi_4Ti_5O_{18}$ transition layer on the properties of $BiFeO_3/Sr_2Bi_4Ti_5O_{18}$ bilayer composite thin films," vol. 46, no. November 2019, pp. 10536–10544, 2020, doi: 10.1016/j.ceramint.2020.01.055.

[223] D. R. Arunkumar, S. Anjelin Ursula Portia, and K. Ramamoorthy, "Design and fabrication of novel Tb doped $BaTiO_3$ thin film with superior light-harvesting characteristics for dye sensitized solar cells," *Surfaces and Interfaces*, vol. 22, no. November 2020, p. 100853, 2021, doi: 10.1016/j.surfin.2020.100853.

[224] K. Y. Yun, M. Noda, M. Okuyama, H. Saeki, H. Tabata, and K. Saito, "Structural and multiferroic properties of $BiFeO_3$ thin films at room temperature," *J. Appl. Phys.*, vol. 96, no. 6, pp. 3399–3403, 2004, doi: 10.1063/1.1775045.

[225] N. Panwar, I. Coondoo, A. Tomar, A. L. Kholkin, V. S. Puli, and R. S. Katiyar, "Nanoscale piezoresponse and magnetic studies of multiferroic Co and Pr co-substituted BFO thin films," *Mater. Res. Bull.*, vol. 47, no. 12, pp. 4240–4245, 2012, doi: 10.1016/j.materresbull.2012.09.026.

[226] P. Yang *et al.*, "Effect of $BaTiO_3$ buffer layer on multiferroic properties of $BiFeO_3$ thin films," *J. Appl. Phys.*, vol. 105, no. 6, 2009, doi: 10.1063/1.3055413.

[227] R. Irandoust and A. Gholizadeh, "A comparative study of the effect of the non-magnetic and magnetic trivalent rare-earth ion substitutions on bismuth ferrite properties: Correlation between the crystal structure and physical properties," *Solid State Sci.*, vol. 101, no. January, p. 106142, 2020, doi: 10.1016/j.solidstatesciences.2020.106142.

[228] S. Priya Balmuchu, S. R. N. K. Mangalampalli, and P. Dobbidi, "Dielectric spectroscopy and ferroelectric studies of multiferroic bismuth ferrite modified barium titanate ceramics for energy

storage capacitor applications," *Mater. Sci. Eng. B Solid-State Mater. Adv. Technol.*, vol. 282, no. February, p. 115791, 2022, doi: 10.1016/j.mseb.2022.115791.

[229] M. L. V. Mahesh, P. Pal, V. V. B. Prasad, and A. R. James, "Fatigue and leakage current characteristics of lead free bilayer thin film structures," *Ceram. Int.*, vol. 48, no. 7, pp. 9006–9013, 2022, doi: 10.1016/j.ceramint.2021.12.082.

[230] S. Yu, C. Zhang, M. Wu, H. Dong, and L. Li, "Ultra-high energy density thin-film capacitors with high power density using $BaSn_{0.15}Ti_{0.85}O_3/Ba_{0.6}Sr_{0.4}TiO_3$ heterostructure thin films," *J. Power Sources*, vol. 412, no. October 2018, pp. 648–654, 2019, doi: 10.1016/j.jpowsour.2018.12.012.

[231] Y. Dai, Q. Gao, C. Cui, L. Yang, C. Li, and X. Li, "Role of ferroelectric/ferromagnetic layers on the ferroelectric properties of magnetoelectric composite films derived by chemical solution deposition," *Mater. Res. Bull.*, vol. 99, no. November 2017, pp. 424–428, 2018, doi: 10.1016/j.materresbull.2017.11.052.

[232] S. Lamichhane, S. Sharma, M. Tomar, A. Kumar, and V. Gupta, "Influence of laser fluence in modifying energy storage property of $BiFeO_3$ thin film capacitor," *J. Energy Storage*, vol. 32, no. May, 2020, doi: 10.1016/j.est.2020.101769.

[233] A. Jamil and M. A. Rafiq, "Ferroelectric, dielectric properties and electrical conduction mechanism of epitaxial $B_{1-x}Dy_xFeO_3$ (x = 0.05, 0.075, 0.1, 0.125) thin films prepared by pulsed laser deposition," *Ceram. Int.*, vol. 44, no. 18, pp. 22574–22582, 2018, doi: 10.1016/j.ceramint.2018.09.031.

[234] M. M. Shehata, M. O. Abdel-Hamed, and K. Abdelhady, "Structural and dielectric properties of Au/perylene-66/p-Si/Al hybrid heterojunction diode," *Vacuum*, vol. 151, pp. 96–107, 2018, doi: 10.1016/j.vacuum.2018.02.014.

[235] R. Gupta, V. Gupta, and M. Tomar, "Structural and dielectric properties of PLD grown BST thin films," *Vacuum*, vol. 159, no. October 2018, pp. 69–75, 2019, doi: 10.1016/j.vacuum.2018.10.010.

[236] J. Sharma, N. Sharma, J. Parashar, V. K. Saxena, D. Bhatnagar, and K. B. Sharma, "Dielectric properties of nanocrystalline Co-Mg ferrites," *J. Alloys Compd.*, vol. 649, no. 108, pp. 362–367, 2015, doi: 10.1016/j.jallcom.2015.07.103.

[237] K. C. Verma, M. Ram, J. Singh, and R. K. Kotnala, "Impedance spectroscopy and dielectric properties of Ce and la substituted $Pb_{0.7}Sr_{0.3}(Fe_{0.012}Ti_{0.988})O_3$ nanoparticles," *J. Alloys Compd.*, vol. 509, no. 15, pp. 4967–4971, 2011, doi: 10.1016/j.jallcom.2011.01.144.

[238] T. Prodromakis and C. Papavassiliou, “Engineering the Maxwell-Wagner polarization effect,” *Appl. Surf. Sci.*, vol. 255, no. 15, pp. 6989–6994, 2009, doi: 10.1016/j.apsusc.2009.03.030.

[239] S. Riaz, S. M. H. Shah, A. Akbar, S. Atiq, and S. Naseem, “Effect of Mn doping on structural, dielectric and magnetic properties of $BiFeO_3$ thin films,” *J. Sol-Gel Sci. Technol.*, vol. 74, no. 2, pp. 329–339, 2015, doi: 10.1007/s10971-014-3461-y.

[240] R. A. Mondal, B. S. Murty, and V. R. K. Murthy, “Maxwell-Wagner polarization in grain boundary segregated NiCuZn ferrite,” *Curr. Appl. Phys.*, vol. 14, no. 12, pp. 1727–1733, 2014, doi: 10.1016/j.cap.2014.10.005.

[241] A. Radoń, D. Łukowiec, M. Kremzer, J. Mikuła, and P. Włodarczyk, “Electrical conduction mechanism and dielectric properties of spherical shaped Fe_3O_4 nanoparticles synthesized by co-precipitation method,” *Materials (Basel).*, vol. 11, no. 5, 2018, doi: 10.3390/ma11050735.

[242] S. P. Balmuchu and P. Dobbidi, “Temperature-dependent broadband dielectric and ferroelectric properties of $Ba_{(1-x)}Sr_xTiO_3$ ceramics for energy storage capacitor applications,” *J. Mater. Sci. Mater. Electron.*, vol. 32, no. 7, pp. 9623–9639, 2021, doi: 10.1007/s10854-021-05624-z.

[243] X. Yan, W. Ren, P. Shi, X. Wu, and X. Yao, “Enhanced tunable dielectric properties of $Ba_{0.5}Sr_{0.5}TiO_3/Bi_{1.5}Zn_{1.0}Nb_{1.5}O_7$ multilayer thin films by a sol-gel process,” *Thin Solid Films*, vol. 520, no. 2, pp. 789–792, 2011, doi: 10.1016/j.tsf.2011.04.118.

[244] S. Yousfi, M. El Marssi, and H. Bouyanfif, “Impedance spectroscopy and conduction mechanism of a $BiFe_{0.95}Mn_{0.05}O_3$ thin film,” *Thin Solid Films*, vol. 724, no. August 2020, p. 138616, 2021, doi: 10.1016/j.tsf.2021.138616.

[245] J. Qian, C. H. Yang, Y. J. Han, X. S. Sun, and L. X. Chen, “Reduced leakage current , enhanced energy storage and dielectric properties in (Ce , Mn) -codoped $Ba_{0.6}Sr_{0.4}TiO_3$ thin fi lm,” *Ceram. Int.*, vol. 44, no. 17, pp. 20808–20813, 2018, doi: 10.1016/j.ceramint.2018.08.082.

[246] S. Satapathy, P. Verma, P. K. Gupta, C. Mukherjee, V. G. Sathe, and K. B. R. Varma, “Structural, dielectric and ferroelectric properties of multilayer lithium tantalate thin films prepared by sol-gel technique,” *Thin Solid Films*, vol. 519, no. 6, pp. 1803–1808, 2011, doi: 10.1016/j.tsf.2010.10.016.

[247] S. Khosravi H, V. K. Veerapandiyan, R. Vallant, and K. Reichmann, “Effect of processing conditions on the structural properties and corrosion behavior of TiO_2–SiO_2 multilayer coatings derived via the sol-gel method,” *Ceram. Int.*, vol. 46, no. 11, pp. 17741–17751, 2020, doi: 10.1016/j.ceramint.2020.04.079.

[248] A. Timoumi, O. O. Alameer, and S. N. Alamri, “Results in Materials Intensive study of coating

multilayer TiO_2 nanoparticles thin films used for optoelectronics devices," *Results Mater.*, vol. 18, no. September 2022, p. 100390, 2023, doi: 10.1016/j.rinma.2023.100390.

[249] S. Y. Lee, J. S. Kim, C. W. Ahn, H. In Hwang, and W. Kim, "Impedance spectroscopy and relaxation phenomena of (Na,K) excess $Na_{0.5}K_{0.5}NbO_3$ thin films grown by chemical solution deposition," *Thin Solid Films*, vol. 519, no. 2, pp. 947–951, 2010, doi: 10.1016/j.tsf.2010.08.133.

[250] V. Purohit and R. N. P. Choudhary, "Fabrication and impedance spectroscopy of lead free magneto-electric compound: $Bi(Ca_{0.25}Ti_{0.25}Fe_{0.5})O_3$," *Appl. Phys. A Mater. Sci. Process.*, vol. 125, no. 2, 2019, doi: 10.1007/s00339-019-2417-z.

[251] Y. Zhao *et al.*, "Interfacial lattice coupling engineering in all-inorganic coupled flexible films for dielectric energy storage," *Acta Mater.*, vol. 264, no. July 2023, p. 119554, 2024, doi: 10.1016/j.actamat.2023.119554.

[252] S. P. Balmuchu, E. Radhika, and P. Dobbidi, "The impact of oxygen partial pressure in modifying energy storage property of lanthanum doped multiferroic bismuth ferrite thin films deposited via pulsed laser deposition," *J. Energy Storage*, vol. 71, no. March, p. 108179, 2023, doi: 10.1016/j.est.2023.108179.

[253] S. P. Balmuchu, S. Sahu, and P. Dobbidi, "Enhanced magnetic properties and leakage current mechanism in bismuth lanthanum ferrite thin films coupled with impedance and magnetic studies," *Vacuum*, vol. 215, no. April, p. 112356, 2023, doi: 10.1016/j.vacuum.2023.112356.

[254] T. Yang, J. Wei, Y. Guo, Z. Lv, Z. Xu, and Z. Cheng, "Manipulation of Oxygen Vacancy for High Photovoltaic Output in Bismuth Ferrite Films," *ACS Appl. Mater. Interfaces*, vol. 11, no. 26, pp. 23372–23381, 2019, doi: 10.1021/acsami.9b06704.

[255] L. Fang, M. Shen, J. Yang, and Z. Li, "Reduced dielectric loss and leakage current in $CaCu_3Ti_4O_{12}/SiO_2/CaCu_3Ti_4O_{12}$ multilayered films," *Solid State Commun.*, vol. 137, no. 7, pp. 381–386, 2006, doi: 10.1016/j.ssc.2005.12.004.

[256] Y. Liu, M. Yao, and X. Yao, "Excellent leakage current performance and energy storage density achieved in Zr-modified $Sr_{0.92}5Bi_{0.05}TiO_3$ thin film," *Mater. Lett.*, vol. 299, p. 130083, 2021, doi: 10.1016/j.matlet.2021.130083.

[257] E. A. C. Astrath *et al.*, "Conduction mechanisms in thin $(0.6)BiFeO_3$-$(0.4)PbTiO_3$ films," *J. Mater. Res. Technol.*, vol. 17, pp. 2888–2896, 2022, doi: 10.1016/j.jmrt.2022.02.024.

[258] P. Wang, X. Wang, G. Li, Y. Li, X. Yao, and Z. Pan, "Interface engineering to optimize polarization and electric breakdown strength of $Ba_2Bi_{3.97}Pr_{0.03}Ti_5O_{18}/BiFeO_3$ ferroelectric thin-

film for high-performance capacitors," *Chem. Eng. J.*, vol. 433, no. P3, p. 133676, 2022, doi: 10.1016/j.cej.2021.133676.

[259] S. Yu, C. Zhang, M. Wu, H. Dong, and L. Li, "Ultra-high energy density thin-film capacitors with high power density using $BaSn_{0.15}Ti_{0.85}O_3/Ba_{0.6}Sr_{0.4}TiO_3$ heterostructure thin films," *J. Power Sources*, vol. 412, no. December 2018, pp. 648–654, 2019, doi: 10.1016/j.jpowsour.2018.12.012.

[260] N. Sun, Y. Li, X. Liu, and X. Hao, "High energy-storage density under low electric field in lead-free relaxor ferroelectric film based on synergistic effect of multiple polar structures," *J. Power Sources*, vol. 448, no. September 2019, p. 227457, 2020, doi: 10.1016/j.jpowsour.2019.227457.

[261] Z. Tang *et al.*, "High energy-storage density of lead-free $BiFeO_3$ doped $Na_{0.5}Bi_{0.5}TiO_3$-$BaTiO_3$ thin film capacitor with good temperature stability," *J. Alloys Compd.*, vol. 757, pp. 169–176, 2018, doi: 10.1016/j.jallcom.2018.05.072.

[262] M. Liu *et al.*, "Energy storage in epitaxial multilayered $BiFeO_3/Na_{0.5}Bi_{0.5}TiO_3/La_{0.7}Sr_{0.3}MnO_3$ thin films," *J. Alloys Compd.*, vol. 967, no. August, p. 171767, 2023, doi: 10.1016/j.jallcom.2023.171767.

[263] S. Xiao, H. Sun, X. Liu, and H. Sui, "High-performance $(Na_{0.5}Bi_{0.5})(Ti_{0.97}Fe_{0.03})O_3$-based heterostructure thin films for energy storage capacitors," *Ceram. Int.*, vol. 48, no. 15, pp. 21448–21456, 2022, doi: 10.1016/j.ceramint.2022.04.106.

[264] T. Zhang *et al.*, "Self-polarization and energy storage performance in antiferroelectric-insulator multilayer thin films," *Compos. Part B Eng.*, vol. 221, no. May, p. 109027, 2021, doi: 10.1016/j.compositesb.2021.109027.

[265] B. Wang *et al.*, "Excellent energy storage performance of Mn-doped $SrTiO_3$-$BiFeO_3$ thin films by microstructure modulation," *J. Alloys Compd.*, vol. 968, no. May, p. 171756, 2023, doi: 10.1016/j.jallcom.2023.171756.